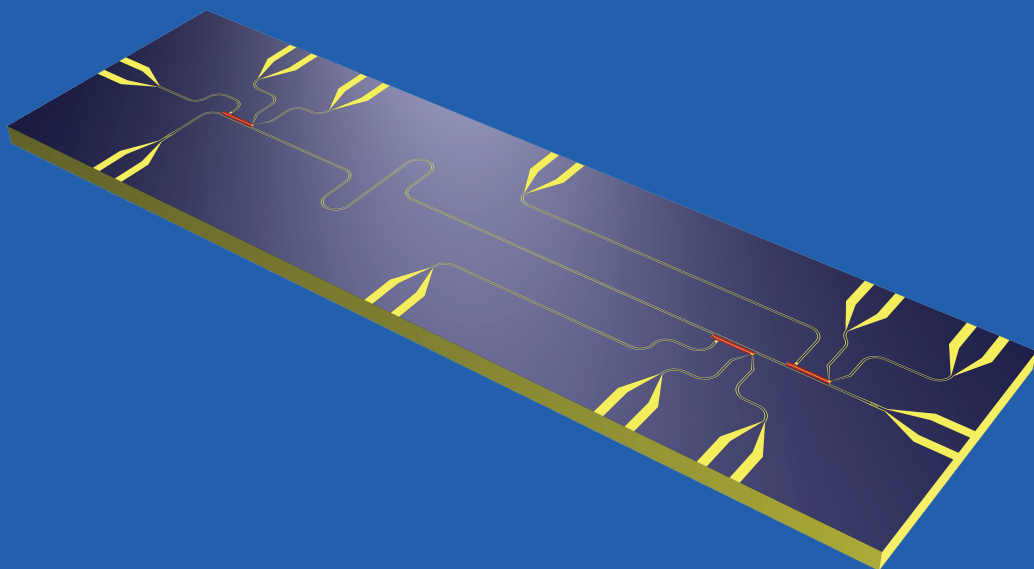


Realizing Quantum Gates and Algorithms

with Three Superconducting Qubits



Matthias Baur

DISS. ETH NO. 20359

**REALIZING QUANTUM GATES AND ALGORITHMS
WITH THREE SUPERCONDUCTING QUBITS**

A dissertation submitted to

ETH ZURICH

for the degree of

Doctor of Sciences

presented by

Matthias Baur

Dipl. Phys., ETH Zurich

born September 21st, 1983

citizen of Winterthur, Switzerland

accepted on the recommendation of

Prof. Dr. Andreas Wallraff, examiner

Dr. Denis Vion, co-examiner

2012

Abstract

Superconducting quantum circuits have become a promising architecture for the potential realization of a scalable quantum computer. These circuits consist of capacitors, inductors and Josephson junctions, and the combination of these elements allows artificial on-chip two-level quantum systems (superconducting qubits) to be engineered, which can be used as the basic units of quantum information.

This thesis presents the realization and characterization of fundamental elements of a quantum processor comprised of up to three superconducting transmon qubits capacitively coupled to a microwave transmission line resonator. In this circuit quantum electrodynamics architecture, the resonator acts as a quantum bus connecting the qubits and simultaneously allows for a joint readout of the three-qubit quantum states. High fidelity single-qubit operations are carried out by applying microwave signals to additional transmission lines coupled to each individual qubit, and fully characterized using quantum process tomography. For the realization of two-qubit operations, two different approaches are discussed. The first is based on sideband transitions between the resonator photons and each qubit. In combination with the single-qubit operations, this allows us to generate and reconstruct highly entangled two-qubit states using state tomography techniques. Furthermore, the generation of photon Fock states with up to five photons inside the resonator is demonstrated. The second approach exploits the fact that two qubits can coherently exchange a single excitation mediated via virtual photons in the resonator. This allows the realization of a conditional phase operation between each pair of the three qubits, which is used to demonstrate the two-qubit Deutsch-Jozsa algorithm, and to generate and fully reconstruct highly entangled three-qubit states useful for quantum teleportation and quantum error correction. Furthermore, a three-qubit Toffoli gate is efficiently implemented by exploiting the third energy level of the transmon qubit. These quantum operations are fully characterized using quantum process tomography.

Zusammenfassung

Supraleitende Quantenschaltungen haben sich zu einer vielversprechenden Architektur für die mögliche Realisierung eines skalierbaren Quantencomputers entwickelt. Diese Schaltungen bestehen aus Kondensatoren, Spulen und Josephson-Kontakten, und die Kombination dieser Elemente ermöglicht die künstliche Fabrikation von Zwei-Niveau-Quantensystemen (supraleitende Qubits) auf einem Mikrochip, welche dann als kleinstmögliche Speichereinheiten in der Quanteninformationsverarbeitung eingesetzt werden können.

Diese Doktorarbeit präsentiert die Realisierung und Charakterisierung von grundlegenden Elementen eines Quantenprozessors anhand von bis zu drei supraleitenden Transmon-Qubits, welche kapazitiv an einen Wellenleiterresonator im Mikrowellenbereich gekoppelt sind. In dieser Schaltkreis-Quantenelektrodynamik Architektur fungiert der Resonator als ein Quantenbus der die Qubits miteinander verbindet und ermöglicht gleichzeitig die simultane Messung aller drei Qubit-Zuständen. Operationen auf einem einzelnen Qubit mit hoher Genauigkeit können mit kurzen Mikrowellenpulsen ausgeführt, und mit Quanten-Prozess-Tomographie charakterisiert werden. Für die Realisierung von Zwei-Qubit Operationen werden zwei verschiedene Möglichkeiten diskutiert. Die Eine basiert auf Seitenbandübergängen zwischen Photonen im Resonator und den einzelnen Qubits. Dies ermöglicht uns in Kombination mit den Ein-Qubit Operationen stark verschränkte Zwei-Qubit-Zustände zu präparieren und mit Hilfe von Zustands-Tomographie komplett zu rekonstruieren. Zusätzlich wird die Erzeugung von Photonen Fock-Zuständen mit bis zu fünf Photonen innerhalb des Resonators gezeigt. Die zweite Möglichkeit nutzt die Tatsache, dass zwei Qubits mit Hilfe von virtuellen Photonen im Resonator eine einzelne Anregung austauschen können. Dies ermöglicht die Realisierung eines kontrollierten Phasengatters zwischen jedem Paar der drei Qubits, welches dann verwendet wird um den Deutsch-Jozsa Algorithmus mit zwei Qubits zu implementieren. Zusätzlich ermöglicht es uns stark verschränkte Drei-Qubit-Zustände zu präparieren und zu rekonstruieren, welche zur Quantenteleportation und Quantenfehlerkorrektur verwendet werden können. Ferner wird mit Hilfe des dritten Energieniveaus des Transmon-Qubits eine effiziente Implementierung des Drei-Qubit Toffligatters demonstriert, und alle Quantengatter werden mit Quanten-Prozess-Tomographie vollständig charakterisiert.

Contents

1	Introduction	1
2	Short Review of Quantum Information Theory	7
2.1	Quantum bit	7
2.1.1	Many qubits	9
2.2	Quantum operations and quantum circuits	10
2.2.1	Single-qubit operations	11
2.2.2	Multi-qubit operations	12
2.2.3	The power of quantum parallelism	13
3	Quantum Circuits: On-Chip Quantum Processor	17
3.1	Superconducting qubits	18
3.1.1	The Josephson junction	21
3.1.2	The Cooper pair box qubit	25
3.1.3	Transmon qubit	33
3.2	Circuit quantum electrodynamics	36
3.2.1	Generalized Jaynes-Cumming Hamiltonian	39
3.2.2	The dispersive regime	42
3.2.3	Quantum non-demolition readout of the qubit state	46
3.2.4	Driving the qubit through the resonator	48
3.2.5	Transmission line resonator	48

3.2.6	Coplanar waveguide resonator	52
3.2.7	Coupling a transmon qubit to a coplanar waveguide resonator	54
4	Measurement Setup	57
4.1	Mounting the sample	58
4.2	Cryogenic wiring	60
4.3	Qubit control and data acquisition	66
4.3.1	IQ modulation	66
4.3.2	Data acquisition	70
4.3.3	Signal synchronization	71
4.4	Magnetic flux bias line	73
4.4.1	Flux line induced decoherence	75
4.4.2	Optimal pulse control	79
4.4.3	Measuring the flux pulse shape through its interaction with the qubit	84
5	Control of a Single Qubit	87
5.1	Qubit spectroscopy	87
5.2	Strong qubit driving	90
5.2.1	Rabi oscillations	91
5.2.2	Dressed states	92
5.2.3	Measurement of Autler-Townes and Mollow transition	94
5.3	Measurement of the qubit coherences	101
5.3.1	Measurement of the energy decay time	101
5.3.2	Measurement of the phase coherence	101
5.4	Single-qubit gates	104
5.4.1	Rotations around the x and y axis	104
5.4.2	Optimal pulse control for high fidelity single-qubit gates	105
5.4.3	Pulse calibration	108
5.4.4	Rotations around the z axis	109
5.5	Quantum state and process reconstruction	111
5.5.1	Quantum state tomography	112
5.5.2	Quantum process tomography	114
5.6	Conclusion	116

6	Quantum Operations between Multiple Qubits	119
6.1	Qubit-qubit interaction with sidebands	120
6.1.1	Selection rules for the driven Jaynes-Cummings Hamiltonian	122
6.1.2	Cavity quantum electrodynamics with separate photon storage and qubit readout modes	123
6.1.3	Spectroscopy and Rabi oscillations on the blue sideband transition	128
6.1.4	Fock state preparation	133
6.1.5	Bell-state preparation	136
6.1.6	Conclusion	138
6.2	Qubit-qubit interactions controlled with fast magnetic flux pulses .	138
6.2.1	The sample	139
6.2.2	The dispersive J-coupling	142
6.2.3	Controlled-PHASE and controlled-NOT gate	146
6.2.4	Generation of Bell-states	151
6.2.5	Deutsch-Jozsa algorithm	151
6.3	Benchmarking a teleportation circuit	156
6.3.1	Outlook	163
7	Realization of the Toffoli gate	165
7.1	Error correction	165
7.2	Toffoli gate	169
7.2.1	Gate calibration	172
7.2.2	Gate characterization	176
7.3	Conclusion	179
8	Outlook	181
A	Appendix	185
A.1	Derivation of the phase ramping for DRAG	185
A.2	Quantum state and quantum process tomography	188
A.2.1	State maximum-likelihood estimation	188
A.2.2	Quantum process tomography	190
A.2.3	Process maximum-likelihood estimation	192
A.3	Entanglement classes	193
A.4	Entanglement measures	195
A.4.1	Convex roof extension	196

Contents

A.4.2	Concurrence	196
A.4.3	Entanglement of formation	197
A.4.4	Three-tangle	197
A.5	Entanglement witnesses	198
	Bibliography	201
	List of Publications	231
	Acknowledgements	235
	Curriculum Vitae	236

1

Introduction

One of the greatest technological advancements in the last century lies in digital computer science. The idea of storing information and performing calculations in the most simple mathematical model, using strings of 0's and 1's (string of bits), proved to be very successful. In the early years, the basic electronic elements of a computer consisted of vacuum tubes and the whole machine occupied the space of a whole living room. At that time people believed that there was a worldwide demand of no more than five computers. These days however, about every second person in this world has one in their pocket. This amazing development was driven by the discovery of the transistor, in 1947, which became the new basic electronic element. As noticed by Gordon Moore in 1965 the number of transistors in a computer of a given price has been doubling every two years until today (this observation is now known as the Moor's law).

The groundbreaking result for this development was the invention of an abstract mathematical model by Alan Turing in 1936 [[Turing37](#)], describing a hypothetical device of a programmable computing machine, known as the Turing machine. This device, as he claimed, is universal in a sense that if an algorithm can be executed on any machine, than there is an equivalent algorithm that solves the same problem on the Turing machine. This conjecture, also known as the Church-Turing thesis, is now widely accepted even though it is not formally proven. After the first computers had been built, people started to think about how efficiently the Turing machine can solve problems, namely, whether the resources required grow exponentially or polynomially with the problem size. This led to the strong Church-Turing thesis

which states that any machine that performs some algorithm can be efficiently (in polynomial time) simulated using the Turing machine. However, it did not take long until probabilistic algorithms were found for problems that seemed to have no efficient solution on a Turing machine. While this challenge to the strong Church-Turing thesis could then easily be fixed by replacing the Turing machine with a probabilistic Turing machine, it inspired Richard Feynman [Feynman82] and David Deutsch to think about whether the Turing machine can be made even more powerful when including the principles of quantum mechanics. In 1985 David Deutsch presented a model of a universal quantum computer [Deutsch85], that can perfectly simulate any Turing machine, and even any quantum computer or simulator. And indeed, he later discovered the first quantum algorithm (the Deutsch-Jozsa algorithm) which is capable of solving a given problem faster than any classical computer [Deutsch92], but not more efficiently according to the definition as given above. It was Peter Shor in 1994 [Shor94] who first demonstrated the full potential power of a quantum computer by developing an efficient algorithm for the factorization of large integer numbers, which takes polynomial time on a quantum computer but requires, up to now, exponential time for any known classical algorithm. This problem is assumed to be so hard to solve on a classical computer that it is widely used in encryption algorithms (such as RSA encryption) for secure communication. Besides the possibility to decipher secret messages, these results demonstrate a strong indication that quantum computers have the potential of outperforming any machine based on classical physics only.

Very similar to a classical computer, a quantum computer would also store its information in two distinct states 0 and 1, but unlike in classical physics, these states can exist in a quantum superposition. A superposition state can exist in 0 and 1 at the same time. This offers the possibility to process quantum information on many states in parallel, a powerful tool not available on classical computers. Such a quantum bit (qubit) can for example be formed by the ground (0) and first excited state (1) of an electron in an atom. The physical realization of such a computer however turned out to be extremely challenging. While the individual quantum system (for example a single atom) needs to be well isolated from its environment to protect it from noise (decoherence), it must at the same time be coherently controlled with extremely high precision. Furthermore, the qubits then need to be wired together in a complex way to transfer and manipulate quantum information. These tasks are so daunting that many people were in doubt about the feasibility of the physical realization of a quantum computer. The discovery of quantum error-correction schemes [Knill05, Shor95, Steane96b] was thus a

huge breakthrough. These schemes allow for accurate quantum computation even with faulty quantum operations and in the presence of decoherence, as long as the error rate per operation is below a certain threshold (1 – 30 errors per 1000 operations [Knill05, DiVincenzo09]).

Following this discovery a number of physical systems have been proposed and extensively studied in the context of quantum information processing. Some of the most promising quantum systems to date are the polarization states of a photon [Kok07], two energy levels of an electron in a trapped atom [Saffman10] or ion [Häffner08, Duan10], the two spin directions of an electron or nucleus [Vandersypen04] in a magnetic field (NMR), and the quantum states of artificial superconducting electronic circuits [Clarke08]. First building blocks of a quantum computer and first quantum algorithms have been demonstrated with these systems. The Deutsch-Jozsa algorithm could be realized in NMR [Chuang98], ion trap [Gulde03], photonic [Takeuchi00] systems and with superconducting circuits [DiCarlo09]. The more challenging Shor algorithm has only been demonstrated in a compiled version [Beckman96] for the factorization of the number 15 with NMR techniques [Vandersypen01] and photons [Lanyon07, Lu07, Politi09]. First experimental realization of basic quantum error correction schemes have been made in NMR [Cory98], and subsequently in linear optics [Pittman05], ion traps [Chiaverini04, Schindler11] and more recently also in superconducting circuits [Reed12]. Current state of the art experiments carried out in many laboratories routinely achieve coherent manipulation of multiple qubits, and an experiment on a maximal number of 14 qubits has recently been realized with trapped ions [Monz11].

In NMR, trapped ions and photonic systems, the properties of the qubits are given by nature. In contrast, superconducting qubits are made of artificial electronic structures consisting of several circuit components, namely capacitors, inductors and the Josephson elements. Different combinations of these elements allow to design and engineer their properties to a large extent, such as the energy level structure and coupling mechanism to its environment. Some of these properties can also be tuned in-situ using local magnetic fields. Additionally superconducting circuits have the technological appeal that they are fabricated on chips using standard lithography techniques known from conventional integrated circuits, which might be an advantage when scaling up the system to a large number of quantum bits. The characteristic energy of these circuits lies in the microwave frequency range (5 – 20 GHz) with well developed technology available for experiments, due to the applications of similar components in telecommunication and radar systems.

Strong interaction between single microwave photons and superconducting circuits can be reached with the so called circuit quantum electrodynamics (circuit QED) setup, as proposed by Blais *et al.* [Blais04] and first experimentally realized by Wallraff *et al.* [Wallraff04]. This system consists of one or several superconducting qubits which are integrated into a transmission line resonator, and was extremely successful over the last few years for quantum computation and quantum optics experiments. In the context of quantum computation, the resonator isolates the qubits from the electromagnetic environment [Haroche89], allows for qubit read-out [Filipp09, Bianchetti09, Reed10] and acts as a coupling bus between several qubits inside the same resonator [Majer07, Sillanpää07]. This led to several fruitful experiments carried out with superconducting qubits: demonstration of a geometric single qubit phase gate [Leek07], generation of two-qubit entanglement using sideband transitions between resonator and qubit [Leek10], violation of the Bell inequality [Ansmann09, Palacios-Laloy10], demonstration of two-qubit quantum algorithms [DiCarlo09, Yamamoto10, Dewes11], control and tomographic reconstruction of a three-level system [Bianchetti10b], generation and detection of three-qubit entanglement [DiCarlo10, Neeley10, Baur12], observation of quantum jumps [Vijay11], benchmarking of a teleportation protocol [Baur12] and the implementation of a three-qubit Toffoli gate [Fedorov12, Reed12, Mariani11a].

In the context of quantum optics experiments, it was the small mode volume realized in transmission line resonators and the large dipole moment of superconducting artificial atoms that led to novel experimental achievements: demonstration of a single microwave-photon source [Houck07], observation of single-artificial atom lasing [Astafiev07], observation of the \sqrt{n} nonlinearity of the Jaynes-Cummings ladder in frequency [Fink08, Bishop09] and time domain [Johansson06, Hofheinz08, Altomare10], observation of the Lamb shift [Fragner08], cooling and amplification with a qubit [Grajcar08], generation of Fock states [Hofheinz08] and arbitrary superpositions of Fock states [Hofheinz09], observation of the Autler-Townes doublet [Baur09, Sillanpää09] and Mollow triplet [Astafiev10, Lang11], electromagnetically induced transparency [Abdumalikov10], Bloch-Siegert shift [Forn-Díaz10, Niemczyk10] in a ultrastrongly coupled qubit-resonator system, first measurement of microwave frequency photon antibunching [Bozyigit11] using linear amplifiers and on-chip beam splitters, tomographic reconstruction of itinerant microwave photons [Eichler11b, Mallet11], two mode squeezing [Eichler11a] and entanglement of photons [Wang11].

Outline of the Thesis

In this thesis I present our work carried out on superconducting qubits from 2008 to 2012 in the Quantum Device Lab at ETH Zurich. Even though some contributions to the progress in quantum optics experiments have been made, I mainly focus here on the contributions made to quantum computation. Before going to the detailed discussion of our system, I first give a short review of the basics of quantum information theory in [Chapter 2](#). This includes a description of quantum bits, how they can be manipulated and how a quantum computer differs from classical computers. In [Chapter 3](#) I introduce our quantum processor consisting of superconducting charge qubits and a transmission line resonator. The interaction between the qubit and the electromagnetic field inside the resonator is described by the generalized Jaynes-Cummings Hamiltonian. A review of the theoretical description is given and then used to show how this system can be employed to control and readout the state of superconducting qubits. In [Chapter 4](#) I present the measurement setup used to cool down the quantum chip to millikelvin temperatures and to connect the chip to room temperature equipment for qubit manipulation and to digitally acquire the readout signal. The main results of this thesis are given in the last two chapters. In [Chapter 5](#) I discuss a number of important sample characterization measurements, the measurement of Autler-Townes and Mollow-transitions, and a detailed instruction of how to calibrate and characterize high fidelity single qubit quantum gates. Furthermore, I discuss how to fully reconstruct the density matrix of a qubit state and the process matrix of a quantum process. Finally, in [Chapter 6](#), I present two different methods to realize two-qubit quantum operations. The first is based on sideband transitions between qubits and resonator, and the qubit-qubit interaction is generated via transferring of the qubit excitation to a photon in the resonator. The second method uses the interaction mediated by virtual photons inside the resonator. I then use the latter interaction to generate and fully reconstruct the density matrix of two- and three-qubit entangled states relevant to quantum error correction and quantum teleportation schemes. It also allows us to realize the Deutsch-Jozsa algorithm and to demonstrate the realization of a three-qubit Toffoli gate which is useful in the context of quantum error correction.

Short Review of Quantum Information Theory

This chapter is intended to give a short overview on the basic theory of quantum computation and closely follows the description given in the book of Nielsen and Chuang [Nielsen00]. It includes the mathematical and geometric description of a quantum bit, as well as the description of the quantum operations on single and multi-qubit states needed to perform arbitrary quantum computation. At the end I also discuss the quantum parallelism, which describes a method that allows a quantum computer to evaluate a function for a large number of values in parallel, using only one single function call.

2.1 Quantum bit

The smallest unit of information on a classical computer is the so called binary digit (bit) and takes one of two possible states, 0 and 1. Physically these states correspond for example to whether a capacitor is charged or discharged. Any information can then be stored by concatenating many of these bits into larger units. Like the classical bit, a quantum bit (qubit) can also be in states $|0\rangle$ and $|1\rangle$. But instead of corresponding to a classical quantity, these states are quantum states formed by any quantum system with two distinct energy levels, such as the spin of an electron in a static magnetic field. In this case, if the spin is pointing parallel or anti-parallel to the magnetic field, the system is in the low ($|0\rangle$) or high energy state ($|1\rangle$) with energies E_0 and E_1 , respectively. Unlike a classical bit which must be either 0 or 1, the qubit can be in both states at the same time. Such a superposition

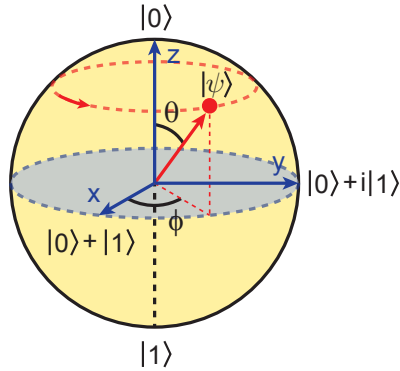


Figure 2.1: Bloch sphere representation of a qubit.

state is mathematically represented by $|\psi\rangle = \alpha|0\rangle + \beta|1\rangle$, where α and β are complex numbers, or in other words, by a vector in a two-dimensional complex vector space with the orthonormal basis states $|0\rangle$ and $|1\rangle$ (computational basis states). One might wonder why $|\psi\rangle$ is called a qubit, as it can be prepared in infinitely many superposition states. The reason is that whenever the state is measured, the result only contains one bit of information. The measurement outcome is 0 with a probability $|\alpha|^2$ or 1 with probability $|\beta|^2$, and the state after measurement is collapsed onto the computational basis states $|0\rangle$ or $|1\rangle$, respectively. Because all probabilities must add up to one, $|\alpha|^2 + |\beta|^2 = 1$ must be satisfied.

It is sometimes useful to have a visual interpretation of a qubit state to better understand the action of quantum operations on the state. To find such a representation we can rewrite an arbitrary qubit state in the form

$$|\psi\rangle = e^{i\gamma} \left(\cos \frac{\theta}{2} |0\rangle + e^{i\phi} \sin \frac{\theta}{2} |1\rangle \right), \quad (2.1)$$

where the global phase factor γ can be set to zero as it is not measurable. The variables θ and ϕ are real and define a point on a three dimensional unit sphere, the so called Bloch sphere, see [Figure 2.1](#). Every point on this sphere represents a qubit state, and the vector pointing to the north pole is the ground state $|0\rangle$ and the vector to the south pole is the excited state $|1\rangle$. The direction of the z axis is defined by the direction of the static magnetic field. The time evolution of the state

vector is governed by the Hamiltonian of a spin 1/2 particle in a magnetic field

$$\hat{H} = \frac{1}{2}\hbar\omega_{01}\hat{\sigma}_z = \frac{1}{2}\hbar\omega_{01} \begin{pmatrix} 1 & 0 \\ 0 & -1 \end{pmatrix} \quad (2.2)$$

where $\hbar\omega_{01} = E_1 - E_0$ is the energy difference between the ground and excited states and $\hat{\sigma}_z$ the Pauli z-matrix. In the Bloch sphere picture the time evolution $\hat{U} = e^{-i\hat{H}t}$ can be understood as a precession of the state vector around the z axis with the Larmor frequency $\omega_{01}/2\pi$. In order to have a better intuition for quantum operations carried out on the qubit, one often considers a frame which rotates the coordinate system with this Larmor frequency about the z axis (rotating frame), such that the state vector is stationary in this frame. Rotations about the other two axes to drive transitions between $|0\rangle$ and $|1\rangle$ are performed using magnetic fields applied perpendicular to the z axis, see [Section 2.2.1](#).

2.1.1 Many qubits

Storing information involves the concatenation of several bits. In the case of two classical bits, this yields the four possible states 00, 01, 10 and 11. Similarly, for two quantum bits these correspond to the computational basis states $|00\rangle$, $|01\rangle$, $|10\rangle$ and $|11\rangle$ (where $|ij\rangle$ stands for the tensor product $|i\rangle \otimes |j\rangle$). But as for a single qubit, the most general two qubit state is given by the linear superposition of the basis states

$$|\psi\rangle = \alpha_{00}|00\rangle + \alpha_{01}|01\rangle + \alpha_{10}|10\rangle + \alpha_{11}|11\rangle, \quad (2.3)$$

where α_{ij} are again complex numbers which fulfill the normalization condition $\sum_{i,j=0}^1 |\alpha_{ij}|^2 = 1$. Since the vector space is now a four dimensional complex space, there is no easy graphical visualization of such a state anymore. Nevertheless, we can still analyze some interesting features of this state which have no classical counterpart. First lets discuss what happens when the state of the first qubit is measured. Similarly to the single qubit case, the probability to obtain the result 0 (1) is given by $|\alpha_{00}|^2 + |\alpha_{01}|^2$ ($|\alpha_{10}|^2 + |\alpha_{11}|^2$). If the measurement outcome is 0, the state will immediately collapse onto the state $(\alpha_{00}|00\rangle + \alpha_{01}|01\rangle) / \sqrt{|\alpha_{00}|^2 + |\alpha_{01}|^2}$. This result has some striking consequences. If the initial state is for example in the special two qubit state

$$|\psi_{\text{Bell}}\rangle = \frac{1}{\sqrt{2}} (|00\rangle + |11\rangle), \quad (2.4)$$

then the measurement of the first qubit immediately projects the second qubit onto the state $|0\rangle$ if the measurement outcome was 0, and onto the state $|1\rangle$ if it was 1. Imagine now that we send the second qubit of the prepared two-qubit state $|\psi_{\text{Bell}}\rangle$ to the moon and keep one on earth. We can then change the state of the qubit on the moon instantaneously, simply by performing a local measurement on our qubit without ever interacting with the second qubit. When our measurement outcome is 0 (1), we know that when someone else on the moon measures their qubit, they will also measure 0 (1). This correlation between the measurement outcomes is stronger than any classical correlation could be as was first pointed out by Einstein, Podolsky and Rosen [Einstein35]. States with this non-classical property are called entangled states and are the key elements for quantum computation algorithms and quantum teleportation protocols, see also [Section 6.3](#).

2.2 Quantum operations and quantum circuits

Besides storing information we also would like to be able to perform operations on the qubits and move information from one qubit to another, in order to perform quantum computation. In analogy to classical computation where bits are connected using wires and gates, a quantum computer can be interpreted in terms of quantum circuits and quantum gates applied to qubits. As an example the following quantum circuit

$$\begin{array}{c}
 |0\rangle \text{ --- } \boxed{\hat{R}_y^{\pi/2}} \text{ --- } \bullet \text{ ---} \\
 |0\rangle \text{ --- } \oplus \text{ ---}
 \end{array} \tag{2.5}$$

can be used to generate the Bell state given in Equation (2.4). This circuit is read from left to right, and each qubit is associated with a quantum wire which corresponds to the passage of time. First a single qubit operation on the first qubit is applied, followed by a two qubit operation which generates the entanglement. Instead of using operators to describe a certain quantum algorithm, these quantum circuit diagrams provide a graphical method to better understand the action of the algorithm on the individual qubits. In the following two sections we describe the most important quantum gates and their circuit symbols used for the quantum operations presented in this thesis.

2.2.1 Single-qubit operations

Any single qubit operation can easily be visualized on the Bloch sphere as a rotation of the state vector around an arbitrary rotation axis. We label these operations as \hat{R}_n^θ where n defines the rotation axis and θ is the rotation angle. The most important operations are the rotation around the x and y axis. In fact, any single qubit operation can be decomposed into a combination of rotations around these two axes.

Bit-flip gates

Mathematically all quantum operations are represented by unitary matrices. In the case of rotations around the x and y axis, these are given by the unitary 2×2 matrices

$$\hat{R}_x^\theta = e^{-i\frac{\theta}{2}\hat{\sigma}_x} = \begin{pmatrix} \cos \frac{\theta}{2} & -i \sin \frac{\theta}{2} \\ -i \sin \frac{\theta}{2} & \cos \frac{\theta}{2} \end{pmatrix} \quad \text{with} \quad \hat{\sigma}_x = \begin{pmatrix} 0 & 1 \\ 1 & 0 \end{pmatrix}, \quad (2.6)$$

$$\hat{R}_y^\theta = e^{-i\frac{\theta}{2}\hat{\sigma}_y} = \begin{pmatrix} \cos \frac{\theta}{2} & -\sin \frac{\theta}{2} \\ \sin \frac{\theta}{2} & \cos \frac{\theta}{2} \end{pmatrix} \quad \text{with} \quad \hat{\sigma}_y = \begin{pmatrix} 0 & -i \\ i & 0 \end{pmatrix}, \quad (2.7)$$

where $\hat{\sigma}_x$ and $\hat{\sigma}_y$ are the Pauli x - and y -matrix. The \hat{R}_y^θ operations can be used to construct the quantum equivalent of a classical NOT gate, which flips the state of the qubit. This is done by choosing a rotation angle $\theta = \pi$, such that it rotates the vector from the south to the north pole or vice versa and maps the state $|1\rangle$ to $|0\rangle$ or $|1\rangle$ to $|0\rangle$. Since $\hat{R}_y^\pi = \hat{\sigma}_x$, this gate is also referred to as the $\hat{\sigma}_x$ -gate. Similarly, when choosing $\theta = \pi/2$, this operation maps a state initially in the ground $|0\rangle$ or excited state $|1\rangle$ into an equal superposition of the two basis states, namely into $\hat{R}_y^{\pi/2}|0\rangle = (|0\rangle + |1\rangle)/\sqrt{2}$ or $\hat{R}_y^{\pi/2}|1\rangle = (|0\rangle - |1\rangle)/\sqrt{2}$, respectively.

For a spin $1/2$ particle in a magnetic field, these operations can be carried out by applying a magnetic field which rotates in the x - y plane with an oscillation frequency equal to the transition frequency of the qubit $\omega_d = \omega_{01}$. The Hamiltonian describing this situation in the frame rotating at the Larmor frequency is given by

$$\hat{H} = \hbar\Omega \left(\cos(\phi)\hat{\sigma}_x + \sin(\phi)\hat{\sigma}_y \right), \quad (2.8)$$

where Ω defines the rate of rotation around an axis defined by the phase ϕ of the transverse magnetic field. When considering other systems than spin $1/2$ particles, these transitions can also be driven using different control fields rather

than oscillating magnetic fields. In our case using superconducting qubits, we do this by applying microwave signals in resonance with the qubit transition frequency, see also [Section 5.4](#).

Phase gate

Another important single qubit gate is the PHASE gate \hat{R}_z^ϕ , which rotates the state vector around the z axis on the Bloch sphere. In other words, it changes the dynamic phase of the state by ϕ such that $\hat{R}_z^\phi(\alpha|0\rangle + \beta|1\rangle) = \alpha|0\rangle + e^{i\phi}\beta|1\rangle$. The matrix which describes this gate is given by

$$\hat{R}_z^\phi = \begin{pmatrix} 1 & 0 \\ 0 & e^{i\phi} \end{pmatrix}. \quad (2.9)$$

For details on how this is implemented see [Section 5.4.4](#).

2.2.2 Multi-qubit operations

One of the most important multi-qubit gate is the controlled-NOT operation (\hat{U}_{CNOT}) acting on two qubits, the target and control qubit. Together with arbitrary single qubit operations, it forms a set of universal quantum gates, which means that any quantum operation carried out on n qubits can be decomposed into single qubit and the two-qubit controlled-NOT operations. It furthermore appears in most of the currently known quantum algorithms. The action of this gate can be describes as follows. It inverts the state of the target qubit if the control qubit is $|1\rangle$, and does nothing if the control qubit is $|0\rangle$. In other words, depending on the state of the control qubit, the gate applies a NOR operation or the identity on the target qubit. The matrix and quantum circuit representation of this gate are given by

$$\hat{U}_{\text{CNOT}} = \begin{pmatrix} 1 & 0 & 0 & 0 \\ 0 & 1 & 0 & 0 \\ 0 & 0 & 0 & 1 \\ 0 & 0 & 1 & 0 \end{pmatrix} \equiv \begin{array}{c} |x\rangle \text{---} \bullet \text{---} |x\rangle \\ |y\rangle \text{---} \oplus \text{---} |x \otimes y\rangle \end{array} \quad (2.10)$$

Here $x, y = 0$ or 1 , \oplus denotes the addition modulo 2 and the controlled-NOT operation is represented in the circuit diagram by a vertical line between the control (\bullet) and target (\oplus) qubit. As we have already seen in Equation (2.5) this gate can be used to generate entanglement. Refer to [Section 6.2.3](#) for a description of an

implementation of this gate with superconducting qubits.

In an experimental realization of the controlled-NOT operation, it is often easier to first generate the controlled-PHASE operation

$$\hat{U}_{cZ11} = \begin{pmatrix} 1 & 0 & 0 & 0 \\ 0 & 1 & 0 & 0 \\ 0 & 0 & 1 & 0 \\ 0 & 0 & 0 & -1 \end{pmatrix} \equiv \text{---} \begin{array}{c} \bullet \\ | \\ \bullet \end{array} \text{---} \quad (2.11)$$

This gate swaps the phase of the target qubit, if the control qubit is $|1\rangle$, and does nothing if it is $|0\rangle$. The controlled-NOT operation is then constructed by applying a $\hat{R}_y^{-\pi/2}$ and $\hat{R}_y^{\pi/2}$ rotation before and after \hat{U}_{cZ11} , respectively.

A three-qubit gate that is important in the context of reversible classical computation and quantum error correction is the Toffoli gate

$$\hat{U}_{\text{Toffoli}} = \begin{pmatrix} 1 & 0 & 0 & 0 & 0 & 0 & 0 & 0 \\ 0 & 1 & 0 & 0 & 0 & 0 & 0 & 0 \\ 0 & 0 & 1 & 0 & 0 & 0 & 0 & 0 \\ 0 & 0 & 0 & 1 & 0 & 0 & 0 & 0 \\ 0 & 0 & 0 & 0 & 1 & 0 & 0 & 0 \\ 0 & 0 & 0 & 0 & 0 & 1 & 0 & 0 \\ 0 & 0 & 0 & 0 & 0 & 0 & 0 & 1 \\ 0 & 0 & 0 & 0 & 0 & 0 & 1 & 0 \end{pmatrix} \equiv \begin{array}{c} \bullet \\ | \\ \bullet \\ | \\ \oplus \end{array} \quad (2.12)$$

It applies a NOT gate on the target qubit only if the two control qubits are in the state $|1\rangle$, and does nothing otherwise. It can be shown that any (irreversible) classical circuit can be efficiently simulated with a reversible circuit consisting only of classical Toffoli gates. The Toffoli gate is thus universal for classical computation. Because it can also be implemented as a quantum logic gate, it directly follows that a quantum computer can simulate any classical computer. In addition, the Toffoli gate is useful for quantum error correction, see also [Section 7](#). For the decomposition of this gate into controlled-NOT and single qubit operations, and its implementation with superconducting qubits, see [Section 7.2](#).

2.2.3 The power of quantum parallelism

One of the most important differences between classical and quantum computers is the fact that a quantum computer can store its information in superposition states.

This ability and the linearity of quantum operations equips a quantum computer with an inherent parallelism that has no counterpart in any classical computer. As an example, a quantum system consisting of $n = 500$ qubits can exist in a superposition of 2^{500} states. This number is larger than the estimated number of atoms in the universe [Nielsen00], and thus impossible to store on a classical computer, not to mention to perform operations on all of them in a reasonable amount of time. A quantum computer however is able to perform a quantum operation on all states at the same time. This ability, referred to as quantum parallelism, leads to a significant speed advantage over classical computers. However, to find algorithms that make full use of this potential power is difficult as briefly explained below.

Let us assume we want to calculate the outcome of a Boolean function $f(x) : \{0, 1\}^n \rightarrow \{0, 1\}^m$ which takes n qubits as an input and m qubits as an output. Furthermore, we assume that we can carry out a unitary operation \hat{U}_f that transforms the state $|x, 0\rangle$ into $|x, f(x)\rangle$, using a sequence of quantum gates. Here x denotes the $d = 2^n$ n -qubit computational basis states of the first register, and $|0\rangle$ denotes all m qubits of the second register in state $|0\rangle$. Instead of applying \hat{U}_f onto all input basis states individually, we first create an equal superposition of all basis states $|x\rangle$ using the following unitary transformation

$$|\psi_{\text{input}}\rangle = \hat{R}_y^{\pi/2} \otimes \hat{R}_y^{\pi/2} \otimes \dots \otimes \hat{R}_y^{\pi/2} |0, 0, \dots, 0\rangle = \frac{1}{\sqrt{d}} \sum_{x=0}^{d-1} |x\rangle. \quad (2.13)$$

We then apply the unitary operation \hat{U}_f onto this superposition state and all qubits of the second register in the state $|0\rangle$

$$|\psi\rangle = \hat{U}_f \left(\frac{1}{\sqrt{d}} \sum_{x=0}^{d-1} |x, 0\rangle \right) \quad (2.14)$$

$$= \frac{1}{\sqrt{d}} \sum_{x=0}^{d-1} |x, f(x)\rangle. \quad (2.15)$$

As a result of the quantum superposition and the linearity of \hat{U}_f , this highly entangled final state contains the solutions of the function $f(x)$ applied to all possible input states x , even though we have evaluated the function f only once! On a classical computer, this would mean to run the computation on 2^n different machines in parallel, which is already more than atoms available in the whole

universe for $n = 500$. Unfortunately, we can not easily access all these solutions. If we measure the final state $|\psi\rangle$, we randomly retrieve the solution of f evaluated for one single value of x with probability $1/d$. This algorithm is thus no better than randomly choosing an x and evaluating $f(x)$ on a classical computer. For quantum algorithms to be faster than any classical counterpart, the quantum parallelism is not sufficient. The algorithm must be adapted such that the state containing the wanted solution is measured with an increased probability compared to all other states, by using quantum interference. One of the first quantum algorithms which makes use of this is the Deutsch-Jozsa algorithm [Deutsch92]. It has been demonstrated with superconducting transmon qubits in Yale [DiCarlo09], and later also with phase qubits [Yamamoto10]. A realization of this algorithm in our laboratory is discussed in [Section 6.2.5](#).

Quantum Circuits: On-Chip Quantum Processor

In this chapter I describe our quantum processor used during this thesis. As an example, a false colored optical image of a three-qubit quantum processor used in a number of experiments presented in this thesis [Baur12, Fedorov12] is shown in Figure 3.1. It consists of a small sapphire chip of size $7 \times 2 \text{ mm}^2$ with electrical circuits patterned in a niobium thin film. Three superconducting transmon qubits [Koch07a] fabricated from aluminum (orange) are coupled to a microwave transmission line resonator [Göppl08] (blue), which serves as a coupling bus [Majer07] between the qubits for two-qubit quantum operations [DiCarlo09]. Simultaneously, the resonator is also operated as a measurement device [Wallraff05]

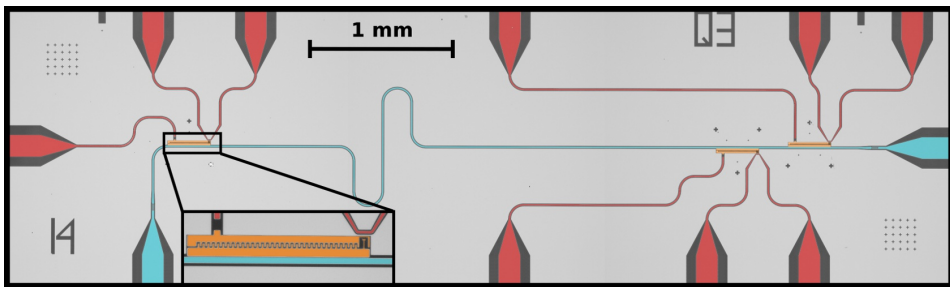


Figure 3.1: False colored optical image of the most recent version of a three-qubit quantum processor used during this thesis, with the qubits colored in orange, the resonator in blue and the local gate lines in red.

to perform a joint readout of the three-qubit quantum states. Single qubit quantum operations are carried out using the local transmission lines passing by each qubit (red). Similarly to a classical central processing unit (CPU), our processor is fabricated using standard photo-lithography and nano ebeam-lithography techniques. A scaled up system can thus easily be fabricated or integrated into other electrical circuits. However, the coherent control over the large scale circuit still remains a great challenge. The processor is operated at microwave frequencies, which is beneficial because the technology in this frequency range used to measure the state of the qubits and to perform quantum operations is well established due to its application in radio-astronomy and telecommunication. To avoid thermal excitation of the qubit states and to maximize coherence, the processor must be operated at ultra low temperatures < 20 mK.

At the beginning of this chapter, in [Section 3.1](#), I describe how electrical circuits can be used to fabricate a quantum bit. An essential building block to realize this goal is the Josephson junction, the properties of which are discussed. In [Section 3.2](#) I discuss how qubits can be coupled to the transmission line resonator, and how this system then can be used to prepare and read out an arbitrary qubit state.

3.1 Superconducting qubits

When talking about quantum mechanics, one usually thinks about microscopic systems such as photons, atoms or electrons. It may thus sound a bit surprising that the macroscopic circuits alluded to above, visible with our bare eyes, can be used to perform coherent quantum information processing. However, macroscopic objects may behave quantum mechanically, as long as the relevant collective degrees of freedom are well enough decoupled from the environment and that the energy dissipation is small enough. In electric circuits, these collective degrees of freedom are the flux Φ stored in an inductor and the charge q on a capacitor. While dissipation is eliminated by using superconducting materials, the isolation from the environment is achieved by carefully designing the electric circuits to decouple the quantum system from the control and measurement devices. In addition, careful magnetic shielding and thermalization of the quantum device to millikelvin temperatures is used to suppress magnetic flux noise and thermal population, respectively. First evidence for the quantum behavior of electrical circuits resulted from experiments with Josephson junction in which macroscopic quantum tunneling was demonstrated [[Voss81](#), [Devoret85](#)]. In 1997, a first ex-

periment was carried out [Nakamura97] which showed spectroscopically that the quantum variable specifying the number of Cooper-pairs on a superconducting island can exist in a superposition state. Later in the year 2000, it was shown with flux qubits [Friedman00, vanderWal00] that the quantum state flux through a superconducting loop can also exist in a superposition of a state described by flux pointing up and flux pointing down.

In order to gain insight about how one can construct a quantum bit with superconducting circuits, I first discuss the parallel LC oscillator (see Figure 3.2a) as a simple quantum circuit. The equation of motion for this circuit is found using Kirchoff's law and reads

$$Ld^2q/dt^2 + (1/C)q = 0. \quad (3.1)$$

It is easy to check that the classical Lagrangian

$$\mathcal{L}(q, \dot{q}) = (1/2)L(dq/dt)^2 - (1/2C)q^2 \quad (3.2)$$

describes the same dynamics according to the Euler-Lagrange equation

$$\frac{d}{dt} \left(\frac{\partial \mathcal{L}}{\partial \dot{q}} \right) - \frac{\partial \mathcal{L}}{\partial q} = 0. \quad (3.3)$$

The circuit can then be quantized using the standard quantization principle (a description of how to quantize a general electrical circuit is given in [Yurke84, Devoret97]). First, the Hamiltonian of the circuit is found using the Legendre transformation $H(p, q) = p\dot{q} - \mathcal{L}(q, \dot{q})$ which yields

$$H(q, \Phi) = q^2/(2C) + \Phi^2/(2L). \quad (3.4)$$

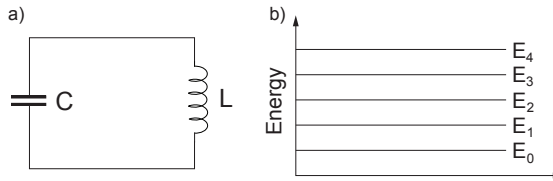


Figure 3.2: a) Circuit diagram of a parallel LC oscillator. b) Harmonic energy level diagram.

Here, the flux $\Phi = p = Ldq/dt = d\mathcal{L}(q, \dot{q})/d\dot{q}$ takes the role of the generalized canonical momentum conjugate to the canonical position q . Once it is known which are the conjugate variables and what the form of the Hamiltonian is, the quantization is done by replacing the classical canonical conjugate variables with quantum mechanical Hermitian operators \hat{q} and $\hat{\Phi}$, which obey the commutation relation $[\hat{q}, \hat{\Phi}] = i\hbar$. One can then express the Hamiltonian operator in terms of dimensionless operators

$$\hat{H} = \hbar\omega \left(\hat{a}^\dagger \hat{a} + \frac{1}{2} \right), \quad (3.5)$$

where $\omega = 1/\sqrt{LC}$ is the resonance frequency of the circuit and $a = (\hat{\Phi} + iZ\dot{q})/\sqrt{2\hbar Z}$ the photon annihilation operator. The charge and flux operators can thus readily be expressed in terms of the creation and annihilation operators as $\hat{q} = i\sqrt{\hbar/2Z}(\hat{a}^\dagger - \hat{a})$ and $\hat{\Phi} = \sqrt{\hbar Z/2}(\hat{a} + \hat{a}^\dagger)$. The energy levels of this system form a harmonic spectrum, in which all the levels are equally separated from each other, see [Figure 3.2b](#).

In order to use a system as a qubit however (for example the ground and first excited state), the transition between those two states must be sufficiently different from the transitions to the next higher states. The only known dissipation free electric element which could produce such an anharmonic spectrum is the Josephson junction, see [Section 3.1.1](#). Therefore, the building blocks to construct a circuit which can be used as a qubit are capacitors with capacitance C , inductors with inductance L and Josephson junctions characterized by their Josephson energy E_J . Numerous of different circuits have been found to be promising candidates and can be categorized into three different types of qubits [[Clarke08](#)]. The *phase qubit* [[Martinis02](#)] consists of a single current biased Josephson junction. For a current bias smaller than the critical current of the junction, the anharmonic potential can be approximated by a cubic potential, and the two lowest energy states with well defined superconducting phase difference across the junction define the qubit state. The *flux qubit* consists of a micrometer sized superconducting loop, interrupted by one [[Friedman00](#)] or three [[vanderWal00](#)] Josephson junctions. The potential is a double well potential with the two quantum ground states in the two wells define, respectively, a magnetic flux pointing up or down. These two states are coupled by the small potential barrier connecting the two potential wells, giving rise to quantum superposition between the two states, which form the qubit states. The *charge qubit* [[Bouchiat98](#), [Nakamura99](#), [Vion02](#), [Koch07a](#)] is defined by a tiny superconducting island which is on one side connected to ground via a Josephson

junction, and on the other side capacitively coupled to a voltage bias source. The qubit states are defined by the quantum states which describe whether n or $n + 1$ Cooper pairs are located on the island. A more detailed discussion of the charge qubit in general, and the transmon qubit in particular is given in [Section 3.1.2](#) and [Section 3.1.3](#).

3.1.1 The Josephson junction

A Josephson junction consists of two superconducting electrodes connected by a “weak link” which limits the flow of supercurrent between the two electrodes. If the closest distance between the electrodes is sufficiently small, the macroscopic wavefunctions of the two superconductors overlap and form a weakly coupled system in which Cooper pairs can coherently tunnel from one electrode to the other, carrying a small supercurrent. The theoretical description for such a system was first proposed in 1962 by the British physicist Brian David Josephson [[Josephson62](#)] and closely followed by an experimental verification in 1963 [[Anderson63](#)]. The “weak link” can be either an insulating barrier (S-I-S junction), a normal metal thin film (S-N-S junction) or a short, narrow constriction in a superconductor (S-c-S junction) [[Tinkham96](#)]. For most superconducting qubit applications S-I-S junctions are used at the current state of the art, consisting of a few Ångström thin oxide layer (usually aluminum oxide Al_2O_3) grown between two superconducting electrodes (usually aluminum Al) using standard nanolithography techniques. A simplified schematic of a current biased S-I-S junction and its equivalent electrical circuit are shown in [Figure 3.3a,b](#). The physical Josephson junction is modeled as an ideal Josephson element shunted by a resistance R and a capacitance C (RCSJ model) [[McCumber68](#)]. There are two contributions to the resistance R . One part is the resistance R_{qp} which accounts for dissipation due to quasi-particle tunneling through the junction. The other part accounts for the frequency dependent dissipation due to the coupling of the Josephson junction to the biasing circuitry and the environment, which is determined by the real part of the admittance $R_{circuitry} = \text{Re}(Y(\omega))$ seen by the junction [[Esteve86](#)], see also [Section 4.4.1](#). The capacitance C reflects the geometric shunting capacitance between the two electrodes. For temperatures smaller than the critical temperature of the superconductor $T < T_c$, the resistance R_{qp} rises exponentially. For the case of very low temperatures $T \ll T_c$, the resistor R_{qp} becomes so large that it can be replaced with an open circuit in the model.

The two fundamental equations describing the relation of current flowing through

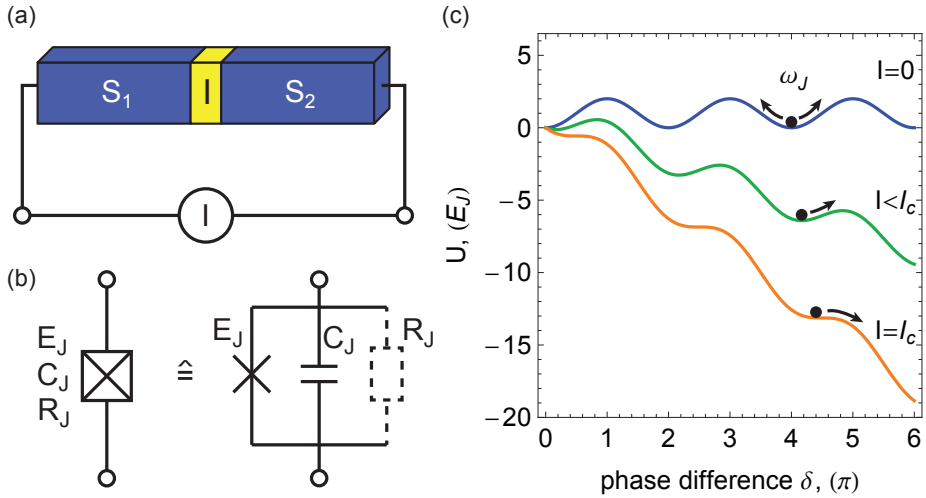


Figure 3.3: a) Schematic of a current biased S-I-S Josephson tunnel junction. It consists of two superconducting electrodes S_1 and S_2 with a thin isolation layer in between. b) A physical Josephson junction can be modeled as an ideal Josephson element with Josephson energy E_J shunted by a resistance R_J and a capacitance C_J . c) Washboard potential for different bias currents I . If the bias current is smaller than the critical current of the junction ($I < I_c$), the potential has well defined minima around which the potential can be approximated with as a weakly anharmonic potential with resonance frequency $\sim \omega_J$.

and the voltage across an ideal Josephson element to the phase difference between the electrodes are summarized below [Tinkham96].

1. *Current phase relation* - When no voltage is applied across the Josephson junction, there is a supercurrent I_s through the junction, which depends on the phase difference δ between the two macroscopic wave functions of the two superconducting electrodes. This effect is called the *DC Josephson effect*

and described with the sinusoidal relation ¹

$$I_s(\delta) = I_c \sin(\delta). \quad (3.6)$$

It can directly be derived from simple boundary conditions for the current phase relation. Here I_c is the critical current, which corresponds to the maximum supercurrent that can flow through the weak link and δ is the gauge-invariant phase difference defined by

$$\delta(\vec{r}, t) = \Theta_2(\vec{r}, t) - \Theta_1(\vec{r}, t) - \frac{2\pi}{\Phi_0} \int_1^2 \vec{A}(\vec{r}, t) d\vec{s}, \quad (3.7)$$

where the integration is from one electrode of the weak link to the other and $\Theta_{1/2}$ are the phases of the macroscopic wavefunction of the two superconducting electrodes. The vector potential \vec{A} accounts for an external magnetic field and vanishes if the magnetic field is zero, and $\Phi_0 = h/2e$ is the magnetic flux quantum.

2. *Voltage phase relation* - When the phase difference δ across the Josephson junction changes in time, a voltage V drops between the two superconductors according to

$$\frac{d\delta}{dt} = \frac{2\pi}{\Phi_0} V. \quad (3.8)$$

Such a state with time dependent phase can in practice be realized by biasing the junction with a DC voltage, with a current exceeding the critical current I_c , or with an AC current. Thus, Equation (3.8) is also referred to as the *AC Josephson effect*.

The only parameter in the above equations that is controllable during fabrication is the critical current I_c . All others are fundamental constants, which is why the Josephson junction is used for voltage standards [Taylor67]. In the context of qubit fabrication, this parameter determines the maximal transition frequency of the qubit and it is thus desirable to have accurate control over the critical current. Its temperature dependence and relation to the normal state resistance R_n (the resistance of the junction in the non superconducting state) is given by the

¹The most general relation would be $I_s(\delta) = \sum_{n=1}^{\infty} \{I_n \sin(n\delta) + J_n \cos(n\delta)\}$. However the one given in Equation (3.6) holds rather well in most cases and is used here for simplicity.

Ambegaokar-Baratoff relation [Ambegaokar63]

$$I_c = \frac{\pi\Delta(T)}{2eR_n} \tanh\left(\frac{\Delta(T)}{2k_B T}\right), \quad (3.9)$$

where $\Delta(T)$ is the band gap of the superconductor. In the limit where the temperature is much smaller than the critical temperature of the superconductor $T \ll T_c$, this relation can be approximated as

$$I_c \approx \frac{\pi\Delta(0)}{2eR_n}. \quad (3.10)$$

The normal resistance $R_n \propto e^{Bd}/A$ is inversely proportional to the area of the junction A and exponential in the barrier thickness d , where B is a material dependent constant. Thus we can control the critical current I_c by simply adjusting the geometry of the junction during the nanolithography process.

The Josephson junction can also be characterized in terms of coupling free energy F stored in the junction and the energy stored in the capacitor $E_{CN} = CV^2/2$. F is derived by integrating the electrical work $F = \int IVdt$ done by a bias current I . Using the two Josephson relations given in Equation (3.6) and Equation (3.8) these two energies are written as

$$F(\delta) = E_J(1 - \cos \delta), \quad (3.11)$$

$$E_{CN} = 4N^2 E_C, \quad (3.12)$$

where $E_J = \Phi_0 I_c / 2\pi$ is the *Josephson energy*. $E_C = e^2 / 2C$ is the *charging energy* which is the energy needed to transfer a single electron from one electrode to the other and N the number of excess Cooper pairs on one electrode relative to the neutral state.

Within the RCSJ model, the dynamics of the phase δ can be determined by using the Kirchhoff's rule for the circuit shown in Figure 3.3b to write the differential equation

$$\begin{aligned} I &= I_c \sin \delta + \frac{V}{R} + C \frac{dV}{dt} \\ &= I_c \sin \delta + \frac{\hbar}{2eR} \dot{\delta} + \frac{\hbar}{2e} C \ddot{\delta}, \end{aligned} \quad (3.13)$$

where I is the bias current. This is the equation of a damped non-linear oscillator.

In the following, we will neglect the damping term which determines the qubit lifetime because it can be made small by operating at low temperatures and carefully designing the circuitry coupled to the Josephson junction. The dynamics described by this equation is the same as that of a particle of mass $(\hbar/2e)^2C$ moving along the δ axis in an effective potential

$$U(\delta) = E_J(1 - \cos \delta) - \frac{\hbar}{2e}I\delta, \quad (3.14)$$

called the *tilted washboard potential* shown in [Figure 3.3c](#). In the absence of bias current ($I = 0$) the potential is sinusoidal and has well defined minima. Around such a minimum, the potential can locally be approximated by the potential of a harmonic oscillator with resonance frequency

$$\omega_J = \sqrt{\frac{2eI_c}{\hbar C}}, \quad (3.15)$$

known as the *plasma frequency* of the Josephson junction. When bias current is applied, the potential becomes tilted, the minima become more shallow and completely disappear when the bias current becomes bigger or equal to the critical current $I \geq I_c$. At this point, δ is finite and a voltage drop occurs across the junction. The slight deviation of $U(\delta)$ from the harmonic potential due to the nonlinearity of the Josephson junction and the tilting of the potential due to the bias current form the basis for quantum information processing with superconducting qubits in general and superconducting phase qubits [[Martinis02](#)] in particular.

Combining this potential energy characterized by the Josephson energy of the junction and the kinetic energy $E_{\text{kin}} = (\hbar\dot{\delta})^2/16E_C$ (found from the last term in Equation (3.13)) characterized by the charging energy, we can immediately write down the Lagrangian of a current biased Josephson junction

$$\mathcal{L}(\delta, \dot{\delta}) = \frac{\hbar^2\dot{\delta}^2}{16E_C} - E_J(1 - \cos \delta) + \frac{\hbar}{2e}I\delta. \quad (3.16)$$

We use this equation later to find the quantization of the circuit shown in [Figure 3.3a](#).

3.1.2 The Cooper pair box qubit

Instead of biasing a Josephson junction with a current as we have seen in the last section, it can also be biased with a voltage as shown in [Figure 3.4a](#). This

circuit is called the Cooper pair box (CPB) and was first theoretically discussed in 1987 by Büttiker [Büttiker87] and experimentally realized by Bouchiat *et al.* in 1997 [Bouchiat98]. It did not take long until coherent quantum dynamics has first been observed in Japan 1999 by Nakamura *et al.* [Nakamura99]. The CPB consists of a small superconducting island (orange), which is connected via a Josephson tunnel junction (yellow) with capacitance C_J and Josephson energy E_J to a large superconducting electrode (blue) that serves as a reservoir of Cooper pairs. Single Cooper pairs can tunnel coherently from the reservoir through the junction to the island and vice versa. If the charging energy of the island is large compared to the Josephson energy of the junction ($4E_C \gg E_J$), the system is in a Coulomb blockade regime, also called the *charge qubit regime*. Then, the amount of excess Cooper pairs N (number of Cooper pairs additional to the neutral state consisting of $\sim 10^{13}$ Cooper pairs) on the island can be controlled by changing the gate voltage V_g applied to the gate capacitance C_g .

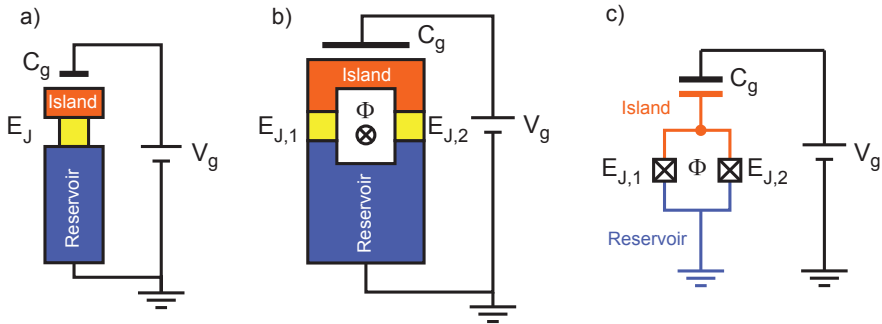


Figure 3.4: a) Schematic of a CPB consisting of a Josephson junction (yellow) which connects a superconducting island (orange) with a reservoir for Cooper pairs (blue). The number of Cooper pairs on the island are controlled with a capacitively coupled voltage source. b) Here the single Josephson junction is replaced with a SQUID loop, to add another control parameter to the CPB Hamiltonian to change the Josephson energy with a magnetic field. c) Circuit diagram corresponding to the schematic in b).

In order to find the Lagrangian for the CPB, we have to determine the kinetic and potential energy of the system. From Section 3.1.1 we already know that the potential energy is determined by the Josephson energy $U(\delta) = E_J(1 - \cos \delta)$ and

the kinetic term is given by the electrostatic energy of the capacitor. Since the structure has two capacitances, the kinetic energy term is given by

$$E_{\text{kin}} = \frac{C_J V_J^2}{2} + \frac{C_g (V_g - V_J)^2}{2}, \quad (3.17)$$

where V_J is the voltage drop over the Josephson junction. By using the voltage phase relation of the Josephson junction (3.8) and adding a constant term (independent of δ and $\dot{\delta}$) that does not influence the dynamics of the system, the Lagrangian can be written as [Wendin05]

$$\mathcal{L}(\delta, \dot{\delta}) = \frac{C_\Sigma}{2} \left(\frac{\hbar}{2e} \dot{\delta} - \frac{C_g}{C_\Sigma} V_g \right)^2 - E_J (1 - \cos \delta), \quad (3.18)$$

where $C_\Sigma = C_J + C_g$. Here the kinetic term can be tuned by the external gate voltage, the potential term however is fixed by the E_J defined during the fabrication process.

In order to add an additional control parameter for the potential term, the CPB is slightly modified as shown in Figure 3.4b. There, the single Josephson junction is replaced by a SQUID (Superconducting QUantum Interference Device) loop consisting of a superconducting loop interrupted by two Josephson junctions. This structure is referred to as the *split CPB*. If the two junctions are equal ($E_{J,1} = E_{J,2} = E_J$), such a SQUID loop can be considered as a single junction with an effective Josephson energy $E_J(\Phi) = E_J^{\text{max}} |\cos(\pi\Phi/\Phi_0)|$, tunable via a magnetic flux Φ applied through the SQUID loop, see [Tinkham96, Chapter 6.4.1]. The maximal Josephson energy $E_J^{\text{max}} = 2E_J$ is given by the sum of the Josephson energies of the two individual junctions. The Lagrangian of the split CPB is then given by

$$\mathcal{L}(\delta, \dot{\delta}) = \frac{C_\Sigma}{2} \left(\frac{\hbar}{2e} \dot{\delta} - \frac{C_g}{C_\Sigma} V_g \right)^2 - E_J(\Phi) (1 - \cos \delta), \quad (3.19)$$

with $C_\Sigma = C_{J,1} + C_{J,2} + C_g$ because the two Josephson junctions are connected in parallel. With the knowledge of the Lagrangian, the circuit can readily be quantized in the same way as described at the beginning of Section 3.1. Subtracting a constant term that does not change the dynamics (again independent of δ and $\dot{\delta}$), we end up with the Hamiltonian [Bouchiat98]

$$\hat{H}_{\text{CPB}} = 4E_C (\hat{N} - n_g)^2 - E_J(\Phi) \cos \hat{\delta}. \quad (3.20)$$

Here, $\hat{N} = \hat{p}/\hbar$ is the operator associated with the number of Cooper pairs in excess from the neutrality in the metallic island and \hat{p} the canonical momentum operator conjugate to the phase operator $\hat{\delta}$. $E_C = e^2/2C_\Sigma$ the charging energy and $n_g = -C_g V_g/2e$ the charge on the gate capacitor (in units of $2e$), which can be tuned by the gate voltage and is therefore, additionally to the magnetic flux, an external control parameter of the CPB Hamiltonian. In order to find the spectrum associated with this Hamiltonian, one has to solve the corresponding eigenvalue equation

$$\hat{H}|k\rangle = E_k|k\rangle, \quad (3.21)$$

which can be done analytically in the phase space representation.

Phase representation

The eigenstates $|\delta\rangle$ and the corresponding eigenvalues δ of the operator $\hat{\delta}$ associated with the superconducting phase drop across the Josephson junction are defined as

$$\hat{\delta}|\delta\rangle = \delta|\delta\rangle. \quad (3.22)$$

The set $\{|\delta\rangle, \delta \in [0, 2\pi[\}$ forms a complete basis for the CPB states [Cottet02]. The representation of the number operator in this phase basis writes

$$\hat{N} = -i \frac{\partial}{\partial \delta}. \quad (3.23)$$

With Equation (3.21), one can then write down the Schroedinger equation

$$E_k \langle \delta | k \rangle = \langle \delta | \hat{H}_{\text{CPB}} | k \rangle \quad (3.24)$$

$$\Leftrightarrow E_k \psi_k(\delta) = \left(4E_C \left(-i \frac{\partial}{\partial \delta} - n_g \right)^2 - E_J(\Phi) \cos(\delta) \right) \psi_k(\delta), \quad (3.25)$$

where $\psi_k(\delta) = \langle \delta | k \rangle$ is the wavefunction of the eigenstate $|k\rangle$ represented in the phase basis. It satisfies the boundary condition $\psi_k(\delta) = \psi_k(\delta + 2\pi)$. This differential equation can be solved analytically and the wavefunctions and the eigenenergies E_k can be given in terms of *Mathieu functions*, see [Cottet02] for a detailed discussion.

The energies E_k calculated from the analytic solution for $k = 0, 1, 2$ as a function of the gate charge n_g are shown in [Figure 3.5](#) for a fixed Josephson energy $E_J(\Phi) = E_C$. To give an intuitive understanding of this energy level diagram, it is useful to represent the CPB Hamiltonian in the charge representation, even though the

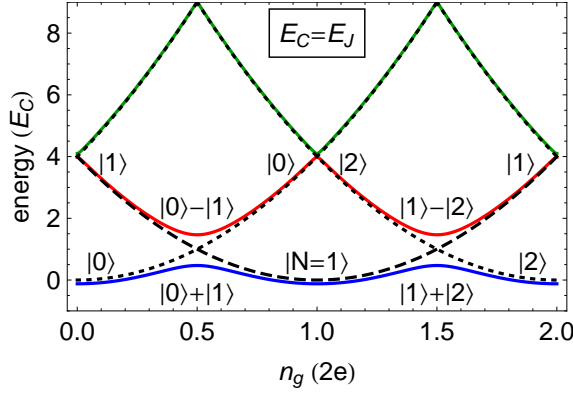


Figure 3.5: Solid lines show the eigenenergies of the CPB for $E_C = E_J$, calculated from the analytic solution of the Schrodinger equation in terms of Mathieu functions. The red, blue and green curves show the ground, first and second excited state energy levels E_0, E_1 and E_2 . Dashed lines show the electrostatic energies of the charge levels with 0, 1, and 2 Cooper pairs on the island. The degeneracies between the energies of neighbouring charge states occurring at $n_g = \pm 0.5, \pm 1.5, \dots$ are lifted by the Josephson coupling.

Schrodinger equation is then not analytically solvable. I will thus briefly discuss the charge representation and review how the CPB can be used as a qubit.

Charge representation

The basis for which the number operator \hat{N} is diagonal are the eigenstates $|N\rangle$ which satisfy the relation

$$\hat{N}|N\rangle = N|N\rangle. \quad (3.26)$$

$|N\rangle$ represents the state with a precise number of excess Cooper pairs N on the island and the set $\{|N\rangle, N \in \mathbb{Z}\}$ forms a complete basis for the states of the CPB for energies lower than the superconducting gap, i.e. when no quasiparticles are present. The diagonal kinetic term of the Hamiltonian can in this basis readily be written as [Bouchiat98]

$$\hat{H}_{\text{kin}} = 4E_C \sum_{N=-\infty}^{\infty} (N - n_g)^2 |N\rangle\langle N|. \quad (3.27)$$

Since δ and N are conjugate variables, the number states $|N\rangle$ can be related to the phase states using the Fourier transform [Tinkham96]

$$|N\rangle = \frac{1}{2\pi} \int_0^{2\pi} e^{-iN\delta} |\delta\rangle d\delta. \quad (3.28)$$

With this relation it directly follows that

$$e^{\pm i\hat{\delta}} |N\rangle = |N \mp 1\rangle. \quad (3.29)$$

The Josephson coupling term $\propto \cos \hat{\delta} = (e^{i\hat{\delta}} + e^{-i\hat{\delta}})/2$ of the CPB Hamiltonian is thus the sum of two terms which raise and lower, respectively, the number of Cooper pairs on the island by one. This describes exactly the behavior of Cooper pairs tunneling through the Josephson junction at a rate E_J/\hbar , leading to the full CPB Hamiltonian in the charge representation

$$\hat{H}(n_g) = \sum_{N=-\infty}^{\infty} \left[4E_C(N - n_g)^2 |N\rangle\langle N| - \frac{E_J}{2} (|N\rangle\langle N+1| + |N+1\rangle\langle N|) \right]. \quad (3.30)$$

Starting from this Hamiltonian, we can now understand how the energy level diagram shown in [Figure 3.5](#) comes about. Let us first look at the situation where $E_J = 0$. For a fixed number of Cooper pairs N on the island, the energy depends quadratically on the gate charge n_g , leading to the dotted and dashed parabolae. At the crossing points of the parabolae, the two charge states are energetically degenerate. If we now turn on the Josephson coupling term $E_J > 0$, the degeneracy between neighbouring parabolae is lifted due to the coupling between the two charge states $|N\rangle$ and $|N+1\rangle$, leading to an avoided crossing. Let us now consider the regime where the charging energy is much larger than the Josephson energy ($4E_C \gg E_J$), the so called charge regime. At the degeneracy point $n_g = 0.5$, the two new eigenstates with lowest energy are given by the symmetric and antisymmetric superposition states $(|0\rangle \pm |1\rangle) / \sqrt{2}$ whose eigenenergies are separated by $E_J(\Phi)$, which can be tuned externally with a magnetic field. More generally, when restricting ourselves to a gate charge that stays around the degeneracy point ($0 \ll n_g \ll 1$), the only charge states $|N\rangle$ relevant for the lowest two energy levels are $|0\rangle$ and $|1\rangle$. All the other states are separated by energies much higher than the coupling energy E_J and can be considered to be decoupled.

The two-level approximation

We can thus restrict ourselves to the space spanned by the two charge states $|0\rangle$ and $|1\rangle$. The CPB Hamiltonian projected onto this subspace is given by

$$\hat{H} = \frac{\epsilon}{2} (|1\rangle\langle 1| - |0\rangle\langle 0|) - \frac{E_J}{2} (|0\rangle\langle 1| + |1\rangle\langle 0|), \quad (3.31)$$

where a constant energy term was subtracted such that $\epsilon = 4E_C(1 - 2n_g)$ is zero at the degeneracy point $n_g = 0.5$. The eigenenergies $E_{0,1}$ and the corresponding symmetric and antisymmetric eigenstates of this Hamiltonian are given by

$$E_{0,1} = \mp \frac{1}{2} \sqrt{E_C^2(1 - 2n_g)^2 + E_J^2}, \quad (3.32)$$

$$|\psi_{s,a}\rangle = \cos\left(\frac{\vartheta}{2}\right)|0\rangle \mp \sin\left(\frac{\vartheta}{2}\right)|1\rangle, \quad (3.33)$$

where $\vartheta = \arctan(E_J/\epsilon)$ is the mixing angle. Defining the computational ground and excited states as the symmetric and antisymmetric eigenstates respectively $|0_C\rangle = |\psi_s\rangle$ and $|1_C\rangle = |\psi_a\rangle$, we end up with the well known Hamiltonian of a spin 1/2 particle in a magnetic field

$$\hat{H}/\hbar = \frac{1}{2}\omega_{01}\hat{\sigma}_z, \quad (3.34)$$

where $\omega_{01} = (E_1 - E_0)/\hbar$ is the transition frequency between ground and excited state, and $\hat{\sigma}_z$ the Pauli matrix. Note also that in our notation the computational states are labeled with a C such that they are not confused with the number state.

Driving the qubit

Instead of biasing the qubit with a constant gate voltage, one could add a time dependent driving term oscillating with a frequency ω_D close to the qubit transition frequency ω_{01} . To take this into account in the CPB Hamiltonian, V_g in Equation (3.20) is replaced with the voltage $V_g = V_g^{\text{DC}} + V(t)$, with $V(t) = V_D \cos(\omega_D t)$. Expanding the square gives

$$\hat{H}_{\text{kin}} = 4E_C(\hat{N} - n_g^{\text{DC}})^2 + \frac{E_C C_g^2}{e^2} V(t) (2V_g^{\text{DC}} + V(t)) - \frac{4E_C C_g}{e} V(t) \hat{N} \quad (3.35)$$

for the kinetic term of the Hamiltonian. The first term is just the original electrostatic term with the DC bias. The second term is a constant additional energy stored in the system which is not state dependent (does not depend on \hat{N}), and thus does not influence the dynamics of the qubit. The last term describes the coupling of the driving field to the qubit and depends both on the drive strength V_D and the state of the CPB. When restricting ourselves as in the last section to the space spanned by the two charge states $|0\rangle$ and $|1\rangle$, we get additionally to Equation (3.31) the driving Hamiltonian

$$\hat{H}_{\text{drive}}/\hbar = \frac{\tilde{\Omega}}{2} \cos(\omega_D t) (|1\rangle\langle 1| - |0\rangle\langle 0|), \quad (3.36)$$

with $\tilde{\Omega} = 4E_C C_g V_D / e\hbar$. In the charge basis, it is always diagonal and thus orthogonal to the qubit Hamiltonian when the Cooper pair box is operated at the degeneracy point $n_g = 0.5$. When rotating the basis such that the qubit Hamiltonian is diagonal, the driving is completely transverse and proportional to $\hat{\sigma}_x$. If the Cooper pair box is biased away from the sweet spot however, the driving term also consists of a $\hat{\sigma}_z$ term which depends on the mixing angle ϑ

$$\hat{H}_{\text{drive}}/\hbar = \frac{\tilde{\Omega} \sin(\vartheta)}{2} \cos(\omega_D t) \hat{\sigma}_x + \frac{\tilde{\Omega} \cos(\vartheta)}{2} \cos(\omega_D t) \hat{\sigma}_z. \quad (3.37)$$

For the condition that the drive strength is small enough such that $\tilde{\Omega} \ll \omega_D$ is fulfilled, then the $\hat{\sigma}_z$ term in Equation (3.37) can be neglected and we arrive at the final driven two-level Hamiltonian

$$\hat{H} \approx \frac{1}{2} \omega_{01} \hat{\sigma}_z + \Omega \cos(\omega_D t) \hat{\sigma}_x, \quad (3.38)$$

where $\Omega = \tilde{\Omega} \sin(\vartheta)/2$ is the Rabi frequency of the drive. This is exactly the Hamiltonian we need to perform arbitrary single qubit rotations, see also [Section 2.2.1](#).

Pros and cons of the Cooper pair box

The two crucial parameters for the usefulness of the CPB for quantum computation tasks are the anharmonicity and the charge dispersion of the energy levels. The anharmonicity $\alpha = \omega_{12} - \omega_{01}$ is a measure of how well the system can be treated as a two-level system. It is defined as the difference in the transition frequencies between the first two energy levels $\omega_{01} = E_{01}/\hbar = (E_1 - E_0)/\hbar$ and between the next higher neighbouring energy levels $\omega_{12} = E_{12}/\hbar = (E_2 - E_1)/\hbar$. A large enough

anharmonicity (large $|\alpha|$) is needed to carry out fast quantum operations within the two-level approximation, without exciting higher excited energy levels outside the computational basis states [Gambetta11], see also Section 5.4.2. As we have seen above, this is very well fulfilled by the CPB in the charge regime.

The charge dispersion describes the variation of the energy levels as a function of the gate charge and environmental offset charges, and determines the sensitivity of the CPB to charge noise. The smaller the charge dispersion, the less the qubit transition frequency varies due to gate charge fluctuations. In current state of the art CPB qubit experiments, the qubit is biased to the so called “sweet spot” at $n_g = 0.5$, where the qubit frequency is to first-order insensitive to charge noise. This was made use of for the first time with a quantronium qubit [Vion02, Vion03]. Indeed, the coherence times are drastically increased by working at this point, but still limited by higher-order effects of the $1/f$ charge noise [Ithier05]. The best dephasing times and energy decay times reached so far with a CPB are $T_2 = 2 \mu\text{s}$ [Leek07] and $T_1 = 200 \mu\text{s}$ [Kim11] respectively. Also the long term stability of the gate charge bias is marginal, due to quasiparticles tunneling through the Josephson junction. The latter changes the bias by $n_g = 0.5$ which in turn drastically shifts the qubit frequency. Every time such an event happens, the CPB has to be re-biased to the sweet spot. In our early experiments [Leek07] the CPB had to be re-biased every several minutes, which would have made it impossible to perform the multi-qubit experiments shown at the end of this thesis, where long term stabilities of several hours were required. This has been achieved by drastically reducing the charge dispersion by going into the phase regime where $E_J \gg E_C$.

3.1.3 Transmon qubit

The main problem with the CPB is the sensitivity to charge fluctuations in the nearby surroundings caused by quasiparticles and surface charges. A natural way to solve this problem is to make the box independent of the gate charge by going to a regime where $E_J \gg E_C$, the so called *transmon* regime [Koch07a]. While the increased ratio E_J/E_C flattens the energy bands in the charge direction, the qubit frequency can be tuned by controlling the magnetic flux applied through the SQUID loop. The flattening of the energy bands is illustrated in Figure 3.6, where the first three eigenenergies (E_0, E_1, E_2) of the CPB Hamiltonian (3.20) are shown as a function of gate charge for different ratios of E_J/E_C . A quantity which defines the sensitivity to charge noise is the charge dispersion. It can be defined as the

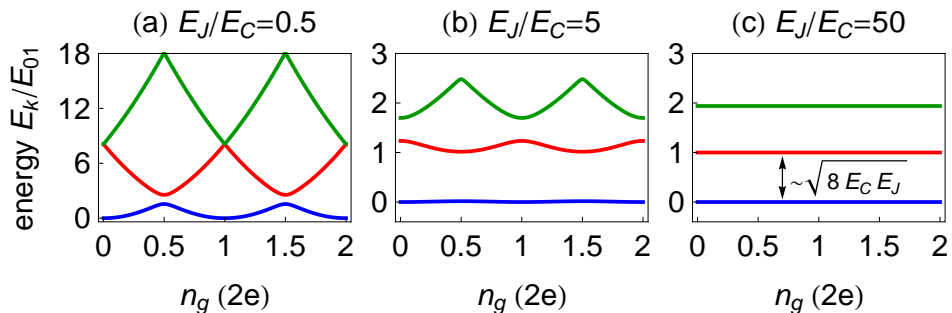


Figure 3.6: Eigenenergies for the first three energy levels ($k = 0, 1, 2$) of the CPB Hamiltonian (3.20) for different E_J/E_C ratios. The energies are given in units of the energy difference E_{01} evaluated at the degeneracy point $n_g = 0.5$. The energy bands get less and less sensitive to gate charge, as the E_J/E_C is increased from the charge regime with a ratio of 0.5 (a) to the transmon regime with a ratio of 50 (c).

maximal spread in the transition energy between neighboring energy levels

$$\epsilon_k = E_{k,k+1}(n_g = 0.5) - E_{k,k+1}(n_g = 0), \quad (3.39)$$

where $E_{ij} = E_j - E_i$ is the energy difference between energy levels i and j . As is shown in [Koch07a], this charge dispersion decreases exponentially fast as E_J/E_C is increased

$$\epsilon_k \propto e^{-i\sqrt{8E_J/E_C}}, \quad (3.40)$$

and ϵ_0 becomes smaller than 1 kHz at a ratio bigger than 60, making the transmon qubit almost immune to low frequency charge noise. To reach this ratio of energies, it is sufficient to slightly increase E_J in comparison to the charge regime, and to reduce the charging energy E_C by adding a large shunting capacitance C_S in parallel to the Josephson junctions, see Figure 3.7d. Typical transmon qubits as shown in Figure 3.7a-c, have energies in the range of $E_C/\hbar \approx 200 - 400$ MHz and $E_J/\hbar \approx 10 - 30$ GHz.

Unfortunately the reduction in the sensitivity to charge noise does come at the price of typically a reduction in the anharmonicity α . Since for quantum computation tasks only the first three energy levels are considered, a natural definition for α

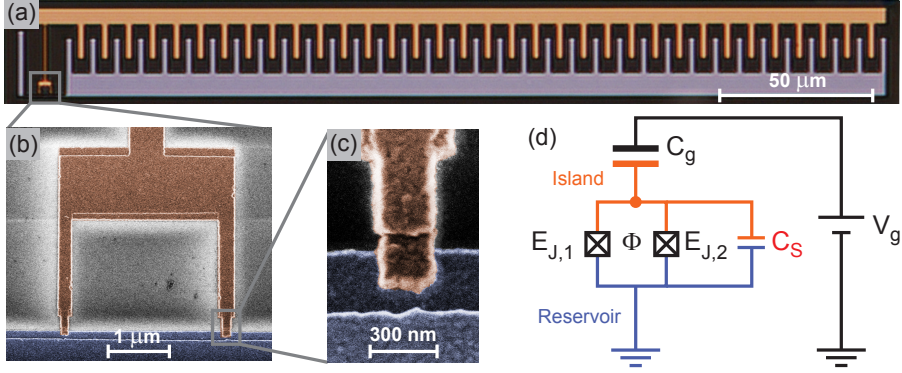


Figure 3.7: a) False colored optical microscope image of a transmon qubit. The large finger capacitor shunts the two Josephson junctions of the SQUID loop, in order to get a small enough charging energy E_C . Blue and orange colored electrodes are the reservoir and the island, respectively. b)-c) False colored SEM images of the SQUID loop and a single Josephson junction of the transmon. d) Lumped element model of the transmon qubit shown in a).

is given by the difference between the first two transition energies

$$\hbar\alpha = E_{12} - E_{01}. \quad (3.41)$$

However, the anharmonicity only decreases with a weak power law, while the charge dispersion decreases exponentially with E_J/E_C . The transmon thus still maintains a sufficiently large anharmonicity to do quantum operations when using specially shaped control pulses to minimize the effect of higher excited states outside the computational bases (see [Section 5.4.2](#) for details). For the typical parameter ranges given above, the anharmonicity is approximately given by the charging energy [[Koch07a](#)]

$$\alpha \approx -E_C/\hbar. \quad (3.42)$$

Also for these parameters, the transition energy between the first two energy levels can be approximated by

$$E_{01} \approx \sqrt{8E_C E_J^{\max} |\cos(\pi\Phi/\Phi_0)|} - E_C. \quad (3.43)$$

It can thus still be varied with a magnetic field applied to the SQUID loop.

3.2 Circuit quantum electrodynamics

Studying the interaction of electromagnetic fields with single atoms or other nonlinear quantum systems is interesting in fundamental physics, but also for applications in quantum information processing. In the context of this thesis, it allows to read out the state of the atom (or in our case the transmon qubit) by monitoring changes in the electromagnetic field transmitted through a resonator. This interaction however is usually very small due to the small cross-section of a single atom for optical photons in free space. In a system referred to as cavity quantum electrodynamics (cavity QED) [Haroche89, Raimond01], the atom is placed into a cavity formed by two highly reflective optical mirrors, see [Figure 3.8a](#), which can be designed to have a considerably smaller mode volume compared to free space. This leads to an increased electric field strength for a given photon number, and therefore to an increased interaction strength between single atoms and single photons. Additionally to the small mode volume, cavities with high quality factors can be engineered to study the consecutive coherent exchange of energy between the two systems. Their dynamics is described by the Hamiltonian

$$\hat{H}/\hbar = \frac{1}{2}\omega_{01}\hat{\sigma}_z + \omega_r\hat{a}^\dagger\hat{a} + g(|0\rangle\langle 1| + |1\rangle\langle 0|)(\hat{a}^\dagger + \hat{a}). \quad (3.44)$$

Here, the first term describes the atom (approximated as a two-level system with transition frequency ω_{01}), the second term describes the single mode of the electromagnetic field in the cavity with resonance frequency ω_r and the last term the interaction between the two with a coupling strength g . The operators $\hat{a}^{(\dagger)}$ are the (creation) annihilation operators of the cavity mode. The energy conserving terms proportional to $|0\rangle\langle 1|\hat{a}^\dagger$ ($|1\rangle\langle 0|\hat{a}$) describe the process in which one excitation is removed from (added to) the atom and a photon is created (annihilated) in the resonator mode. The other terms describing simultaneous excitation (de-excitation) of both the atom and the resonator field mode are not energy conserving. In the regime where $g \ll \omega_{01}, \omega_r$ and the detuning $|\Delta_0| = |\omega_{01} - \omega_r| \ll \omega_r + \omega_{01}$, these two terms can be dropped. After making this rotating wave approximation, the Hamiltonian (3.44) reduces to the Jaynes-Cummings Hamiltonian [Jaynes63]

$$\hat{H}_{\text{JC}}/\hbar = \frac{1}{2}\omega_{01}\hat{\sigma}_z + \omega_r\hat{a}^\dagger\hat{a} + g|0\rangle\langle 1|\hat{a}^\dagger + |1\rangle\langle 0|\hat{a}, \quad (3.45)$$

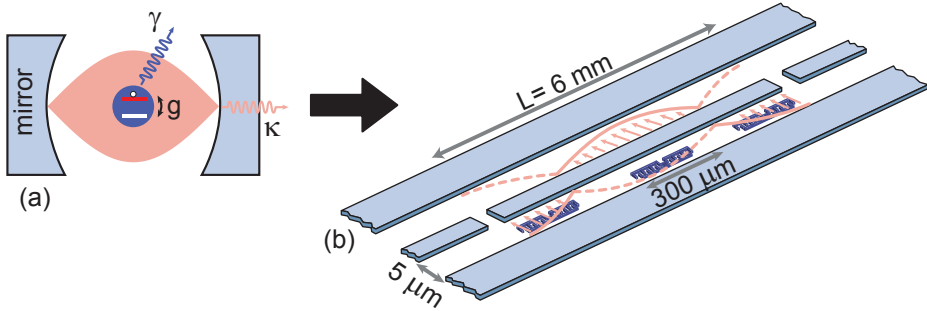


Figure 3.8: a) Cavity QED architecture, where a two-level atom is coupled to the electromagnetic field mode of a cavity, formed by two highly reflecting mirrors. If the coupling strength g is larger than the decay rate of the atom and the rate with which a photon leaves the cavity, single excitations can be coherently exchanged between cavity and atom. The system is then called to be in the strong coupling regime. b) Circuit QED architecture with three transmon qubits (dark blue) at the center and the ends of a coplanar waveguide resonator (blue). At resonance frequency (~ 10 GHz) set by the distance between the end capacitors, the electromagnetic field inside the resonator forms a standing wave (electric field is shown in pink). For maximal interaction strength, each qubit is placed at an anti-node of the electric field. The resonator can be driven externally by applying a microwave signal to the transmission line coming from one side, and transmission is measured by detecting the signal on the other side.

which can be diagonalized analytically, see [Section 3.2.1](#).

In addition to the enhanced interaction strength, the cavity strongly modifies the spontaneous decay rate of the atom. In contrast to free space which supports a continuum of electromagnetic field modes, the cavity only supports a single mode. This results in a strongly inhibited [[Hulet85](#), [Jhe87](#)] spontaneous decay rate of the atom when the cavity resonance frequency is far detuned from the atomic transition frequency, because there is no mode available into which the atom can emit a photon. The cavity thus protects the atom from decay, which is highly beneficial for quantum information processing. On the other hand, if the cavity is nearly on resonance with the atom, the spontaneous decay of the atom is enhanced by the Purcell effect [[Purcell46](#)]. Additionally to the effects on the decay rate, the cavity also shifts the transition frequency of the atom, called the Lamb shift [[Lamb47](#)],

induced by the vacuum fluctuations inside the cavity.

In the strong coupling regime ($g \gg \gamma, \kappa$), where the coupling strength g is much larger than the decay rate of the atom γ and the photon inside the cavity κ , single quantum excitations can be coherently exchanged between the atom and the cavity. First signatures of this exchange were observed by spectroscopically measuring the vacuum Rabi mode splitting [Thompson92], and later by directly detecting the time-resolved vacuum Rabi oscillations [Brune96]. With this system it was then possible to perform a quantum non-demolition measurement of single photons [Nogues99] and to generate and fully reconstruct non-classical cavity field states [Deleglise08]. Additionally it was possible to observe photon blockade [Birnbaum05], which can be used as a single photon source, and more recently to prepare and stabilize photon-number states inside the cavity using real-time quantum feedback [Sayrin11].

In 2004, A. Blais *et al.* [Blais04] proposed the idea to realize such a cavity QED system with superconducting electrical circuits. Rather than using atoms and optical cavities, superconducting qubits are coupled to a superconducting transmission line resonator formed by a coplanar waveguide with two gap capacitors interrupting the center conductor (see Figure 3.8b). This system is referred to as circuit QED and operated at microwave frequencies. It has first been realized in the Schoelkopf Lab at Yale [Wallraff04], and a good review is found in the thesis of David Schuster [Schuster07a]. Even though many different types of superconducting quantum circuits could in principle be coupled to such a resonator, I only discuss the transmon qubit that was used throughout this thesis. In analogy to cavity QED, a microwave photon in the resonator is bouncing between these two gap capacitors acting as mirrors, or speaking in a classical electrical engineering language, the electromagnetic field in the resonator forms a standing wave. Maximal capacitive coupling between the resonator field and the transmon qubit is reached when it is positioned at an anti-node of the electric field. This architecture has many advantages compared to cavity QED. It is possible to fabricate the whole system on a small chip with the size of several square millimeters. This is beneficial in context of scalability, an important requirement for quantum information processing. It also allows to freely position the qubits within the resonator (compared to cavity QED where atoms are flying through the cavity, or have to be held on position with complicated traps) and to engineer the coupling strength g to the resonator field (fixed in cavity QED).

In this section I review the basics of such a circuit QED architecture. I first discuss in more detail the generalized Jaynes-Cummings Hamiltonian which describes the interaction between a transmon qubit and a microwave resonator, and

then explain how this system can be used as a quantum information processor, i.e. how to prepare and to read out the qubit state (Section 3.2.3-Section 3.2.4). I then review the basics of transmission line resonators (Section 3.2.5) and coplanar waveguide (CPW)'s (Section 3.2.6). Finally I discuss in Section 3.2.7 how the transmon qubit is coupled to a CPW resonator and derive the Jaynes-Cummings Hamiltonian starting from the Hamiltonian of an LC oscillator and the CPB.

3.2.1 Generalized Jaynes-Cumming Hamiltonian

When coupling a transmon qubit to a resonator, it is not enough to simply consider a two-level system due to the small anharmonicity of the transmon qubit. The system is thus described by the Hamiltonian [Koch07a]

$$\hat{H}/\hbar = \sum_{i=1}^{N-1} \omega_i |i\rangle\langle i| + \omega_r \hat{a}^\dagger \hat{a} + \sum_{i=0}^{N-2} g_{i,i+1} (|i\rangle\langle i+1| + |i+1\rangle\langle i|) (\hat{a} + \hat{a}^\dagger). \quad (3.46)$$

The first term describes the transmon qubit including N energy levels, where the lowest energy level with energy $E_0 = \hbar\omega_0$ is set to zero and the second term is the usual Hamiltonian of a harmonic oscillator. The last term is the interaction Hamiltonian, where only coupling terms between neighbouring energy levels are included, because all others are negligible due to the near harmonicity of the transmon qubit (see Section 3.2.7). In the regime where $g_{i,i+1} \ll \omega_i, \omega_r$ and the detunings $|\Delta_i| = |\omega_{i,i+1} - \omega_r| \ll \omega_r + \omega_{i,i+1}$, with $\omega_{i,j} = \omega_j - \omega_i$ being the transition frequency between energy levels i and j , the rotating wave approximation can be applied. Throughout this thesis, this approximation is always valid. Recently however, a regime where this approximation breaks down (ultra strong coupling) has been reached with superconducting circuits [Niemczyk10, Forn-Díaz10]. The generalized Jaynes-Cummings Hamiltonian then reads

$$\hat{H}/\hbar = \sum_{i=1}^{N-1} \omega_i |i\rangle\langle i| + \omega_r \hat{a}^\dagger \hat{a} + \sum_{i=0}^{N-2} (g_{i,i+1} |i\rangle\langle i+1| \hat{a}^\dagger + h.c.). \quad (3.47)$$

For a two-level system ($N = 2$) this Hamiltonian can analytically be diagonalized and yields the excited states [Haroche92]

$$|+_q, n_p\rangle = \cos \vartheta_n |1_q, (n-1)_p\rangle + \sin \vartheta_n |0_q, n_p\rangle, \quad (3.48)$$

$$|-_q, n_p\rangle = -\sin \vartheta_n |1_q, (n-1)_p\rangle + \cos \vartheta_n |0_q, n_p\rangle, \quad (3.49)$$

$$\text{with } \vartheta_n = \frac{1}{2} \arctan\left(\frac{2g\sqrt{n}}{\Delta_0}\right), \quad (3.50)$$

and the ground state $|0_q, 0_p\rangle$. Whenever there is the potential for confusion, we will add the subscripts q and p , which label the qubit and photonic state, respectively. The corresponding eigenenergies are

$$E_{\pm,n} = n\hbar\omega_r \pm \frac{\hbar}{2} \sqrt{4g_{01}^2 n + \Delta_0^2}, \quad (3.51)$$

$$E_{0,0} = -\frac{\hbar\Delta_0}{2}. \quad (3.52)$$

These energies are depicted in [Figure 3.9](#) for two different regimes. In the resonant regime, where the qubit is on resonance with the resonator $\omega_{01} = \omega_r$, the product states $|0_q, n_p\rangle$ ($|1_q, (n-1)_p\rangle$) with the qubit in the ground (excited) state and n ($n-1$) photons in the resonator are no longer eigenstates of the Hamiltonian. Their degeneracy is lifted by the interaction term and the new eigenstates are equal superpositions of the qubit and the resonator $|\pm_q, n_p\rangle = (|0_q, n_p\rangle \pm |1_q, (n-1)_p\rangle) / \sqrt{2}$ and the ground state $|0_q, 0_p\rangle$. Qubit and resonator can no more be considered as individual systems, they rather form a new hybridized entangled system, similarly as the hybridization of the electron orbitals in a molecule. The two symmetric and antisymmetric states are split by the energy $2g_{01}\sqrt{n}$, see [Figure 3.9a](#), which is called the vacuum Rabi mode splitting for one excitation $n=1$ in the system. This splitting manifests itself in the time domain as a vacuum Rabi oscillation. When the system is initially prepared in the state where the qubit is excited and the resonator left empty $|1_q, 0_p\rangle$, the vacuum fluctuations in the resonator will cause the qubit to relax into its ground state by emitting a photon into the resonator. After some time, this photon is again reabsorbed by the qubit, leading to an oscillation between the states $|1_q, 0_p\rangle$ and $|0_q, 1_p\rangle$ with a frequency g_{01}/π , or with $\sqrt{n}g_{01}/\pi$ when starting with n excitations in the system. This \sqrt{n} scaling is a direct quantum signature of the system, because no classical model can explain it, and could only recently be measured in a circuit QED [[Fink08](#), [Hofheinz08](#), [Bishop09](#), [Altomare10](#)] and a cavity QED system [[Brune96](#), [Schuster08](#)]. As observed in [[Fink08](#)], this $2g_{01}\sqrt{n}$ splitting is slightly renormalized due to the presence of higher transmon levels if the anharmonicity α is similar to g_{01} . A requirement for this achievement was to reach the strong coupling regime $g \gg \kappa, \gamma$, where the coupling strength is much larger than the photon decay rate κ and the qubit relaxation rate into a mode other than the resonator mode γ . In this limit, the vacuum Rabi mode splitting can be

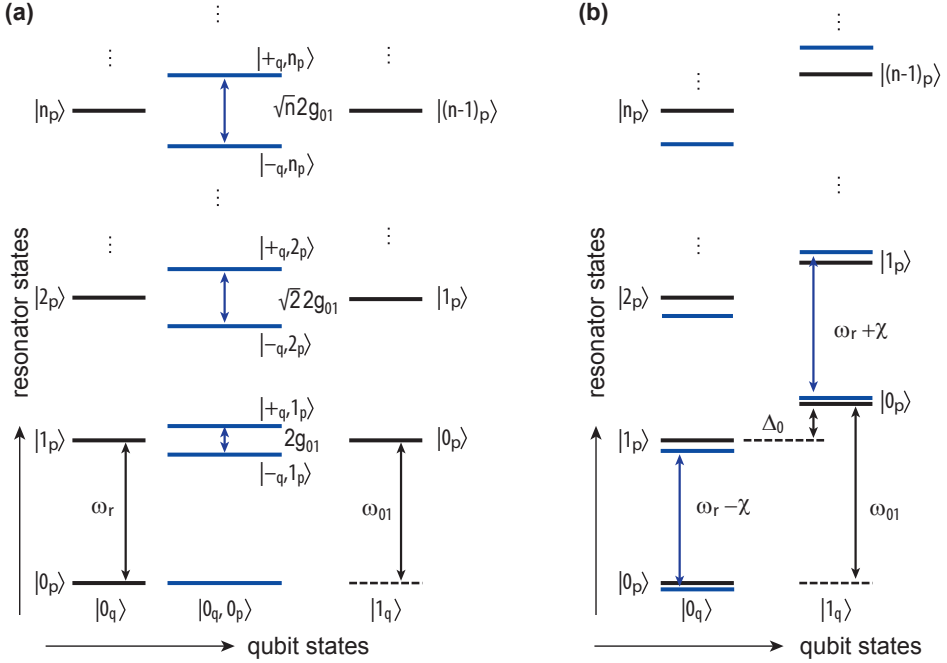


Figure 3.9: Energy level diagram of the dressed Jaynes-Cummings eigenstates, including two transmon levels. The uncoupled energy ladder of the uncoupled product states $|0_q, n_p\rangle$ (left) and $|1_q, n_p\rangle$ (right), where the qubit and photon states are labeled with a subscript q and p for clarity, are depicted by the black lines. a) In the resonant case where $\omega_r = \omega_{01}$, the degeneracy of the uncoupled states is split in frequency by $\sqrt{n}2g_{01}$ and the new dressed states are $|\pm_q, n_p\rangle$. b) In the dispersive regime where $\Delta_0 \gg g_{01}$, the coupling only manifests itself in a shift of the energy levels.

well resolved with spectroscopy and many vacuum Rabi oscillation periods can be measured before losing the excitation to the environment. The energy level diagram shown in [Figure 3.9b](#), where qubit and resonator are not on resonance with each other is discussed in the next section.

3.2.2 The dispersive regime

We now describe the dispersive limit in which the transmon qubit is operated at a frequency for which the detunings $\Delta_i = \omega_{i,i+1} - \omega_r$ between the transmon and resonator are large. In particular where $g_{01} \ll |\Delta_0|, |\Delta_1|$. In this regime, no excitations are exchanged between qubit and resonator, but the state of one system still has an influence on the energy of the other, see [Figure 3.9b](#). This dispersive interaction is particularly interesting because it allows to readout the qubit by measuring the phase and amplitude of a microwave signal transmitted through the resonator near resonance, and to control the qubit by driving the resonator off-resonantly with short microwave pulses.

The dispersive Hamiltonian can be found by performing the transformation $e^{\hat{S}} \hat{H} e^{-\hat{S}}$ which eliminates the direct interaction between the resonator and the transmon qubits, where [[Koch07a](#)]

$$\hat{S} = \sum_{i=0}^{N-1} \frac{g_{i,i+1}}{\Delta_i} (\hat{a}|i+1\rangle\langle i| - \hat{a}^\dagger|i\rangle\langle i+1|). \quad (3.53)$$

Due to the small anharmonicity of the transmon, at least three energy levels need to be included in this transformation. Only after this it is possible to make a two level approximation. Using the Baker-Campbell-Hausdorff expansion $e^{\hat{S}} \hat{H} e^{-\hat{S}} = \hat{H} + [\hat{S}, \hat{H}] + \frac{1}{2!} [\hat{S}, [\hat{S}, \hat{H}]] + \dots$ and keeping the terms up to order $g_{i,i+1}^2/\Delta_i^2$, we get the dispersive Hamiltonian [[Koch07a](#)]

$$\begin{aligned} \hat{H}_{\text{disp}}/\hbar = & \left(\omega_r - \chi_{01}|0\rangle\langle 0| + \sum_{i=1}^{N-1} (\chi_{i-1,i} - \chi_{i,i+1})|i\rangle\langle i| \right) \hat{a}^\dagger \hat{a} \\ & + \sum_{i=0}^{N-1} (\omega_i|i\rangle\langle i| + \chi_{i,i+1}|i+1\rangle\langle i+1|) + \sum_{i=0}^{N-1} (\eta_i \hat{a} \hat{a} |i+2\rangle\langle i| + h.c.), \end{aligned} \quad (3.54)$$

where

$$\begin{aligned}\chi_{i,i+1} &= \frac{g_{i,i+1}^2}{\Delta_i}, \\ \eta_i &= \frac{g_{i,i+1}g_{i,i+2}[(\omega_{i+1} - \omega_{i+2}) - (\omega_i - \omega_{i+1})]}{2(\omega_{i+1} - \omega_i - \omega_r)(\omega_{i+2} - \omega_{i+1} - \omega_r)}.\end{aligned}\quad (3.55)$$

The coupling between resonator and qubit now only shows up by state dependent dispersive energy shifts $\chi_{i,i+1}$ and a two-photon process term proportional to the two-photon transition rates η_i . Because the η_i are small, this last term can safely be neglected. We can now make a two-level approximation by evaluating the sums in Equation (3.54) only up to $N = 2$, but keeping terms including the coupling to the second excited level, and arrive at the Hamiltonian

$$\hat{H}_{\text{disp}}/\hbar = \frac{1}{2} \left(\omega_{01} + \frac{g_{01}^2}{\Delta_0} \right) \hat{\sigma}_z + (\tilde{\omega}_r + \chi \hat{\sigma}_z) \hat{a}^\dagger \hat{a}. \quad (3.56)$$

This has exactly the same form as if we started from the normal Jaynes-Cummings Hamiltonian including only a two-level system, but with a renormalized resonator frequency $\tilde{\omega}_r - g_{12}^2/2\Delta_1$ due to the interaction with higher transmon levels. The first term describes the qubit with a transition frequency $\tilde{\omega}_{01} = \omega_{01} + g_{01}^2/\Delta_0$ renormalized by the Lamb shift g_{01}^2/Δ_0 [Fragner08], induced by the vacuum fluctuations in the resonator. The second term is similar to the Hamiltonian of a harmonic oscillator, with an oscillation frequency $\tilde{\omega}_r + \chi \hat{\sigma}_z$ depending on the qubit state (χ is discussed below). If the qubit is in its ground state $|0\rangle$, the resonator frequency is $\tilde{\omega}_r - \chi$, if the qubit is in its excited state, the resonator frequency is $\tilde{\omega}_r + \chi$, see Figure 3.10. Measuring this frequency shift can be used to perform a quantum non-demolition readout of the qubit state (Section 3.2.3). The second term is also responsible for the AC Stark effect [Schuster05], which can be easily explained by rewriting the Hamiltonian (3.56) in the form

$$\hat{H}_{\text{disp}}/\hbar = \frac{1}{2} (\tilde{\omega}_{01} + 2\chi \hat{a}^\dagger \hat{a}) \hat{\sigma}_z + \tilde{\omega}_r \hat{a}^\dagger \hat{a}. \quad (3.57)$$

Depending on the number of photons n inside the resonator, the qubit frequency gets AC Stark shifted by the frequency $2\chi n$. If the resonator is prepared in a state consisting of a superposition of several photons (for example a classical coherent state), the qubit spectrum shows well resolved photon number peaks, called photon

number splitting [[Schuster07b](#), [Gambetta06](#)].

The dispersive shift for a two-level system is simply given by $\chi = \chi_{01}$. For the transmon qubit however, it has to be substituted by $\chi = \chi_{01} - \chi_{12}/2$ due to the level repulsion between pairwise coupled higher energy states. In the regime where $E_J \gg E_C$, the dispersive shift can be approximated as [[Koch07a](#)]

$$\chi \approx \frac{g_{01}^2 E_C}{\Delta_0(\Delta_0 - E_C)}. \quad (3.58)$$

For negative detunings $\Delta_0 < 0$ and positive detunings larger than the qubit anharmonicity $\Delta_0 > E_C$, this shift is always negative. For small positive detunings $0 < \Delta_0 < E_C$, where the resonator frequency ω_r is in between the transition frequencies ω_{01} and ω_{12} , the values of χ can become very large. This so called *straddling regime* can be particularly interesting for qubit readout or fundamental exploration of the Jaynes-Cummings Hamiltonian [[Hoffman11](#)].

The eigenstates (3.48-3.49) of the full Jaynes-Cummings Hamiltonian can be approximated in the dispersive regime as

$$|+q, n_p\rangle \approx |1_q, (n-1)_p\rangle + \frac{g_{01}}{\Delta_0} |0_q, n_p\rangle, \quad (3.59)$$

$$|-q, n_p\rangle \approx -\frac{g_{01}}{\Delta_0} |1_q, (n-1)_p\rangle + |0_q, n_p\rangle, \quad (3.60)$$

and the ground state $|0_q, 0_p\rangle$. For large detunings $g_{01}/\Delta_0 \ll 1$, these states are nearly given by the product states $|0_q, n_p\rangle$ and $|1_q, n_p\rangle$, which means that the transmon and resonator can nearly be considered as individual systems. The computational basis states $|0\rangle = |0_q, 0_p\rangle$ and $|1\rangle = |+q, 1_p\rangle$ mainly consist of the transmon qubit states and only contains a small resonator part. Even though this part can be made small, it still opens up a new decay channel for the computational qubit state $|1\rangle$. The excitation can be lost through the decay of the photonic part in the resonator, called the *Purcell effect* [[Purcell46](#), [Houck08](#), [Houck07](#)], with the rate

$$\gamma_\kappa = \kappa \frac{g_{01}^2}{\Delta_0^2}, \quad (3.61)$$

where κ is the rate with which the resonator loses its photon.

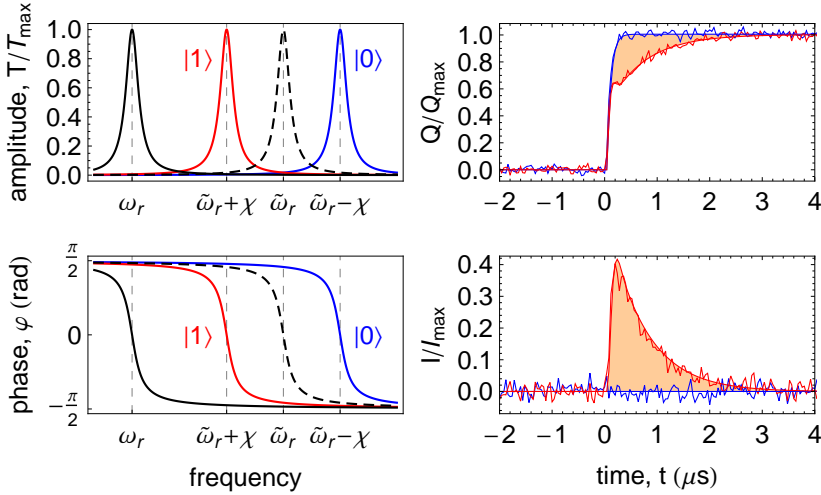


Figure 3.10: Left panels: Calculated amplitude and phase of the resonator transmission spectrum for the uncoupled resonator with bare resonance frequency ω_r and for the coupled resonator qubit system. The coupled qubit renormalizes the resonator frequency to $\tilde{\omega}_r$. The solid lines show the dispersively shifted resonator spectra for the qubit in its ground state $|0\rangle$ (blue), and the qubit in the excited state $|1\rangle$ (red). Right panels: Measured time response of the I/Q-quadratures of the transmitted signal for the qubit in the ground state (blue) and the excited state (red), when the resonator is driven with a coherent microwave field on the frequency $\tilde{\omega}_r - \chi$. The solid lines represent a fit to cavity Bloch equations [Bianchetti09] with the following parameters: qubit energy decay and dephasing times of $T_1 = 700$ ns and $T_2 = 600$ ns, respectively, a dispersive frequency shift of the resonator of $\chi/2\pi = 1.1$ MHz and a resonator line width of $\kappa/2\pi = 4.5$ MHz.

3.2.3 Quantum non-demolition readout of the qubit state

When the circuit QED system is operated in the dispersive limit, the qubit state dependent shift of the resonator by the frequency of $\pm\chi$, see left panels of [Figure 3.10](#), can be used to perform a quantum non-demolition measurement of the qubit state [[Blais04](#), [Wallraff05](#), [Bianchetti09](#)]. We do this by measuring the transmission of a weak coherent microwave drive applied to the resonator described by the Hamiltonian

$$\hat{H}_d = \hbar\varepsilon_d(\hat{a}^\dagger e^{-i\omega_d t} + \hat{a}e^{i\omega_d t}) \quad (3.62)$$

with amplitude ε_d and frequency ω_d . The in-phase $I(t) = \langle \hat{a}^\dagger + \hat{a} \rangle$ and quadrature $Q(t) = \langle i(\hat{a}^\dagger - \hat{a}) \rangle$ components of the transmitted field depend non-linearly on the dispersive shift operator $\hat{\chi} = \chi\hat{\sigma}_z$, and are thus different for the qubit in the ground or the excited state. The right panels of [Figure 3.10](#) show examples of the measured I/Q signals when the measurement drive, turned on at time $t = 0$, is applied on resonance with the resonator for the qubit in the ground state. For each trace, the experiment was repeated 65 000 times and the measurement signal is averaged to directly extract the expectation values $I(t)$ and $Q(t)$, and to eliminate the noise in the measurement signal. If the qubit is initially prepared in $|0\rangle$ (blue trace), the resonator response reaches its steady state at the rate κ , seen in the exponential rise of the Q-quadrature. The phase of the measurement drive was chosen such that the I-quadrature always stays zero. When the qubit is initially prepared in $|1\rangle$ (red trace), the response shows the behavior of an off-resonantly driven resonator due to the dispersive resonator pull of χ , and then approaches the steady-state as the qubit decays to $|0\rangle$ with the energy decay rate of the qubit γ . The numerical fit to theory (solid lines) shows the good agreement of the time response of the resonator with theory. An analytical solution in terms of an effective qubit measurement operator $\hat{M}'_{I,Q}(t)$ can be given in the limit of vanishing qubit decay. The I and Q components for the qubit initially prepared in state $\hat{\rho}$ before the measurement are given by $I(t), Q(t) = \langle \hat{M}'_{I,Q} \rangle = \text{Tr}[\hat{\rho} \hat{M}'_{I,Q}]$ and the measurement operators are determined by the solution to the master equation of the Hamiltonian $\hat{H}_d + (3.56)$ [[Bianchetti09](#)]

$$\hat{M}'_I(t) = \varepsilon \frac{e^{-\kappa t/2} [2(\hat{\chi} + \Delta_{\text{rm}}) \cos((\hat{\chi} + \Delta_{\text{rm}})t) + \kappa \sin((\hat{\chi} + \Delta_{\text{rm}})t)] - 2(\hat{\chi} + \Delta_{\text{rm}})}{(\hat{\chi} + \Delta_{\text{rm}})^2 + (\kappa/2)^2}, \quad (3.63)$$

$$\hat{M}'_Q(t) = \varepsilon \frac{e^{-\kappa t/2} [\kappa \cos((\hat{\chi} + \Delta_{\text{rm}})t) - 2(\hat{\chi} + \Delta_{\text{rm}}) \sin((\hat{\chi} + \Delta_{\text{rm}})t)] - \kappa}{(\hat{\chi} + \Delta_{\text{rm}})^2 + (\kappa/2)^2}, \quad (3.64)$$

where $\Delta_{\text{rm}} = \tilde{\omega}_r - \omega_d$ is the detuning of the measurement drive. These operators are diagonal in the qubit basis and stay diagonal for all times, because of the quantum non-demolition nature of the measurement [Blais04]. They may thus be written in a much simpler and time independent way as

$$\hat{\mathcal{M}}_{I,Q} = \alpha_0^{I,Q}|0\rangle\langle 0| + \alpha_1^{I,Q}|1\rangle\langle 1|. \quad (3.65)$$

Here $\alpha_i^{I,Q} = 1/N \int_0^T [\langle |i\rangle\langle i| \hat{\mathcal{M}}_{I,Q} \rangle - \langle |0\rangle\langle 0| \hat{\mathcal{M}}_{I,Q} \rangle] dt$ are defined by the integral of the measured signal for qubit in state $|i\rangle$ from the start of the measurement $t = 0$ to the final time T , with the ground state response subtracted. This corresponds to the shaded area in between the measured traces in Figure 3.10. Due to the finite qubit lifetime, this integration only runs up to several microseconds. The normalization N is chosen such that $\alpha_1^{I,Q} = 1$. The measurement operator for one qubit is thus by definition given by $\hat{\mathcal{M}}_{I,Q} = |1\rangle\langle 1|$, and its expectation value $\langle \hat{\mathcal{M}}_{I,Q} \rangle = \text{Tr}[\hat{\rho} \hat{\mathcal{M}}_{I,Q}]$ (which is the normalized area between the measured transmitted signal for the qubit in the state $\hat{\rho}$ and in the ground state) directly yields the population of the qubit.

This measurement operator can easily be generalized to read out multiple levels of the transmon qubit, by extending the sum in Equation (3.65) over the projectors on all energy levels, and was used to perform quantum state tomography of a three-level system [Bianchetti10b]. Similarly one can generalize the measurement operator to multiple qubits for a joint measurement, by running the sum over the projectors onto all computational basis states. For example, if two qubits are coupled to one single resonator, the measurement operators are given by [Filipp09] $\hat{\mathcal{M}}_{I,Q} = \alpha_0^{I,Q}|00\rangle\langle 00| + \alpha_1^{I,Q}|01\rangle\langle 01| + \alpha_2^{I,Q}|10\rangle\langle 10| + \alpha_3^{I,Q}|11\rangle\langle 11|$, which is equivalent to

$$\hat{\mathcal{M}}_{I,Q} = \beta_0^{I,Q} \hat{I} + \beta_1^{I,Q} \hat{I} \otimes \hat{\sigma}_z + \beta_2^{I,Q} \hat{\sigma}_z \otimes \hat{I} + \beta_3^{I,Q} \hat{\sigma}_z \otimes \hat{\sigma}_z. \quad (3.66)$$

Each $\beta_i^{I,Q}$ and $\alpha_i^{I,Q}$ respectively is calibrated by measuring the averaged transmission signal for each corresponding computational basis state. A single measurement trace of the transmitted signal then gives information about the joint qubit state, including the two-qubit correlations $\hat{\sigma}_z \otimes \hat{\sigma}_z$. This joint readout is used throughout this thesis and allowed us and other groups to perform full quantum state tomography of two-qubit [Filipp09, Leek09, DiCarlo09] and three-qubit states [DiCarlo10, Baur12], as well as full quantum process tomography of two- and three-qubit quantum operations [Fedorov12, Reed12]. A discussion about quantum state and process tomography using this joint readout can be found in Section 5.5.1 and Section 5.5.2.

3.2.4 Driving the qubit through the resonator

Besides using local drive lines (Section 3.1.2), the coherent control of the qubit state can also be achieved by applying a strong microwave drive to the resonator, described by the Hamiltonian \hat{H}_d (3.62). In contrast to the measurement of the qubit, the drive is applied far off-resonant from the resonator frequency, but on resonance with the qubit frequency $\omega_d = \omega_{01}$. In this limit, the drive does not measure the state of the qubit, because there is only very little phase and amplitude difference in the transmitted signal for the two qubit states. As a result, there is no significant unwanted entanglement between the resonator field and the qubit when controlling the qubit state [Blais07].

Because of the large detuning from the resonator, most of the drive is reflected at the input port. Only a small part enters the resonator and populates it with an average number of photons of $\bar{n} = (\epsilon_d/\Delta_{\text{rm}})^2$ and drives the qubit transition with the Rabi frequency $\Omega_R \approx 2g\sqrt{\bar{n}}$. Due to the large drive strength, the drive can be considered as a classical drive, described by the Hamiltonian [Blais07]

$$\hat{H}_d = \frac{\Omega_R}{2} \hat{\sigma}_x. \quad (3.67)$$

This drive therefore allows to rotate the state of the qubit around the x axis on the Bloch sphere, and when changing the phase of the drive by $\pi/2$ around the y axis.

3.2.5 Transmission line resonator

A good reference for the theory of transmission lines is the book [Pojar93, Chapters 2 and 3]. They can schematically be represented as a two-wire line (Figure 3.11a), because transmission lines for TEM wave propagation (which is used in our setup) always have at least two conductors. One can model the transmission line as series of infinitesimally small circuits of lumped elements that have the same impedance per unit length as the transmission line, see Figure 3.11b, where the different elements are given by

- the series resistance per unit length R^* for both conductors in Ω/m representing the resistance due to the finite conductivity of the conductors,
- the series inductance per unit length L^* for both conductors in H/m representing the total self-inductance of the two conductors,

- the shunt conductance per unit length G^* in S/m due to dielectric loss in the material between the conductors,
- the shunt capacitance per unit length C^* in F/m due to the close proximity of the two conductors.

Applying Kirchhoff's law to the circuit shown in **Figure 3.11**, one can derive the differential equations for a traveling wave with frequency ω in a transmission line. The solutions for the voltage V and current I are given by

$$V(x, t) = \text{Re} \left[\left(V_0^+ e^{-\gamma x} + V_0^- e^{\gamma x} \right) e^{-i\omega t} \right], \quad (3.68)$$

$$I(x, t) = \frac{1}{Z_0} V(x, t), \quad (3.69)$$

$$Z_0 = \sqrt{\frac{R^* + i\omega L^*}{G^* + i\omega C^*}}, \quad (3.70)$$

where Z_0 is the frequency dependent characteristic impedance of the transmission line and V_0^\pm the voltages of the wave propagating in the positive and negative x -direction respectively. The imaginary part ($\beta = \text{Im}[\gamma]$) of the complex propagation constant $\gamma = \alpha + i\beta = \sqrt{(R^* + i\omega L^*)(G^* + i\omega C^*)}$ describes the phase of the wave and the loss is given by the real part ($\alpha = \text{Re}[\gamma]$) which is called the attenuation constant.

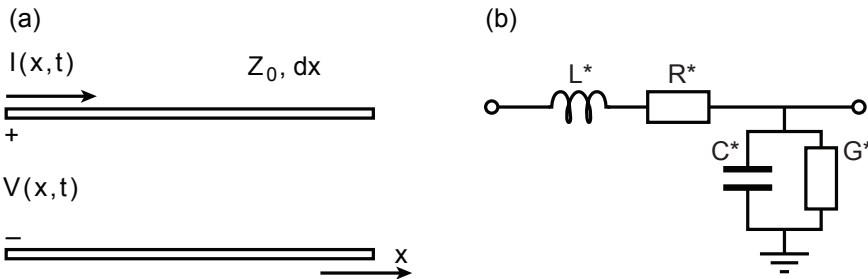


Figure 3.11: a) Schematic of a transmission line with characteristic impedance Z_0 . b) Lumped element model of an infinitesimally small segment of the transmission line with same impedance per unit length.

Terminated transmission line

Let us now consider a transmission line which is terminated at $x = 0$ with a load impedance Z_L . If it is different from the characteristic impedance $Z_L \neq Z_0$, an incident wave $V^+ e^{-i\gamma x - i\omega t}$ must excite a wave reflecting back at the end to fulfill the boundary condition. Here V^+ is referenced at $x = 0$. The ratio between the reflected and incident wave at a distance l from the load is given by the *reflection coefficient*

$$\Gamma(l) = \frac{Z_L - Z_0}{Z_L + Z_0} e^{-2\gamma l}, \quad (3.71)$$

which can be derived from the condition that the load impedance at position $x = 0$ is given by

$$Z_L = \frac{V(0, t)}{I(0, t)} = \frac{V_0^+ + V_0^-}{V_0^+ - V_0^-} Z_0. \quad (3.72)$$

The voltage in the transmission line can thus be written as $V(x, t) = \text{Re}[V_0^+(e^{-\gamma x} + \Gamma(x)e^{\gamma x})e^{-i\omega t}]$ and the input impedance Z_{in} looking into the line in the positive x -direction from a distance l of the load is then

$$Z_{\text{in}} = \frac{V(-l)}{I(-l)} = Z_0 \frac{Z_L + Z_0 \tanh(\gamma l)}{Z_0 + Z_L \tanh(\gamma l)}. \quad (3.73)$$

Open-ended transmission line resonator

We now consider the special case for which the transmission line is terminated with a perfect open circuit with impedance $Z_L = \infty$. For this condition, the incident and the reflected waves have the same voltage amplitudes ($\Gamma(0) = 1$) and form a standing wave. The voltage $V(x, t_0)$ (blue) and current amplitudes $I(x, t_0)$ (red) at time t_0 oscillate with the position on the line, see [Figure 3.12a](#). The input impedance seen looking into the line in positive x -direction therefore also varies with position, see [Figure 3.12b](#), and is given at distance $l = -x$ by

$$Z_{\text{in}}^{\text{open}} = Z_0 \coth(\gamma l). \quad (3.74)$$

Such an open-ended transmission line shows two different resonance types. Whenever the length of the line is an integer multiple of a half wavelength ($l = n\lambda/2 = \pi v/\omega_0$), there will be high impedance resonance. Whenever the length is odd multiple of a quarter wavelength ($l = (2n + 1)\lambda/4$), there will be high admittance resonance. In this thesis, the $\lambda/2$ high impedance resonance is

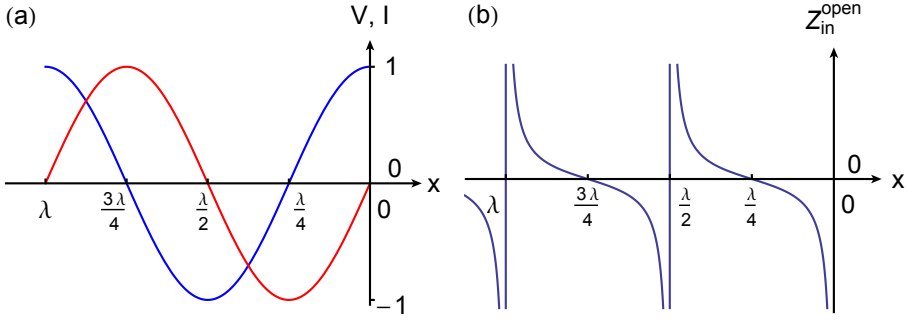


Figure 3.12: a) The amplitude of the voltage V (blue) and the current I (red) oscillate with the length of a transmission line that is open on one end ($x = 0$). b) The impedance Z_{in}^{open} as a function of the position on the open transmission line.

used by adding another open circuit termination at $x = -\lambda/2$. For frequencies ω close to the resonance frequency ω_0 , the impedance given in Equation (3.74) can be approximated for small losses $\alpha l \ll 1$ as

$$Z_{in}^{open} \approx \frac{Z_0}{\alpha l + i\pi \frac{\omega - \omega_0}{\omega_0}}. \quad (3.75)$$

Comparing this expression with the impedance of a parallel RLC oscillation circuit allows one to map this model to the parallel RLC circuit around the resonance frequency ω_0 with the substitution

$$R = \frac{Z_0}{\alpha l}, \quad C = \frac{\pi}{2\omega_0 Z_0}, \quad L = \frac{1}{\omega_0^2 C} = \frac{2Z_0}{\pi\omega_0}. \quad (3.76)$$

The resonance frequency is given by

$$\omega_0 = \frac{1}{\sqrt{LC}}, \quad (3.77)$$

and the quality factor Q of the transmission line can then be written as

$$Q = \omega_0 RC = \frac{\pi}{2\alpha l} = \frac{\beta}{2\alpha}. \quad (3.78)$$

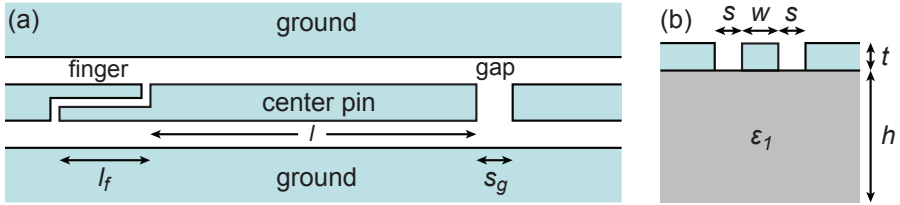


Figure 3.13: a) Top view of a CPW resonator of length l with a finger capacitor of length l_f on the left and a gap capacitor of length s_g on the right side, and the two lateral ground planes. b) Cross section of the CPW resonator design. Center conductor with width w and lateral ground planes spaced by a distance s (light blue) on top of an isolating substrate (gray). The metallization layer consists of a $t \approx 200$ nm thick sputtered niobium patterned with a standard photo lithography etching process. The substrate is a $h \approx 500$ nm thick c-cut sapphire with a relative permittivity of $\epsilon_1 \approx 11$.

3.2.6 Coplanar waveguide resonator

Probably the most well known transmission line is the coaxial cable consisting of an inner-conductor surrounded by an insulator and a conducting shield. This is convenient for testing applications but not for integrated circuits to fabricate complex microwave components. Planar transmission lines such as the stripline, microstrip, slotline or coplanar waveguide (CPW) provide a compact alternative which can easily be integrated in complex microwave circuits with standard photo lithography methods. The CPW can be seen as a two dimensional version of the coaxial cable consisting of a median strip with a width w separated by two narrow gaps of width s from the lateral ground planes as depicted in [Figure 3.13](#). The electric field is localized in these two gaps, with roughly half the electric field in the vacuum and the other half in the substrate. A detailed discussion about CPW resonators can be found in [[Göppl08](#)]. We chose this type of transmission line because it has several advantages compared to the others: it is easy to fabricate, the characteristic impedance of the line is determined by the ratio $s/(s + 2w)$ which makes it possible to reduce the size of the transmission line to values only limited by the fabrication process. Additionally, cross-talk between adjacent lines is small because of the existence of the lateral ground planes in between the lines.

The resonance frequency ω_0 of the resonator is determined by its length l and

the phase velocity $v_{\text{ph}} = c/\sqrt{\epsilon_{\text{eff}}}$ of the microwave signal propagation in the CPW

$$\omega_0 = 2\pi \frac{c}{\sqrt{\epsilon_{\text{eff}}}} \frac{1}{2l}. \quad (3.79)$$

Here the effective relative permittivity $\epsilon_{\text{eff}} \approx 5.9$ is determined by the relative permittivity of the substrate dielectric ($\epsilon_r \approx 11$ for c-cut sapphire) and the geometry of the CPW, and c is the speed of light in vacuum. The capacitance C^* and inductance L^* per unit length of the CPW can be determined with conformal mapping techniques. For a large substrate thickness h , they are given by [Simons01]

$$C^* = 4\epsilon_0\epsilon_{\text{eff}} \frac{K(k_0)}{K(k'_0)}, \quad (3.80)$$

$$L^* = \frac{\mu_0}{4} \frac{K(k'_0)}{K(k_0)}, \quad (3.81)$$

where K is the complete elliptic integral of the first kind with the arguments $k_0 = \frac{w}{w+2s}$ and $k'_0 = \sqrt{1-k_0^2}$. Assuming that the CPW only has small losses ($R^* \ll \omega L^*$ and $G^* \ll \omega C^*$), we can write the impedance of the line as

$$Z_0 \approx \sqrt{\frac{L^*}{C^*}} = \frac{1}{4} \sqrt{\frac{\mu_0}{\epsilon_0\epsilon_{\text{eff}}}} \frac{K(k'_0)}{K(k_0)}. \quad (3.82)$$

Our typical CPW resonators have a center pin with a width of $w = 10 \mu\text{m}$ and gap sizes of $s = 4.5 \mu\text{m}$ to the lateral ground planes, which leads to a characteristic impedance of $Z_0 = 50 \Omega$. It is possible to map this CPW resonator to the parallel RLC circuit model for frequencies around the resonance frequency $\omega \sim \omega_0$ with Equation (3.76)

$$L = \frac{2L^*l}{\pi^2}, \quad C = \frac{C^*l}{2}, \quad R = \frac{Z_0}{\alpha l}. \quad (3.83)$$

In other words, the CPW resonator can be approximated as an RLC resonator. If the loss is zero ($R = \infty$), it can thus be quantized the same way as an LC resonator, leading to the Hamiltonian of a usual harmonic oscillator

$$\hat{H} = \hbar\omega_0 \hat{a}^\dagger \hat{a}. \quad (3.84)$$

Input/output coupling

In order to drive the resonator and to read out the transmission spectrum, it is capacitively coupled to input/output transmission lines with impedance Z_0 , see [Figure 3.13](#). The coupling capacitance C_L is typically varied from 0.2 fF up to 60 fF by using gap capacitors with a gap of $s_g \approx 50 \mu\text{m}$ or finger capacitors with 8 fingers with finger lengths $l_f \approx 100 \mu\text{m}$. This coupling has several effects on the properties of the resonator, see [\[Göppl08\]](#) for details. First, the resonance frequency is shifted due to the parallel contribution $C_p = C_L/(1 + \omega_0^2 C_L^2 R_L^2)$ of the coupling capacitance to $\tilde{\omega}_0 = 1/\sqrt{L(C + 2C_p)}$. Second, one has to distinguish between the internal quality factor $Q_{\text{int}} = \omega_0 RC$ determined by conductor and dielectric losses in the resonator, and the external quality factor $Q_{\text{ext}} = \omega_0 C(1 + \omega_0^2 C_L^2 R_L^2)/(2\omega_0^2 C_L^2 R_L)$ determined by the coupling capacitance and external resistive loading R_L . The total quality factor is then given by $1/Q = 1/Q_{\text{int}} + 1/Q_{\text{ext}}$. Using superconducting materials, internal quality factors of up to 10^6 have been reached and are thought to be limited by impurities in the metal to dielectric interface [\[Megrant12, Pappas11, Wisbey10\]](#).

3.2.7 Coupling a transmon qubit to a coplanar waveguide resonator

Even though the transmon qubit is insensitive to DC voltage, it still couples to an AC voltage oscillating close to the transition frequency, as described in [\[Koch07a\]](#). For a transmon qubit positioned in the gap of a CPW resonator, this AC voltage is given by the electric field generated between the center pin and the ground planes. The gate voltage V_g in the kinetic term of the CPB Hamiltonian [\(3.20\)](#) is thus given by a DC component and the quantum voltage \hat{V} generated by photons inside the resonator

$$\hat{V}_g = V_g^{\text{DC}} + \hat{V}. \quad (3.85)$$

Since the CPW resonator can be seen as an LC oscillator, see [Section 3.2.6](#), the operator $\hat{V} = \hat{q}/C$ can be written in terms of the charge operator \hat{q} introduced in the beginning of [Section 3.1](#), which then yields

$$\hat{V} = \sqrt{\frac{\hbar\omega_r}{2C}}(\hat{a} + \hat{a}^\dagger) = V_{\text{rms}}^0(\hat{a} + \hat{a}^\dagger), \quad (3.86)$$

where V_{rms}^0 is the vacuum voltage of the resonator in the ground state. Substituting this gate voltage into the Hamiltonian (3.20) and following the same calculations as were done for the derivation of the driving Hamiltonian (3.36) of a CPB we get

$$\hat{H} = 4E_C (\hat{N} - n_g^{\text{DC}})^2 - E_J(\Phi) \cos \hat{\delta} + \hbar\omega_r \hat{a}^\dagger \hat{a} + 2e\beta V_{\text{rms}}^0 (\hat{a}^\dagger + \hat{a})\hat{N}. \quad (3.87)$$

Here the first two terms correspond to the usual DC biased CPB Hamiltonian, the third term is the energy of the resonator, the last term is the coupling Hamiltonian and $\beta = C_g/C_\Sigma$ accounts for the fact that some of the voltage drops between the center conductor and the island, and the other between island and reservoir of the CPB and depends on the geometry of the box. Rewriting this Hamiltonian in the basis of the uncoupled CPB eigenstates $|k\rangle$, we obtain the generalized Jaynes-Cummings Hamiltonian

$$\hat{H}/\hbar = \sum_k \omega_k |k\rangle\langle k| + \omega_r \hat{a}^\dagger \hat{a} + \sum_{k,l} g_{k,l} |k\rangle\langle l| (\hat{a}^\dagger + \hat{a}), \quad (3.88)$$

where the coupling energies are determined by the matrix element of the charge operator and the vacuum voltage of the resonator

$$\hbar g_{ij} = 2e\beta V_{\text{rms}}^0 \langle i|\hat{N}|j\rangle = \hbar g_{ji}^*. \quad (3.89)$$

If the CPB is operated in the charge regime and at the charge degeneracy point n_g^{DC} , only the first two energy levels are considered and the matrix elements of the charge operator are simply given by $\hbar g_{01} = \hbar g_{10} = e\beta V_{\text{rms}}^0$ and $g_{00} = g_{11} = 0$. In the transmon regime, the matrix elements are given by [Koch07a]

$$|\langle j+1|\hat{N}|j\rangle| \approx \sqrt{\frac{j+1}{2}} \left(\frac{E_J}{8E_C} \right)^{1/4}, \quad (3.90)$$

$$|\langle j+k|\hat{N}|j\rangle| \xrightarrow{E_J/E_C \rightarrow \infty} 0, \quad \text{for } |k| > 1. \quad (3.91)$$

All off-diagonal elements with $|k| > 1$ are nearly zero because of the near harmonicity of the transmon qubit and will be neglected in the following. The matrix elements $g_{i,i+1}$ are proportional to E_J/E_C ratio. This is a rather remarkable result. While the sensitivity to DC charge fluctuations decreases exponentially with increasing E_J/E_C , the coupling strength $g_{i,i+1}$ induced by AC charge fluctuations increases with a weak power law. It is even larger than the one in the charge regime

with large charge dispersion. An intuitive picture that explains this result is nicely described in [Koch07a]. Substituting these coupling strengths into Equation (3.88) and applying the rotating wave approximation, which drops the coupling terms $|k-1\rangle\langle k|\hat{a}$ and $|k\rangle\langle k-1|\hat{a}^\dagger$ which excite or lower both the qubit and the resonator simultaneously, results in the effective generalized Jaynes-Cummings Hamiltonian

$$\hat{H}/\hbar = \sum_{k=0}^{N-1} \omega_k |k\rangle\langle k| + \omega_r \hat{a}^\dagger \hat{a} + \sum_{k=1}^{N-1} \sqrt{k} g_{01} (|k-1\rangle\langle k|\hat{a}^\dagger + |k\rangle\langle k-1|\hat{a}). \quad (3.92)$$

which is equal to the generalized Jaynes-Cummings Hamiltonian described in Section 3.2.1. Due to the small anharmonicity α of the transmon qubit which is similar to the coupling strength g_{01} , at least three energy levels need to be included to get accurate results. For the resonant case, this was experimentally demonstrated in [Fink08].

4

Measurement Setup

Controlling a quantum system at millikelvin temperatures and on a single quantum level with room temperature equipment is a challenging task. While it must couple strong enough to the control instruments for qubit manipulation and readout, it must be effectively isolated from its environment, such as from high frequency electromagnetic fields (e.g. thermal radiation from room temperature traveling along the cables connected to the sample), low frequency magnetic fields and electrical noise. Here I summarize the techniques used to achieve this task in the Quantum Device Lab at ETH Zurich. At the beginning of this chapter, in [Section 4.1](#), I describe how to connect the millimeter sized quantum chip to coaxial microwave cables and how to protect the quantum system from electromagnetic radiation and magnetic fields using a sample box and magnetic shielding. In [Section 4.2](#) the cabling from millikelvin to room temperature within the dilution refrigerator is discussed, including the different filtering and thermal anchoring techniques to reduce the Johnson-Nyquist noise. The microwave signal synthesis for qubit manipulation, the signal down-conversion and digitization of the qubit readout signal for post-processing at room temperature is discussed in [Section 4.3](#). And finally, in [Section 4.4](#), the on-chip magnetic flux lines for fast individual qubit frequency tuning and its implication on the qubit coherence is discussed. Furthermore, I describe an optimal pulse control technique ([Section 4.4.2](#)) for accurate local magnetic flux pulses applied to the transmon SQUID loop.

4.1 Mounting the sample

The quantum processor is fabricated on a $2 \times 7 \times 0.5$ mm polished sapphire chip using standard lithography techniques. The resonator structure with feature size of $2 \mu\text{m}$ is patterned into a magnetron sputtered niobium thin film of thickness 150 nm using reactive ion etching. Smaller qubit structures with feature size ~ 100 nm are then written into a double layer resist film using a beam of electrons with an energy of 30 keV, followed by a double angle shadow evaporation of two thin aluminum films (20 nm and 80 nm) interrupted by a short oxidation step. Because a detailed discussion of the individual fabrication processes can be found in [Göppl09, Fink10], I will not discuss fabrication any further in this thesis.

In order to connect the on-chip quantum processor to the qubit control and read out cabling, a printed circuit board (PCB) with room for eight coaxial cable ports is used, see [Figure 4.1](#). The chip is glued with PMMA into the small cutout located at the center and then contacted with the PCB under a microscope using short $\sim 30 \mu\text{m}$ thin aluminum wire bonds. While we use 2 – 3 bonds to make contact between the respective coplanar waveguide launchers, about 10 bonds per millimeter are used to connect the chip ground planes to the PCB ground at the circumference. Additionally, we use another ~ 20 bond wires to connect partitioned on-chip ground planes with each other to eliminate spurious resonances. The right angle surface mount *Rosenberger* SMP launchers are soldered with a heat gun onto the PCB and mounted bullet adapters serve as intermediaries for SMP connection to microwave coaxial cables.

When designing the PCB we take care of properly suppressing any parasitic resonance modes and impedance mismatches. The former is achieved by connecting the top ground plane with the back copper metallization using small via holes, which suppress any resonance modes between these two plates. Choosing a spacing of 1 mm gives acceptable results up to ~ 20 GHz. To have no resonances within the sample area, the chip was chosen small enough such that the cut-off frequency is larger than the relevant frequencies of the quantum processor. The impedance mismatch at the interface between the chip and PCB can be minimized by choosing dielectrics with similar dielectric constants for both parts, such that the waveguide launchers have similar dimensions. We thus choose a low loss woven glass laminate *AD1000* dielectric from *Arlon* with a relative dielectric constant of $\epsilon_r = 10.2$ at 10 GHz for the PCB, compared to sapphire which has $\epsilon_r = 11$.

The PCB is then mounted in a fully closed sample box made out of solid oxygen free copper to shield the chip from electromagnetic radiation, see [Figure 4.1](#). This

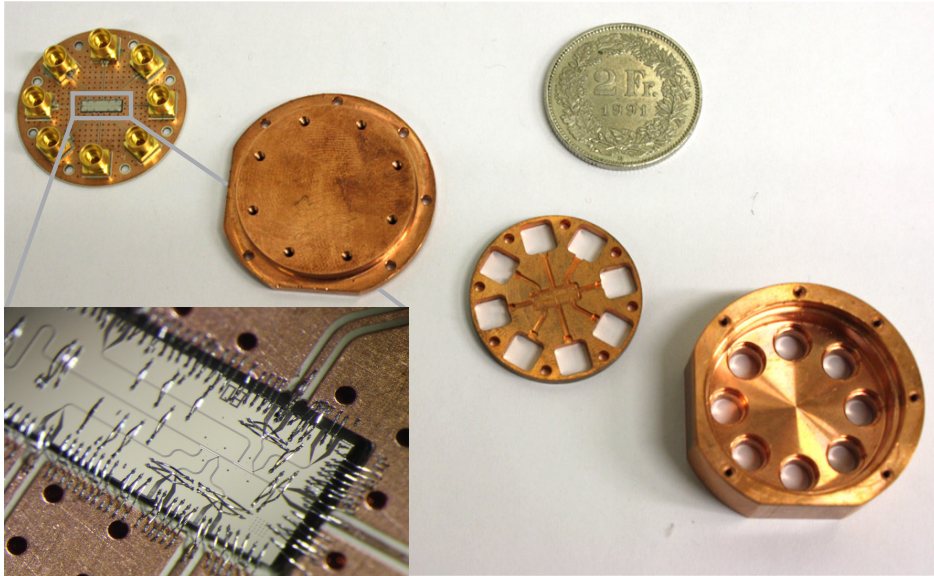


Figure 4.1: The chip is glued onto a PCB to make connection to the microwave cables (left). The connection from the PCB onto the chip is done using thin wire bonds (left bottom). Before mounting the PCB into the sample holder (right), it is screwed onto the base sample mount (second from the left) and covered with a shim (second from the right) to fill all remaining empty space and remove unwanted spurious modes in the otherwise empty cavity.

box consists of three parts, a base (second from the left) onto which the PCB is screwed, a cover (second from the right) and a lid (right). The eight holes in the lid are used as a feed-through for the SMP connectors of the semi-rigid microwave cables and entirely closed when fully assembled. Any free space inside the sample mount can support resonance modes at frequencies similar to the operation frequencies of the processor. In particular we observed a resonance at around 10 GHz. We suppress this mode by filling the empty space with the sample cover, shown in the middle of [Figure 4.1](#). This copper spacer is mounted flush with the top of the PCB. Milled slots with a depth of $500\ \mu\text{m}$ at the positions of the waveguide structures and the chip prevent from shorting any lines and bond wires. With this design the free space is drastically reduced to dimensions for which the cut-off frequency is well above 20 GHz.

The fully assembled sample holder with three superconducting coils (two coils with an inner diameter of 4 mm and a big coil on top with an inner diameter of 11 mm) mounted onto the outer part of the base underneath the chip is shown in [Figure 4.2a](#). The magnetic field generated by these coils is local enough to be able to dc bias each individual frequency of three different transmon qubits. Fast tuning of qubit frequency is achieved using on-chip transmission lines (see [Section 4.4](#)). The coil bodies are made out of *Stycast®1266* epoxy which is non conductive and thermalizes well at millikelvin temperatures and the superconducting wire used is a 35 μm thin niobium-titanium wire of type *SC-T48B-M* from *Supercon Inc.* More details can be found in [[Bianchetti10a](#)].

The sample holder is then mounted onto the 20 mK plate of the dilution refrigerator with a long threaded rod and shielded from external magnetic fields using two layers of a high permeability nickel-iron alloy (*Cryoperm 10*), see [Figure 4.2b](#) and [c](#).

4.2 Cryogenic wiring

Connecting the quantum processor at 20 mK to room temperature equipment for qubit control and readout requires special care in the design of the cryogenic setup, with the main goal to minimize the electric Johnson-Nyquist noise, generated by the thermal agitation of charge carriers inside a conductor, and the heat transferred along the wiring to the sample. At the same time, the power dissipated at the different temperature stages of the refrigerator needs to be below the maximal cooling power of the cryostat. Depending on the function of the wire different methods are used to achieve these goals. These include filtering, attenuation, thermal anchoring and the choice of cables. In our setup we need to distinguish between the microwave input lines used to manipulate qubit state and to drive the readout resonator, the output lines of the resonator, the cabling for the flux lines and the DC bias lines for the magnetic coils, see [Figure 4.2c,d](#) and [Figure 4.3](#) for an overview of the cabling.

Microwave input lines

The microwave signals are generated at room temperature with a commercial microwave source *E8257D* from *Agilent* which provide maximal signal powers of 20 dBm, much larger than the room temperature Johnson-Nyquist noise. To

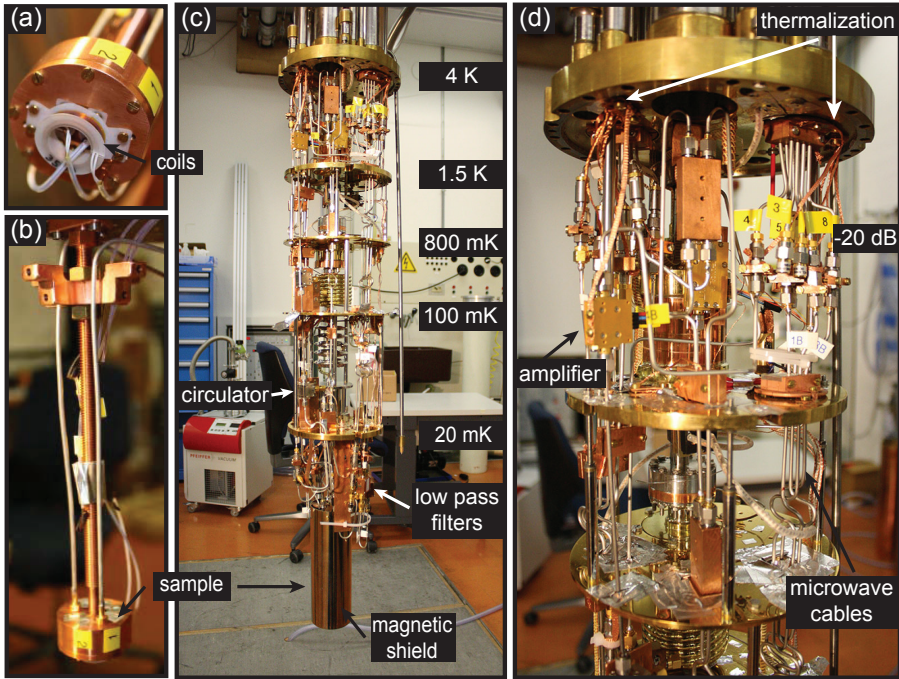


Figure 4.2: a) Closed sample holder with the magnetic coils mounted underneath the chip. b) Mounted sample holder with the holder for the magnetic shielding. c) Fully wired insert of our dilution refrigerator showing the different temperature plates. The mounted double-walled magnetic shield covering the sample is seen at the bottom. d) Close up of the 800 mK to the 4 K temperature plates with one of the HEMT amplifiers thermally anchored to the 4 K plate (left side). The other HEMT amplifier thermally anchored to the 1.5 K plate is only barely visible. Every input microwave cables are attenuated with -20 dB and thermally anchored to the 4 K plate.

4 Measurement Setup

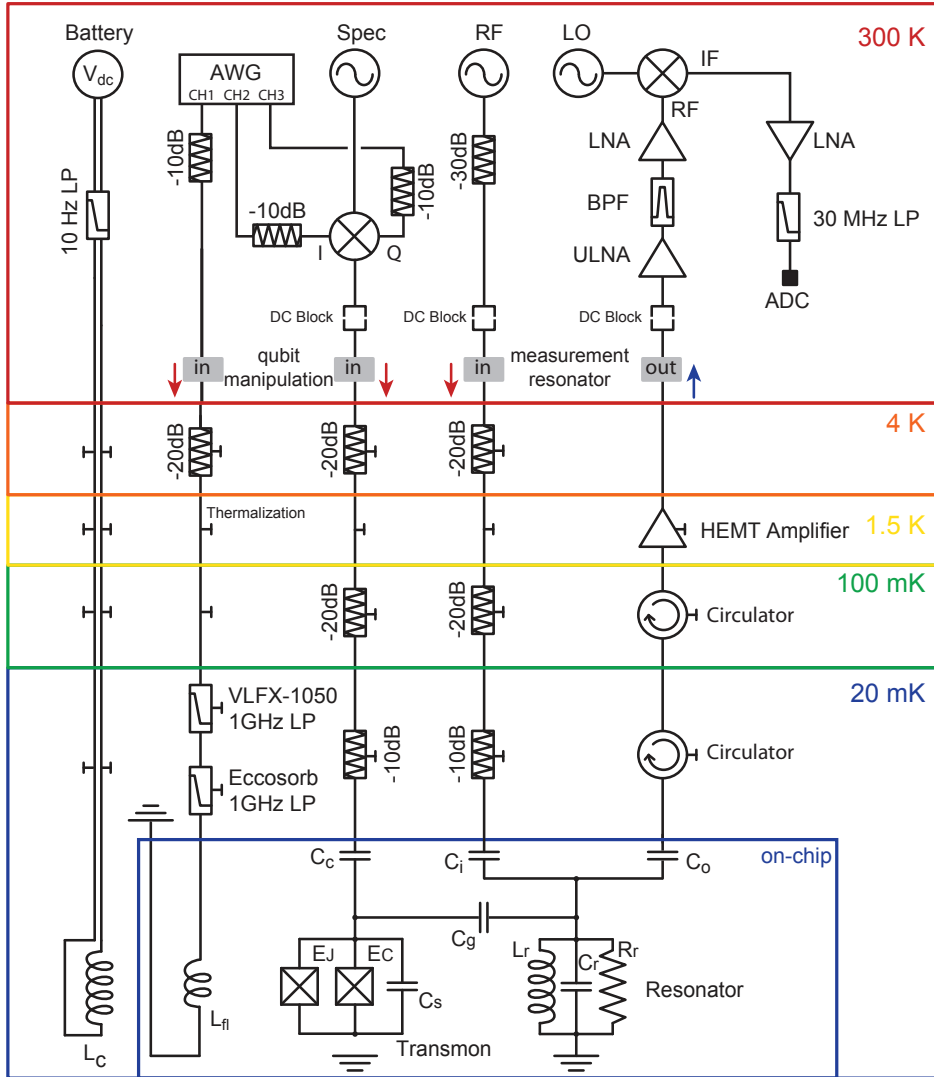


Figure 4.3: Schematic of the cryogenic measurement setup. The transmon qubit is biased with the magnetic coil L_c and manipulated on the nanosecond time scale with an on-chip magnetic flux line inductively coupled L_{fl} and an on-chip microwave line capacitively coupled C_c to the qubit. The readout of the qubit is carried out by measuring transmission through the input (C_i) and output (C_o) coupling port of a resonator, which is capacitively coupled (C_g) to the qubit.

control and readout the qubit state however, no more than -50 dBm and -120 dBm of power at the sample is required, respectively. The easiest method in this case to eliminate the Johnson-Nyquist noise is to just attenuate the entire signal at low temperatures. For temperatures above 1 K, the noise power spectral density $S_{v^2}(\omega) \approx 4k_BTR$ emitted by a resistor with resistance R in the 1 – 20 GHz regime depends linearly on temperature T . We therefore mount a 20 dB attenuator for each microwave input line at 4 K, which reduces the noise from room temperature below the noise generated at 4 K. To further suppress the noise from temperatures higher than the base temperature, it turned out to be sufficient to add another 20 dB at 100 mK and 10 dB at 20 mK [Bianchetti10a]. Even though all attenuation could also be installed at 20 mK, the heat load due to dissipation of the control and measurement signal would be large enough to significantly increase the base temperature. Since the higher temperature stages of the cryostat have higher cooling power, it is desirable to dissipate most of the energy at 1.5 K and 4 K. This method of signal attenuation to reduce the Johnson-Nyquist noise only works if the cables are well thermalized with the different temperature stages. We therefore thermally anchor the outer conductor of each cable at every temperature state with solder braids. Due to the poor thermal conductance of the dielectric of the coaxial cables, the inner conductor is effectively only thermalized at each attenuator, filter or amplifier, where the inner conductor is in contact with the outer conductor.

Besides transferring electrical noise, the cables can also transfer significant amount of heat towards the sample. Using standard semi-rigid cables made out of copper for example would inevitably warm up the cryostat. For this reason, all microwave input lines connecting different temperature stages are made entirely out of stainless steel.

Microwave output lines

When performing readout of the qubit state, the resonator is populated with only a few photons \bar{n} on average. For a typical resonator line width $\kappa/2\pi \approx 2$ MHz and resonator frequency $\omega_r = 8$ GHz, the transmitted power $P_m = \hbar\omega_r\bar{n}\kappa \approx 10^{-17}$ W is extremely small and has to be amplified by a factor of more than 10^{10} to be detectable, using several amplification steps. Even with the best commercially available amplifiers, a significant amount of noise larger than the signal itself is added to the weak signal during this process. To get a good signal to noise ratio, it is thus essential to avoid attenuation on the output line. We therefore use a microwave cable with silver plated center conductor, or in newer setups, superconducting

cables based on a niobium-titanium alloy for the connection between the sample and the first amplifier.

Since the signal to noise ratio is mainly limited by the noise added by the first amplifier, we use an ultra low noise HEMT amplifier from *Caltech* or the *Low Noise Factory*, operated at cryogenic temperatures. They typically have a gain of 30 – 35 dB and a very low noise temperature of 4 K with a bandwidth from 4 – 8 GHz. Due to the significant amount of power dissipated in such a device ($\sim 20 - 30$ mW) it is thermally anchored to the 4 K or 1.5 K stage rather than to the base plate. Any Johnson noise from room temperature is blocked by the output port of the amplifier. The remaining 4 K/1.5 K Johnson-Nyquist noise and amplifier noise that could travel along the output line from the input port of the amplifier down to the sample is blocked with two circulators from *Pamtech*¹. This is a passive non-reciprocal three-port device, which redirects microwaves entering any port i to port $i + 1$, but never to $i - 1$. When terminating port 3 with 50Ω and using the port 1(2) as the input (output) port, then the measurement signal coming from the sample is transmitted from port 1 to 2. But the noise entering port 2 is always redirected to port 3, where it is dissipated in the 50Ω termination.

At room temperature, the measurement signal is further amplified by 60 dB and band-pass filtered before it is downconverted to an intermediate frequency, amplified and digitized for detection, see [Section 4.3.2](#).

Flux lines

On-chip magnetic flux lines are used for fast tuning of the individual qubit frequencies, using short current pulses generated with an arbitrary waveform generator (AWG) from *Tektronix* (*AWG5014*). These instruments have a sampling rate of 1.2 GS/s, which means that they can generate signals with maximal bandwidth of 600 MHz. At the same time, these lines should also allow for local dc biasing. The cabling therefore requires a bandwidth of DC-600 MHz. In contrast to the microwave input lines where the Johnson noise is eliminated by attenuation, this is not possible due to the heat load generated by the large currents of 1 – 10 mA flowing through the flux line. Instead, we have installed a low pass filter *VLFX-1050* from *Mini-Circuits* at the base plate, with a cut-off frequency of around 1 GHz and a stop band reflection larger than 40 dB. The cut-off is chosen significantly larger than the required bandwidth, to distort the current pulse as little as possible. In

¹At the same time they also serve as thermal anchors for the center conductor

addition, we add an Eccosorb low pass filter [[Santavicca08](#)], which attenuates the signals above the cut-off frequency of 1 GHz, rather than to reflect the signals. This ensures that the qubit sees a constant load impedance of $50\ \Omega$ for all frequencies when looking into the flux line, such that the influence on the qubit coherence due to the capacitive coupling between the qubit and the flux line is minimized (see also [Section 4.4](#)). At the 4 K plate where more than 1 W of cooling power is available, we use 20 dB of attenuation. This setup is sufficient for short flux pulses, but not for dc biasing due to heating issues. The only dissipative element at the lower temperature plates are the stainless steel coaxial cables. Replacing these with superconducting cables may eliminate this problem.

DC bias line for the coils

The large mutual inductance between the coils and the transmon SQUID loops requires careful low-noise biasing to avoid $1/f$ flux noise which leads to dephasing of the qubit. For this reason, we use isolated voltage battery sources *SIM928* from *Stanford Research Systems* to provide an ultra low noise output. The voltage can be set from $-20\ \text{V}$ to $20\ \text{V}$ with only $10\ \mu\text{V}_{\text{rms}}$ of noise within a 1 kHz bandwidth. Additionally, we add a simple *RC*-filter at room temperature to the output with a cutoff frequency below 10 Hz to further decrease the noise, see [[Bianchetti10a](#)] for details. At the same time, it converts the voltage source into a current source by using $20\ \text{k}\Omega$ resistors in series within the filter. The source then still provides enough current since only $\sim 100\ \mu\text{A}$ are required to apply one single flux quantum through the SQUID loop.

The wiring and connection to the cryostat is done with an electromagnetically shielded twisted pair cable and shielded *LEMO* connectors. Within the cryostat, standard twisted pair looms out of copper are used from room temperature to 1.5 K, and superconducting Nb-Ti looms for connection down to base temperature to avoid heating due to dissipation. At every temperature stage, each loom is thermally anchored by winding it around a copper rod and fixing it with GE low-temperature varnish (*C5-101*).

Grounding

Because there are many different instruments and cables connected to the cryostat, it can easily happen that the grounds of two instruments attached to different power supplies are both connected to the cryostat, creating a so called ground loop.

Whenever the two grounds are on slightly different potentials, equalizing currents will flow along unpredictable paths within the cryostat. Since the center pin of our flux line is grounded on one end, these fluctuating currents can generate a magnetic field at the position of the qubit, leading to fluctuating qubit frequencies, and therefore dephasing. To avoid these problems, we connect only the ground of the AWG used to generate the fast flux pulses via the flux line to the cryostat. All other grounds are isolated with DC blocks.

4.3 Qubit control and data acquisition

4.3.1 IQ modulation

The time resolved manipulation of superconducting qubits requires accurate control over the amplitude, phase and frequency of a microwave carrier signal at the qubit frequency on nanosecond timescale. This is accomplished by modulating the in-phase (I) and quadrature (Q) components of the carrier signal with an IQ-mixer. A schematic of such a device is shown in [Figure 4.4](#). A continuous wave $s_{LO} = A \cos(\omega_{LO}t)$ with a frequency ω_{LO} of up to 20 GHz is generated with an analog signal generator *E8257D* from *Agilent* and fed into the local oscillator (LO) port of the mixer. Since these IQ-mixers obtain their bias from the power supplied by the LO signal, this power should be kept constant within the designed range of the IQ-mixer (10 – 13 dBm or 13 – 16 dBm for our IQ-mixers). This LO signal is then split into two signals. One of them is in phase with the carrier and multiplied with the voltage applied to the I port s_I using a mixer, and the other one is phase shifted by $-\pi/2$ and multiplied with the Q voltage s_Q . Adding these two signals with a power combiner results in the output waveform

$$s_{RF} = I \cos(\omega_{LO}t) + Q \sin(\omega_{LO}t) = A \cos(\omega_{LO}t + \phi), \quad (4.1)$$

where $I = A \cos(\phi)$ and $Q = A \sin(\phi)$. We can thus control the amplitude and phase of the carrier wave, by manipulating the amplitude of the separate I and Q input signals. This is often referred to as quadrature upconversion. Instead of using DC voltages, we can also apply the waves $I \cos(\omega_{IF}t + \phi)$ and $Q \cos(\omega_{IF}t + \phi_Q + \phi)$ with an intermediate frequency ω_{IF} to the I and Q ports, respectively. In general, the resulting output signal will then consist of two sideband signals with frequencies $\omega_{LO} \pm \omega_{IF}$ centered around the carrier frequency. For the special case that $\phi_Q = \pm\pi/2$ and $I = Q$, either the right or the left sideband is canceled, resulting in a

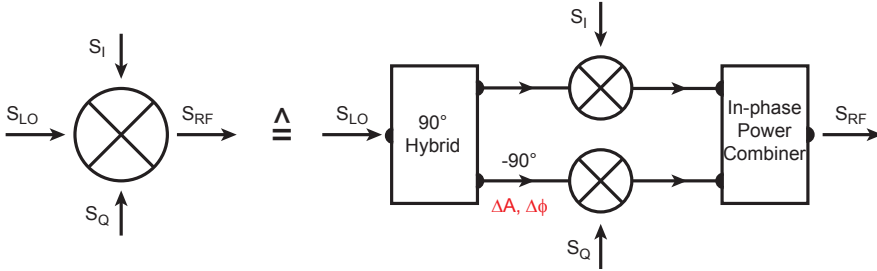


Figure 4.4: Schematics of an in-phase/quadrature mixer used for up/down conversion of microwave signals. It consists of two mixers, a 90 deg hybrid and an in phase power combiner. Amplitude and phase errors of the hybrid, power combiner and cables can be combined to single errors and are indicated by ΔA and $\Delta\phi$.

single frequency output signal, shifted by ω_{IF} from the carrier. The amplitude and phase of this signal is manipulated with the amplitude $I = Q$ and phase ϕ of the two IQ waves. This type of mixing, referred to as single sideband mixing, has the advantage that imperfections in real physical mixers are easier to calibrate, as described below.

Mixer imperfections

In our measurement setup, we use an arbitrary waveform generator, typically an *AWG5014* from *Tektronix*, to generate the I and Q signals, and the *IQ - 0307* or *IQ - 4509* mixers from *Marki Microwave* for IQ modulation, as depicted in [Figure 4.5a](#). The output signals of the AWG are attenuated by 10 dB before they are connected to the mixer, in order to reduce the broadband noise of the AWG output which is upconverted to the qubit frequency. Additionally to the channel outputs, the AWG also provides DC voltage outputs which are connected to a simple voltage divider and then added to the channels using the rear panel inputs. This is convenient as no additional bias tees are required to add DC offsets to the I and Q ports used to calibrate for offset related imperfections of the mixers. These imperfections can be categorized into the phase $\Delta\phi$ (phase imbalance), amplitude ΔA (amplitude imbalance) and offset error. The former two are caused by the imperfect hybrid and power combiners within the IQ-mixer, see [Figure 4.4](#), as well as by differences in the length of the cables connecting the AWG and the I/Q

4 Measurement Setup

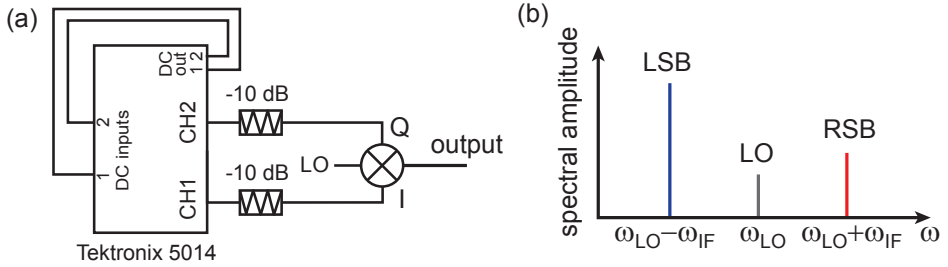


Figure 4.5: a) Microwave pulse generation setup, with modulation intermediate frequency signals generated by an arbitrary waveform generator and then upconverted to qubit frequencies using an IQ-mixer. b) The output signals for single sideband upconversion. Due to imperfections in the mixer, the output contains three instead of a single frequency. Carrier leakage is attributed to DC offset errors, while the imperfect sideband suppression is caused by phase and amplitude errors.

ports of the mixer. These errors manifest themselves in the output spectrum as an imperfect suppression of the unwanted sideband (Figure 4.5b). Small DC offsets at the IQ ports result in leakage of the carrier signal at the LO frequency, even if no voltage is applied to the IQ ports. For the *Marki* mixers used, the isolation between the LO and RF port (carrier leakage) is typically about 30 – 40 dB, and the phase and amplitude errors are about $\Delta\phi < 5$ deg and $\Delta A < 0.3$ dB, respectively. For a tiny phase imbalance of only 1 deg, the unwanted sideband suppression is already reduced to only 40 dBc, and typical mixers have a sideband suppression of about 25 dBc.

It now becomes clear why we prefer to use sideband mixing rather than mixing with DC voltages on the IQ port. In the latter case, the upconverted qubit drive is at the same frequency as the LO leakage, resulting in an unwanted qubit drive even if no signal is applied to the IQ port. Regardless of whether this leakage can be drastically reduced or completely removed, there is still the problem that the phase of the output signal strongly depends on the phase and amplitude imbalances. To realize high fidelity single qubit gates, these imbalances must be calibrated.

For the case of sideband mixing however, the carrier leakage and the unwanted sideband are off-resonant from the qubit transition (we typically chose a ω_{IF} of 100 MHz), and thus have much less influence on the gate fidelity. Additionally, the phase of the output signal is fully determined by the phase of the I and Q signals

only, which can accurately be defined while generating the signals with the AWG, even if no calibration is carried out. Nevertheless, for optimal single qubit gates, we still calibrate for the imbalances.

Mixer calibration

Calibrating the mixer allows us to enhance the LO to RF port isolation to about 80 dB and the sideband suppression to ~ 65 dBc. The leakage error is reduced by adding DC voltage offsets to the IF signal on the I and Q ports. We run a routine which searches the I and Q voltages which minimize the carrier leakage. To reach good results, these voltages must be chosen with an accuracy better than $200 \mu\text{V}$. To understand how to calibrate for the amplitude and phase imbalances, we calculate the output signal including these two errors, yielding

$$s_{\text{RF}} = \frac{1}{2} [I \cos(\omega_{\text{LO}}t) \cos(\omega_{\text{IF}}t + \phi) + (1 + \Delta A)Q \sin(\omega_{\text{LO}}t) \cos(\omega_{\text{IF}}t + \phi + \phi_Q)], \quad (4.2)$$

$$= \frac{1}{4} [I(\cos((\omega_{\text{LO}} + \omega_{\text{IF}})t + \phi) + \cos((\omega_{\text{LO}} - \omega_{\text{IF}})t - \phi)) + (1 + \Delta A)Q(\sin((\omega_{\text{LO}} + \omega_{\text{IF}})t - \Delta\phi + \phi + \phi_Q) + \sin((\omega_{\text{LO}} - \omega_{\text{IF}})t - \Delta\phi - \phi - \phi_Q))]. \quad (4.3)$$

When the upper sideband should be used for qubit driving, the lower sideband can be canceled by choosing the amplitude $Q = I/(1 + \Delta A)$ and phase $\phi_Q = \pi/2 - \Delta\phi$. The signal on the upper sideband is then given by

$$s_{\text{RF}}^{\text{RSB}} = \frac{1}{2} I \cos(\Delta\phi) \cos((\omega_{\text{LO}} + \omega_{\text{IF}})t + \phi - \Delta\phi). \quad (4.4)$$

Similarly, when using the lower sideband we choose $Q = I/(1 + \Delta A)$ and $\phi_Q = -\pi/2 + \Delta\phi$, yielding the output

$$s_{\text{RF}}^{\text{LSB}} = \frac{1}{2} I \cos(\Delta\phi) \cos((\omega_{\text{LO}} - \omega_{\text{IF}})t - \phi - \Delta\phi). \quad (4.5)$$

Note the different signs in the phase of the signal, depending on which sideband is used. This must be considered when choosing the rotation axis for a single qubit gate operation.

The optimal values of Q and ϕ_Q are in practice found by determining the values

for which the power in the unwanted sideband is minimized. Since this calibration is not independent of the LO frequency, it needs to be redone whenever the frequency is changed. To make it more convenient for the user, we have written a *Labview* program which executes the calibration routine automatically.

4.3.2 Data acquisition

The readout of the qubit states requires the time resolved measurement of a microwave signal transmitted through the readout resonator in the 6 – 10 GHz range. The small number of photons involved in this measurement signal (in typical experiments the resonator is populated with less than 10 photons on average) makes it necessary to repeat the same experiment a number of times in order to average out the dominant noise added by the amplification chain. In principle, this signal could be digitized using a real time high frequency oscilloscope. They are however expensive and inefficient in averaging. Since the bandwidth of the measurement signal is only a few MHz due to the filtering effect of the resonator, we instead downconvert the high frequency signal ω_{RF} to an intermediate frequency of typically $\omega_{\text{LO}} = 25$ MHz, using a mixer and a local oscillator with a frequency of $\omega_{\text{RF}} - \omega_{\text{LO}}$ (heterodyne detection). This signal is further amplified by another 30 dB and low pass filtered with an anti-aliasing filter with cut-off frequency of 30 MHz. It can then easily be digitized with a PCI data acquisition card from *Acquiris* with a sampling rate of 1 GS/s. The I and Q quadratures containing the information about the qubit population (see also [Section 3.2.3](#)) are extracted with a further digital downconversion to DC (digital homodyne). This is achieved by simply multiplying the detected signal $A(t) \cos(\omega_{\text{RF}} + \phi(t))$ with a sine and a cosine

$$I(t) = A(t) \cos(\omega_{\text{IF}} + \phi(t)) \cos(\omega_{\text{IF}}t), \quad (4.6)$$

$$Q(t) = A(t) \cos(\omega_{\text{IF}} + \phi(t)) \sin(\omega_{\text{IF}}t), \quad (4.7)$$

which folds the signal from ω_{IF} to DC and $2\omega_{\text{IF}}$. The upper sideband is removed with a digital low pass filter, by evaluating the convolution of the I and Q signals with a square window function of length $2\pi/\omega_{\text{IF}}$. The maximal bandwidth of the detection is thus limited by ω_{IF} .

If higher bandwidth is required, the analog signal can also be downconverted directly to the DC I and Q components before digitization, using an IQ-mixer and an LO frequency equal to ω_{RF} (homodyne detection). The bandwidth is then limited by the IQ-mixer bandwidth and the sampling rate of the data acquisition

card. Imperfections in the IQ-mixer, namely amplitude and phase imbalance, and DC offsets however introduce errors in the detected signal, which need to be carefully calibrated. In contrast, the digital homodyne downconversion is perfect and the analog heterodyne downconversion also introduces no errors, because only one channel of the downconversion mixer is used. Additionally, any DC offsets are removed by the digital filter. A detailed discussion of the different detection schemes can be found for example in [Schuster07a].

4.3.3 Signal synchronization

Our experiment involves the interplay between several microwave instruments. At least one microwave signal generator and two AWG output channels are needed per qubit for manipulation, two additional signal generators for measurement and heterodyne detection, and an analog to digital converter for data acquisition. The synchronization of all these devices involves three parts, as sketched in [Figure 4.6a](#). First, all devices are phase locked to an ultra stable 10 MHz reference provided by an atomic frequency standard *FS725* from *Stanford Research Systems* (red), specified with an Allan variance of $\sigma_y(\tau = 1 \text{ s}) < 2 \cdot 10^{-11}$ ($\sigma_y(\tau = 100 \text{ s}) < 2 \cdot 10^{-12}$). This measure is interpreted as the relative root mean square (rms) value of the frequency deviation between two observations τ apart. For a 10 Hz this results in a rms frequency fluctuation of $< 20 \mu\text{Hz}$ in 1 s intervals. This phase locking technique ensures the same time-base for all devices. In other words it makes sure that when setting a certain frequency, all devices deliver exactly this frequency in the given time-base. In our typical experiments, the microwave signal transmitted through the resonator is averaged over a time period of several minutes to a few hours. The frequency error between the measurement and local oscillator signal for downconversion must therefore be much less than 0.001 Hz, corresponding to a relative error of only 10^{-10} percent for a wave in the GHz regime! Otherwise, the error would lead to a phase randomization of the acquired signal and the complete loss of information when averaging over many experimental realizations. Second, a trigger signal is used to define the start of an experiment (blue). A square pulse generated with an 80 MHz AWG *33250A* from *Agilent* and a typical repetition rate of 50 kHz is sent to the trigger input of the *Tektronix* AWG's, which triggers the output of the qubit control waveform. Additionally, two marker outputs generate a square pulse which in turn trigger the measurement and data acquisition card (third part, green).

The main consideration when realizing this triggering setup is primarily on the

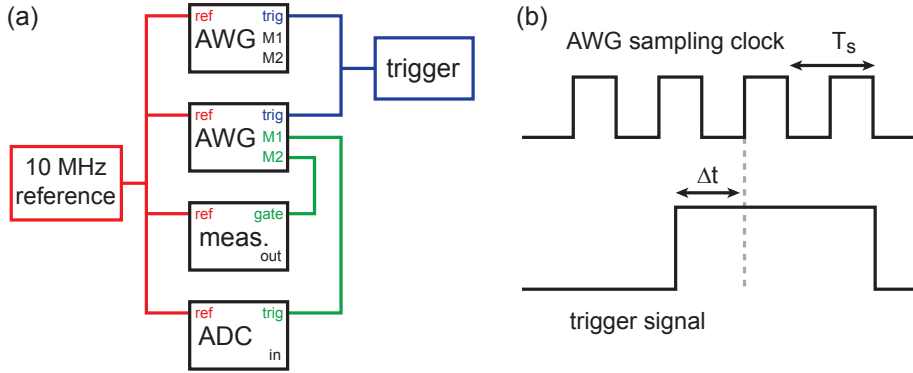


Figure 4.6: a) Synchronization of all microwave generators (AWG and measurement source) and the data acquisition card (ADC) is done with three parts. Phase locking of all devices to a 10 MHz reference (red), triggering of the AWG’s using a trigger source (blue), and triggering the measurement and data acquisition card using a marker output of an AWG (green). b) Schematic of the timing between the sampling clock of an AWG and the square pulse of the trigger signal.

timing jitter of the output signals. This is especially critical for signals involved in qubit manipulation. To understand how jitter can occur, let us take a look at the schematic in [Figure 4.6b](#), depicting the sample clock of the *Tektronix* AWG with sampling period T_s and the square pulse of the trigger signal. For synchronous trigger operation, the trigger input must occur within a valid time window with respect to the sampling clock, specified by the delay between the rising edge of the trigger to the first rising edge of the sampling clock Δt . This is because the analog output from the AWG is produced at a time determined by this first rising edge. If Δt is too small, the AWG will jump back and forth between the two rising edge of the clock at Δt and $\Delta t + T_s$, leading to a jitter in the output signal of T_s . To insure that such a state never occurs, it is important to have a fixed timing between the trigger signal and the sampling clock. Unfortunately, this can not be achieved using the output channel of the *33250A* AWG used to produce the trigger, as it always changes the timing when the output is turned off and on again. Instead, we use the sync output for which the timing is fixed. Since the phase of the sampling clock is different for all *Tektronix* AWG’s, we adjust the timing for each instrument individually by adjusting the trigger level of the trigger input. This needs to be redone whenever the instrument is restarted. Additionally, the repetition period of

the trigger must always be set to an integer multiple of the sampling clock.

4.4 Magnetic flux bias line

Quantum operations between two qubits can be realized with fast qubit frequency tuning on the nanosecond timescale using short magnetic flux pulses. The magnetic coils used to bias the qubit frequencies however have an inductance of $L \approx 0.04 - 0.8 \text{ H}$ and are biased with a $R \approx 10 \text{ k}\Omega$ feed line. This serial combination of inductance and resistance acts as a low pass filter for a current pulse sent through the coil, with a time constant $\tau = L/R$ on the order of micro- to milliseconds. Furthermore, the number of coils that can be mounted on the sample holder underneath the chip is limited, which makes it difficult to scale the system to more than five qubits while maintaining individual qubit biasing. Both problems can be resolved by adding local on-chip flux lines which allow for individual tuning of each qubit frequency on the nanosecond timescale.

The two flux line designs (FL_A and FL_B) used in our lab are shown in [Figure 4.7a](#) and [b](#). FL_B consists of a transmission line that is terminated with a short next to the transmon SQUID loop, where the current is split into two opposite directions. We place the line slightly off-centered, such that the magnetic field generated by the current is maximal at the position of the SQUID loop. This design has the advantage that the line can be brought very close to the qubit without harnessing the coherence, see [Section 4.4.1](#), needed to reach large mutual inductance. However, the currents fed onto the on-chip ground plane flow along poorly controlled paths across the whole chip, leading to cross-couplings to the other qubits (on the order of 10%) and might lead to unpredictable time response. This problem is resolved in the FL_A design, where the transmission line is terminated with a short on the PCB ground rather than on-chip. Since the PCB ground is resistive, the current is dissipated without influencing other qubits (measured cross-couplings are smaller than 1%). Even though the realizable mutual inductance is smaller compared to the FL_B design without limiting the qubit lifetime, it is still large enough for our experiments. We have thus decided to use the FL_A design through out this thesis.

The minimal mutual inductance M required for the flux line to be useful is set by the maximal amount of current we can send through the line and the possibility to apply at least half a magnetic flux quantum Φ_0 through the SQUID loop to guarantee enough tunability of the qubit frequency. The former is limited by the maximal current the room temperature electronics is able to provide, the critical

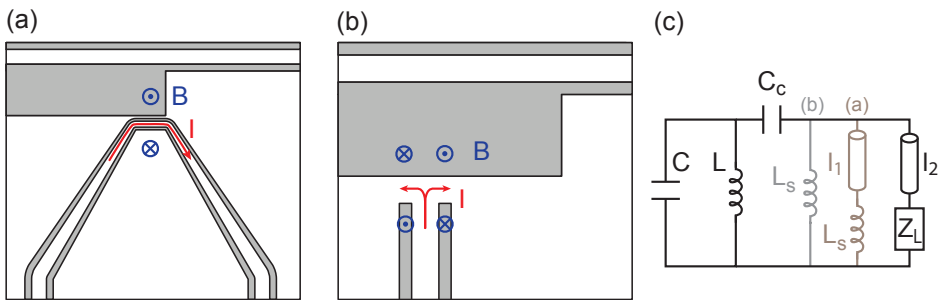


Figure 4.7: Two different flux line designs. a) FL_A consists of a transmission line passing close by the qubit and is shorted on the PCB. b) FL_B consists of a transmission line which is shorted near the qubit. c) Equivalent circuit model for calculating the energy decay rate due to the capacitive coupling of the flux line to the qubit with a coupling capacitance C_c . The qubit is modeled as a simple LC oscillator and the short termination of the flux lines as an inductance L_s . Z_L is the impedance of the termination of the input side of the flux line, and l_1 and l_2 the lengths of the transmission lines from the qubit to the short and load impedance Z_L , respectively.

current/magnetic field of the superconducting transmission line and most importantly, the maximal cooling power of the dilution refrigerator. In our experiments, we observe significant heating of several millikelvins already with dc currents of about 1 mA, due to energy dissipation in the 20 dB attenuation connected to the 4 K stage or in the normal conducting microwave cables connected to the 20 mK stage. Replacing these cables with superconducting cables might eliminate the problem to some degree.

The mutual inductance can be controlled in the design by the distance between the SQUID loop and the flux line, and by the size of the loop. A lower bound for the distance is given by the capacitive coupling of the qubit to the $50\ \Omega$ transmission line which negatively influences the qubit lifetime, see [Section 4.4.1](#). Regarding the loop size, it is not clear how large it can be made without influencing the dephasing of the qubit. Measurements on the flux noise in SQUID loops have only shown weak dependence on geometry [[Wellstood87](#)]. Nevertheless, we have taken a conservative approach and designed a rather small loop of size $4.6\ \mu\text{m} \times 3.6\ \mu\text{m}$ in our most recent three-qubit processor to minimize the influence of external stray magnetic fields. With a minimal distance of the flux line to the SQUID loop of $5.8\ \mu\text{m}$ we experimentally found a mutual inductance of $M \approx 250\ \Phi_0/\text{A}$. While this is enough for short flux pulses, it is too small for dc biasing without significant heating. We thus still do the biasing with the coils attached underneath the chip.

4.4.1 Flux line induced decoherence

Energy relaxation

The coupling of the flux line to the qubit opens several new channels for energy relaxation. As mentioned in [[Koch07a](#)], there is the relaxation induced by flux coupling. This includes two types of couplings. One is the generation of Josephson energy noise generated by current noise in the flux line via the mutual inductance M . The other one describes the loss of energy, because the oscillating magnetic field generated by the qubit described as a simple LC oscillator, induces a voltage in the flux bias line. The $50\ \Omega$ environment then dissipates this energy and reduces the relaxation time. As long as the flux line is properly thermalized at the respective temperature stages of the cryostat and well filtered to eliminate high frequency noise from room temperature Johnson noise, these two energy relaxation channels can be neglected. Koch *et al.* [[Koch07a](#)] estimated energy relaxation times of $> 20\ \text{ms}$ for typical transmon parameters.

The more relevant energy relaxation channel is the capacitive coupling to the flux line. We can model this situation with the equivalent circuit diagram shown in [Figure 4.7c](#). Since the transmon qubit is nearly a harmonic oscillator, it can be approximated as a simple LC oscillator with capacitance $C = e^2/2E_C$. This oscillator is capacitively coupled to the flux line which on one side consists of a transmission line of length l_1 terminated on PCB with a short modeled as an inductor with inductance L_s (or only a short L_s for FL_B), and on the other side of a transmission line with length l_2 terminated with a load impedance Z_L . We can then map this circuit to a parallel LRC oscillator by replacing $R \rightarrow 1/\text{Re}(Y(\omega))$ with the real part of the admittance seen by the qubit [[Esteve86](#), [Houck08](#)]. Since the decay time of such an LRC oscillator is given by $1/\kappa = RC$, where κ is the half width at half maximum of the resonance, we find a qubit energy decay time of

$$T_1(\omega) = \frac{C}{\text{Re}[Y(\omega)]} = \frac{e^2}{2E_C \text{Re}[Y(\omega)]}. \quad (4.8)$$

The value of Z_L strongly depends on the filtering used on the flux line. If low pass filters with reflective stopbands are used, this impedance is frequency dependent and significantly differs from the characteristic impedance $Z_0 = 50 \Omega$ of the transmission line. The impedance mismatches at the short and the filter then form a resonator which may enhance qubit relaxation if the qubit frequency is close to the resonance frequency. In order to suppress this resonance, we have added an Eccosorb low pass filter [[Santavicca08](#)] in between the reflective filter and the sample, which attenuates rather than reflects the signal at the stopband frequencies, such that the load impedance seen by the qubit when looking into the flux line towards the filters is close to $Z_L \approx Z_0$. Since the form of $Y(\omega)$ is rather complicated for an arbitrary Z_L , we assume in the following that $Z_L = Z_0$. The real part of the admittance can then easily be calculated and yields

$$\text{Re}[Y^{\text{short}}(\omega)] = \frac{Z_0 C_c^2 L_s^2 \omega^4}{L_s^2 \omega^2 + Z_0^2 (1 - C_c L_s \omega^2)^2} \quad (4.9)$$

for the flux line FL_B. For FL_A we further simplify the calculations by only considering the case where the shorted transmission line is neglected. Since this part is non-dissipative and shunts Z_L , it can only reduce the total dissipation of the system. Neglecting it thus gives a lower bound for T_1 . For this case, we find a real part of

the admittance of

$$\text{Re}[Y(\omega)] = \frac{Z_0}{Z_0^2 + \frac{1}{C_c^2 \omega^2}}. \quad (4.10)$$

From numerical simulations with the *ANSYS Maxwell* software we find a coupling capacitance of $C_c \approx 0.1$ fF for the FL_A design, resulting in an energy relaxation time of $T_1 > 50 \mu\text{s}$ for frequencies below 8 GHz. As this is only a lower bound, we are confident that the flux line is not the limiting factor for our measured T_1 of $\sim 1 \mu\text{s}$. For the case that the T_1 can be increased in the future, we can also think about protecting the qubit from decay into the flux line by carefully designing the shorted transmission line, using similar techniques as in Reference [Houck08]. There, the qubit has been protected from Purcell decay into the resonator using a stub tuner.

Dephasing

Low frequency current noise in the flux line that is not filtered by the low pass filters translates into fluctuations $\Delta\Phi$ in the flux Φ penetrating the SQUID loop, leading to fluctuations in the qubit frequency ω_{01} . The sensitivity of $\hbar\omega_{01} = \sqrt{8E_C E_J^{\text{max}} |\cos(\Phi/\Phi_0)|} - E_C$ to $\Delta\Phi$ strongly depends on the bias point of the qubit. At the so called ‘‘sweet spot’’ ($\Phi \approx \Phi_0$) for example, the frequency is to first order independent on $\Delta\Phi$ and is thus the point with best phase coherence. Assuming a $1/f$ noise power spectrum $S_\phi(\omega) = 2\pi(\Delta\Phi)^2/\omega$, where $\Delta\Phi$ is the amplitude of the fluctuations at 1 Hz, the dephasing time away from the sweet spot is simply given by the first derivative of ω_{01} with respect to Φ [Koch07a]

$$T_\phi \simeq \frac{1}{\Delta\Phi \left| \frac{\partial \omega_{01}}{\partial \Phi} \right|} = \frac{\hbar\Phi_0}{\pi \Delta\Phi \sqrt{2E_J^{\text{max}} E_C |\sin(\pi\Phi/\Phi_0) \tan(\pi\Phi/\Phi_0)|}}. \quad (4.11)$$

Since this equation diverges at the flux sweet spot, the dephasing for $\Phi = \Phi_0$ must be calculated by including second-order contributions, yielding

$$T_\phi^{\text{sweetspot}} \simeq \frac{1}{\pi^2 \Delta\Phi^2 \left| \frac{\partial^2 \omega_{01}}{\partial \Phi^2} \right|} = \frac{\hbar\Phi_0^2}{\Delta\Phi^2 \pi^4 \sqrt{2E_J^{\text{max}} E_C}}. \quad (4.12)$$

Even without including the flux line, the T_ϕ is limited by local flux noise in the SQUID loop from an origin that was for a long time unidentified. A multiple of independent measurements of $\Delta\Phi$ report a more or less geometry and material inde-

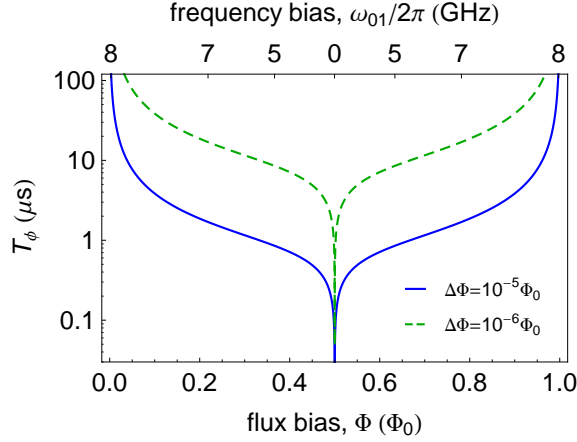


Figure 4.8: Dephasing time T_ϕ as a function of flux bias Φ calculated using Equation (4.11), for a $1/f$ flux noise spectrum with amplitude $\Delta\Phi = 10^{-5}\Phi_0$ (solid blue line), $\Delta\Phi = 10^{-6}\Phi_0$ (dashed green line) and typical transmon parameters $E_C/h = 300$ Mhz, $E_J^{\max} = 28.7$ GHz. The second order contribution at the sweet spot results in a dephasing time of $T_\phi^{\text{sweetspot}} \approx 4.7$ ms and $T_\phi^{\text{sweetspot}} \approx 470$ ms, respectively.

pendent value of $\Delta\Phi = (10^{-6} - 10^{-5})\Phi_0$ [Wellstood87, Yoshihara06, Yoshihara10]. Figure 4.8 shows the calculated dephasing times T_ϕ using Equation (4.11) for these values of $\Delta\Phi$ and typical transmon parameters as an example. Recent experiments and theories suggest the existence of a high density of spins on the surface of superconducting electrodes due to defects in the surface oxides or disorders in the interface between dielectric and metal as the origin of this noise [Bluhm09, Sendelbach09, Koch07b, Faoro08, Choi09]. Eliminating these spins will be important to enhance the T_ϕ times in the future.

When coupling a flux line to the qubit, the additional flux noise should thus be smaller than $\Delta\Phi_{\text{FL}} < 10^{-6}\Phi_0$. With a mutual inductance of $M = 250\Phi_0/A$ and including the 20 dB of attenuation at the 4 Kelvin stage to eliminate the room temperature Johnson noise, this results in an upper bound for the current and voltage noise spectral density of the room temperature electronics of $\Delta I(1 \text{ Hz}) = 10\Delta\Phi/(\text{MHz}^{1/2}) < 40 \text{ nA} \cdot \text{Hz}^{-1/2}$ and

$$\Delta V(1 \text{ Hz}) = \Delta I \cdot 50 \Omega < 2 \mu\text{V} \cdot \text{Hz}^{-1/2}, \quad (4.13)$$

respectively. While the ultra low noise voltage/current source *SRS SIM928* we already use for biasing the coils, specified with $V_{\text{rms}}(1 \text{ Hz}) = 300 \text{ nV} \cdot \text{Hz}^{-1/2}$, would likely be suitable for biasing through the flux lines, it is less clear for the *Tektronix AWG5014* since the company does not provide specifications for the voltage noise. In our experiments we see a reduction of T_ϕ when connecting an output of the *AWG5014* to the flux line, and thus we add a further 10 dB of attenuation to the flux line at room temperature. Since the AWG is only needed for pulsing, adding a high pass filter with a cut off in the MHz range might further reduce the influence on T_ϕ .

4.4.2 Optimal pulse control

The precise knowledge of the pulse shape applied to a flux line is important to achieve high fidelity two-qubit gates that rely on fast tuning of the qubit frequency (Section 6.2.3). In particular, in these experiments the qubit frequency needs to be changed by $\sim 1 \text{ GHz}$ in several nanoseconds and the precision has to be better than 5 MHz, requiring flux pulses with an accuracy of less than one percent. Even though an AWG can in principle generate any arbitrary analog signal with a bandwidth smaller than half the sampling rate, it is not a trivial task to determine the discrete digital pattern one has to load onto the AWG to achieve the desired analog output signal. Additionally, frequency dependent attenuation in the microwave cables, the low pass filters and imperfections in the on-chip circuitry significantly distorts the signal when traveling along the flux line. Here I describe how to tackle these problems, based on previous work carried out by Deniz Bozyigit during his master thesis in our lab [Bozyigit10], using standard signal processing techniques.

Theory of signal reconstruction

The main function of an AWG is to output a time-continuous analog output signal by programming the device with a discrete digital version (waveform). In theory, the relation between these two signals is given by the Nyquist-Shannon sampling theorem, which states that any continuous signal $s(t)$ is fully determined by the sampled signal $x[n] = s(nT_s)$, as long as $s(t)$ has no frequency components higher than half the sampling rate $1/T_s$. More specifically, the continuous signal can always be reconstructed from the discrete version by the convolution between $x[n]$

and the kernel $h(t) = \text{sinc}(t/T_s)$

$$s(t) = x[n] * h(t - nT_s) = \sum_{n=-\infty}^{\infty} x[n] \text{sinc}\left(\frac{t - nT_s}{T_s}\right), \quad (4.14)$$

where $\text{sinc}(x) = \sin(\pi x)/\pi x$ is the normalized sinc function. In practice however, this ideal reconstruction can never be precisely implemented, since the sinc function extends to infinite times. Instead, another kernel with finite length must be found that approximates the sinc function well enough. The error introduced by this approximation is referred to as the interpolation error. A common choice in practical devices is the zero-order hold kernel, a rectangular function which is 1 for $0 < t < T_s$ and 0 otherwise. Since the frequency spectrum of this kernel has nonzero components above $1/2T_s$, the output signal is low pass filtered afterwards. However, a practical filter can only attenuate and not totally eliminate the high frequency components. This introduces another error which is referred to as aliasing.

Even though the Nyquist-Shannon sampling theorem as given above is not fulfilled anymore, the output signal can still be reconstructed by convolution with the new kernel function h_{AWG} of the AWG. Since the exact function is not known in advance, it has to be measured in order to predict the output of the AWG.

Before doing so, let us first describe a system consisting of the AWG whose output is connected to cables (acting as a filter) and filters. Since the action of a filter can be described in time-domain by a convolution between the signal and a time window $g(t)$, the output signal is given by

$$\tilde{s}(t) = g(t) * (x[n] * h_{\text{AWG}}(t - nT_s)), \quad (4.15)$$

$$= x[n] * (g(t) * h_{\text{AWG}}(t - nT_s)), \quad (4.16)$$

$$= x[n] * \tilde{h}(t - nT_s). \quad (4.17)$$

In other words, any system consisting of an AWG connected to a series of linear components can be described by a single kernel $\tilde{h}(t)$. We can easily measure this kernel by loading a waveform given by the delta function $x[n] = \delta[n]$ (one single point is 1, all others are 0) and measuring the resulting output signal

$$\delta[n] * \tilde{h}(t - nT_s) = \tilde{h}(t). \quad (4.18)$$

Once this impulse response is measured, we can fully predict the output signal $\tilde{s}(t)$

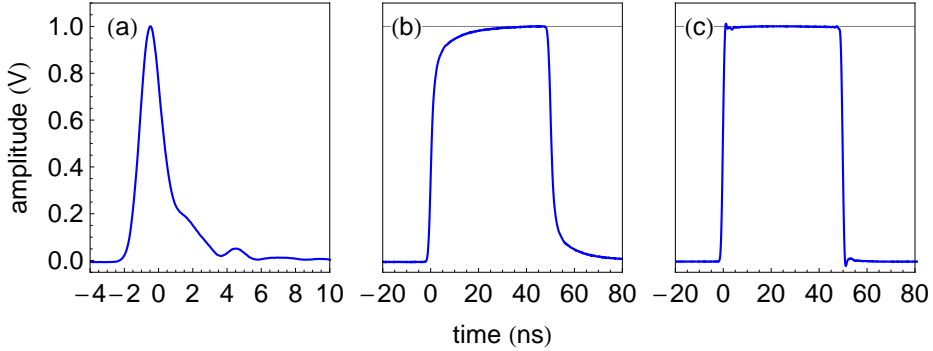


Figure 4.9: a) Combined impulse response of the AWG5014 from *Tektronix* and the flux line cabling until the sample holder. b) Uncorrected square pulse generated by the AWG. c) Corrected square pulse using the impulse response shown in a).

for any waveform $x[n]$ according to Equation (4.17). As an example, [Figure 4.9a](#) shows the measured impulse response for a *Tektronix AWG5014* operated at a sampling frequency of 1.2 GS/s, which is connected to the flux line cabling and filtering. The signal is recorded at room temperature using a 6 GHz oscilloscope from *LeCroy* running at a sampling rate of 20 GS/s right before the cable is connected to the sample, and was averaged 1000 times to reduce the noise. To demonstrate the interpolation error caused by the deviation of this kernel from the sinc function, we measure the output of a waveform which is given by a 50 ns long square pulse filtered with a 350 MHz Gaussian low pass filter, see [Figure 4.9b](#). Instead of a flat top, the pulse slowly increases for about 40 ns until it flattens out. Also, it takes roughly the same time until the pulse is completely turned off. Obviously this would be a substantial problem for fast qubit manipulation.

Pulse correction

Being able to predict the output signal for an arbitrary waveform allows us to find the waveform that corrects for all the distortions caused by the AWG, cabling and filtering, and results in an output that is close to a desired signal. Due to bandwidth restrictions of the AWG this is clearly impossible to achieve for any arbitrary desired signal. We thus use a method which finds the waveform that approximates

the desired signal in a linear least-square sense.

To do so, we discretize the desired signal $\tilde{s}(t)$ with a very high sampling rate $1/T_a$ and write the quasi continuous signal and the waveform as vectors \vec{s} and \vec{x} , with entries $\tilde{s}_m = \tilde{s}(mT_a)$ and $x_n = x[n]$. Since the convolution is a linear function, we can rewrite the discretized version of the convolution Equation (4.17) in matrix form

$$\vec{s} = H \cdot \vec{x}, \quad (4.19)$$

where H is a rectangular matrix with l_x columns and l_s rows, and fully determined by the kernel function \tilde{h} . Comparing (4.17) and (4.19), we find for the entries of the matrix

$$H_{m,n} = \tilde{h}(mT_a - nT_s). \quad (4.20)$$

The length l_x and l_s are determined by the maximal length of the desired signal and the sampling rates T_s and T_a . As an example, if the desired pulse is nonzero during the time $0 < t < L$, we typically sample the signal from $-50 \text{ ns} < t < L + 300 \text{ ns}$ to insure that all pre and post oscillations are contained in the corrected waveform. The dimensions of the matrix are thus given by $l_x = (L + 350 \text{ ns})/T_s$ and $l_s = (L + 350 \text{ ns})/T_a$. While T_s is given by the sampling rate of the AWG, we typically chose $T_a = 10 \cdot T_s$.

The task now is to find the vector \vec{x} that fulfills Equation (4.19) for a desired output signal \vec{s} . Since $l_s \gg l_x$, the system of linear equations (4.19) is overdetermined in the sense that it has more equations than unknowns. Such a system usually is not solvable for all equations ($H\vec{x} \neq \vec{s}$ for all \vec{x}). The best solution is therefore to find a vector \vec{x} which minimizes the error $\|\vec{s} - H\vec{x}\|_2^2$, where $\|x\|_2$ is the L2-norm. This can be done with linear regression using the *LeastSquares* function in Mathematica.

To demonstrate how good this procedure works, we remeasured the output of the pulse shown in Figure 4.9b when first applying the pulse correction procedure. As can be seen in Figure 4.9c, the pulse now rapidly reaches its voltage maximum, and the top of the pulse is almost perfectly flat. Only a small ringing with an amplitude of $\sim 1\%$ relative to maximal amplitude and a duration of 5 ns – 10 ns at the rising and falling edge of the pulse is observable.

Measuring the impulse response of cold cables

We now know how to accurately compensate for distortions caused by cables, filters and the AWG at room temperature. But how does our correction perform when cooling down the cables in the cryostat to 20 mK? As a test experiment, we have

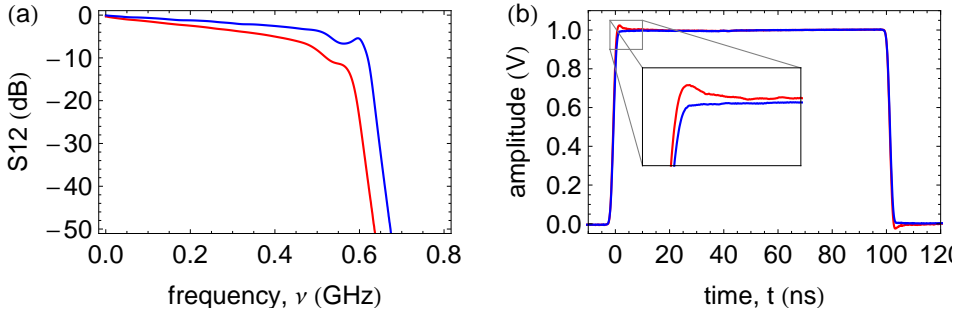


Figure 4.10: a) Measured S12 parameters of two microwave transmission line cables of ~ 2 m length with two *Mini-Circuits VLX-400* low pass filters connected in between, measured at room temperature (red) and 4 Kelvin (blue) b) Measurement of a corrected square pulse sent through the cables at 4 K using the impulse response measured for warm cables (red) and cold cables (blue).

compared the frequency response of two 2 m long microwave cables connected to two low pass filters *VLX – 400* from *Mini-Circuits* at room temperature (red) and at 4 Kelvin (blue), by dipping the components into liquid helium, see [Figure 4.10a](#). The attenuation of the cables is reduced by several dB at 4 K, since a metal normally has an increased conductivity when going to lower temperatures. Additionally, the cutoff frequency of the low pass filter is significantly shifted by about 50 MHz to higher frequencies. How this manifests itself in time domain is shown in [Figure 4.10b](#). The red curve shows a corrected pulse sent through the cables at 4 K, but using a pulse response measured at room temperature. The overcompensation for the cable attenuation and the wrong low pass filter cutoff results in an overshoot and undershoot of $\sim 2\% - 3\%$ at the beginning and end of the pulse, respectively. As a control measurement, we have also recorded the corrected pulse when using the pulse response for cold components, which results in the expected pulse shape.

While it is easy to measure the impulse response through cables dipped into liquid helium, it is not straightforward how to measure the impulse response for a cable in the cryostat that extends from room temperature down to the sample holder. This is because it is not possible to attach an oscilloscope to the output of the cable at 20 mK. Instead, we connect two nominally identical lines with a through such that we can measure all the S-parameters S^{both} of both cables from room temperature down to 20 mK and back again using a network analyzer. In

order to eliminate reflections between the low pass filters, we add an additional 6 dB of attenuation in between the two cables. With the knowledge of S^{both} we can reconstruct the S-parameters S^{ind} of each individual cable by first converting the scattering matrix S^{both} into the transmission matrix $ABCD^{\text{both}}$. Under the assumption that both microwave lines are identical, the transmission matrix for each individual line is given by $\sqrt{ABCD^{\text{both}}}$, which can then be mapped back to the S-parameters of the individual lines S^{ind} , see [Poazar93, Table 4.2] for details about how this mapping is calculated.

With the knowledge of the S-parameters of the flux line cabling in the cryostat and the impulse response of the AWG and the room temperature cabling \tilde{h} , we can reconstruct the full impulse response using the relation

$$\tilde{h}_{\text{full}} = \mathcal{F}^{-1}[\mathcal{F}(\tilde{h}) \cdot S_{12}^{\text{ind}}]. \quad (4.21)$$

Here, $\mathcal{F}(x)$ is the discrete Fourier transform of the list x and S_{21}^{ind} the complex transmission coefficient of the cold cables.

4.4.3 Measuring the flux pulse shape through its interaction with the qubit

In the previous section I have described how to accurately control the shape of the flux pulse which arrives at the input port of the on-chip flux line. I now go a step further and analyze the influence of the on-chip circuitry on the pulse shape by measuring the shape of the flux pulse on-chip. The only way this can be done is by directly probing the time response of the on-chip magnetic field with the qubit itself, since connecting an oscilloscope or network analyzer is impossible.

The pulse scheme for such an experiment is shown in **Figure 4.11a**. A short corrected square current pulse with length $L = 50$ ns and amplitude h is applied to the flux line which shifts the qubit by around 900 MHz away from its sweet spot ($\omega_{01}/2\pi = 6$ GHz) to $\omega_{01}/2\pi = 5.1$ GHz. At the same time, the qubit frequency is detected by sweeping the frequency ω_d of a Gaussian shaped spectroscopy pulse with a total length of 20 ns around 5.1 GHz. The amplitude of this spectroscopy pulse is chosen such that it is exactly a π pulse when the drive is on resonance with the qubit ($\Delta\nu_d = (\omega_{01} - \omega_d)/2\pi = 0$). We repeat this measurement for different delays τ of the spectroscopy pulse to the leading edge of the flux pulse to extract its time response. The resulting spectrum shown in **Figure 4.11b** displays a large overshoot of about 40 MHz at the beginning of the pulse followed by an undershoot

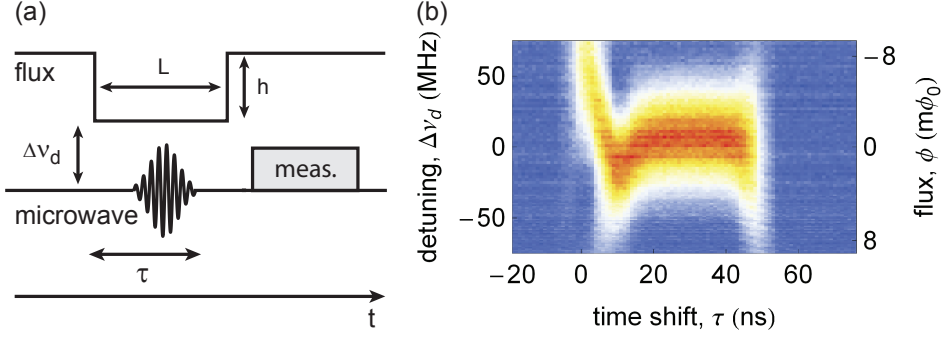


Figure 4.11: a) Schematic of the pulse sequence used to probe the shape of the on-chip flux pulse with the qubit. b) Measured amplitude of the resonator transmission as a function of the frequency detuning $\Delta\nu_d$ of the drive pulse from the qubit and the delay τ to the leading edge of the flux pulse.

of ~ 20 MHz several nanoseconds later. This result seems to indicate a rather poor control over the pulse shape, as 40 MHz error for a tuning range of 900 MHz is rather large. To estimate the corresponding error in the current flowing through the flux line, we first convert the frequencies into magnetic flux applied through the SQUID loop of the qubit using the relation (3.43), as it depends linearly on the current. We then find that while the flux is changed from 0 to $240 m\Phi_0$, the overshoot only corresponds to $\pm 4 m\Phi_0$. The tiny error of 1 – 2% in the current pulse thus transforms into a large error in qubit frequency due to the nonlinear dependence, demonstrating the high demand on the control of the pulse shape for these type of experiments. In fact, for our two-qubit and three-qubit experiments shown towards the end of this thesis, we add a short step at the beginning of the flux pulse to reduce this overshoot, see Section 6.2.3 for details. The origin of this 1 – 2% error remains unclear, might however be related to screening currents flowing on the ground planes of the chip, the accuracy for the calibration of the cold cables or the finite accuracy of the real-time oscilloscope, all of which are hard to verify.

5

Control of a Single Qubit

In this chapter I discuss a number of important characterization experiments that are regularly carried out when analyzing a new sample. This includes the determination of the resonance frequency and quality factor of the resonator, the Josephson energy and charging energy ([Section 5.1](#)) as well as the coherence times of the qubit ([Section 5.3](#)). I then discuss in [Section 5.2](#) the measurement of Autler-Townes and Mollow transitions, which occur between dressed eigenstates of a strongly driven many-level system. This provides useful insights about the influence of the third qubit level when driving a qubit with an anharmonicity similar to the drive strength. In [Section 5.4](#) I give a detailed explanation about how to calibrate single qubit gate operations using optimal control techniques to reduce errors caused by the third transmon level. Using quantum state and quantum process tomography, I show in [Section 5.5](#), that these techniques allow us to carry out single qubit operations with fidelities of $> 97\%$.

5.1 Qubit spectroscopy

Resonator spectrum

The first step when characterizing a new sample is to measure the resonator spectrum, as the resonator is used later as a measurement device to read out the qubit state. This is done by sweeping the frequency $\nu_{rf} = \omega_{rf}/2\pi$ of a microwave tone applied to the resonator input across the designed resonance frequency while mea-

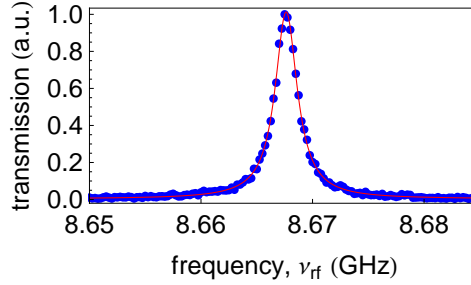


Figure 5.1: Measured power transmission spectrum of the fundamental mode of a coplanar waveguide resonator.

suring the transmitted signal, see [Figure 5.1](#). The transmitted power spectrum $P(\omega)$ is as for all driven linear oscillators given by a Lorentzian that is centered around the resonance frequency ω_r

$$P(\omega) = P_0 \frac{(\kappa/2)^2}{(\omega - \omega_r)^2 + (\kappa/2)^2}, \quad (5.1)$$

where κ is the half width at half maximum and P_0 the transmitted power on resonance. Fitting the data to this Lorentzian then allows to extract the precise resonator frequency $\omega_r/2\pi = 8.667$ GHz, as well as the quality factor $Q = \omega_r/\kappa = 3600$ which quantifies the rate of energy loss relative to the stored energy inside the resonator. The lifetime of a single photon inside the resonator is given by $1/\kappa$.

Qubit spectrum

The qubit transition frequency is determined using a dispersive spectroscopy measurement [[Wallraff04](#)]. This is done by applying two continuous microwave signals to the resonator¹. One is the measurement signal applied on resonance with the resonator frequency for the qubit in the ground state, as determined above. The other microwave signal has a frequency ν_{spec} which is far detuned from the resonator and swept over a large range. When the qubit is initially in the ground state and ν_{spec} is on resonance with the qubit transition frequency $\omega_{01}/2\pi$, population is transferred to the excited state. In fact, if the drive frequency is fixed for a time much longer than the coherence time of the qubit, the transition saturates and the

¹Of course, the spectroscopy signal could also be applied directly to the local qubit drive lines.

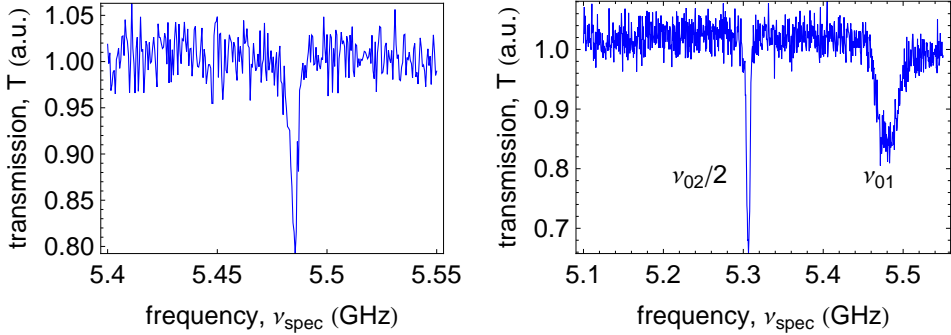


Figure 5.2: Left panel: Qubit spectroscopy of the $0 \leftrightarrow 1$ transition Right Panel: High power spectroscopy of the two photon $0 \leftrightarrow 2$ transition

qubit ends up in a mixed state with probability 0.5 to be in the ground or excited state. Due to the off-resonant coupling, the resonator frequency is then shifted by the dispersive shift 2χ . This is detected as a change in the transmitted amplitude and phase of the measurement signal. The left panel of [Figure 5.2](#) shows an example of such a measurement, for which the transmission amplitude is unity when ν_{spec} is off-resonant, and drops when it is on resonance at $\omega_{01}/2\pi = 5.485$ GHz. In this scheme, the resonator is populated with photons which lead to an AC Stark shift of the qubit frequency while carrying out spectroscopy [[Schuster05](#)], see also [Section 3.2.2](#). This shift is increased when increasing the power of the measurement signal. Additionally, fluctuations in the number of photons induce dephasing in the qubit state and can also lead to photon number splitting [[Schuster07b](#)]. The measurement drive should thus be weak enough such that the average number of photons inside the resonator is smaller than one photon. Alternatively, one can also carry out pulsed spectroscopy, for which the measurement signal is turned on only after the qubit was populated by a pulsed spectroscopy signal, see for details [[Göppl09](#)].

Measurement of E_J^{max} and E_C

Further characterization of the qubit, i.e. to determine the two parameters E_J^{max} and E_C , which fully determine the transmon Hamiltonian ([3.20](#)), can be made by increasing the power of the spectroscopy drive. At slightly lower frequencies next

to the power broadened qubit spectral line, another sharper peak then appears² corresponding to a two-photon process, see right panel of [Figure 5.2](#). This two-photon transition from the ground state to the second excited transmon state $|2\rangle$ appears at half the transition frequency $2\pi\nu_{02}/2 = \omega_{02}/2$ because two photons of equal energy are involved. This directly allows us to measure the anharmonicity of the transmon qubit $\alpha = \omega_{02} - 2\omega_{01}$ for this specific frequency. For the special case that we perform this measurement exactly at the maximal qubit transition frequency, we can even completely characterize the transmon parameters, namely the charging energy E_C and the maximal Josephson energy E_J^{\max} . Because we know that the magnetic flux applied through the SQUID loop of the transmon qubit is zero at this position, these two measurements are enough to extract E_C and E_J^{\max} from a fit of the measured frequencies ω_{01} and ω_{12} to the analytic solutions (Mathieu functions) of the energies of the CPB Hamiltonian.³

5.2 Strong qubit driving

For the spectroscopy measurement presented before, the qubit is generally driven in a weak driving limit, with a drive rate smaller than the decoherence rate of the qubit. What is then measured by spectroscopy is the incoherent mixing between the excited and the ground state of the qubit. For the case of strong driving however, the qubit state undergoes coherent Rabi oscillations between the ground and excited state. This coherent process then forms so called dressed states in the driven qubit energy level diagram which are split in frequency by the Rabi frequency. When detecting the photons emitted from such a driven two-level system, a three peaked fluorescence spectrum referred to as the Mollow triplet [[Mollow69](#)] can be observed. When probing transitions into a third level of the qubit, two characteristic spectroscopic lines separated by the Rabi frequency appear, a feature which is called the Autler-Townes doublet [[Autler55](#)]. In this section I first describe how Rabi oscillations are driven and observed in our system, explain the dressed states of a driven many-level system and then present the first measurements of Autler-Townes and Mollow-Transitions [[Baur09](#)] in superconducting qubits.

²In order to see this two-photon process, the driving power must be increased by about 30 dB relative to the power needed to detect the $0 \leftrightarrow 1$ transition.

³A Mathematica function that automatically makes this fit is *FindEcEj* which can be found in the library *TransmonFunctions.m*.

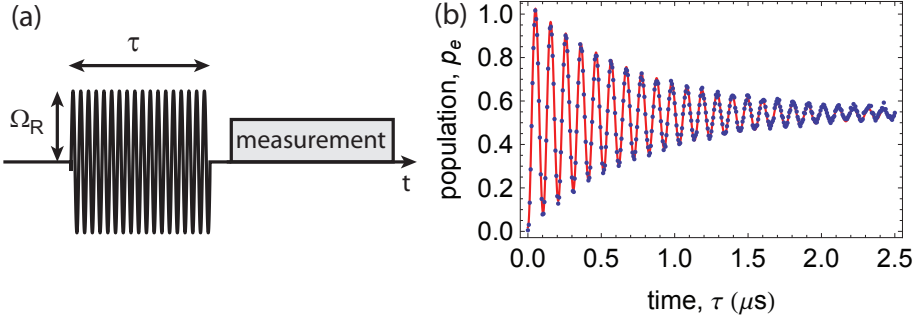


Figure 5.3: a) Pulse scheme for a Rabi oscillation measurement. b) Measured excited state population of the qubit as a function of the pulse length τ while keeping the Rabi frequency $\Omega_R/2\pi = 9.7$ MHz fixed.

5.2.1 Rabi oscillations

As we have already seen in [Section 3.2.4](#), the Hamiltonian of a driven transmon qubit can be written as

$$\hat{H} = \frac{1}{2}\omega_{01}\hat{\sigma}_z + \Omega_R \cos(\omega_d t)\hat{\sigma}_x. \quad (5.2)$$

For the special case that the drive is on resonance with the qubit $\omega_d = \omega_{01}$, the microwave field induces transitions between $|0\rangle$ to $|1\rangle$. If the qubit is initially in the ground state, the probability of being in $|1\rangle$ after a microwave pulse of length τ is $|p_e|^2 = \sin^2(\Omega_R\tau/2)$. This probability thus oscillates in time with the Rabi frequency Ω_R until the drive is turned off. In the Bloch sphere picture, this can be visualized by a rotation of the state vector around the x axis from the north to the south pole and back again.

Such an experiment is performed using the pulse sequence depicted in [Figure 5.3a](#). The qubit is driven for a short time with a square pulse of length τ and an amplitude Ω_R and read out afterwards with a pulsed measurement. The amplitude of the pulse determines the Rabi frequency Ω_R of the rotation on the Bloch sphere, and the total area under the pulse determines the angle of rotation Θ . By varying the length or amplitude of the pulse, we can therefore calibrate pulses with $\Theta = \pi$ which flips the qubit between the ground and the excited state, or with $\Theta = \pi/2$ which brings a qubit initially in the ground or excited state into

an equal superposition. An example of such a Rabi oscillation measurement is shown in [Figure 5.3b](#), which shows the population of the excited state p_e as a function of the pulse length τ for a constant Rabi frequency Ω_R . As expected, we observe a sinusoidal dependence of the population on the pulse area. Due to pure dephasing and energy decay, these oscillations show an exponential decay with decay time τ_R . In the limit of large driving fields, where the Rabi rate is much larger than the energy decay rate γ_1 and the pure dephasing γ_ϕ ($\Omega_R \gg \gamma_1, \gamma_\phi$), the time dependence is predicted to be given by [\[Allen87, Bianchetti09\]](#)

$$p_e(t) \simeq \frac{1}{2} - \frac{1}{2} e^{-\tau/\tau_R} \cos(\Omega_R t/2), \quad (5.3)$$

where $\tau_R = 4/(3\gamma_1 + 2\gamma_\phi)$. The red solid line in [Figure 5.3b](#) represents a fit of the data to this function and yields a Rabi decay time of $\tau_R \approx 770$ ns. We will use such Rabi oscillations later to calibrate the single qubit gate operations, as described in [Section 5.4.3](#)

5.2.2 Dressed states

Whenever a two-level system is coherently coupled to an electromagnetic field, new eigenstates are formed, which are called dressed states [\[Cohen-Tannoudji98\]](#). For the case of strong fields, such as in a Rabi oscillation experiment, we can treat the field classically because many photons are involved. However, we will then later include the number of photons in the drive again in order to give an interpretation of the Mollow triplet. Also, to explain the Autler-Townes doublet, we will instead of a two-level system consider a many-level system. Let us first discuss the new eigenstates of a Hamiltonian describing a five-level transmon qubit with a drive that only couples the first two levels. We first transform the Hamiltonian into a frame rotating each transmon level i with a multiple of the drive frequency $i\omega_d$ by using the unitary operation $\hat{U} = \exp(-\sum_i i\omega_d |i\rangle\langle i|t)$ which results in the time independent Hamiltonian

$$\hat{H} = \sum_{i=2}^4 (\omega_{i-1,i} - i\omega_d) |i\rangle\langle i| + \frac{\Omega_R}{2} (|0\rangle\langle 1| + |1\rangle\langle 0|). \quad (5.4)$$

Here we assume that the drive $\omega_d = \omega_{01}$ is on resonance with the $0 \leftrightarrow 1$ transition. Since the drive only couples the lowest two energy eigenstates, only $|0\rangle$ and $|1\rangle$ get modified and the new eigenstates are given by $|\pm\rangle = (|0\rangle \pm |1\rangle)/\sqrt{2}$ and $|i\rangle$ for $i > 1$.

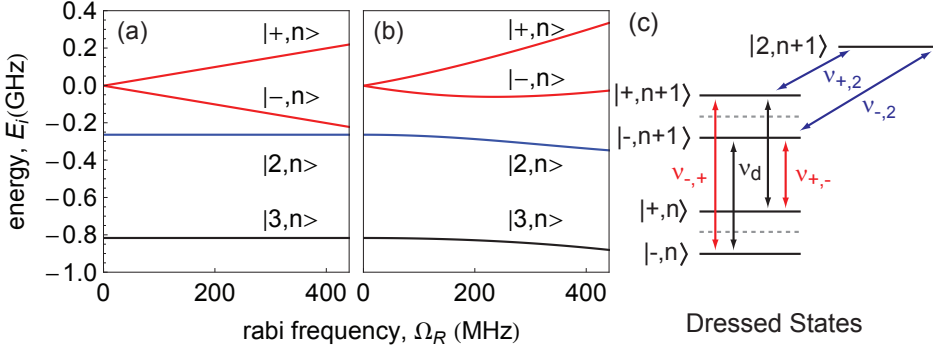


Figure 5.4: [a),b)] Dressed energy eigenstates of a driven five-level transmon qubit in the rotating frame of the drive on resonance with the $0 \leftrightarrow 1$ transition, and in the subspace of n drive photons. a) The drive only couples to the $0 \leftrightarrow 1$. b) The drive couples to all transitions between neighbouring states. c) The Mollow triplet can be interpreted as the decay of the dressed states from the $n + 1$ to the n drive photon subspace. The central line at frequency ν_d is indicated as black arrows, and the sidebands with frequencies $\nu_{-,+}$ and $\nu_{+,-}$ as red arrows. The Autler-Townes doublet involves transitions between the dressed states and the second excited transmon qubit state.

The corresponding eigenenergies for the first four levels in the rotating frame are plotted in Figure 5.4a as a function of the drive strength Ω_R . While the energies of $|2\rangle$ and $|3\rangle$ stay constant, the energies of $|\pm\rangle$ are split by the energy of the drive Ω_R . This is the direct consequence of the coherent Rabi oscillations in the time domain. When treating the electromagnetic field quantum mechanically, the eigenstates also have a photonic part and $|\pm\rangle$ will become the symmetric and antisymmetric superposition of the bare states $|\pm, n\rangle = (|0, n + 1\rangle \pm |1, n\rangle) / \sqrt{2}$ and are called dressed states because they share an excitation between the drive field and the qubit. Due to this dressing, the system forms an energy ladder of doublets separated by the energy of the drive photons $\hbar\omega_d$, see Figure 5.4c. The other eigenstates are simply the product states $|i, n\rangle$ for $i > 2$.

In this framework it is now possible to give an intuitive interpretation of the three peaked Mollow triplet fluorescence spectrum, see also [Cohen-Tannoudji98] for details. In this energy ladder of doublets there are now four possible spontaneous

transitions between the dressed states, as depicted in [Figure 5.4c](#). A photon can be spontaneously emitted at the qubit transition frequency $\omega_{01} = \omega_d$ when the system decays from the states $|\pm, n+1\rangle$ to $|\pm, n\rangle$ (black arrows), and in the limit of $n \gg \sqrt{n}$ at a frequency $2\pi\nu_{-,+} = \omega_{01} + \Omega_R$ when decaying from $|+, n+1\rangle$ to $|-, n\rangle$ and at a frequency $2\pi\nu_{+,-} = \omega_{01} - \Omega_R$ when decaying from $|-, n+1\rangle$ to $|+, n\rangle$ (red arrows). This leads to the triplet structure in fluorescence formed by the central line at ω_{01} and the sidebands offset by $\pm\Omega_R$, which can be observed whenever Ω_R is (much) larger than the dephasing and energy decay rates.

When, instead of measuring the fluorescence spectrum, detecting the absorption of a second drive field swept around the frequency of the $1 \leftrightarrow 2$ transition, the splitting of the dressed states can be observed as a doublet at frequencies $2\pi\nu_{\pm,2} = \omega_{01} \pm \Omega_R/2$ in the absorption spectrum (blue arrows), known as the Autler-Townes doublet.

So far we have only considered a drive that couples to the transition between $|0\rangle$ and $|1\rangle$. However, when the Rabi frequency becomes similar to the anharmonicity of the transmon qubit, here assumed to be $\alpha/2\pi = -260$ MHz, then this assumption is not valid. The Hamiltonian in the rotating frame which describes the coupling of the single drive to all transitions between neighboring states⁴ is given by

$$\hat{H} = \sum_{i=2}^4 (\omega_{i-1,i} - i\omega_d) |i\rangle\langle i| + \sum_{i=1}^4 \frac{\sqrt{i} \cdot \Omega_R}{2} (|i-1\rangle\langle i| + |i\rangle\langle i-1|). \quad (5.5)$$

Now, the new eigenstates do not have the simple structure anymore as before, since they are now given by a superposition of all qubit levels. And in contrast to the two-level case where $|\pm, n\rangle$ have the same contribution of the $|0\rangle$ and $|1\rangle$ states, the two states now have different contributions of the other transmon levels. This reflects itself in the energy spectrum by a repelling of the states corresponding to $|-, n\rangle$ and $|2, n\rangle$ as they get closer, while the state $|+, n\rangle$ is much less affected, leading to an asymmetric fluorescence spectrum and also asymmetric Autler-Townes doublet.

5.2.3 Measurement of Autler-Townes and Mollow transition

The Mollow triplet and the Autler-Townes doublet were observed for the first time in an atomic beam of sodium [[Schuda74](#)] and in a microwave spectroscopy of molecules by Autler and Townes themselves [[Autler55](#)], respectively. Later

⁴Transitions between non neighboring states can be neglected because their coupling strength are nearly zero due to the near harmonicity of the transmon qubit.

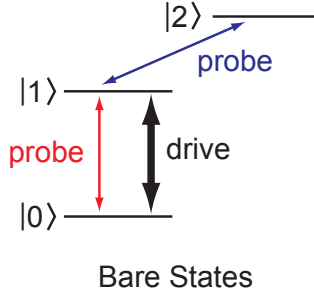


Figure 5.5: Energy-level diagram of a bare three-level system. The drive and probe transitions to measure the Autler-Townes doublet and the sideband of the Mollow transitions are indicated by black and red/blue arrows.

they have been measured in single molecules [Wrigge08, Tamarat95], single atoms [Walker95] and more recently also in quantum dots [Xu07, Nick Vamivakas09, Muller07]. Here we discuss our results on the first observation of Autler-Townes and Mollow transitions with superconducting qubits [Baur09], where we instead of observing the fluorescence spectrum, carry out a pump and probe measurement. Later, the Autler-Townes doublet has also been observed with phase qubits [Sillanpää09] and the Mollow triplet could be measured for a strongly driven transmon qubit in a transmission line [Astafiev10] and for a two-level system formed by the ground state and a polariton state of a transmon qubit resonantly coupled to a microwave resonator [Lang11]. The properties of superconducting qubits dressed by strong drive fields have also been studied experimentally in References [Tuorila10, Wilson07, Oliver05].

The sample used for this experiment consists of a single resonator with resonance frequency of $\omega_r/2\pi \approx 6.439$ GHz and photon decay rate of $\kappa/2\pi \approx 1.6$ MHz coupled to two transmon qubits located at both ends of the resonator. For all experiments, only one qubit is used and the other one is maximally detuned to low frequencies. The relevant qubit has a coupling strength to the resonator of $g_{01}/2\pi \approx 133$ MHz, a charging energy of $E_C/h = 233$ MHz and a maximal Josephson energy $E_J^{\max}/h = 32.8$ MHz, and for these experiments is always driven through the resonator input port.

We measure the Autler-Townes and the Mollow spectral lines according to the scheme shown in Figure 5.5. First, we tune the qubit to the frequency $\omega_{01}/2\pi \approx 4.811$ GHz, where it is strongly detuned from the resonator by $\Delta_0/2\pi = 1.63$ GHz.

At this frequency, the qubit has an anharmonicity of $\alpha \approx -260$ MHz. We then strongly drive the transition $|0\rangle \leftrightarrow |1\rangle$ with a first microwave tone of amplitude ε applied to the qubit at the fixed frequency $\omega_d/2\pi = 4.812$ GHz. The drive field is described by the Hamiltonian $H_d = \hbar\varepsilon(a^\dagger e^{-i\omega_d t} + ae^{i\omega_d t})$ where the drive amplitude ε is given in units of a frequency. The qubit spectrum is then probed by sweeping a weak second microwave signal over a wide range of frequencies ω_p including ω_{01} and ω_{12} . Simultaneously, amplitude T and phase ϕ of a microwave signal applied to the resonator are measured [Wallraff04]. We have adjusted the measurement frequency to the qubit state-dependent resonance of the resonator under qubit driving for every value of ε . Figure 5.6a and b show the measurement response T and ϕ for selected values of ε . For drive amplitudes $\varepsilon/2\pi > 65$ MHz, two peaks emerge in amplitude from the single Lorentzian line at frequency ω_{12} corresponding to the Autler-Townes doublet, see Figure 5.6a. The signal corresponding to the sidebands of the Mollow triplet is only visible at high drive amplitudes $\varepsilon/2\pi > 730$ MHz in phase, see Figure 5.6b. The central line is not observed in our measurements as the corresponding transition is completely saturated by the strong drive tone. Black lines in Figure 5.6 are fits of the data to Lorentzians from which the dressed qubit resonance frequencies are extracted.

We have plotted these extracted frequencies of the Autler-Townes doublet (blue dots) and of the Mollow triplet sidebands (red dots) in Figure 5.7. The splitting of the spectral lines in pairs separated by Ω_R and $2\Omega_R$, respectively, is observed for Rabi frequencies up to $\Omega_R/2\pi \approx 300$ MHz corresponding to about 6% of the qubit transition frequency ω_{01} and is larger than the anharmonicity of the qubit α .

In the simplest model, the continuous classical drive at frequency ω_d is expected to induce Rabi oscillations between the qubit levels $|l\rangle$ and $|l+1\rangle$ at the frequency [Blais07]

$$\Omega_{l,l+1} \approx \frac{2\varepsilon g_{l,l+1}}{\omega_r - \omega_d}, \quad (5.6)$$

depending linearly on the drive amplitude ε . Therefore, one would expect that the strong drive at the qubit transition frequency $\omega_d \approx \omega_{01}$ should lead to a square-root dependence of the Autler-Townes and Mollow spectral lines on the drive power $P_d \propto \varepsilon^2$. However, the Autler-Townes spectral lines show a clear power dependent shift, see Figure 5.7, and the splitting of both pairs of lines scales weaker than linearly with ε . As we have seen in Section 5.2.2, these effects can be understood by considering more than two transmon levels. We have numerically diagonalized the Hamiltonian given in Equation (5.5) which only takes into account the drive

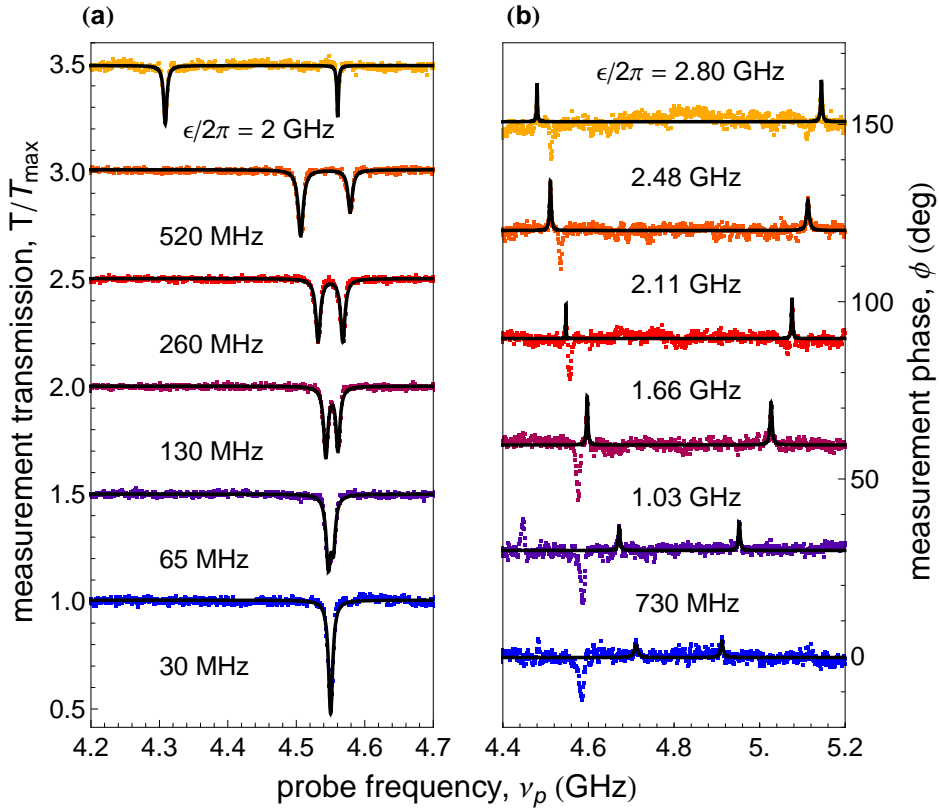


Figure 5.6: a) Autler-Townes spectrum as a function of drive amplitude ϵ . Traces are normalized to the maximum transmission through the resonator, and separated from each other with a vertical offset of 0.5. b) Mollow spectrum in phase. Traces are offset by 30 degrees. Black solid lines are fits to Lorentzians. Peaks not fitted with Lorentzians correspond to the phase response of the Autler-Townes doublet.

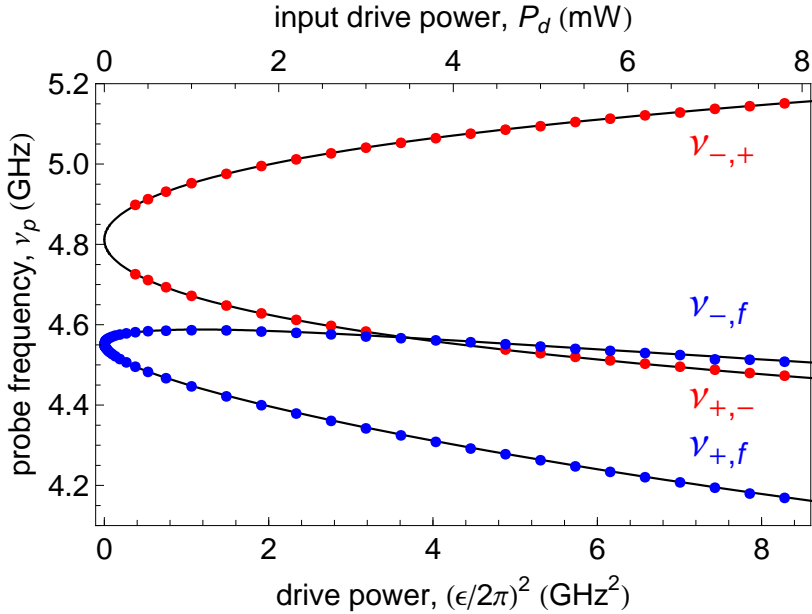


Figure 5.7: Measured Autler-Townes doublet (blue dots) and Mollow triplet side-band frequencies (red dots) vs. drive power P_d at a fixed drive frequency $\omega_d/2\pi = 4.812$ GHz. Black solid lines are transition frequencies calculated by numerically diagonalizing the Hamiltonian (5.5) taking into account the lowest 5 transmon levels.

terms between nearest neighbor energy levels since other transitions are strongly suppressed due to the near harmonicity of the transmon [Koch07a]. This model is in good agreement with our data when considering the lowest 5 qubit levels, see solid black lines in Figure 5.7. Because of the low anharmonicity [Koch07a] and large drive amplitude, many qubit levels must be included in the description. The calibration factor between the externally applied drive amplitude and ε is the only free parameter in the fit.

Numerical diagonalization of Equation (5.5) also leads to a qualitative understanding of the amplitude and phase information contained in the measurement signal. This is done by first calculating the pulled cavity frequencies using the prefactor of $\hat{a}^\dagger \hat{a}$ of the dispersive Jaynes-Cummings Hamiltonian as given in Equation (3.54). Since the measurement rate is small [Gambetta08], the measured signal is given by the averaged response of all the dressed-state pulled frequencies contained in the steady-state reached by the qubit under the strong drive tone. In the Autler-Townes configuration, the weak probe tone transfers a small population from the dressed ground and excited states ($|\pm, n\rangle$) to the dressed $|2, n\rangle$ state, resulting in a change in the cavity frequency and a drop of transmitted signal. On the other hand, in the Mollow configuration, population is exchanged by the probe tone from the $|\mp, n\rangle$ to the $|\pm, n+1\rangle$ dressed-states. At low drive power, the dressed states $|\pm, n\rangle$ are equal superpositions of the bare $|0, n\rangle$ and $|1, n\rangle$ states such that no signal is measured. As the power is increased, these states get dressed in different proportion with $|2\rangle$ (see also Section 5.2.2) and a signal is measured.

Finally, plotting the difference between the two Autler-Townes spectral lines (blue dots) and the sidebands of the Mollow spectrum (red dots) versus drive amplitude ε , the nonlinearity of the dressed state splitting becomes more apparent, see Figure 5.8a. The dashed line shows the linear dependence of the Rabi frequency in Equation (5.6) on the drive amplitude ε , which only fits to the data at low ε . The non-linear dependence at high ε , instead, agrees very well only with our full model, black solid line.

To confirm the direct relationship between the measured dressed state splitting frequency and the Rabi oscillation frequency of the excited state population we have also performed time resolved measurements of the Rabi frequency up to 100 MHz, see Figure 5.8c. The extracted Rabi frequencies (orange dots) are in good agreement with the spectroscopically measured Rabi frequencies (blue squares) over the range of accessible ε , as shown in Figure 5.8b.

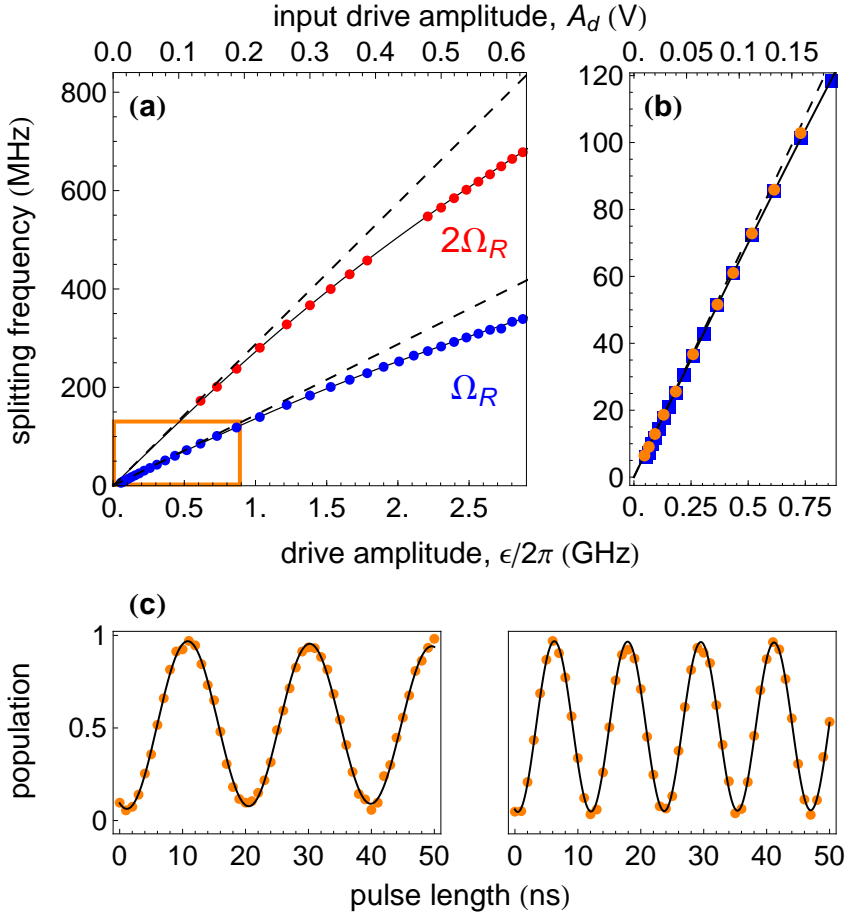


Figure 5.8: a) Extracted splitting frequencies of the Mollow triplet sidebands (red dots) and the Autler-Townes doublet (blue dots) as a function of the drive field amplitude. Dashed lines: Rabi frequencies obtained with Equation (5.6)). Black solid lines: Rabi frequencies calculated by numerically diagonalizing the Hamiltonian in Equation (5.5) taking into account 5 transmon levels. b) Zoom in of the region in the orange rectangle in a). Orange dots: Rabi frequency Ω_R vs. drive amplitude ϵ extracted from time resolved Rabi oscillation experiments, lines as in a). c) Rabi oscillation measurements between states $|0\rangle$ and $|1\rangle$ with $\Omega_R/2\pi = 50$ MHz and 85 MHz.

5.3 Measurement of the qubit coherences

The fidelity with which a quantum operation can be carried out in superconducting circuits is at the current state of the art mainly limited by the coherence times of the qubits. Identifying the sources of loss in these systems is thus an important step towards the realization of a scalable quantum processor. Since the first superconducting qubit has been realized, the energy decay (phase coherence) times have drastically been improved [Steffen11] by almost five orders of magnitude from 1 ns (1 ns) [Nakamura99] up to $\sim 60 \mu\text{s}$ ($\sim 20 \mu\text{s}$) [Paik11] to date with superconducting qubits embedded in three dimensional microwave cavities. During this process it turned out that one of the most important contribution to decoherence is likely the dielectric loss from two-level states at metal to air and metal to substrate interfaces [Martinis05]. Other results suggest that quasiparticles generated from stray infrared light might also play a significant role [Barends11, Córcoles11]. A prerequisite for this development was the ability to measure the coherence times and is thus shortly explained here. A good overview of coherence measurements and sources of decoherence in superconducting qubits can also be found in [Ithier05].

5.3.1 Measurement of the energy decay time

The pulse sequence to measure the energy decay of a qubit state is shown in Figure 5.9a. The qubit is first excited from the ground state $|0\rangle$ to $|1\rangle$ with a resonant π pulse inferred from Rabi oscillations. We then wait for a time τ during which the qubit may decay and then measure the remaining population of the excited state p_e . A typical result is shown in Figure 5.9b which shows an exponential decay of the population with time. We extract the energy decay time $T_1 = 1.14 \mu\text{s}$ from an exponential fit $p_e(t) = e^{-t/T_1}$. Of course, this time strongly depends on the operation frequency of the qubit and is consistently higher when going to lower frequencies. In fact, in the regime where the Purcell effect can be neglected [Houck08], the energy decay time shows a $1/f$ dependence, consistent with the theory of dielectric loss [Martinis05].

5.3.2 Measurement of the phase coherence

Additionally to the energy decay, there also exists a decoherence process which is purely quantum. It describes the loss of quantum information, by losing the knowledge about the phase of a quantum state. This decoherence mechanism

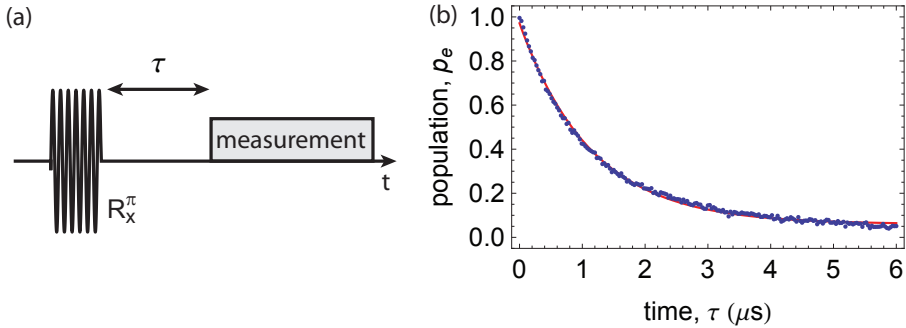


Figure 5.9: a) Pulse sequence for the measurement of the energy decay time. The qubit is first excited to the state $|1\rangle$ and then measured after waiting a time τ . b) The measured population of the excited state p_e decays exponentially with time with a decay time of $T_1 = 1.14 \mu\text{s}$ extracted from a fit (solid red line).

referred to as phase damping or dephasing has two contributions:

$$\frac{1}{T_2} = \frac{1}{2T_1} + \frac{1}{T_\phi}. \quad (5.7)$$

The first arises from the energy decay with decay time T_1 , and the second arises due to random adiabatic variation of the qubit frequency induced by low frequency noise (only the noise power spectrum at frequencies much smaller than ω_{01} are relevant for dephasing), called the pure dephasing T_ϕ . In the absence of pure dephasing, the dephasing time can thus maximally be $2T_1$.

The dephasing is apparent in the decay of the off-diagonal elements of the density matrix and is thus not directly accessible by projective readout, which only gives information about the diagonal terms. Instead, one applies a so called Ramsey interference pulse sequence [Ramsey50] as depicted in Figure 5.10a consisting of two short $\pi/2$ pulses separated by a free evolution time τ . This experiment can be explained in the Bloch sphere picture using a frame rotating with the frequency of the drive. When starting with the qubit in its ground state, the first $\pi/2$ pulse rotates the state around the x axis onto y . The state then precesses around the z axis for time τ . The final $\pi/2$ pulse around the y axis rotates the $\pm x$ component of the state onto $\mp z$ and leaves the $\pm y$ components the same. When the drive is on resonance with the qubit, the state in the rotating frame always stays on the y axis during the

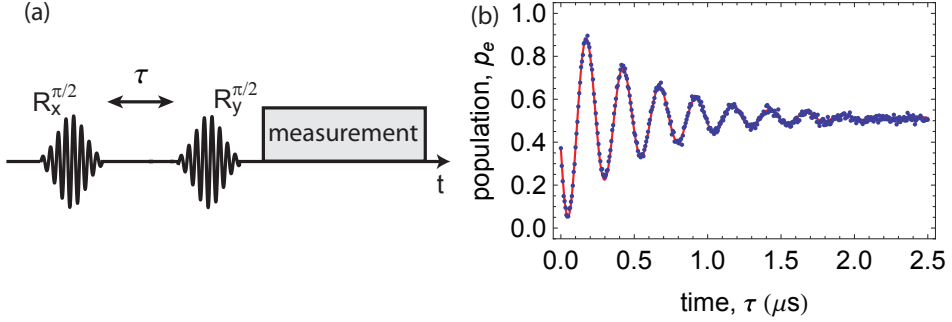


Figure 5.10: a) Pulse sequence of a typical Ramsey experiment to determine the dephasing time T_2^* of a qubit. b) Measured Ramsey oscillations for $\Delta\omega = 4$ MHz and a decay time of $T_2^* = 0.54 \mu\text{s}$ extracted from a fit to Equation (5.8) (solid red line).

free evolution time. The final state will then be an equal superposition of $|0\rangle$ and $|1\rangle$, and does not depend on τ . For a slightly off-resonant drive with a detuning of $\Delta\omega$ however, the state does precess around $\pm z$ with a frequency $|\Delta\omega|$ and a direction determined by the sign of $\Delta\omega$. The final state then shows a sinusoidal time dependence on τ (see Figure 5.10b) and is given by

$$p_e = \frac{1}{2} + \frac{1}{2} e^{-\tau/T_2^*} \cos(\Delta\omega \cdot \tau \pm \pi/2). \quad (5.8)$$

The decay of the envelope of these Ramsey oscillations is exponential for $1/f$ noise and the decay time is given by T_2^* (difference to T_2 is explained below) and the phase of the oscillation is determined by the sign of $\Delta\omega$ ⁵. From a fit of the data to this function we extract a dephasing time $T_2^* = 0.54 \mu\text{s}$.

In these Ramsey oscillation measurements, one has to distinguish between the T_2 defined as in Equation (5.7), and the T_2^* [Clarke08] which is the result of an ensemble average. In the measurement shown above, the same experiment is repeatedly acquired many times ($\sim 500\,000$) to get enough statistics and to increase

⁵This is the reason why the final pulse rotates around the y axis, because the Ramsey oscillations then also contain the information whether the drive is positively or negatively detuned from the qubit frequency. If both pulses were applied around the same axis, this information could not be extracted as the phase is the same in both cases.

the signal to noise ratio. While the individual runs of the experiment are nominally equal, slow fluctuations between the runs slightly change the experimental settings (such as $\Delta\omega$) and as such reduce the observed decay time $T_2^* \leq T_2$. If we are interested in the real T_2 of each single run, a spin-echo sequence [Hahn50, Ithier05] can be used, which eliminates the noise with frequencies lower than the inverse of the time a single run takes.

5.4 Single-qubit gates

5.4.1 Rotations around the x and y axis

As seen in Section 5.2.1, we can rotate the qubit state around the x axis on the Bloch sphere by applying a microwave pulse to the qubit. The angle of rotation is controlled by the area under the pulse, by either changing the length or amplitude of the pulse. To see how we can rotate around the y axis, let us look at the more general Hamiltonian of a driven two-level system including the phase ϕ of the drive

$$\hat{H} = \frac{1}{2}\omega_{01}\hat{\sigma}_z + \frac{\Omega_R}{2}\left(e^{i(\omega_d t + \phi)} + e^{-i(\omega_d t + \phi)}\right)(\hat{\sigma}_- + \hat{\sigma}_+). \quad (5.9)$$

For $\phi = 0$, this is exactly the Hamiltonian discussed in Equation (5.2). Transforming this Hamiltonian into the frame rotating at the drive frequency ω_d and performing the rotating wave approximation we get

$$\hat{H} = \delta_1\hat{\sigma}_z + \frac{\Omega_R}{2}\left(\cos(\phi)\hat{\sigma}_x + \sin(\phi)\hat{\sigma}_y\right), \quad (5.10)$$

where $\delta_1 = \omega_{01} - \omega_d$. With the phase of the microwave drive, we can thus rotate about any arbitrary axis on equatorial plane of the Bloch sphere. As an example, the drive will rotate the state about the y axis when choosing $\phi = +\pi/2$.

One might ask the question what phase we have to set on the microwave generator to rotate around the x axis, or what is the definition of zero phase? Also, the phase set on the microwave generator might change from one experiment to another, will this be a problem? In the experiment, all microwave generators are phase locked to a common reference clock with an arbitrary but stable absolute phase. We define this arbitrary phase of the microwave generator used to output the first pulse applied to the qubit as the zero phase $\phi = 0$, which in turn defines the x axis. The rotation axis of all subsequent pulses are defined by the phase relative to

this arbitrary initial phase. Between different experiments, this arbitrary phase is allowed to be different, as long as the time between the two experiments is longer than the phase coherence, such that the qubit completely forgot about the phase of the previous experiment.

5.4.2 Optimal pulse control for high fidelity single-qubit gates

The error rate of a quantum gate useful for large scale quantum computers is required to be below a specific threshold, which is estimated to be around 1–30 errors per 10 000 operations [Knill05, DiVincenzo09]. However, the implementation of high fidelity quantum gates for a system with more than two levels and limited anharmonicity is challenging. On one hand, the gate operation needs to be fast relative to the coherence time of the system which requires large driving fields. On the other hand the leakage out of the computational subspace should be inhibited. As described in the dressed state picture (Section 5.2.2), the higher excited energy levels significantly shift the energy of the dressed states when driving a multi-level system on the $0 \leftrightarrow 1$ transition with a Rabi rate similar to the anharmonicity. In the context of single qubit gate operations these AC Stark shifts lead to a non-zero population of the state $|2\rangle$ after the pulse and significant phase errors on the dynamic phase of the prepared qubit state due to population of $|2\rangle$ during the pulse. While the leakage into the state $|2\rangle$ can be reduced by using Gaussian shaped pulses instead of square pulses due to the narrower Fourier spectrum, the phase errors in fact become larger as larger maximal Rabi rates are required for the same gate duration. To solve these problems, we instead use an optimal pulse control technique developed by Motzoi *et al.* [Motzoi09, Gambetta11], which has also been experimentally realized in [Chow10, Lucero10]. Their method, which is called derivative removal by adiabatic gate (DRAG), gives an analytic solution for the optimal pulse shapes. We call a pulse optimized by this procedure a DRAG pulse.

In [Motzoi09, Gambetta11] the authors consider a weakly anharmonic three-level system with only neighboring level coupling for which the Hamiltonian including the drive in the rotating frame with respect to the drive frequency ω_d and

after the rotating wave approximation is

$$H = \begin{pmatrix} 0 & \frac{\varepsilon_x(t)}{2} - i\frac{\varepsilon_y(t)}{2} & 0 \\ \frac{\varepsilon_x(t)}{2} + i\frac{\varepsilon_y(t)}{2} & \delta_1(t) & \sqrt{2}\left(\frac{\varepsilon_x(t)}{2} - i\frac{\varepsilon_y(t)}{2}\right) \\ 0 & \sqrt{2}\left(\frac{\varepsilon_x(t)}{2} + i\frac{\varepsilon_y(t)}{2}\right) & \alpha + 2\delta_1(t) \end{pmatrix}. \quad (5.11)$$

Here, ε_x and ε_y are the amplitudes of the two quadratures of the drive $\varepsilon(t) = \varepsilon_x(t) \cos(\omega_d t) + \varepsilon_y(t) \sin(\omega_d t)$ and α is the anharmonicity. In addition, the authors assume that the frequency of ω_{01} can be tuned *in-situ* while the drive frequency ω_d is fixed and $\delta_1(t) = \omega_{01}(t) - \omega_d$. The optimal value for the quadrature amplitudes and drive detuning found to cancel the AC Stark shift (phase) error are given by [Motzoi09]

$$\varepsilon_y(t) = -\frac{1}{\alpha} \frac{\partial \varepsilon_x(t)}{\partial t} \quad \text{and} \quad \delta_1 = \frac{-\varepsilon_x^2}{2\alpha}. \quad (5.12)$$

This is calculated to eliminate the leakage to order ε_x^4/α^3 . To have no discontinuities in ε_y , ε_x must be a smooth function. We have chosen a Gaussian pulse which is forced to start and end with an amplitude zero and is given by

$$\varepsilon_x(t) = A \frac{\exp\left[-\frac{(t-\sigma \cdot f_i)^2}{2\sigma^2}\right] - \exp\left[-\frac{(\sigma \cdot f_i)^2}{2\sigma^2}\right]}{1 - \exp\left[-\frac{(\sigma \cdot f_i)^2}{2\sigma^2}\right]}, \quad (5.13)$$

where $t \in [0, 2\sigma \cdot f_i]$, σ is the standard deviation and A the maximal amplitude of ε_x . With f_i we choose after how many σ the pulse is truncated on both sides. The quadrature amplitudes and the qubit detuning for a DRAG pulse with the typical values for the total pulse duration of 10 ns, a standard deviation of $\sigma = 2.5$ ns and a truncation factor $f_i = 2$ are shown in Figure 5.11 a.

In our experiment it is difficult to accurately control the frequency of the qubit, or δ_1 , as the relation between the current applied to the flux line and the qubit frequency must be carefully calibrated. We can however precisely control the phase of our drive, and $\delta_1(t)$ can be replaced by phase ramping, see Appendix A.1 for the derivation. Another approach is to just set $\delta_1 = 0$ and scale the amplitude of ε_y by a scaling factor q_s . In the Reference [Gambetta11] this is called the *Y-only* correction, and is shown to perform better according to their numerical simulations, with a

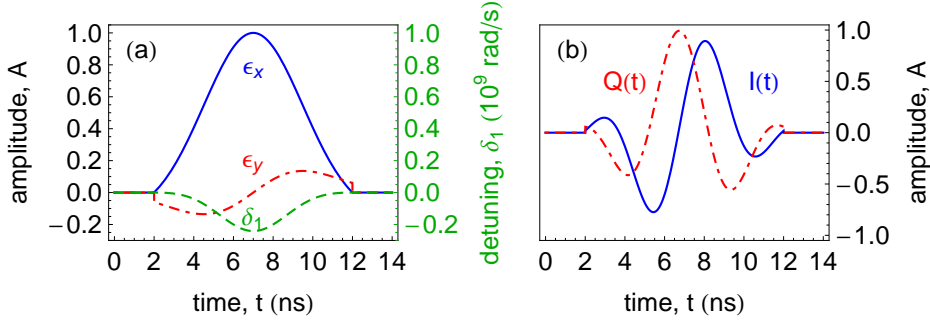


Figure 5.11: An example of the DRAG pulse as it is applied to the I and Q port of the upconversion mixer for qubit driving, in two different IQ-mixer operation modes. The DRAG parameters are $\alpha = 330$ MHz, $\sigma = 2.5$ ns and $f_t = 2$. a) DC mode: The Gaussian pulse with amplitude $\epsilon_x(t)$ (blue solid line) is directly applied to the I port, while the correction quadrature $\epsilon_y(t)$ (red dash-dot line) is applied to the Q-port. The qubit frequency control δ_1 (green dashed line) is in experiment replaced by phase ramping, or set to zero and as a compensation $\epsilon_y(t)$ is scaled by a factor q_s . b) Signal applied to the IQ-mixer in single sideband mixing mode. Here the typical sideband frequency of 100 MHz is chosen.

scale of $q_s = 0.5$. In our experiments, we have not observed an improvement when including the phase ramping. Thus we have decided to use the Y -only corrected pulse in our implementation of DRAG pulses.

Depending on how we operate our upconversion mixer, we have to further process ϵ_x and ϵ_y before the signal is applied to the IQ ports. If we use the IQ-mixer in DC-mode, we directly apply the values above. However, if we operate it in the single sideband mixing mode, see [Section 4.3.1](#), we apply a signal given by $I(t) = B(t) \sin(\omega_{\text{IF}}t + \phi(t))$ and $Q(t) = B(t) \cos(\omega_{\text{IF}}t + \phi(t))$ with the amplitude $B(t) = \sqrt{\epsilon_x^2 + \epsilon_y^2}$, the phase $\phi(t) = \arctan[\epsilon_x(t)/\epsilon_y(t)]$ and the sideband frequency ω_{IF} . [Figure 5.11b](#) shows these signals for the same values as before and $\omega_{\text{IF}}/2\pi = 150$ MHz.

5.4.3 Pulse calibration

For all single qubit operations used in our experiments, we choose a fixed pulse duration (typically about 8 – 12 ns), and control the amount of rotation by adjusting the amplitude of the pulse. Our procedure to calibrate the single qubit π and $\pi/2$ pulses is outlined below. It consists of a sequence of Rabi and Ramsey experiments to find the accurate pulse amplitudes and qubit frequency, and finally also a DRAG calibration procedure to find the experimentally optimal scaling factor q_s . Even though there are more sophisticated procedures to accurately calibrate the amplitude of the π and $\pi/2$ pulses [Vaughan72, Chow09], our method results in gate fidelities of $\sim 0.98 \pm 0.01$ extracted from a randomized benchmarking experiment [Chow09] and quantum process tomography (Section 5.5.2). We have done the same characterization using the more sophisticated pulse calibration procedures and observed no improvement of the fidelity. For qubits with enhanced coherence times, these methods however might become more relevant.

Calibration procedure

1. Find the approximate qubit frequency ω_{01} with spectroscopy.
2. Drive Rabi oscillations at this frequency and determine the approximate amplitude values for π and $\pi/2$ pulses.
3. Measure Ramsey oscillations with a drive detuned by ~ 4 MHz from the qubit transition frequency and determine the accurate value of ω_{01} from a fit to the data.
4. Calibrate the upconversion mixer for the desired LO-frequency and keep this fixed for all subsequent experiments. The drive frequency is now always adjusted with the IF frequency ω_{IF} used for sideband mixing.
5. Measure Rabi oscillations again on the accurate qubit transition frequency with approximate DRAG pulse calibration. Extract from a fit the accurate ε_x amplitude required for a π and $\pi/2$ pulse.
6. Run the DRAG calibration procedure and determine the scaling factor q_s , see below.
7. Repeat the Rabi experiment again to determine the final amplitudes for the π and $\pi/2$ pulses using a sinusoidal fit to the measured Rabi oscillations.

DRAG calibration

We experimentally determine the optimal value of q_s by measuring the excited state population of the qubit after a sequence of pulses that are particularly susceptible to phase errors as a function of q_s . More specifically, we repeat three such experiments where we apply first a $\pi/2$ -pulse around the x axis followed by a π -pulse around the x , y or $-y$ axis, respectively. For ideal pulses, all these sequences result in the same qubit population of 0.5, and any phase errors of the first pulse result in a deviation of the qubit population from 0.5 when the second pulse rotates about a different axis. As shown in [Figure 5.12a](#), this is observed in our data, where the deviations in the population from 0.5 have opposite signs for the two cases where the second pulse rotates around the y (green dots) or $-y$ axis (red dots), while no deviation is observed when both pulses perform rotations around the same axis (blue dots). From a linear fit to the data (solid lines), we extract the optimal scaling factor $q_s = -0.178$ from the position where all three lines cross in a single point at 0.5 population, in contrast to a normal Gaussian pulse ($q_s = 0$) where population errors of 5% – 10% are observed. Our scaling factor drastically differs from the theoretically optimal value of $q_s = 0.5$. While the sign difference remains unclear (sometimes it is positive and sometimes negative, and depends on the frequency of the qubit), the difference in the amplitude is likely to be caused by signal distortions due to imperfections of the cabling between the room temperature equipment and the chip, or a coupling strength ratio g_{01}/g_{12} other than $\sqrt{2}$. A similar scheme was used in [\[Chow10\]](#), and another scheme which measures the phase errors in a more direct way is presented in [\[Lucero10\]](#).

5.4.4 Rotations around the z axis

Even though it is possible to decompose any unitary single qubit operation into a sequence of rotation operators about the x and y axis, it is still useful in some cases to be able to carry out rotations about the z axis. In fact, we use it for eliminating the dynamic phases after a controlled-PHASE gate which is particularly useful for the implementation of the Toffoli gate, see [Section 7.2](#). As can be seen in [Equation \(5.10\)](#), the Hamiltonian of a two-level system in the rotating frame contains a $\hat{\sigma}_z$ term whenever the qubit frequency is detuned from the drive. We can thus realize a rotation about the z axis by shortly shifting the qubit transition frequency out of resonance in between the microwave pulses, using a fast magnetic flux pulse applied to the qubit. While the rate at which the qubit acquires the

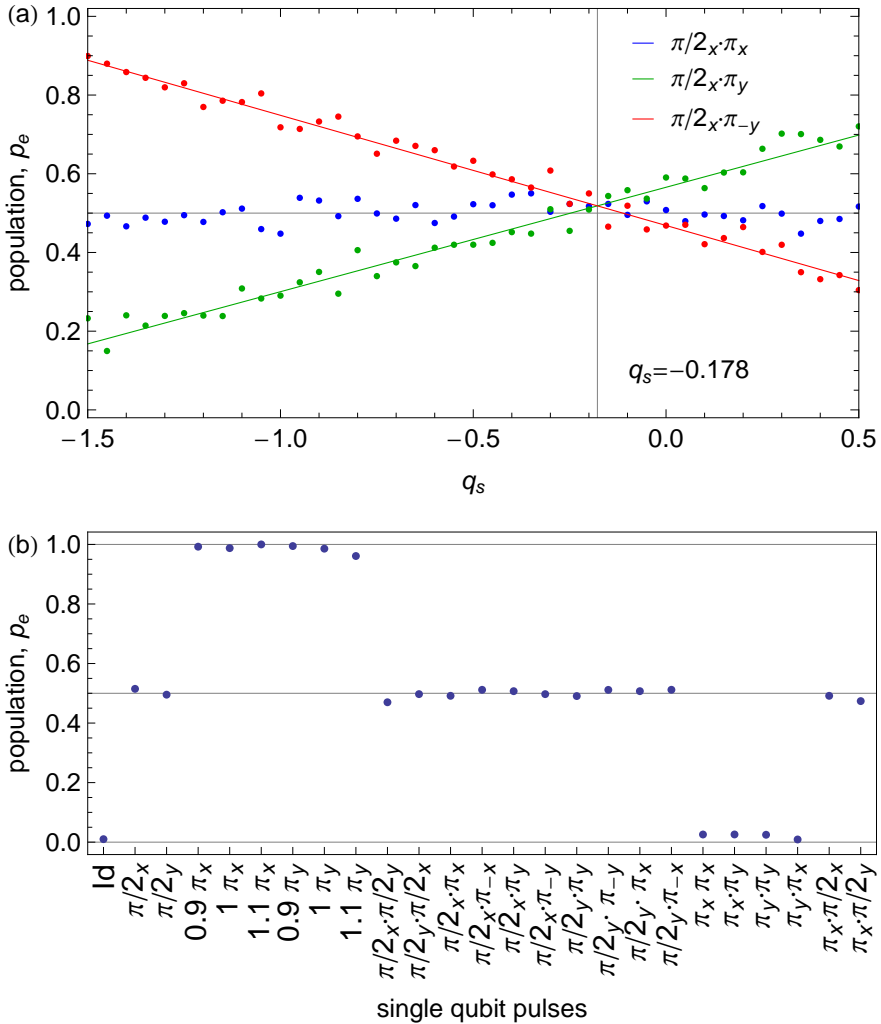


Figure 5.12: DRAG pulse calibration. a) The scaling factor q_s for the ε_y quadrature can be calibrated by measuring the population of the qubit after the three different pulse combinations as a function of q_s . An optimal pulse would always result in $p_e = 0.5$, and the optimal q_s is found where the measured populations cross each other. b) The measured population after different combinations of pulses as a check of the calibration from a). Using randomized benchmarking, we reach an average fidelity of ~ 0.98 for the x and y pulses using this calibration technique, with $\sigma = 2.5$ ns and $f_t = 2$.

dynamic phase is determined by the detuning $\delta_1(t)$, the amount of rotation is given by the integral $\phi = \int_0^T \delta_1(t)dt$ where T is the length of the flux pulse.

We calibrate ϕ in a Ramsey type experiment depicted in [Figure 5.13a](#). The short flux pulse with length T (in this case $T = 3$ ns) and amplitude A is sandwiched in between two $\pi/2$ pulses applied on resonance with the qubit. Starting from state $|0\rangle$, the first $\pi/2$ pulse brings the qubit into a superposition state $(|0\rangle + |1\rangle) / \sqrt{2}$. During the short frequency excursion during the flux pulse, the state $|1\rangle$ acquires a dynamic phase ϕ relative to the state $|0\rangle$ such that the qubit ends up in the state $|0\rangle + e^{i\phi}|1\rangle$. This phase is then mapped onto the population $p_e = \cos(\phi)$ of the qubit by the second $\pi/2$ pulse to make it detectable. Measuring p_e as a function of A results in a sinusoidal oscillation in the regime where δ_1 can be approximated to depend linearly on A , as confirmed in experiment, see [Figure 5.13b](#). From a fit to a cosine function (red solid line), we can for example extract the amplitude $A \approx 0.43$ corresponding to a $\phi = \pi$ rotation. In contrast to the two-qubit operation described in [Section 6.2.3](#), the shape of the flux pulse has no influence on the accuracy of the gate. Only the total area under the pulse is of relevance.

This pulse scheme can also be useful to calibrate the flux pulse amplitude required to shift the qubit by a certain frequency. As an example, for $A = 0.43$ we can readily extract the average qubit detuning of $\bar{\delta}_1 = \phi/(2\pi T) \approx 167$ MHz during the 3 ns short flux pulse. Using a $\pi/2$ pulse about the y instead of about the x axis would also allow to determine whether the qubit is positively or negatively detuned from the drive, and as such determine the sign of δ_1 and of the phase ϕ accumulated during the flux pulse.

5.5 Quantum state and process reconstruction

Before proceeding with more complicated experiments involving two-qubit gates, we first need to verify that we are able to accurately prepare an arbitrary single qubit state. We do this by reconstructing the full density matrix of the prepared state with a method called quantum state tomography and then compare the result with the theoretically expected state. Similarly, we can also fully characterize an arbitrary quantum operation applied to our qubit using quantum process tomography. This is a useful tool to verify correct operations of two and three qubit gates, see [Section 6](#). I will thus shortly describe the two methods. A more detailed description of quantum process tomography can be found in the [Appendix A.2](#).

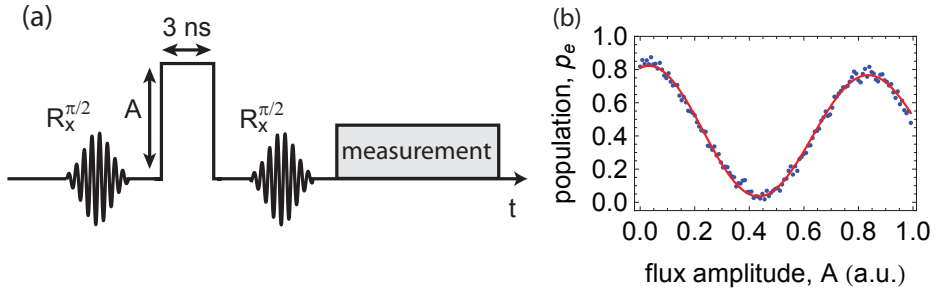


Figure 5.13: Calibration of a single qubit PHASE gate is carried out using a Ramsey type experiment. a) The pulse sequence consists of a magnetic flux pulse of length $T = 3$ ns and varying amplitude A , sandwiched in between two $\pi/2$ pulses applied on resonance. During the short frequency excursion during the flux pulse, the qubit acquires dynamic phase which depends on the area under the pulse. This phase is then mapped onto the population p_e of the qubit by the second $\pi/2$ -pulse. b) Recording p_e as a function of A results in the expected sinusoidal oscillation (red solid line is a fit to a sine function).

5.5.1 Quantum state tomography

As outlined in [Section 3.2.3](#), a transmission measurement of the resonator allows to extract the expectation value of the measurement operator $\langle \hat{M} \rangle = \text{Tr}(\hat{\rho} \hat{M})$, which for the single qubit case is just the population of the state $\hat{\rho}$ being in the excited state, which is equivalent to $\langle \hat{\sigma}_z \rangle = \text{Tr}(\hat{\rho} \hat{\sigma}_z)$. The full reconstruction of a density matrix is thus not possible with a single transmission measurement, as it only provides information about the diagonal terms, or speaking in the Bloch sphere picture, only determines the projection of the state onto the z axis. Since the measurement operator is fixed by the form of the Jaynes-Cummings Hamiltonian, we can not directly rotate the measurement basis to measure the x and y components of the state. However we can use the relation

$$\langle \hat{M}_k \rangle = \text{Tr}[\hat{\rho} \hat{U}_k^\dagger \hat{M} \hat{U}_k] = \text{Tr}[\hat{U}_k \hat{\rho} \hat{U}_k^\dagger \hat{M}] \quad (5.14)$$

to convince ourselves that instead of changing the measurement basis, we can just rotate the prepared state by the unitary operation \hat{U}_k prior to measurement to extract

the projections onto the other axes. In fact, when using the operators

$$\{\hat{U}_k\} = \{\hat{I}, e^{-i\frac{\pi}{4}\hat{\sigma}_x}, e^{-i\frac{\pi}{4}\hat{\sigma}_y}, e^{-i\frac{\pi}{2}\hat{\sigma}_x}\} \quad (5.15)$$

we find an expectation value $\langle \hat{M}_k \rangle$ which is equivalent to $\langle \hat{\sigma}_z \rangle$, $\langle -\hat{\sigma}_y \rangle$, $\langle \hat{\sigma}_x \rangle$ and $\langle -\hat{\sigma}_z \rangle$, and thus unambiguously defines the state vector on the Bloch sphere.

We calculate the density matrix of the prepared state by solving the set of linear equations

$$m_k = \text{Tr} \left[\hat{\rho}(\vec{r}) \hat{U}_k^\dagger \hat{M} \hat{U}_k \right], \quad (5.16)$$

for the variables \vec{r} . Here, m_k are the estimates of the expectation values $\langle \hat{M}_k \rangle$ extracted from experiment, and

$$\hat{\rho}(\vec{r}) = \frac{r_1 \hat{I} + r_2 \hat{\sigma}_x + r_3 \hat{\sigma}_y + r_4 \hat{\sigma}_z}{2} \quad (5.17)$$

is a decomposition of the density matrix into Pauli and identity operators, which span the one-qubit density matrix space. This decomposition however does not include the normalization, such that the trace of the resulting matrix gives a measure of how well our state reconstruction worked. If the trace is far off from one, we know that there is a systematic error in the tomography procedure. The measurement operator \hat{M} is extracted from independent measurements of the resonator response for both computational basis states $|0\rangle, |1\rangle$

For the case of n-qubit state tomography, we apply the 4^n possible combinations for the tensor product of the single qubit operations $\{\hat{U}_k\}^{\otimes n}$ before measurement, to get 4^n expectation values used to extract the 4^n unknown elements of the $2^n \times 2^n$ density matrix from a set of linearly independent equations. Analogous to the single qubit case, the set of all possible combinations of tensor products between Pauli and identity matrices $\{\hat{I}, \hat{\sigma}_x, \hat{\sigma}_y, \hat{\sigma}_z\}^{\otimes n}$ form an orthonormal basis for the space of $2^n \times 2^n$ complex Hermitian matrices. The density matrix can thus be decomposed as

$$\hat{\rho}(\vec{r}) = \sum_{i=1}^{4^n} r_i \sigma_i. \quad (5.18)$$

The measurement operator \hat{M} is determined from independent measurements of the resonator response for all computational basis states $\{|0\rangle, |1\rangle\}^{\otimes n}$.⁶

⁶We have written a Mathematica function which automatically returns the density matrix for an arbitrary number of qubits. It is called *GetDensityMatrix* and is found in the library *StateTomogra-*

Due to noise in the measurement, the reconstructed density matrix is not necessarily physical, i.e. a positive-semidefinite matrix with trace one (the matrix is always Hermitian as it was already required by the decomposition of the density matrix). We therefore run a maximum likelihood algorithm given in [Smolin12] and summarized in Appendix A.2.1. This method numerically finds the density matrix, which gives the measured expectation values with highest probability under the assumption that the noise is Gaussian.⁷

In order to demonstrate how well our state reconstruction works, we have prepared a full set of basis states $\{|0\rangle, |1\rangle, (|0\rangle - i|1\rangle)/\sqrt{2}, (|0\rangle + |1\rangle)/\sqrt{2}\}$ using π and $\pi/2$ pulses about the x/y axis and reconstructed their density matrices, see Figure 5.14. How well these states have been prepared can be quantified by calculating the state fidelity⁸ given by

$$F = \left(\text{Tr} \sqrt{\sqrt{\hat{\rho}_t} \hat{\rho}_m \sqrt{\hat{\rho}_t}} \right)^2, \quad (5.19)$$

where $\hat{\rho}_m$ and $\hat{\rho}_t$ are the experimentally obtained and the theoretically expected density matrices, respectively. Calculating the fidelity for the prepared states yields 0.986, 0.99, 0.99 and 0.99, respectively, demonstrating the exceptionally good control over a single qubit state.

5.5.2 Quantum process tomography

A quantum process which returns a state $\hat{\rho}' = \mathcal{E}(\hat{\rho})$ when acting on a state $\hat{\rho}$, be it a measurement, decoherence or a unitary operation, can always be described by a so called χ matrix defined as

$$\mathcal{E}(\hat{\rho}) = \sum_{mn} \chi_{mn} \hat{E}_m \hat{\rho} \hat{E}_n^\dagger, \quad (5.20)$$

Here, \hat{E}_m form a fixed set of basis operators for the operators acting on the state space and χ_{mn} are the 4^n entries of the positive semidefinite Hermitian χ matrix describing an n qubit process, represented in the basis $\{\hat{E}_m\}$. This is very similar to

phy.m. The order of the measured expectation values $\langle \hat{M}_k \rangle$ and the elements of the measurement operator given to the function have to be the one as given above!

⁷We have implemented this algorithm in Mathematica and can be found under the name *MLState* in the *StateTomography.m* library.

⁸Note that the fidelity is sometimes also defined without the square.

the density matrix formalism, where the full quantum state is described by a matrix $\hat{\rho}$, typically represented in the basis formed by the computational states $\{|k\rangle\} = \{|0\rangle, |1\rangle\}^{\otimes n}$. The entries of this matrix are then determined from the expansion $\hat{\rho} = \sum_{kl} \rho_{kl} |k\rangle\langle l|$. For a quantum process, the basis is not formed by states, but rather by operators, and the expansion is given by Equation (5.20). Once the χ matrix is fully determined using quantum process tomography, we can calculate the output $\mathcal{E}(\hat{\rho})$ of the quantum process for every arbitrary input state $\hat{\rho}$. Throughout this thesis, we use the commonly used basis operators $\{\hat{E}_m\} = \{\hat{I}, \hat{\sigma}_x, -i\hat{\sigma}_y, \hat{\sigma}_z\}^{\otimes n} = \{\hat{I}, \hat{X}, \hat{Y}, \hat{Z}\}^{\otimes n}$.

As an example, let us discuss how to determine the χ matrix for the unitary operation $\hat{R}_x^{\pi/2} = \exp(-i\frac{\pi}{4}\hat{\sigma}_x)$ describing the $\pi/2$ rotation about the x axis. To do so we first decompose $\hat{R}_x^{\pi/2}$ into the basis operators \hat{E}_m

$$\hat{R}_x^{\pi/2} = \frac{1}{\sqrt{2}} \begin{pmatrix} 1 & -i \\ -i & 1 \end{pmatrix} = \sum_m a_m \hat{E}_m = \frac{1}{\sqrt{2}} \hat{I} - i \frac{1}{\sqrt{2}} \hat{\sigma}_x \quad (5.21)$$

Using Equation (5.20), we can directly see that the diagonal terms of the χ matrix are given by $\chi_{mm} = a_m a_m^*$ and the off-diagonal ones by $\chi_{mn} = a_m a_n^*$, yielding the χ matrix

$$\chi = \frac{1}{2} \begin{pmatrix} 1 & 1 & 0 & 0 \\ -1 & 1 & 0 & 0 \\ 0 & 0 & 0 & 0 \\ 0 & 0 & 0 & 0 \end{pmatrix}. \quad (5.22)$$

For unitary dynamics, the χ matrix can be read fairly easy, since it directly gives the decomposition of the unitary into the basis operators. However, extracting information about non-unitary dynamics such as decoherence is not so straight forward [Kofman09].

The procedure to experimentally determine χ for an arbitrary n -qubit process is as follows:

1. Prepare all 4^n n -qubit states $\{\hat{\rho}_j\} = \{|0\rangle\langle 0|, |1\rangle\langle 1|, |-\rangle\langle -|, |+\rangle\langle +|\}^{\otimes n}$, where $|-\rangle = (|0\rangle - i|1\rangle)/\sqrt{2}$ and $|+\rangle = (|0\rangle + |1\rangle)/\sqrt{2}$. This set forms a linearly independent basis of the state space consisting of $2^n \times 2^n$ matrices.
2. Apply the quantum process to each prepared basis state and reconstruct the output states $\hat{\rho}'_j = \mathcal{E}(\hat{\rho}_j)$ (do not run a maximum likelihood algorithm on these states).

3. Reconstruct the χ matrix from the measured $\hat{\rho}'_j$.⁹

A more detailed description of quantum process tomography can be found in [Appendix A.2.2](#).

As for quantum state tomography, the extracted χ matrix is not necessarily physical (positive semidefinite, Hermitian and trace preserving) due to noise in the measurement. We thus apply an iterative maximum likelihood algorithm [[Ježek03](#)] which finds the physical χ matrix, which is most likely to give the measured values under the assumption that the noise is Gaussian (see also [Section A.2.3](#)).¹⁰

We test the quantum process tomography procedure on four different single qubit gates, the identity \hat{I} , the $\pi/2$ and π rotation about the x axis, and the π rotation about the y axis, see [Figure 5.14](#). We quantify the accuracy of the quantum gates with the process fidelity

$$F_P = \text{Tr}(\chi_t \cdot \chi_m), \quad (5.23)$$

where χ_t is the theoretically expected and χ_m the experimentally reconstructed χ matrix of the intended process. Calculating F_P for the experimentally realized processes yields 0.96, 0.98, 0.98 and 0.98, respectively.

5.6 Conclusion

In this chapter, we have demonstrated high fidelity single qubit operations. Due to the weak anharmonicity of the transmon qubit, optimal pulse control techniques have to be used to eliminate the phase and population errors due to leakage into the third transmon level. Using quantum state and quantum process tomography, we have fully characterized our gates, and show gate fidelities of $\sim 98\%$. In order to run simple quantum algorithms, we need in addition to be able to carry out two-qubit operations. The next chapter describes two possible approaches to do so.

⁹ Use the Mathematica function *CalculateChiNQ* which is found in the library *QuantumProcessTomography.m*. Note here that it is important to pass the reconstructed $\hat{\rho}'_j$ in the correct order to the function.

¹⁰ Use the Mathematica function *ProcessMaxLikelyHood* in the *QuantumProcessTomography.m* library to run this algorithm.

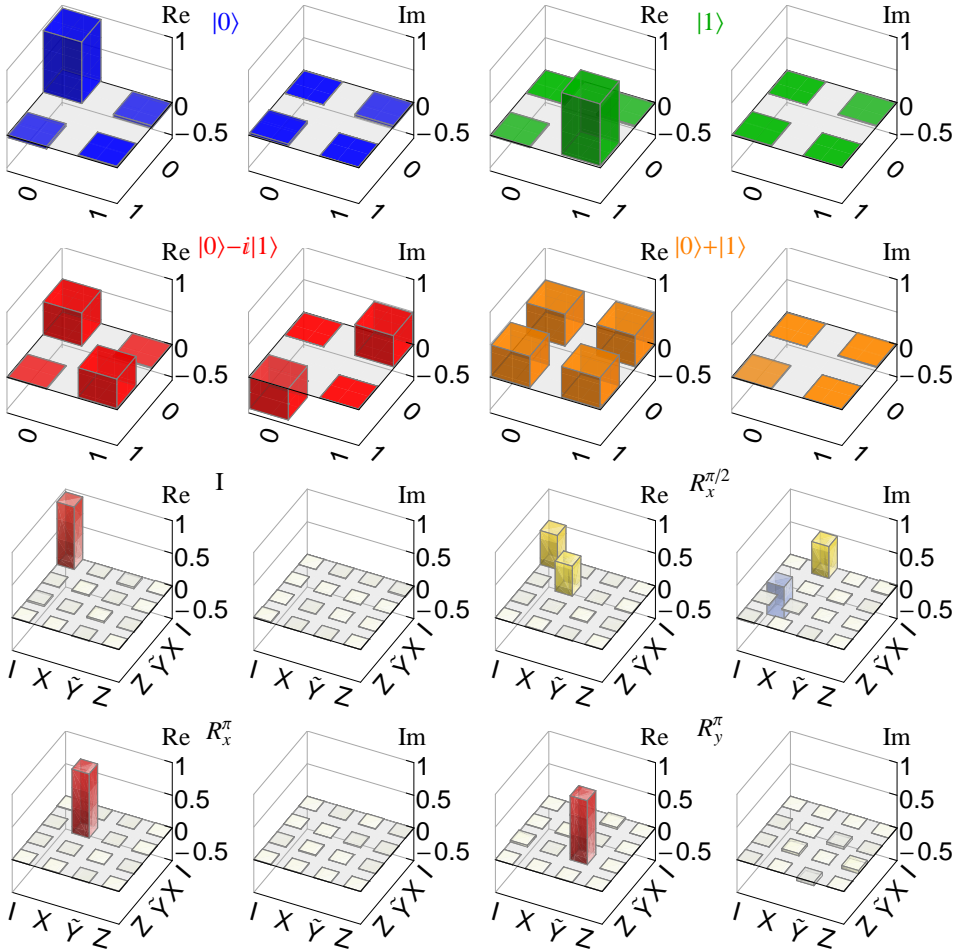


Figure 5.14: Quantum State and Process Tomography. First two rows show the real and imaginary part of the measured one-qubit density matrices with a fidelity of 0.986, 0.990, 0.999, 0.999 with respect to the ideal states $|0\rangle$, $|1\rangle$, $|0\rangle - i|1\rangle$ and $|0\rangle + |1\rangle$, respectively. Last two rows show the measured χ matrices with a process fidelity of 0.96, 0.98, 0.98, 0.98 with respect to the ideal processes of identity, π and $\pi/2$ rotation around x axis and π rotation around y axis.

Quantum Operations between Multiple Qubits

In this chapter I describe two different approaches for the realization of two-qubit operations. In both cases, the qubits are operated in the dispersive regime. The first is based on sideband transitions between the qubits and the resonator, and the interaction between qubits is realized by exchanging a single excitation between the qubits via a photon inside the resonator [Wallraff07, Leek09, Leek10], see [Section 6.1](#). The other approach exploits the fact that two qubits can exchange a single excitation via virtual photons inside the resonator when their transition frequencies are resonant, even though they are far detuned from the resonator [Majer07, DiCarlo09, Yamamoto10, Strauch03], see [Section 6.2](#).

Both approaches have their advantages and disadvantages. For the former it is beneficial that the qubits always stay at their optimal bias points with maximized coherence and two-qubit operations are carried out only with microwave drives, no flux pulses are required. However, due to selection rules in circuit QED, strong drives are required to drive the sideband transitions and the operations are relatively slow. Another all-microwave approach with the same advantages has recently been used to demonstrate a high fidelity controlled-NOT gate [deGroot10, Chow11]. The latter approach has the benefit that the qubit-qubit interaction is much faster. However, it requires the fast tuning of qubit frequencies with flux pulses, which adds additional complexity, see also [Section 4.4](#).

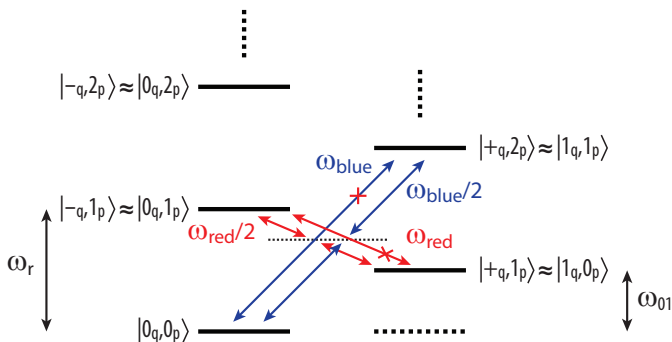


Figure 6.1: Energy level diagram of the combined qubit resonator system in the dispersive regime. The blue (red) sideband transition, indicated with blue (red) arrows, at frequency $\omega_{\text{blue}} = \omega_r + \omega_{01}$ ($\omega_{\text{red}} = |\omega_r - \omega_{01}|$) is forbidden to first order with one photon, but may be driven using two photons, for example, both at a frequency of $\omega_{\text{blue}}/2$ ($\omega_{\text{red}}/2$).

6.1 Qubit-qubit interaction with sidebands

In atomic systems, sideband transitions couple the harmonic quantized motion, e.g. of the atom in a trap, with the internal degrees of freedom of the atom. They are very successfully used for sideband cooling [Wiemann99] to cool the motion of atoms to the ground state and in the context of quantum computation, to perform multi-qubit operations between trapped ions [Cirac95, Monroe95, Sørensen99, Childs00, Schmidt-Kaler03, Lanyon11]. In circuit QED, sidebands can be driven between the qubit and the resonator and have first been observed with a flux qubit coupled to an LC oscillator [Chiorescu04] and later with a CPB coupled to a CPW resonator [Wallraff07].

In this section I describe our experiments [Leek09, Leek10] on sidebands with our circuit QED system, which extend the previous work, including the observation of coherent two-photon Rabi oscillations on the sideband transition, the preparation of n photon Fock states up to $n = 5$, the measurement of the energy decay and phase coherence of the one photon Fock state, and finally the generation of two-qubit entangled Bell states. A key element for the success of these experiments was a special design of our resonator, which has drastically different photon lifetimes in different harmonic modes. We designed one harmonic mode to have short photon

lifetimes for fast qubit readout, and another harmonic mode to have long photon lifetimes for photon storage.

The energy level diagram of the coupled transmon-resonator system in the dispersive regime is depicted in [Figure 6.1](#). Although the qubit and resonator do not directly exchange energy in this case, the residual dispersive coupling allows sideband transitions to be accessed using strong microwave drive fields. Blue sideband transitions involve simultaneous excitation of both qubit and resonator at a transition frequency $\omega_{\text{blue}} = \omega_r + \omega_{01}$ (blue arrow), while the red sideband involves the exchange of an excitation between the two systems at a transition frequency $\omega_{\text{red}} = |\omega_r - \omega_{01}|$ (red arrow). Due to symmetry considerations of the Jaynes-Cummings Hamiltonian, single-photon sideband transitions with either a CPB biased at charge degeneracy or a transmon qubit are forbidden to first order [[Blais07](#)], see also [Section 6.1.1](#). They may, however, be accessed using two photons with frequencies $\omega_{d_1}, \omega_{d_2}$, whose sum or difference frequency is equal to one of the sideband transition frequencies $\omega_{\text{blue(red)}}$. In our experiments, we restrict ourselves to drive the sideband transitions with two photons of equal energy, using a single microwave drive of frequency $\omega_{\text{blue(red)}}$ /2. In this configuration, the drive is equally detuned from the qubit and resonator, maximizing the selectivity of the sideband transition with respect to the undesired off-resonant driving of the bare-qubit transition and off-resonant population of the resonator.

The system including the two drives for the two-photon excitation is described by the Jaynes-Cummings Hamiltonian

$$\hat{H}/\hbar = \omega_r \hat{a}^\dagger \hat{a} + \frac{\omega_{01}}{2} \hat{\sigma}_z + g_{01} (\hat{a}^\dagger \hat{\sigma}_- + \hat{\sigma}_+ \hat{a}) + \hat{H}_{d_1} + \hat{H}_{d_2}, \quad (6.1)$$

where the driving terms depend on whether the drives are applied to the resonator input or to the local qubit driving lines. For the former case they are given by $\hat{H}_{d_i}/\hbar = \varepsilon_{d_i}(t) (\hat{a}^\dagger e^{-i\omega_{d_i}t} + \hat{a} e^{i\omega_{d_i}t})$ with the amplitude ε_{d_i} , while for the latter case they are given by $\hat{H}_{d_i}/\hbar = (\Omega_{d_i}(t)/2) \hat{\sigma}_x \cos(\omega_{d_i}t)$, where the driving strength is determined by the Rabi frequency $\Omega_{d_i}(t)$. From this Hamiltonian (6.1), one can find an effective Hamiltonian [[Blais07](#)] which includes the terms

$$\hat{H}_{\text{blue}}/\hbar = g_{01} \frac{\Omega_{d_1}}{2(\omega_{01} - \omega_{d_1})} \frac{\Omega_{d_2}}{2(\omega_{01} - \omega_{d_2})} (\hat{\sigma}_+ \hat{a}^\dagger + \hat{\sigma}_- \hat{a}) = \frac{\Omega_{\text{blue}}}{2} (\hat{\sigma}_+ \hat{a}^\dagger + \hat{\sigma}_- \hat{a}) \quad (6.2)$$

$$\hat{H}_{\text{red}}/\hbar = g_{01} \frac{\Omega_{d_1}}{2(\omega_{01} - \omega_{d_1})} \frac{\Omega_{d_2}}{2(\omega_{01} - \omega_{d_2})} (\hat{\sigma}_+ \hat{a} + \hat{\sigma}_- \hat{a}^\dagger) = \frac{\Omega_{\text{red}}}{2} (\hat{\sigma}_+ \hat{a} + \hat{\sigma}_- \hat{a}^\dagger), \quad (6.3)$$

corresponding to two-photon blue and red sideband transitions driven with the Rabi rate Ω_{blue} and Ω_{red} , respectively. Terms corresponding to one-photon sideband transitions (i.e. including only one drive) do not appear due to symmetry properties of the drives and the Jaynes-Cummings Hamiltonian.

6.1.1 Selection rules for the driven Jaynes-Cummings Hamiltonian

The fact that sideband transitions in circuit QED are forbidden, can be attributed to the symmetry of the Jaynes-Cummings Hamiltonian [Blais07]. In particular, the operator $\hat{C} = \hat{a}^\dagger \hat{a} + \hat{\sigma}_z/2$ commutes with the Hamiltonian and as a result, the number of excitations is a conserved quantity. It is thus not possible to drive transitions with one photon that involve the excitation of zero (red sideband) or two (blue sideband) excitations. To see this more clearly, one can introduce the parity operator (the natural unitary extension of \hat{C}) $\hat{P} = e^{-i\pi \hat{a}^\dagger \hat{a}} \hat{\sigma}_z = \sum_{n=0}^{\infty} (-1)^n |n\rangle \langle n| \hat{\sigma}_z$. The parity of a state $|\psi\rangle$ is said to be even (odd), if it is an eigenstate of \hat{P} with eigenvalue $p = 1$ ($p = -1$). Since the parity operator anticommutes with the drive Hamiltonian H_{d_i} in a frame rotating at the drive frequency, we can write the following relation

$$0 = \langle \psi_f | \hat{H}_{d_i} \hat{P} + \hat{P} \hat{H}_{d_i} | \psi_i \rangle = (p_i + p_f) \langle \psi_f | \hat{H}_{d_i} | \psi_i \rangle, \quad (6.4)$$

where $|\psi_i\rangle$ and $|\psi_f\rangle$ label the initial and final state of a transition we would like to drive. If the parity of both states is the same, the right hand side can only be zero if the matrix element of the drive $\langle \psi_f | \hat{H}_{d_i} | \psi_i \rangle$ vanishes. The drive can thus only cause transitions between states with different parity $p_i = -p_f$.

In order to find the allowed and forbidden transitions in circuit QED, we first have to write down the parity of the eigenstates (3.48-3.49) of the Jaynes-Cummings Hamiltonian

$$\hat{P}|0, 0\rangle = -|0, 0\rangle, \quad \hat{P}|\pm_q, n_p\rangle = (-1)^{n-1} |\pm_q, n_p\rangle. \quad (6.5)$$

The blue sideband transition indicated in Figure 6.1 corresponds to a transition between $|0_q, 0_p\rangle$ and $|+_q, 2_p\rangle$ which have the same parity, and is thus forbidden.

Similarly, the red sideband corresponds to a transition between $| -_q, 1_p \rangle$ and $| +_q, 1_p \rangle$ and is also forbidden. In contrast, driving the single qubit transition connecting $| 0_q, 0_p \rangle$ and $| +_q, 1_p \rangle$ is allowed. When using two drives, the selection rules are reversed since the operator $\hat{H}_{d_1} + \hat{H}_{d_2}$ commutes with the parity operator \hat{P} .

6.1.2 Cavity quantum electrodynamics with separate photon storage and qubit readout modes

In [Section 3.2.3](#) we have described the weak dispersive quantum non-demolition readout of a qubit state in circuit QED by measuring the transmission of microwave photons through a coplanar waveguide resonator. One important condition to be able to extract useful information about the qubit state with this procedure is that the photon lifetime inside the resonator is much shorter than the qubit energy decay time. If this condition is not fulfilled, the signal to noise ratio of the transmitted measurement signal is significantly reduced. This is because with high probability, the qubit state is already decayed before any transmitted photons could be detected, significantly reducing the measurement contrast between the ground and excited state of the qubit. On the other hand, if we want to carry out coherent operations between qubit and photons, maximum photon lifetimes are required. One way to combine these two requirements and to carry out experiments with photons of different lifetimes would be to couple the qubit to two different resonators [[Johnson10](#), [Mariantoni11a](#), [Wang11](#), [Mariantoni11b](#)]. However, this significantly increases the space occupied on chip and the complexity of the design. We have instead found a method of doing such experiments by controlling the quality factors of different harmonic modes of a single resonator.

Design of a multi-Q resonator

The schematics of a resonator with significantly different quality factors between the odd and even-symmetry harmonic resonance modes is shown in [Figure 6.2a](#). In addition to the coupling capacitors at the ends of the resonator, two coupling capacitors are added at the center. The first-harmonic mode with frequency ω_1 and all other even-symmetry modes have an electric field distribution with an antinode in the center and are hence strongly coupled to the center ports 3 and 4. Conversely, the fundamental (ω_0) and higher odd-symmetry harmonic modes have an electric field node at the center of the resonator and couple only weakly to the center ports. Choice of the coupling capacitors with capacitance C_{34} at ports 3 and 4 allows one

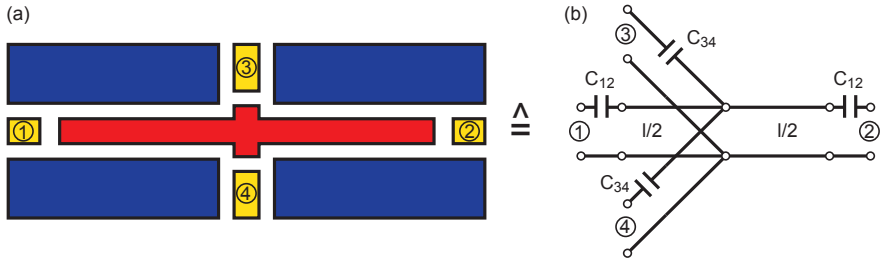
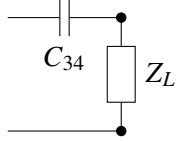


Figure 6.2: a) Schematics of a resonator with individually adjustable (in fabrication) quality factors of the fundamental and first harmonic resonance mode. b) Equivalent circuit model of the device shown in a).

to define an external quality factor at the even harmonic modes Q_{even} as described in Section 3.2.6, leaving the quality factor of the odd harmonic modes Q_{odd} almost unaffected. The capacitors on ports 1 and 2 with capacitance C_{12} however have an effect on all modes because the electric field always has an electric field antinode at the ends of the resonator. This design thus has the feature that the odd harmonic modes have higher quality factors than the even modes. Of course one could also think of other designs for which the frequency spacing between harmonic modes can be adjusted and has the flexibility to choose which mode should be high/low Q , which could be investigated in future experiments.

In order to calculate the S parameters of such a device, the multi-Q resonator can be modeled with the equivalent circuit shown in Figure 6.2b. A transmission line with characteristic impedance of $Z_0 = 50 \Omega$ and length l is capacitively coupled to ports 1 and 2. Additionally, a capacitive coupling is added in the middle of the transmission line to ports 3 and 4. The different 2-port S parameters can now be calculated with the ABCD matrix formalism. If we are interested in the parameters between port 1 and 2, we terminate ports 3 and 4 with a $Z_L = 50 \Omega$ load and calculate the admittance Y_{34} of the line connecting these ports with the transmission line. It simply consists of a capacitor and a load impedance connected

in series, resulting in two admittances of



$$Y_{34} = 1/Z_{34} = \left(\frac{1}{i\omega C_{34}} + Z_L \right)^{-1} \quad (6.6)$$

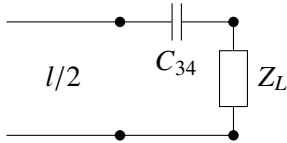
connected in parallel in the center of the transmission line. The ABCD matrix of the whole circuit can thus be readily calculated as

$$\begin{pmatrix} A & B \\ C & D \end{pmatrix}_{12} = \begin{pmatrix} 1 & 1/i\omega C_{12} \\ 0 & 1 \end{pmatrix} (ABCD)_{TL}^{l/2} \begin{pmatrix} 1 & 0 \\ 2Y_{34} & 1 \end{pmatrix} (ABCD)_{TL}^{l/2} \begin{pmatrix} 1 & 1/i\omega C_{12} \\ 0 & 1 \end{pmatrix}. \quad (6.7)$$

The ABCD matrix of the transmission line with length $l/2$ and characteristic impedance Z_0 can be found in [Pozar93, Table 4.1] and is given by

$$(ABCD)_{TL}^{l/2} = \begin{pmatrix} \cos(\beta l/2) & iZ_0 \sin(\beta l/2) \\ iY_0 \sin(\beta l/2) & \cos(\beta l/2) \end{pmatrix}. \quad (6.8)$$

Similarly, if we are interested in the S parameters for port 3 and 4, we terminate ports 1 and 2 with a $50\ \Omega$ load and calculate the admittance of the transmission line with length $l/2$ terminated with a capacitor and a load impedance connected in series



$$Y_{12} = \left(Z_0 \frac{Z_L + 1/i\omega C_{12} + iZ_0 \tan(\pi\omega/2\omega_0)}{Z_0 + i(Z_0 + 1/i\omega C_{12}) \tan(\pi\omega/2\omega_0)} \right)^{-1}. \quad (6.9)$$

The ABCD matrix of the whole 2-port network is then given by

$$\begin{pmatrix} A & B \\ C & D \end{pmatrix}_{34} = \begin{pmatrix} 1 & 1/i\omega C_{34} \\ 0 & 1 \end{pmatrix} \begin{pmatrix} 1 & 0 \\ 2Y_{12} & 1 \end{pmatrix} \begin{pmatrix} 1 & 1/i\omega C_{34} \\ 0 & 1 \end{pmatrix}. \quad (6.10)$$

For the network between port 1 and 3, a combination of the two methods explained above are used. From the ABCD values, the S parameters for the different 2 port networks is extracted by using the relations in [Pozar93, Table 4.2].

Figure 6.3 shows the calculated transmission parameters between the different ports as an example for coupling capacitors with capacitances of $C_{12} = 10\ \text{fF}$

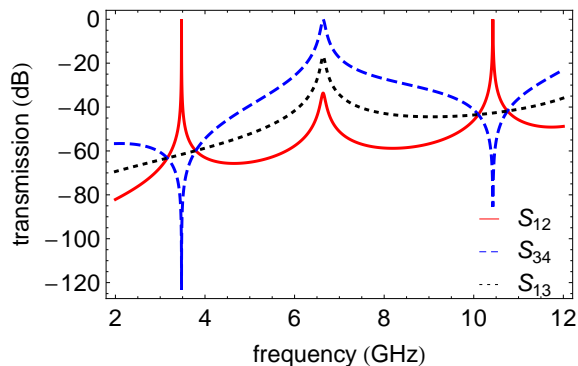


Figure 6.3: Calculated transmission between the different ports of the equivalent circuit model shown in [Figure 6.2b](#).

and $C_{34} = 70$ fF. Transmission between the end ports S_{12} (solid red line) clearly shows resonances at around $\nu_0 = 3.5$ GHz and $\nu_2 = 10.5$ GHz, corresponding to the fundamental and 2^{nd} harmonic resonance modes with a high quality factor. The first harmonic mode resonance at $\nu_1 = 7$ GHz is largely suppressed because most of the signal is lost into the center coupled lines. Transmission through the center ports S_{34} (dashed blue line) has as expected a resonance at the first harmonic mode with low quality factor and unit transmission at resonance and has an antiresonance at the high Q modes. The spectrum between an end port and a center port (dotted black line) only shows one resonance at ν_1 in the displayed range. Although all modes are excited by driving an end port, only signals at the first harmonic mode can be detected with the center port.

Physical implementation

[Figure 6.4a](#) shows an optical image of a fabricated chip consisting of the multi-Q resonator coupled to two qubits at the ends of the resonator. Because the center ports 3 and 4 disconnect the ground planes on both sides at the center of the resonator, air-bridges, or in our case bond wires are used to reconnect the ground planes. This is essential to suppress mode conversion from the even CPW mode to other spurious propagation modes. The same is true for the local gate lines 5 and 6 used for individual qubit driving. For an initial check of how well such a multi-Q design performs in an experiment, we have fabricated a first device (I) with

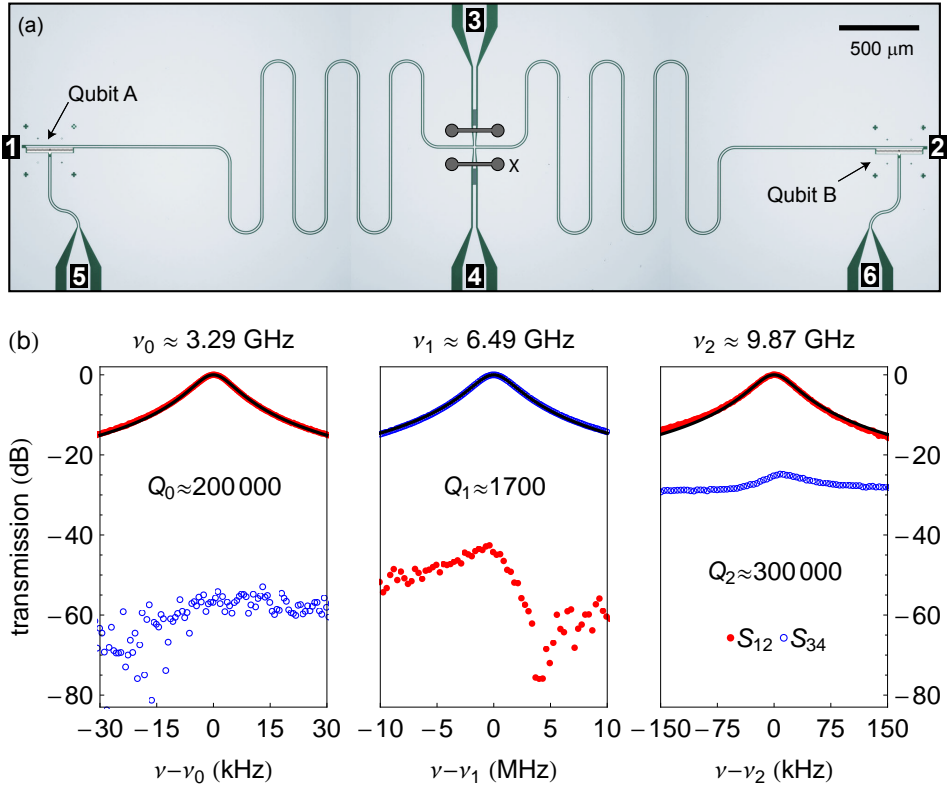


Figure 6.4: a) Optical image (colorized) of a multi Q device with two transmon qubits (device II). Grounding bond wires are shown schematically at position X. b) Normalized transmission spectrum for a four-port center and end-coupled resonator measured at a temperature of 20 mK (device I). Transmission between the end ports S_{12} (red closed circles) and the center ports S_{34} (blue open circles) around the fundamental (ν_0), 1st (ν_1) and 2nd (ν_2) harmonic resonance frequencies are shown.

weakly capacitively coupled end ports 1 and 2 and no qubits. The capacitances were chosen small enough ($C_e \approx 1$ fF) to have little effect on the quality factor of the first three harmonic modes, while the center ports were strongly coupled ($C_c \approx 15$ fF). Measurements of the first 3 harmonics are shown in [Figure 6.4b](#). The data is normalized to a resonant transmission of 0 dB in each case. The center coupled transmission (S_{34} , blue open circles) shows a resonance at $\nu_1 \approx 6.49$ GHz with a quality factor $Q_1 \approx 1700$ consistent with the chosen value of C_c , but low transmission around ν_0 and ν_2 . The end-coupled transmission (S_{12} , red closed circles) shows resonances at $\nu_0 \approx 3.29$ GHz and $\nu_2 \approx 9.87$ GHz with much higher measured quality factors $Q_0 \approx 3 \cdot 10^5$ and $Q_2 \approx 2 \cdot 10^5$, respectively, and low transmission at ν_1 . These Q factors are on the same order as those measured for weakly end-coupled two-port resonators, showing that the fundamental and 2nd harmonic in our multi-Q device are negligibly coupled to the center ports. Hence the device performs as desired, with a low Q first harmonic mode for qubit read-out, and the high Q odd modes for optimal photon storage times.

We then fabricated a second device (II) as it is shown in [Figure 6.4a](#) with qubits for actual qubit experiments. The left and right qubits are labeled A and B, respectively. This device has higher mode frequencies than device (I), and no end ports (1 and 2) for maximized photon lifetime in the high Q mode. The qubits both have a charging energy $E_C/h \approx 305$ MHz and a maximal Josephson energy $E_J^{\max}/h \approx 150$ GHz, which corresponds to a maximal transition frequency of around 19 GHz. Direct microwave drive lines (ports 5 and 6) allow selective driving of the individual qubits. The resonant coupling strengths $g_{01,1}/2\pi \approx 119$ MHz of the qubits to the 1st harmonic at $\nu_1 = 7.01$ GHz were extracted from a standard resonator transmission S_{34} measurement of the vacuum Rabi mode splitting for each qubit. The coupling strength $g_{01,2}/2\pi \approx 183$ MHz to the 2nd harmonic at $\nu_2 = 10.74$ GHz was instead obtained from a spectroscopic measurement of the qubit transition frequency using the 1st harmonic mode when the qubit is tuned across the 2nd harmonic mode.

6.1.3 Spectroscopy and Rabi oscillations on the blue sideband transition

For initial sideband experiments, we have tuned qubit A between the 1st and 2nd harmonic mode of the resonator, to around $\nu_{01} \approx 9.718$ GHz, and biased qubit B far away to around 6 GHz. At this position, the blue sideband transition frequency between qubit A and the 2nd harmonic high Q mode is expected to be at a frequency

of $\omega_{\text{blue}}^A = \omega_{01}^A + \omega_{r,2} \approx 20.458$ GHz. In order to verify this, we have performed a spectroscopy measurement by sweeping the frequency of a single strong microwave drive applied to the selective drive line of qubit A and simultaneously measuring the phase of resonator transmission at the 1st harmonic low-Q mode. We repeated this experiment for different drive powers, see [Figure 6.5a](#). Note that these powers are quoted at the input port of the cryostat and not at the device itself. At a power of around -15 dBm, a spectral line appears corresponding to the two-photon blue sideband transition at $\omega_{\text{blue}}^A/2$. Even though the theoretical description of the two-photon sideband driving involves two different microwave drives, in experiment a single one with a high enough power is sufficient to provide two photons of equal energy. The difference in frequency between the expected $\omega_{\text{blue}}^A/2 \approx 10.229$ GHz and the measured frequency of 10.22 GHz can be attributed to the ac-Stark effect [[Schuster05](#)]. The strong microwave drive needed to drive the sideband applied above the qubit transition frequency ω_{01} ac-Stark shifts ω_{01} , and thus also ω_{blue} , to lower frequencies. This behavior is also seen in [Figure 6.5a](#) as the drive power is increased. Additionally, the measurement response of the off-resonantly driven qubit transition becomes visible on the left side for increasing drive powers. As an example, [Figure 6.5b](#) shows a single spectroscopy trace at a drive power of -7 dBm.

Knowing that the sideband can be saturated by a two-photon transition, we can

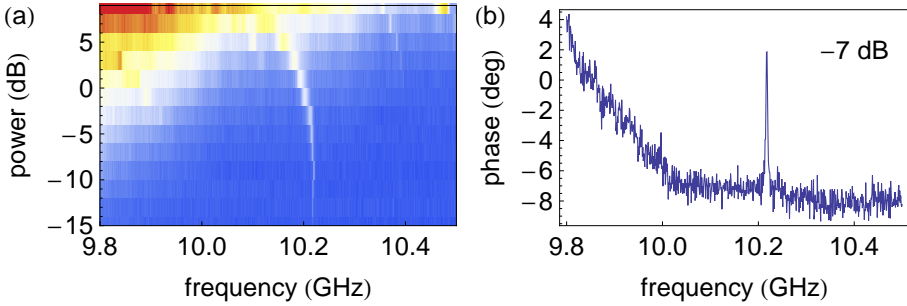


Figure 6.5: a) Spectroscopy of the sideband transition at frequency $\nu_{\text{blue}} \approx 10.22$ GHz as a function of the drive power (the power at the input port of the cryostat). Dark blue and dark red correspond to a phase of -10 deg and 40 deg of the transmitted measurement signal, respectively. b) The phase of the transmitted measurement signal for a single spectroscopy trace at a driving power of -7 dBm.

drive time-resolved Rabi oscillations on the blue sideband with the 2nd harmonic mode between the states $|0_q, 0_p\rangle$ and $|1_q, 1_p\rangle$ by applying square microwave pulses of fixed amplitude and varying length, at the Stark-shifted two-photon blue sideband frequency, to the gate line of qubit A. The measured qubit excited-state population (red solid dots) for a drive power of about 3 dBm and the qubit A biased at $\nu_{01} \approx 9.22$ GHz, $\Delta_0 \approx 1.52$ GHz detuned from $\nu_{r,2}$, is shown in [Figure 6.6a](#). The time evolution can be well understood with numerical simulations, using the simple Hamiltonian

$$\hat{H}/\hbar = \Delta\omega_r \hat{a}^\dagger \hat{a} + \frac{\Omega_{\text{blue}}}{2} (e^{i\phi_{\text{blue}}} \hat{\sigma}_- \hat{a} + e^{-i\phi_{\text{blue}}} \hat{\sigma}_+ \hat{a}^\dagger), \quad (6.11)$$

written in a frame rotating the qubit with frequency ω_{01} and the resonator with $2\omega_d - \omega_{01}$, where ω_d is the frequency of the microwave drive. For simplicity, we assume that the transition can be driven with one photon at $2\omega_d$ and Rabi rate Ω_{blue} . Due to dissipation, the quantum state during the time evolution is in general a mixed state described by the density matrix $\hat{\rho}$. The equation governing the time evolution of $\hat{\rho}$ is the *master equation* in the *Lindblad* form [[Lindblad76](#)]

$$\frac{d\hat{\rho}(t)}{dt} = -\frac{i}{\hbar} [\hat{H}, \hat{\rho}(t)] + \gamma_1 \mathcal{D}[\hat{\sigma}_-] \hat{\rho}(t) + \frac{\gamma_\phi}{2} \mathcal{D}[\hat{\sigma}_z] \hat{\rho}(t) + \kappa \mathcal{D}[\hat{a}] \hat{\rho}(t) + 2\kappa_\phi \mathcal{D}[\hat{a}^\dagger \hat{a}] \hat{\rho}(t) \quad (6.12)$$

where $\mathcal{D}[\hat{L}] \hat{\rho} = \hat{L} \hat{\rho} \hat{L}^\dagger - \hat{L}^\dagger \hat{L} \hat{\rho} / 2 - \hat{\rho} \hat{L}^\dagger \hat{L} / 2$ and \hat{L} are the *Lindblad operators* describing the non-unitary dynamics associated with dissipation and dephasing. A fit to the numerical solution of this master equation is shown in [Figure 6.6a](#) as black solid line. The only fit parameter is the sideband Rabi rate $\Omega_{\text{blue}}/2\pi = 9.8$ MHz and demonstrates the good understanding of the system. The other parameters used for qubit and photon energy decay time $1/\gamma_1 = 730$ ns and $1/\kappa = 1.45$ μ s, respectively, as well as for the qubit and photon pure dephasing time $1/\gamma_\phi = 1.2$ μ s and $1/\kappa_\phi = 5.5$ μ s, respectively, have been taken from separate independent measurements (see [Section 6.1.4](#) for a detailed description of how κ and κ_ϕ was measured).

To demonstrate the importance of the multi-Q device for these sideband experiments, we repeated the experiment above with qubit A biased at a transition frequency of $\omega_{01}/2\pi = 5.49$ GHz, but now driving the blue sideband transition between the 1st harmonic low-Q mode and the qubit (blue, open circles). The detuning Δ_0 to the relevant resonator mode was chosen the same as before, and also the Rabi rate of the sideband drive $\Omega_{\text{blue}}/2\pi = 10.4$ MHz was chosen to be similar. The rapidly decaying Rabi oscillation is consistent with the simulations for

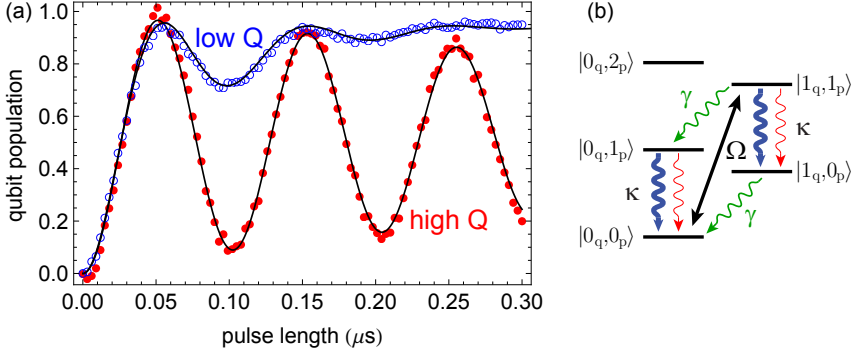


Figure 6.6: a) Rabi oscillations on the blue sideband with the low Q 1st harmonic (blue open circles), and with the high Q 2nd harmonic (red closed circles) resonator mode. Master equation simulations with photon lifetime and sideband drive rate as fit parameters are shown as solid lines. b) Energy level diagram showing the relevant energy decay paths when driving the blue sideband transition. The photon decay with rate κ is indicated with blue thick arrows (low Q 1st harmonic) and red thin arrows (high Q 2nd harmonic). Energy decay of the first excited qubit state with rate γ_1 is indicated with green arrows.

a short photon lifetime of $1/\kappa = 39$ ns that is in turn consistent with the linewidth of the resonator spectrum. The other simulation parameters are again consistent with independent measurements ($1/\gamma_1 = 1 \mu\text{s}$, $1/\gamma_\phi = 420$ ns and $\kappa_\phi = 0$ was chosen to be zero, because the dephasing rate of the 1st harmonic resonator mode is mainly limited by the short photon lifetime). This experiment demonstrates that the multi-Q device works as expected, with drastically different photon lifetimes of the even and odd modes of the resonator, corresponding to $Q_1 = 2\pi\nu_{r,1}/\kappa_1 \approx 1700$ and $Q_2 = 2\pi\nu_{r,2}/\kappa_2 \approx 98000$. The quality factor of the high-Q mode is now by a factor of two lower compared to the sample measured with no qubits, which might be an indication that the qubit fabrication process lowers the quality factor of the resonator.

It is interesting to note that the Rabi oscillations of the blue sideband transition with the low-Q 1st harmonic mode are asymmetric. For long pulse lengths, it can be seen that the qubit excited-state population tends to a steady-state value of $p_{10,ss} \approx 0.95$. This can be explained by considering the different drive and decay channels present in the system, see [Figure 6.6b](#). Since the state $|1_q, 0_p\rangle$ has no

blue sideband transition and $\gamma_1 \ll \kappa_1$, driving the sideband from the ground state $|0_p, 0_q\rangle$ results in a buildup of population in $|1_q, 0_p\rangle$. Taking only energy decay into account, we can write down the rate equations for the four level system

$$\begin{aligned}\frac{dp_{11}}{dt} &= \Omega_{\text{blue}}p_{00} - \Omega_{\text{blue}}p_{11} - (\kappa + \gamma_1)p_{11}, \\ \frac{dp_{10}}{dt} &= \kappa p_{11} - \gamma_1 p_{10}, \\ \frac{dp_{01}}{dt} &= \gamma_1 p_{11} - \kappa p_{01}, \\ \frac{dp_{00}}{dt} &= \Omega_{\text{blue}}p_{11} - \Omega_{\text{blue}}p_{00} + \kappa p_{01} + \gamma_1 p_{10},\end{aligned}$$

where p_{ij} is the population of the state $|i_q, j_p\rangle$. Solving this set of equation for the steady state and the boundary condition that $p_{00} + p_{01} + p_{10} + p_{11} = 1$, we get (in the limit where $\kappa \gg \gamma_1$) $p_{10,ss} = \kappa\Omega_{\text{blue}}/(\kappa\Omega_{\text{blue}} + \gamma_1\kappa + \gamma_1\Omega_{\text{blue}}) = 0.948$, in good agreement with experiment. It is worth noting that an increase in the ratio κ/γ_1 could be used to generate population inversion and to realize a high fidelity excited-state preparation of the qubit by pumping of the blue sideband.

With these coherent sideband Rabi oscillations between the qubit and the high-Q mode, it is now possible to prepare non-classical photon states and to entangle the qubit with a photon. For example, applying a π -pulse with a length of ~ 50 ns on the blue sideband and a subsequent π -pulse on the qubit, creates a single photon in the resonator, the so called one photon Fock state. On the other hand if one applies a $\pi/2$ -pulse of length ~ 25 ns on the blue sideband, the resonator is maximally entangled with the qubit, described by the state $(|0_q, 0_p\rangle + |1_q, 1_p\rangle)/\sqrt{2}$. Adding another qubit, this entanglement can even be swapped onto qubit-qubit entanglement, as described in the next two sections. The speed of these qubit-resonator operations is limited by the maximal drive rate on the blue sideband transition. If it is driven too strongly, off-resonant driving of the direct qubit transition at frequency ω_{01} becomes significant. As can be approximated from spectroscopy shown in [Figure 6.5a](#), the maximal sideband Rabi rate we could use is about $\Omega_{\text{blue}} \approx 12$ MHz at a power of around 6 dBm. Another issue is the large ac-Stark shift during sideband driving, which was about ~ 70 MHz for the sideband experiments shown in [Figure 6.6a](#). Due to the finite rise time of the square pulse used for driving, the sideband transition is at the beginning and the end of the pulse driven off-resonantly, which causes phase and amplitude errors. These errors get more significant as the pulses get shorter. The same problem also

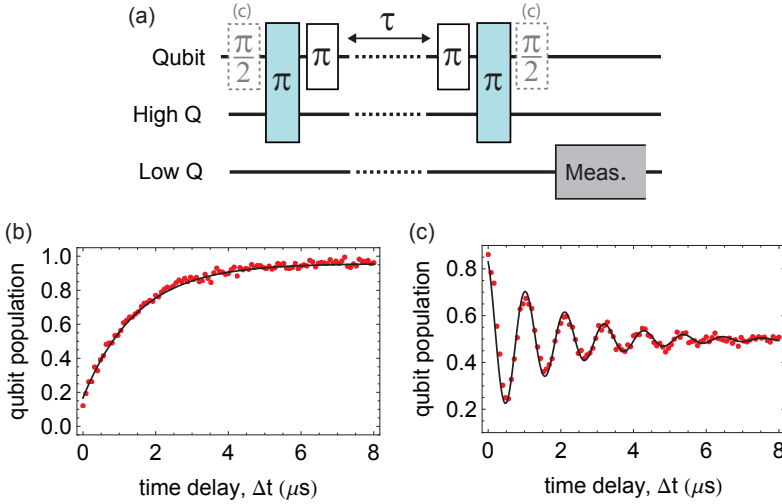


Figure 6.7: a) Pulse sequence used to measure the energy decay and dephasing time of a single photon in the high Q 2nd harmonic resonator mode. b) Results of the photon lifetime $T_1^{K_2} = 1.45 \mu\text{s}$ c) Results of the Ramsey experiment to measure the photon dephasing time $T_2^{*K_2} = 1.9 \mu\text{s}$. Master equation simulations are shown as solid lines.

makes it hard to apply any pulse shapes other than the square pulse, because the drive frequency would have to be changed while varying the amplitude, to stay on resonance. Nevertheless, driving these sideband transitions still allowed us to perform interesting experiments on the preparation of photon Fock states and the entanglement between two qubits, as discussed below.

6.1.4 Fock state preparation

Using a sequence of blue sideband and direct qubit pulses, we now demonstrate a photon storage experiment with the long lifetime mode. The system is first excited to the state $|1_q, 1_p\rangle$ using a blue sideband π -pulse. A direct π -pulse on the qubit returns the qubit to the ground state and leaves the resonator in a single photon Fock state $|0_q, 1_p\rangle$. After a storage time τ , the two pulses are repeated in reverse order. For perfect photon storage the qubit population should return to state $|0\rangle$. However, when the photon is lost the qubit ends up in state $|1\rangle$. The

measured result is shown in **Figure 6.7a**, along with a master equation simulation fitted to the data, with a photon lifetime of $T_1^{\kappa_2} = 1/\kappa_2 = 1.45 \mu\text{s}$, consistent with the fits of the sideband Rabi data to theory (**Figure 6.6a**). This corresponds to a quality factor of $Q_2 = 97\,000$. We also measure the photon dephasing time using a Ramsey type pulse sequence, in which we now carry out the pulse sequence of the storage experiment sandwiched between two $\pi/2$ -pulses on the qubit transition, see **Figure 6.7a** inset. The blue sideband π -pulses are now detuned by $\Delta\omega_d/2\pi \approx 0.46$ MHz from resonance, to result in a Ramsey oscillation frequency of $f_{\text{Ramsey}} = 0.92$ MHz $= 2\Delta\omega_d/2\pi$ due to the two-photon sideband transition. A dephasing time of $T_2^{*\kappa_2} = 1.9 \mu\text{s}$ is found by fitting the data to a master equation simulation, see **Figure 6.7b**. The fact that $T_2^{*\kappa_2} < 2T_1^{\kappa_2}$ indicates the presence of some fluctuation of the resonator frequency, which may be partially accounted for by the dispersive coupling to the qubit, which at the chosen transition frequency has a separately measured dephasing time of $T_2^* = 250$ ns.

The excellent coherence properties of such a long-lived cavity mode could enable its use as a quantum memory, collectively accessible to multiple qubits. Besides the ability to measure the dephasing time of the resonator, this Ramsey type experiment can also be useful to accurately calibrate the frequency of the sideband transition.

The high Q of the 2nd harmonic also allows us to carry out more complex sideband pulse sequences to generate Fock states $|n\rangle$ of the long-lived microwave field, and to observe Rabi oscillations on the blue sideband between the states $|0_q, n-1_p\rangle$ and $|1_q, n_p\rangle$ up to $n = 5$. The state $|0_q, n_p\rangle$ is generated by applying a sideband π -pulse followed by a direct qubit π -pulse which remove the qubit excitation and repeating this n times, see **Figure 6.8b**. It is important to note here, that each additional photon in the high-Q mode shifts the qubit transition frequency by the dispersive shift $2\chi \approx 7.5$ MHz. For each repetition, the frequency of the direct qubit and sideband pulses thus has to be properly adjusted. In **Figure 6.8b** we show the results of sideband Rabi oscillation experiments starting from the experimentally generated Fock states with $n = 1, 2, 3, 4, 5$. A fit to $P_1(t) = A - Be^{-t/\tau} \cos(\Omega_n t)$ yields Rabi frequencies Ω_n that are in very close agreement with the expected \sqrt{n} scaling of the coupling strength, see **Figure 6.8c**, which has also been measured with spectroscopic techniques in a regime where qubit and resonator are in resonance [**Fink08**]. Master equation simulations are also shown in **Figure 6.8c**, agreeing qualitatively with the measured data, but deviating for the longer pulse sequences. This is likely due to build up of errors due to off-resonant driving of other transitions, and will be important to characterize and correct before taking operation complexity further in future experiments of this type.

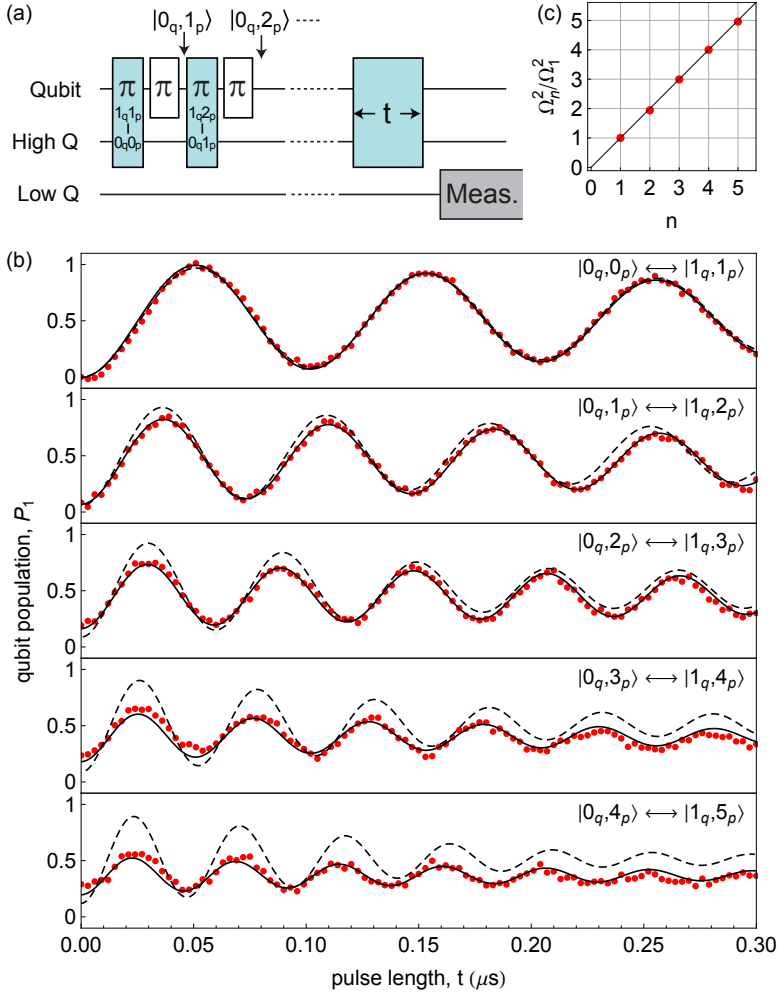


Figure 6.8: a) Pulse sequence for generation of Fock states in the high Q mode, and driving of sideband Rabi oscillations $|0_q, (n - 1)_p\rangle \leftrightarrow |1_q, n_p\rangle$. b) Measurement of the sequence depicted in a), for $n=1, 2, 3, 4, 5$ (red dots). Fits to a cosine with an exponential decay envelope are shown as solid lines, while master equation simulations are shown as dashed lines. c) Plot of the squared normalized sideband Rabi frequencies extracted from the fits shown in b). Expected linear dependence on the number of photons n in the high Q mode is shown as a black solid line.

6.1.5 Bell-state preparation

After demonstrating the coherent control between single photons and one qubit, we show the realization of a two-qubit operation based on blue sideband transitions between two qubits (labeled as qubit A and qubit B) coupled to the same high-Q mode. For this experiment, the qubits have been biased at frequencies $\omega_{01}^A = 9.2$ GHz and $\omega_{01}^B = 8.11$ GHz, respectively. This large frequency separation between the qubits was chosen to keep the residual dispersive qubit-qubit coupling, mediated by virtual excitations of the resonator, negligibly small, and to reduce the cross-talk of the direct qubit and sideband drives of one qubit onto the other qubit, because they have different transition frequency. Additional isolation of about ~ 20 dB in power between the drives of different qubits has been reached by applying the drives through the individual gate lines of the qubits. The pulse sequence used to generate two-qubit entangled Bell states, shown in [Figure 6.9a](#), is similar to that implemented in trapped ions [[Roos04](#)]. First, the system is prepared in its ground state $|0_A, 0_B, 0_p\rangle$ and a resonant π -pulse is applied to qubit B, generating the state $|0_A, 1_B, 0_p\rangle$. A $\pi/2$ -pulse on the blue sideband of qubit A then generates a state $|0_A, 1_B, 0_p\rangle + e^{i\phi'}|1_A, 1_B, 1_p\rangle$ that contains entanglement between qubit A and a photon in the high-Q mode. This qubit-resonator entanglement is then transferred to qubit-qubit entanglement with a π -pulse on the blue sideband of qubit B, generating a Bell state between both qubits $|\Psi\rangle = |0_A, 1_B\rangle + e^{i\phi}|1_A, 0_B\rangle$ and returning the high-Q resonator mode to its unentangled ground state $|0_p\rangle$. The phase ϕ of the state is adjusted with the phase difference between the two blue sideband pulses in the sequence. An additional single-qubit π -pulse may now be applied to qubit A to generate the Bell state $|\Phi\rangle = |0_A, 0_B\rangle + e^{-i\phi}|1_A, 1_B\rangle$. The length of the full pulse sequence is 110 ns, with the entanglement generating sideband pulses and the single qubit operations lasting ~ 85 ns and 10 ns, respectively.

As an example, we have prepared and fully reconstructed the resulting density matrix $\hat{\rho}$ for the two Bell states $|\Phi_+\rangle = (|0_A, 0_B\rangle + |1_A, 1_B\rangle)/\sqrt{2}$ and $|\Psi_+\rangle = (|0_A, 1_B\rangle + |1_A, 0_B\rangle)/\sqrt{2}$ with quantum state tomography and a maximum likelihood method, see [Figure 6.9b,c](#). The fidelities $F = \langle\psi|\hat{\rho}|\psi\rangle$ with respect to the theoretically ideal states $|\psi\rangle = |\Phi_+\rangle$ and $|\Psi_+\rangle$ are $F = 0.74$ and $F = 0.75$, respectively. By comparing the measured density matrices with the expected density matrices resulting from master equation simulations, we conclude that fidelities are mainly limited by the decoherence of qubit and resonator. The calculated concurrences [[Wootters98](#)] for our measured states $C = 0.51$ and 0.52, which quantifies the amount of entanglement present in a two-qubit state, proves that those

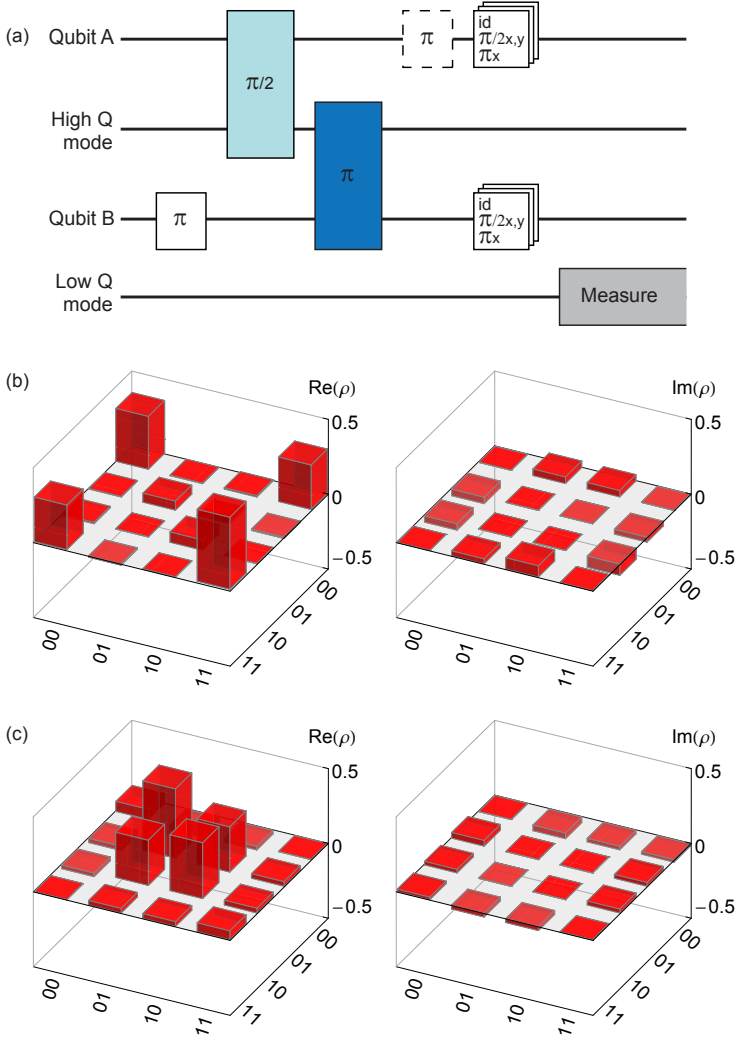


Figure 6.9: a) Pulse sequence to generate and characterize Bell states. Direct resonant qubit pulses are shown in white, while blue sideband pulses between the resonator and qubits A and B are shown in light and dark blue, respectively. [b) and c)] Real and imaginary parts of the two-qubit density matrix of the Bell states $|\Phi_+\rangle$ and $|\Psi_+\rangle$ generated according to the sequence shown in a). The fidelities with respect to the ideal states are $F = 0.74$ and $F = 0.75$.

two-qubit states contain two-qubit entanglement. Another commonly used measure is the entanglement of formation [Bennett96], which can readily be calculated from the concurrence for two qubits [Wootters98] and yields 0.37 for both states. See also Appendix A.4 for a discussion about the concurrence and entanglement of formation measures.

6.1.6 Conclusion

In this section we have demonstrated coherent operations between qubits and single resonator photons using sideband transitions. This allowed us to prepare highly entangled two-qubit Bell states and up to five photon Fock states. As demonstrated with trapped ions [Cirac95, Monroe95, Childs00, Schmidt-Kaler03], it is possible to implement controlled-NOT operations between two qubits using such sideband transitions, either by applying a sequence of sideband pulses with different phase and length, or by carrying out a 2π rotation on a sideband transition involving an auxiliary qubit state outside the computational basis. However, the time required for such a gate operation in our circuit QED architecture would be too long to achieve high fidelity gates. The maximal Rabi frequency of 10 MHz on the blue sideband transition is limited by off-resonant qubit driving, even though the sideband drive is more than 500 MHz detuned from the qubit transition frequency. We have thus decided to use another approach to realize controlled-NOT operations using fast magnetic flux pulses [Strauch03, DiCarlo09], as described in the next section.

6.2 Qubit-qubit interactions controlled with fast magnetic flux pulses

In the previous section I have described how to perform two-qubit operations using sideband transitions. There, the interaction between the two qubits is mediated by a photon created in the resonator. However, it is also possible to couple two qubits by exchanging their excitations via a virtual photon [Majer07, Filipp11a]. Such an exchange occurs when two qubits are dispersively coupled to the same resonator and tuned into resonance with each other. This coupling is sometimes also called the J-coupling and is of the form $(\hat{\sigma}_- \otimes \hat{\sigma}_+ + h.c.)$. Using fast magnetic flux pulses, it can be turned on and off on nanosecond timescale by tuning one of the qubits in and out of resonance with another qubit and is thus useful for fast two-qubit operations [Strauch03, DiCarlo09, Bialczak10, Yamamoto10].

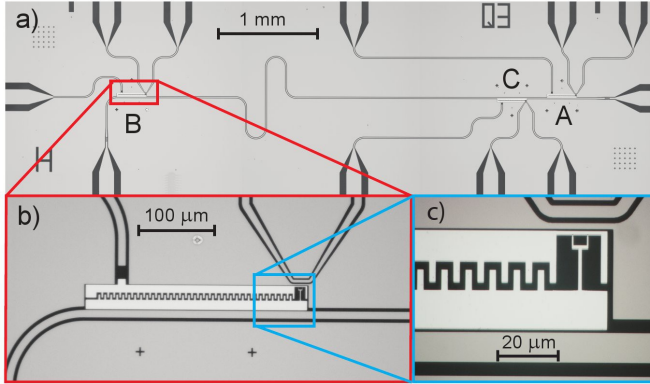


Figure 6.10: Optical microscope image of the sample with three qubits coupled to a coplanar waveguide resonator with individual local microwave and magnetic flux-bias lines for each qubit.

In this section, I describe our three-qubit sample fabricated to investigate this J-coupling, see [Section 6.2.1](#). I then describe in [Section 6.2.2](#) how the J-coupling is derived by transforming the generalized Jaynes-Cummings Hamiltonian including three transmon qubits into the dispersive limit and how these couplings are observed in experiment. [Section 6.2.3](#) explains how we realize the universal two-qubit controlled-PHASE and controlled-NOT gates [[DiCarlo09](#), [Yamamoto10](#)]. We then employ these gates to generate two-qubit entanglement ([Section 6.2.4](#)) and to demonstrate the two-qubit Deutsch-Jozsa algorithm [[Deutsch92](#), [DiCarlo09](#), [Yamamoto10](#)] ([Section 6.2.5](#))

6.2.1 The sample

The following experiments are carried out with the three-qubit sample shown in [Figure 6.10](#), similar to the sample used in [[DiCarlo09](#)]. The qubits are referred to as qubit A, B and C. They are dispersively coupled to a single microwave transmission line resonator with a bare resonance frequency of $\omega_r/2\pi = 8.625$ GHz and a quality factor of $Q = 3300$. Besides acting as a measurement device to perform a joint readout [[Wallraff05](#), [Filipp09](#)], the resonator acts as a coupling bus between all three qubits [[Majer07](#)], as described in [Section 6.2.2](#). All qubits are equipped with individual drive lines for single qubit manipulations and magnetic flux lines for two-qubit and single qubit PHASE gates. For optimal coherence, we have designed the

qubits to have maximal transition frequencies smaller than ω_r , because we consistently measured smaller energy decay times T_1 above the fundamental mode of the resonator on different samples. From spectroscopy measurements we have extracted maximum transition frequencies $\omega_{01}^{\max}/2\pi = \{6.714, 6.050, 4.999\}$ GHz, charging energies $E_c/h = \{0.264, 0.296, 0.307\}$ GHz and coupling strengths to the resonator of $g_{01}/2\pi = \{0.360, 0.30, 0.34\}$ GHz for qubits A,B,C. To maximize coherence, we biased each qubit at the flux sweet spot [Vion02, Vion03] for time resolved measurements, where we found energy relaxation times $T_1 = \{0.55, 0.70, 1.10\}$ μ s and phase coherence times $T_2^* = \{0.45, 0.60, 0.6\}$ μ s.

Since all qubits have maximal transition frequencies below the resonator, it is not possible to extract g_{01} from a Vacuum Rabi mode splitting. Instead, we have spectroscopically measured the resonator frequency and the transition frequencies of all qubits while tuning the frequency of one qubit over a large range and keeping the frequency of the other two constant.¹ As an example, such a measurement is shown in Figure 6.11a when qubit A is tuned in frequency and the spectroscopy drive is applied to the input of the resonator to detect all three qubits at the same time. Since the frequency of qubit B and C is constant, we have only extracted the frequencies of qubit A (see Figure 6.11c) and the resonator (see Figure 6.11c), and fitted the data (solid lines) to the eigenenergies of the full Jaynes-Cumming Hamiltonian describing the three-qubit system

$$\hat{H}/\hbar = \sum_{q=A,B,C} \sum_{i=1}^{N-1} \omega_i^q |i\rangle\langle i|_q + \omega_r \hat{a}^\dagger \hat{a} + \sum_{q=A,B,C} \sum_{i=0}^{N-2} \sqrt{i+1} g_{01}^q (\hat{a}^\dagger |i\rangle\langle i+1|_q + h.c.), \quad (6.13)$$

where the qubit frequency dependence with magnetic flux $\omega_i(\phi)$ is determined with the exact Mathieu equations. The fit parameters were $g_{01}^A, E_J^{A,\max}, \omega_r$, the flux periodicity and a small offset of the flux. As can be seen in the figure, the fit is in very good agreement with the data.

¹The individual qubit frequency tuning is achieved by applying magnetic fields with three external current biased coils attached on the sample holder underneath the qubits, see Figure 4.2a. The required currents are determined by first measuring the mutual inductances between each coil and all three qubits, and then solving a set of linear equations.

²This data set was taken on the same sample as generally discussed here, but for an earlier cool down. Qubit A thus has a slightly higher maximal transition frequency of 7.184 GHz.

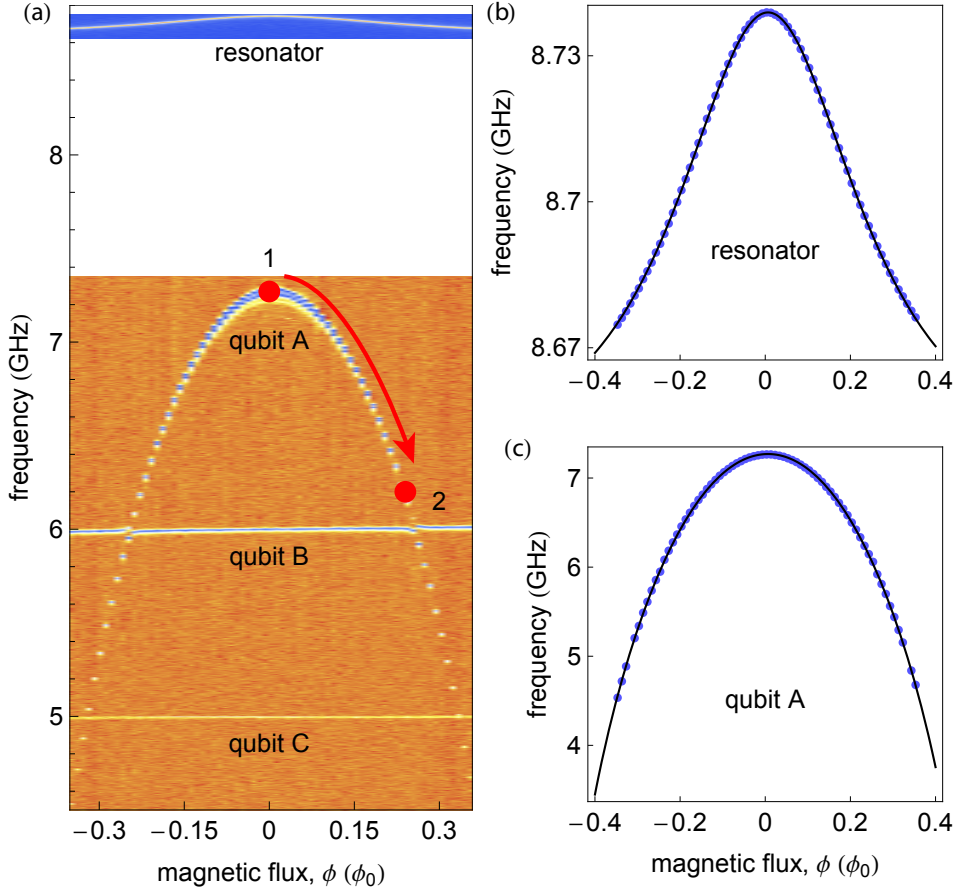


Figure 6.11: a) Simultaneous spectroscopy of all three qubits and the resonator, when qubit A is tuned over a larger range of frequencies by applying a magnetic flux to the SQUID-loop of qubit A. b) and c) show the extracted frequencies of the resonator and qubit A (blue dots) for the different values for the magnetic flux. The data is fitted to the generalized Jaynes-Cummings Hamiltonian (6.13), to extract the coupling strength g_{01}^A of qubit A to the resonator.²

6.2.2 The dispersive J-coupling

We transform the Hamiltonian (6.13) into the dispersive regime by performing the transformation $e^{\hat{S}} \hat{H} e^{-\hat{S}}$ which eliminates the direct interaction between the resonator and the transmon qubits using the generator

$$\hat{S} = \sum_{q=A,B,C} \sum_{i=0}^{N-1} \frac{g_{i,i+1}^q}{\Delta_i^q} (\hat{a}|i+1\rangle\langle i|_q - h.c.). \quad (6.14)$$

Keeping only the terms up to order $g_{i,i+1}^2/\Delta_i^2$ and neglecting the two photon transitions yields in the dispersive Hamiltonian (see also Section 3.2.2 for the single transmon case)

$$\begin{aligned} \hat{H}_{\text{disp}}/\hbar = & \left(\omega_r + \sum_{q=A,B,C} \left(-\chi_0^q |0\rangle\langle 0|_q + \sum_{i=1}^{N-1} (\chi_{i-1}^q - \chi_i^q) |i\rangle\langle i|_q \right) \right) \hat{a}^\dagger \hat{a} \\ & + \sum_{q=A,B,C} \sum_{i=0}^{N-1} \left(\omega_i^q |i\rangle\langle i|_q + \chi_i^q |i+1\rangle\langle i+1|_q \right) \\ & + \frac{1}{2} \sum_{q \neq q'} \sum_{i,i'=0}^{N-1} J_{ii'}^{qq'} \left(|i\rangle\langle i+1|_q |i'+1\rangle\langle i'|_{q'} + |i+1\rangle\langle i|_q |i'\rangle\langle i'+1|_{q'} \right). \end{aligned} \quad (6.15)$$

In addition to the dispersively shifted resonator and transmon qubit energy terms (first two lines), the third describes the coupling between each pair of transmon qubits via a virtual photon state in the resonator. When a transition connecting neighboring transmon levels of one qubit ($|i\rangle_q \leftrightarrow |i+1\rangle_q$) is on resonance with a transition of another qubit ($|i'\rangle_{q'} \leftrightarrow |i'+1\rangle_{q'}$), one single excitation is exchanged by the transverse interaction Hamiltonian at a rate determined by the J-coupling

$$J_{ii'}^{qq'} = g_{i,i+1}^q g_{i',i'+1}^{q'} \frac{\Delta_i^q + \Delta_{i'}^{q'}}{2\Delta_i^q \Delta_{i'}^{q'}}. \quad (6.16)$$

When the two transitions are detuned from each other, with a detuning much larger than the J-coupling $|\omega_{i,i+1} - \omega_{i',i'+1}| \gg J_{ii'}$, the coupling term is energy non-conserving and can be transformed away with a rotating wave approximation. We can thus turn the coupling on and off, by moving the transition frequencies

in and out of resonance. While the coupling J_{00} only couples states within the computational subspace, all other $J_{ii'}$ involve coupling to non-computational states and are thus interesting for the implementation of controlled-PHASE operations between two qubits.

For the experiments shown in this thesis, only the first three transmon levels are relevant. We can then approximate the Hamiltonian (6.15) to get the simpler form

$$\hat{H}/\hbar = \omega_{01}^A |1\rangle\langle 1|_A + \omega_{12}^A |2\rangle\langle 2| + \omega_{01}^B |1\rangle\langle 1|_B + \omega_{12}^B |2\rangle\langle 2| + J_{00}^{AB} \left[(|0\rangle\langle 1|_A + \sqrt{2}|1\rangle\langle 2|_A) \otimes (|1\rangle\langle 0|_B + \sqrt{2}|2\rangle\langle 1|_B) + h.c. \right]. \quad (6.17)$$

Here we have only considered two qubits, and we have removed the energy term of the resonator because we are only interested in the cases where the resonator always stays in the ground state. Additionally we assume that $J_{10}, J_{01} \approx \sqrt{2}J_{00}$ and $J_{11} \approx 2J_{00}$, only valid for detunings much larger than the qubit anharmonicities $\Delta_0 \gg \alpha$. With ω_{01} and ω_{12} , we now refer to the dispersively shifted frequencies.

The $|01\rangle \leftrightarrow |10\rangle$ coupling

First we discuss how we characterize the coupling strength J_{00} between each pair of qubits in our sample. For this purpose we spectroscopically monitor their transition frequencies when tuning one of the qubits through resonance of the other, see Figure 6.12a. The coupling term proportional to $(|0\rangle\langle 1|_A |1\rangle\langle 0|_B + h.c.)$ then manifests itself in an avoided level crossing with a minimal size of the splitting of $2J_{00}$ when the qubits are on resonance. From this measurement we can extract the coupling strength by fitting the data to the eigenenergies of the Hamiltonian (6.17) which yields $J_{00}^{AB} = 2\pi \cdot 25$ MHz at 6 GHz. We have repeated this experiment with the other two qubits to determine their coupling, which gives $J_{00}^{BC} = 2\pi \cdot 15$ MHz at 4.935 GHz and $J_{00}^{AC} = 2\pi \cdot 3$ MHz at 4.999 GHz. In addition to the avoided crossing, the formation of a dark state can be observed by the disappearance of the spectroscopic line for the upper state near resonance. This dark state can be attributed to the symmetry of the states with respect to the drive applied to the resonator [Majer07, Filipp11a]. On resonance the eigenstates of the system can be approximated by the symmetric triplet states $|00\rangle, |11\rangle, |\psi_+\rangle = (|01\rangle + |10\rangle)/\sqrt{2}$ as well as the antisymmetric singlet state $|\psi_-\rangle = (|01\rangle - |10\rangle)/\sqrt{2}$, where $|\psi_+\rangle$ is the one with the higher frequency. This state can not be excited as the drive applied to the resonator $\propto (\hat{\sigma}_x^A - \hat{\sigma}_x^B)$ is antisymmetric under qubit permutation, while ψ_+ is symmetric. Moreover, this state does also not couple to the resonator, which

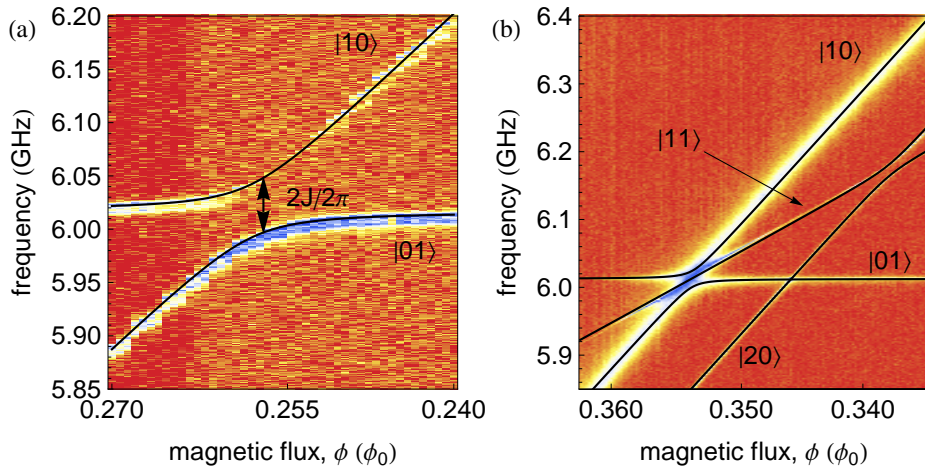


Figure 6.12: a) Pulsed spectroscopy measurement of the avoided crossing when qubit A is tuned through resonance with qubit B. The minimal splitting is given by $2J_{00}$. With this interaction it is possible to realize an *iswap* gate. b) High power pulsed spectroscopy of qubit A when it is tuned through resonance with qubit B. The 01 -transition of qubit A $|10\rangle$ is power broadened due to the strong drive applied to the local gate line, and the line $|20\rangle$ corresponds to a two-photon process from the ground state to $|20\rangle$. This line shows an avoided crossing of size $2J_{10}$ with the state $|11\rangle$, when $\omega_{01}^A - \alpha^A = \omega_{01}^B$, and is used to implement a controlled-PHASE gate. The data set b) is taken on a different sample than generally discussed in this section and J_{00} can thus not be directly compared with J_{10} .

protects it against the Purcell decay through the resonator [Filipp11b].

In the context of quantum computation, this J_{00} -coupling can be used to generate an *iswap* gate as shown with capacitively coupled phase and transmon qubits [Bialczak10, Dewes12]. There one uses the fact, that when the two qubits are prepared in either of the states $|10\rangle$ or $|01\rangle$ and then tuned in resonance, the system starts to oscillate between these two states at a rate $2J_{00}$. Waiting a time $t = \pi/2J_{00}$, the states are swapped such that $|10\rangle \rightarrow i|01\rangle$ and $|01\rangle \rightarrow i|10\rangle$, while the other computational states $|00\rangle$ and $|11\rangle$ remain unchanged, and thus implements an *iswap* gate. Eventhough this gate is universal, it requires two *iswap* gates and 5 single qubit operations to generate the *cnot* gate, often used in quantum algorithms. However, by using the coupling terms that couple a computational basis state with a state outside the computational subspace, it is possible to construct a *cnot* gate more directly.

The $|11\rangle \leftrightarrow |20\rangle$ coupling

As can be seen in Equation (6.15), the dispersive interaction through the resonator also couples the computational state $|11\rangle$ to a state outside the computational basis $|02\rangle$ by the term $J_{10}^{AB}(|2\rangle\langle 1|_A|0\rangle\langle 1|_B + \text{h.c.})$. In order to determine J_{01}^{AB} we perform a high power spectroscopy when qubit A is tuned through resonance with qubit B, see Figure 6.12b (Note that this measurement data was not available for the sample generally discussed in this section. The figure thus shows data taken on another sample and has not the same coupling parameters). The drive is applied to the local gate line of qubit A. Nevertheless, the spectral line of qubit B ($|01\rangle$) at the frequency $\omega_{01}^B \approx 6.01$ GHz is still just visible due to the cross-talk of the drive to qubit B³. In addition to the power broadened spectral line of qubit A ($|10\rangle$), a sharper line appears at a lower frequency corresponding to the two-photon transition from the ground state to $|20\rangle$. The frequency separation between the two lines is given by half the anharmonicity of qubit A. Besides the avoided-level crossing between $|10\rangle$ and $|01\rangle$, we can now see another anticrossing of the two-photon line at 6.18 GHz, where the state $|11\rangle$ is resonant with $|20\rangle$. The fit of the data (black solid lines) to the eigenenergies of the Hamiltonian (6.17) shows good agreement to theory and shows that this coupling is by a factor of $\sqrt{2}$ stronger than J_{00} . Using time resolved measurements performed on the sample shown in Figure 6.10, we extracted $J_{10}^{AB} = 2\pi \cdot 36$ MHz $\approx \sqrt{2}J_{00}^{AB}$ and $J_{10}^{BC} = 2\pi \cdot 22$ MHz $\approx \sqrt{2}J_{00}^{BC}$.

³Usually a drive applied to a local gate line is isolated from the other qubits by about 20 dB in power

Between qubit A and C, no coupling could be observed, most likely due to the direct capacitive coupling which destructively interferes with the coupling via the resonator. In the next section, we describe how this coupling is used to construct a CNOT and controlled-PHASE gate.

6.2.3 Controlled-PHASE and controlled-NOT gate

As has been theoretically proposed for directly coupled phase qubits by Strauch *et al.* [Strauch03], the coupling between the states $|11\rangle$ and $|02\rangle$ can be used to construct a controlled-PHASE gate. Later it has first been experimentally implemented at Yale by Leonardo DiCarlo *et al.* [DiCarlo09] with transmon qubits to demonstrate first quantum algorithms and three-qubit entanglement [DiCarlo10]. It has then also been realized with phase qubits [Yamamoto10]. In this thesis, we use this coupling for controlled-PHASE and CNOT gates and finally to demonstrate the realization of a three-qubit Toffoli gate.

In order to demonstrate a controlled-PHASE operation, we bias the two qubits, e.g. qubit A and B, to their flux sweet spot at $\omega_{01}^{\max,A} = 6.714$ GHz and $\omega_{01}^{\max,B} = 6.050$ GHz, where the two qubits are well decoupled from both avoided crossings discussed above. We then apply a short magnetic flux pulse to qubit A which shifts the frequency of qubit A close to the one of qubit B (from position 1 to position 2 illustrated in Figure 6.11). For fast enough rise-times of the flux pulse, this shifts the state $|11\rangle$ nonadiabatically⁴ into resonance with $|20\rangle$. The system then starts to oscillate between the two states with a time evolution given by $|\psi(t)\rangle = \cos(2J_{10}t)|11\rangle + i \sin(2J_{10}t)|20\rangle$. Waiting for a time $t = 2\pi/2J_{10}$, the system returns to the initial state with an additional phase factor -1 . When starting with the other basis states $|00\rangle$, $|10\rangle$ and $|01\rangle$, no phase is accumulated because those states are off-resonant from the avoided crossings. In addition to this conditional phase on $|11\rangle$, qubit A picks up a dynamic phase $\phi_A = \int (\omega_{01}^{\max,A} - \omega_{01}^A(t))dt$ during the frequency excursion away from the steady state frequency during the time of the flux pulse. In the presence of flux crosstalk⁵ to the other qubit, also qubit B may pick up some dynamic phase ϕ_B . This procedure then produces the unitary

⁴It is also possible to carry out the gate with adiabatic flux pulses, and was in fact used for the first realization [DiCarlo09]

⁵On this three-qubit sample this crosstalk is below 1%. Additionally, since all qubits are biased at their flux sweet spot, no crosstalk is observed during the controlled-PHASE gate operation.

operation

$$\hat{U}_{cZ_{ij}} = \begin{pmatrix} 1 & 0 & 0 & 0 \\ 0 & e^{i\phi_A} & 0 & 0 \\ 0 & 0 & e^{i\phi_B} & 0 \\ 0 & 0 & 0 & -e^{i(\phi_A+\phi_B)} \end{pmatrix}. \quad (6.18)$$

Adding single qubit PHASE gate operations before or after the flux pulse, we can compensate for these dynamic phases such that $\phi_{A,B} \bmod 2\pi = 0$. This implements the controlled-PHASE gate $\hat{U}_{cZ_{11}}$ which adds a -1 to the state $|11\rangle$. In general, we can also create the other controlled-PHASE gates $\hat{U}_{cZ_{ij}}$ which add the -1 to the state $|ij\rangle$, by tuning the phases $\phi_{A,B} \bmod 2\pi$ to either 0 or π . The CNOT gate can then be constructed by the combination of $\hat{U}_{cZ_{11}}$ and single qubit rotations

$$\hat{U}_{\text{CNOT}} = \hat{I} \otimes \hat{R}_y^{\pi/2} \hat{U}_{cZ_{11}} \hat{I} \otimes \hat{R}_y^{-\pi/2} = \begin{pmatrix} 1 & 0 & 0 & 0 \\ 0 & 1 & 0 & 0 \\ 0 & 0 & 0 & 1 \\ 0 & 0 & 1 & 0 \end{pmatrix}. \quad (6.19)$$

Calibration of the CPHASE gate

In order to calibrate the precise amplitude and length of the flux pulse required for the controlled-PHASE gate, we carry out a time resolved measurement of the coherent oscillations between $|11\rangle$ and $|20\rangle$. The pulse scheme is shown in [Figure 6.13a](#). We first prepare the state $|11\rangle$ with a π -pulse on each qubit and then apply a flux pulse with an amplitude ΔA and length l . The short 5 ns long step with amplitude ΔB in the flux pulse is used to minimize errors due to the overshoot at the beginning of the flux pulse (see also [Section 4.4.3](#)), and simultaneously serves as a single qubit PHASE gate to eliminate the dynamical phase ϕ_A . Because single qubit PHASE gates commute with $\hat{U}_{cZ_{ij}}$, we can apply the PHASE gate before $\hat{U}_{cZ_{ij}}$. Since the measurement contrast is low between the states $|11\rangle$ and $|20\rangle$, we apply again a π -pulse on each qubit at the end of the sequence before measurement, such that the system oscillates between state $|00\rangle$ and $|20\rangle$ which maximizes the measurement contrast. [Figure 6.13b](#) shows the measurement response as a function of ΔA and l , while $\Delta B = -0.5$ is set to a constant value. Minimal oscillation frequency occurs when the two states $|11\rangle$ and $|20\rangle$ are in resonance at $\Delta A_0 = -0.865$. The asymmetry in the picture, i.e. higher visibility when qubit A is shifted across the transition frequency of qubit B and almost vanishing visibility when shifted only close but not across resonance, can be explained by the finite rise time of the flux pulse of

about 1 – 2 ns. This has been confirmed with numerical simulations. From a single trace for amplitude ΔA_0 (Figure 6.13c) we extract the oscillation period $l_0 = 14$ ns, which corresponds to a J-coupling of $J_{10}/2\pi = 1/2l_0 = 35.7$ MHz. This is in good agreement with the value of $J_{00} \approx J_{10}/\sqrt{2}$ we extracted from the independent spectroscopic measurements shown in Figure 6.12a.

In order to check if the state $|11\rangle$ really acquires a -1 after one full oscillation period, we perform a Ramsey type experiment which measures the phase of qubit A conditional on the state of qubit B. Here, we replace the π -pulses of qubit A with $\pi/2$ -pulses, where the second pulse has a phase difference of $\Delta\phi$ with respect to the first. We then measure the resonator response as a function of $\Delta\phi$ for the two cases where qubit B is prepared in state $|1\rangle$ (red dots) or in state $|0\rangle$ (blue dots) before the flux pulse, see Figure 6.13d. The two curves show a sinusoidal dependence on $\Delta\phi$, but shifted by a phase π from each other, confirming the conditional PHASE operation of the cZ_{11} -gate. The overall phase shift of both curves $\Delta\phi_0 = \phi_A$ is equal to the dynamical phase acquired during the whole flux pulse and can be compensated by changing the phase (the rotation axis) of all subsequent microwave pulses to $\phi = \Delta\phi_0$. For the case that the pulse sequence does not involve subsequent microwave pulses, the dynamic phase can be compensated with the short single qubit PHASE gate. The amplitude ΔB is calibrated in a similar way, by fixing $\Delta\phi$ of the $\pi/2$ -pulses and measuring the qubit populations as a function of ΔB and the dynamical phase is then compensated by choosing ΔB for which $\phi_A = 0$. Repeating the same experiment on qubit B, the dynamic phase of qubit B accumulated during the flux pulses on qubit A is determined. Due to the small cross talk of the flux pulse, no compensation is required in our experiment.

Gate fidelity

We quantify the fidelity of the gate with quantum process tomography (for details see Section 5.5.2 and Appendix A.2.2) which determines the χ matrix and fully characterizes the quantum process $\mathcal{E}(\hat{\rho}) = \sum_{mn} \hat{E}_m \hat{\rho} \hat{E}_n^\dagger \chi_{mn}$. Here the matrix χ_{mn} is represented in the operator basis \hat{E}_m given by the tensor product of the Pauli operators $\{\hat{I}, \hat{X}, \hat{Y}, \hat{Z}\}^{\otimes 2} = \{\hat{I}, \hat{\sigma}_x, -i\hat{\sigma}_y, \hat{\sigma}_z\}^{\otimes 2}$. To find this χ matrix, we first prepare a full set of two-qubit basis input states $\{\hat{\rho}_i\} = \{|0\rangle\langle 0|, |1\rangle\langle 1|, |-\rangle\langle -|, |+\rangle\langle +|\}^{\otimes 2}$ with $|-\rangle = (|0\rangle - i|1\rangle)/\sqrt{2}$ and $|+\rangle = (|0\rangle + |1\rangle)/\sqrt{2}$. We then determine the density matrix of each output state $\mathcal{E}(\hat{\rho}_i)$ when applying the controlled-PHASE gate $\hat{U}_{cZ_{11}}$ to each input state $\hat{\rho}_i$. The χ matrix is reconstructed by solving a linear set of equations determined from the 16 measured density matrices. Due to noise in the

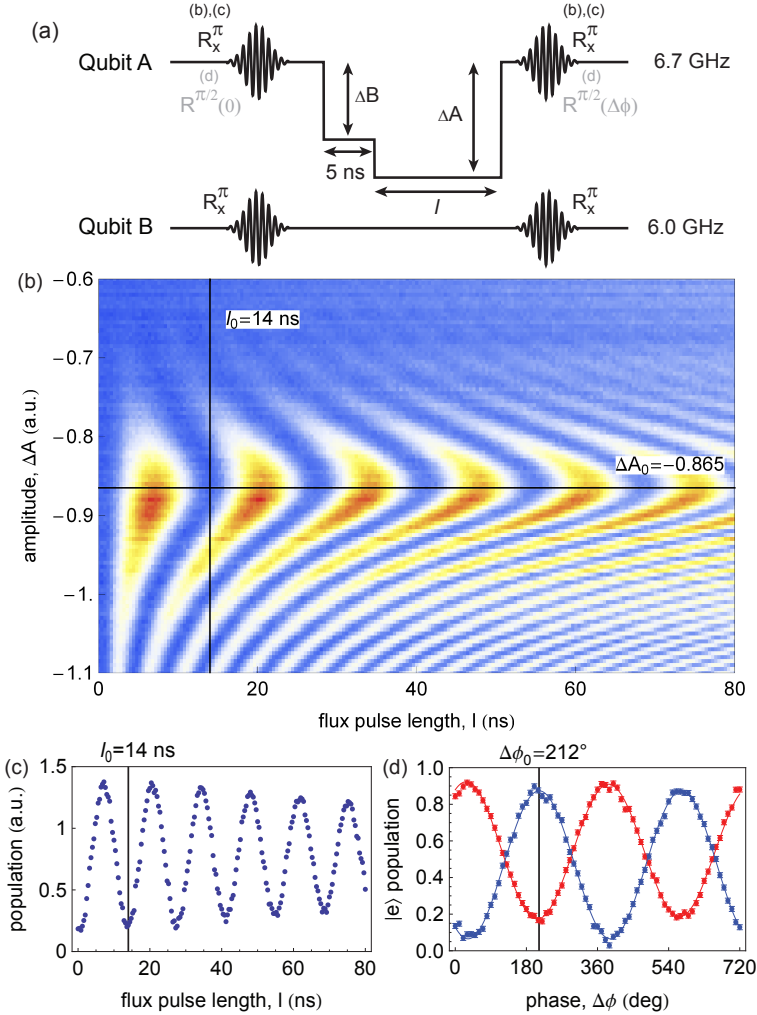


Figure 6.13: a) Pulse scheme to measure the coherent oscillations between states $|11\rangle$ and $|20\rangle$. b) Measured oscillations, with the grid lines indicating the optimal values of the flux pulse length l_0 and amplitude ΔA_0 for the operation of a controlled-PHASE gate. c) A single oscillation trace at the optimal value ΔA_0 used to determine the length l_0 . d) Ramsey type experiment indicated in a) for qubit B prepared in $|0\rangle$ (blue dots) or $|1\rangle$ (red dots) before the flux pulse, indicating the conditional operation of the controlled-PHASE gate. Solid lines are fits to a sinusoidal function to determine the dynamic phase acquired during the controlled-PHASE gate.

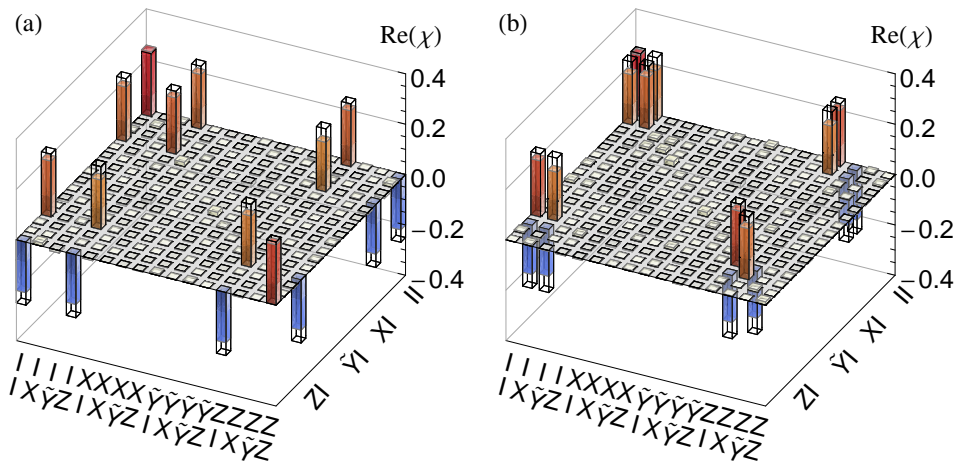


Figure 6.14: Real parts of the measured χ matrices for a) the controlled-PHASE gate $\hat{U}_{cZ_{11}}$ with process fidelity $F_P^{cZ_{11}} = 0.85$ and b) the cNOT gate with $F_P^{\text{CNOT}} = 0.80$.

measurement, this matrix might not describe a physical process, i.e. a completely positive and trace preserving map. We thus apply a maximum likelihood algorithm to find the physically meaningful matrix χ^{ML} which is closest to the measured one [Ježek03], as summarized in Appendix A.2.3. The real part of χ^{ML} is shown in Figure 6.14 for the controlled-PHASE gate $\hat{U}_{cZ_{11}}$ (a) and the controlled-NOT gate (b), and is in very good agreement with the ideal processes χ_t indicated with wireframes. The process fidelity of the gates can be quantified with

$$F_P = \text{Tr}(\chi_m \cdot \chi_t), \quad (6.20)$$

where χ_m is the measured χ matrix. We get a gate fidelity of $F_P^{cZ_{11}} = 0.85$ for $\hat{U}_{cZ_{11}}$ and $F_P^{\text{CNOT}} = 0.80$ for the controlled-NOT operation, mostly limited by decoherence of the qubits. We note here, that for the reconstruction of the χ matrix, we assumed perfect input state preparation and perfect tomography pulses, which is a reasonable approximation since our single qubit operations reach fidelities > 0.97 . However, it still leads to an underestimation of the actual process fidelity, because the errors in the tomography and state preparation pulses is transformed into a gate error. Nevertheless, it is possible to separate the fidelities of the different parts involved by measuring process tomography of many repetitions of the same quantum process.

6.2.4 Generation of Bell-states

With the controlled-NOT operation, we can now prepare all four maximally entangle two-qubit Bell states between qubit A and B, $|\Phi_{\pm}\rangle = (|01\rangle \pm |10\rangle)/\sqrt{2}$ and $|\Psi_{\pm}\rangle = (|00\rangle \pm |11\rangle)/\sqrt{2}$, by applying the unitary operations

$$\begin{aligned}\hat{U}_{\Phi_{\pm}} &= (\hat{R}_y^{\pi} \otimes \hat{I}) \cdot \hat{U}_{\text{CNOT}} \cdot (\hat{R}_y^{\mp\pi/2} \otimes \hat{I}) \\ \hat{U}_{\Psi_{\pm}} &= \hat{U}_{\text{CNOT}} \cdot (\hat{R}_y^{\pm\pi/2} \otimes \hat{I})\end{aligned}\quad (6.21)$$

to the ground state $|00\rangle$. In contrast to the Bell states generated with sideband transitions, this sequence is much faster. While with sidebands it takes about 110 ns, it now takes about 40 ns where 2×8 ns used for single qubit operations, 20 ns for the controlled-PHASE gate and 2×3 ns for pulse separation. Consequently we also reach higher fidelities of $F = 0.91$ and $F = 0.87$ for $|\Phi_{+}\rangle$ and $|\Psi_{+}\rangle$, respectively.

6.2.5 Deutsch-Jozsa algorithm

With a universal two-qubit gate and the ability to perform arbitrary operations on the full single qubit Bloch sphere, we can implement a quantum algorithm. The simplest quantum algorithm with two qubits is the Deutsch-Jozsa algorithm, which solves the following problem. Assume we are given a black box which evaluates a function $f(x) : \{0, 1\}^n \rightarrow \{0, 1\}$ which takes an n bit state x as input and gives 0 or 1 as output. We are assured, that this function is either *constant* for all values of x or *balanced*, that is, equal to 1 for exactly half of all possible values of x , and 0 for the other half. How many times do we have to call this function, in order to find out for sure if it is constant or balanced? In the classical case, we need at least $2^n/2 + 1$ queries, since we need to check the outputs of one more than half the set of input states. In the quantum mechanical case, we only need one query by exploiting quantum parallelism and quantum interference. This algorithm was first demonstrated with transmon qubits [DiCarlo09], and later also with phase qubits [Yamamoto10].

The steps involved in the algorithm for a one bit input state are shown in [Figure 6.16](#). The black box that implements the function $f(x)$ is a unitary two-qubit operation U_f , often called the oracle. It takes the state $|x, y\rangle$ as an input, where x is the input bit of the function $f(x)$ encoded in the data qubit A and y the state of an ancilla/answer qubit B, and outputs the two-qubit state $|x, y \oplus f(x)\rangle$. Note here

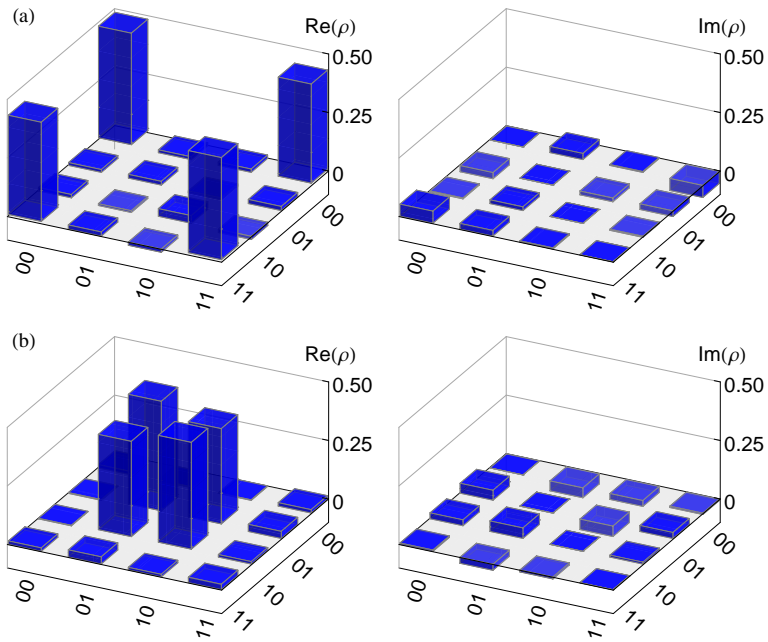


Figure 6.15: [b) and c)] Real and imaginary parts of the measured two-qubit density matrix of the Bell states $|\Phi_+\rangle$ and $|\Psi_+\rangle$. The fidelities with respect to the ideal states are $F = 0.91$ and $F = 0.87$

that the input bit x is left unchanged and the result of the function is written in the answer qubit, necessary for the operation \hat{U}_i to be unitary (reversible). It can easily be verified, that the following unitary operators implement all the four possible functions $f_0(x) = 0$, $f_1(x) = 1$ (constant), $f_2(x) = x$ and $f_3(x) = 1 - x$ (balanced) respectively

$$\hat{U}_0 = \hat{I} \otimes \hat{I}, \tag{6.22}$$

$$\hat{U}_1 = \hat{I} \otimes \hat{R}_x^\pi, \tag{6.23}$$

$$\hat{U}_2 = \left(\hat{I} \otimes (\hat{R}_y^{\pi/2} \hat{R}_x^\pi) \right) \hat{U}_{cZ_{00}} \left(\hat{I} \otimes \hat{R}_y^{\pi/2} \right), \tag{6.24}$$

$$\hat{U}_3 = \left(\hat{I} \otimes (\hat{R}_y^{-\pi/2} \hat{R}_x^\pi) \right) \hat{U}_{cZ_{11}} \left(\hat{I} \otimes \hat{R}_y^{-\pi/2} \right). \tag{6.25}$$

Here $\hat{U}_{cZ_{ij}}$ is a controlled-PHASE gate which adds a -1 to the state $|ij\rangle$ and leaves the other computational basis states unchanged. To understand the result of this circuit shown in **Figure 6.16**, lets see what happens to the input state $|0, 0\rangle$. First, Hadamard gates are applied to both qubits which brings both the data and the answer qubit into a superposition state

$$\left(\frac{|0\rangle + |1\rangle}{\sqrt{2}} \right)_A \otimes \left(\frac{|0\rangle - |1\rangle}{\sqrt{2}} \right)_B.$$

Applying the unitary operation \hat{U}_i onto this state flips the phase of the data qubit if the function is balanced, and does nothing (up to a global phase factor) if the

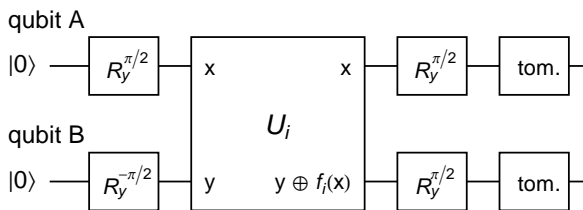


Figure 6.16: Quantum circuit implementing the Deutsch-Jozsa algorithm.

		f_0	f_1	f_2	f_3
$\langle 0, 0 \hat{\rho} 0, 0 \rangle$	ideal	0	0	1	1
	measured	0.07	0.08	0.82	0.89
$\langle 1, 0 \hat{\rho} 0, 1 \rangle$	ideal	0	0	0	0
	measured	0.04	0.03	0.004	0.002
$\langle 0, 1 \hat{\rho} 1, 0 \rangle$	ideal	1	1	0	0
	measured	0.85	0.86	0.07	0.05
$\langle 1, 1 \hat{\rho} 1, 1 \rangle$	ideal	0	0	0	0
	measured	0.03	0.03	0.1	0.06

Table 6.1: Diagonal elements of the density matrices of the Deutsch-Jozsa algorithm output for the four different function $f_0(x) = 0$, $f_1(x) = 1$, $f_2(x) = x$ and $f_3(x) = 1 - x$.

function is constant

$$\begin{cases} \pm \left(\frac{|0\rangle + |1\rangle}{\sqrt{2}} \right)_A \otimes \left(\frac{|0\rangle - |1\rangle}{\sqrt{2}} \right)_B & f(x) \text{ is constant} \\ \pm \left(\frac{|0\rangle - |1\rangle}{\sqrt{2}} \right)_A \otimes \left(\frac{|0\rangle - |1\rangle}{\sqrt{2}} \right)_B & f(x) \text{ is balanced} \end{cases}$$

Finally, applying a Hadamard transformation again on both qubits, the state is transferred into $|10\rangle$ if the function was constant, and into $|00\rangle$ if it was balanced

$$|\psi_{\text{final}}\rangle = \begin{cases} |10\rangle & f(x) \text{ is constant} \\ |00\rangle & f(x) \text{ is balanced.} \end{cases}$$

Measuring the data qubit A directly returns the answer. We have implemented this algorithm using the PHASE gates as shown above and performed full two-qubit tomography on the final state. The absolute value of the output states for all four possible functions $f(x)$ are shown in [Figure 6.17](#) (with wire frames indicating ideal matrices) and the value of the diagonal elements for all density matrices summarized in [Table 6.1](#). The fidelities of the final states for the functions f_0 to f_3 are 0.85, 0.86, 0.82 and 0.89 respectively.

Although we demonstrate fidelities larger than the classical threshold of 0.5, our experiment does not proof a speedup over the classical algorithm. This is because our measurement is too noisy, such that we have to average over 65 000

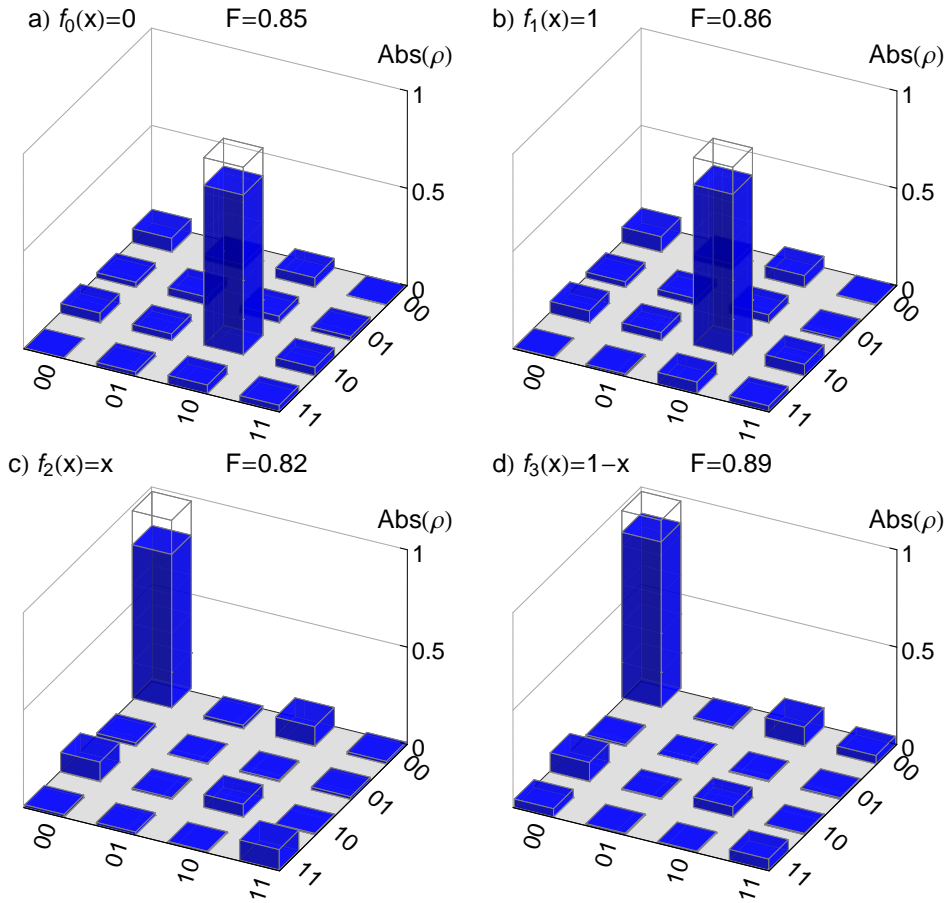


Figure 6.17: Absolute value of the output states of the Deutsch-Jozsa algorithm for the two constant f_0, f_1 and the two balanced functions f_2 and f_3 .

experimental realizations to be able to reconstruct these density matrices. In other words, we have to apply the oracle 65 000 times until we know if it implements a constant or balanced function. However, this speed up has been demonstrated with phase qubits [Yamamoto10]. Another two qubit algorithm, the Groover search algorithm, was also realized [DiCarlo09], and quantum speed up for this algorithm was later demonstrated by the group of Saclay [Dewes11].

6.3 Benchmarking a teleportation circuit

Here we demonstrate our efforts [Baur12] made towards the realization of on-chip quantum teleportation of macroscopic quantum states. Due to the stringent requirements on the control and read-out fidelity achievable for the multi qubit quantum system, full teleportation with single shot read-out and real-time feedback has so far only been experimentally realized in microscopic degrees of freedom with single photon [Bouwmeester97, Boschi98, Marcikic03, Jin10] or continuous variable states [Furusawa98, Lee11] and, more recently, with ions [Riebe04, Barrett04, Riebe07, Olmschenk09].

Quantum teleportation achieves the transfer of a quantum state from one physical location to another, even if the sender has no knowledge about both the state to be teleported and the location of the receiver [Bennett93]. In addition to its use in quantum communication [Gisin02], for example in context of quantum repeaters [Briegel98], quantum teleportation also enables universal and fault-tolerant quantum computation [Gottesman99, Zhou00, Childs05, Aliferis04, Jorrand05]. In early experiments with spins using nuclear magnetic resonance techniques [Nielsen98], single-shot readout and feedback was replaced by dephasing and controlled unitary operations. Here, we demonstrate the implementation of teleportation with superconducting circuits by replacing the single shot read-out [Mallet09] and real-time feedback [Doherty99], both of which are challenging to realize simultaneously in a three-qubit superconducting quantum processor at the current state of the art, with quantum state tomography. Even without explicitly realizing these steps, our benchmarking method allows us to provide crucial information on the entanglement generated during the teleportation protocol and the fidelity of the teleportation process up to the measurement. It thus presents an important step towards making use of teleportation in quantum processors realized in superconducting circuits.

In the standard protocol, non-local quantum correlations combined with classical

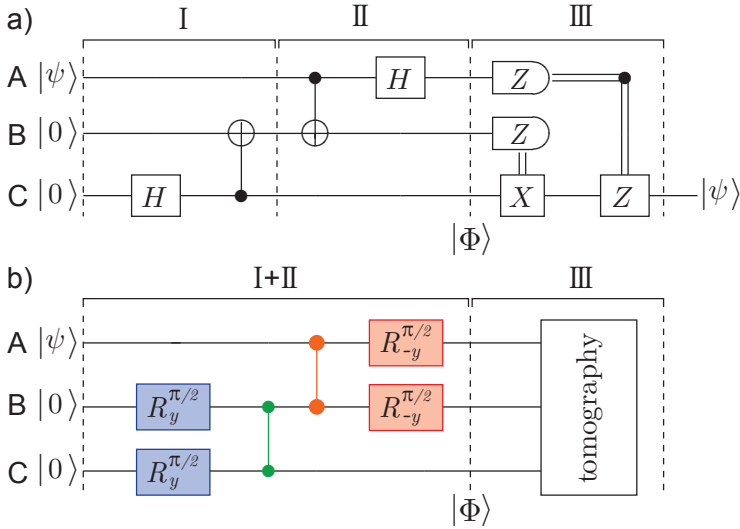


Figure 6.18: a) Circuit diagram of the standard protocol to teleport the state $|\psi\rangle$ of qubit A to qubit C. Here, \hat{H} is the Hadamard gate, \hat{Z} and \hat{X} are the Pauli matrices $\hat{\sigma}_x$ and $\hat{\sigma}_y$. The CNOT gate is represented by a vertical line between the control qubit (\bullet) and the target qubit (\oplus). b) The circuit implemented in this experiment with controlled-PHASE gates, indicated by vertical lines between the relevant qubits (\bullet), and single qubit rotations \hat{R}_n^θ of angle θ about the axis n .

communication is used to perform teleportation. In this scheme (see Figure 6.18a) the sender is in possession of qubit A in an arbitrary state $|\psi\rangle$. In the first step (I), a maximally entangled pair is generated, e.g. using a Hadamard (H) gate followed by a controlled-NOT (CNOT) gate, and shared between the sender (qubit B) and the receiver (qubit C). In the second step (II) the sender applies a CNOT gate on his two qubits followed by a H gate on qubit A generating an entangled three-qubit state $|\Phi\rangle$. In step III, the sender performs a measurement on his two qubits, which combined with step II is equivalent to a measurement performed in the Bell basis. He then sends the digital results to the receiver over a classical communication channel. Depending on these results, the receiver applies one of four unitary operations to his qubit to transform the state of qubit C into the state $|\psi\rangle$, completing the teleportation protocol.

In our approach using superconducting qubits we realize steps I and II by

combining single qubit rotations and two-qubit controlled-PHASE gates, as illustrated in [Figure 6.18b](#), to create the entangled state

$$|\Phi\rangle = \frac{1}{2} \{ |00\rangle \otimes |\psi\rangle + |01\rangle \otimes (-\hat{\sigma}_x)|\psi\rangle + |10\rangle \otimes (-\hat{\sigma}_z)|\psi\rangle + |11\rangle \otimes (-i\hat{\sigma}_y)|\psi\rangle \}, \quad (6.26)$$

where $\hat{\sigma}_i$ are the Pauli matrices (abc) denotes the states of qubits A,B,C, where $|0\rangle$ is the ground and $|1\rangle$ the excited state). In this notation, it becomes obvious that a measurement of qubits A and B collapses qubit C onto one of four possible states. If the measurement outcome is 00, 01, 10, or 11, qubit C is projected to either one of the states $|\psi\rangle$, $-\hat{\sigma}_x|\psi\rangle$, $-\hat{\sigma}_z|\psi\rangle$ or $-i\hat{\sigma}_y|\psi\rangle$, respectively. Instead of performing single qubit measurements on qubits A and B in step III, we analyze the three-qubit entangled state $|\Phi\rangle$ with full quantum state tomography and reconstruct the teleported state by calculating the projection of qubits A and B onto the basis states $|00\rangle$, $|01\rangle$, $|10\rangle$ and $|11\rangle$. We then characterize the transfer of the input state $|\psi\rangle$ to qubit C by performing process tomography conditioned on the projection onto the basis states of qubits A and B.

The full pulse sequence applied to the device for the generation and reconstruction of the three qubit entangled state $|\Phi\rangle$ using quantum state tomography is shown in [Figure 6.19](#). We repeated this scheme for a complete set of input basis states $|\psi\rangle = \{|0\rangle, |1\rangle, |-\rangle, |+\rangle\}$, with $|-\rangle = (|0\rangle - i|1\rangle)/\sqrt{2}$ and $|+\rangle = (|0\rangle + i|1\rangle)/\sqrt{2}$. As an example, the measured density matrix $\hat{\rho}_m$ for the input state $|\psi\rangle = |-\rangle$ is shown in [Figure 6.20a](#). We apply a maximum likelihood method [[Smolin12](#)] to ensure that $\hat{\rho}_m$ is physical and determine the fidelity $F = \langle \Phi | \hat{\rho}_m | \Phi \rangle = 0.74 \pm_{0.06}^{0.06}$ with respect to ideal state $|\Phi\rangle$. We note that for this particular input state, $|\Phi\rangle$ is a cluster state useful for one way quantum computation [[Raussendorf01](#)]. The error bars are estimated by re-sampling from the Gaussian distributions inferred from the measurements before executing the maximum likelihood method. This procedure is repeated to gather statistics. The 5th and 95th percentile are reported as the error bar boundaries, while the median is reported as the nominal value, since the values calculated all had unimodal distributions. For the input states $|\psi\rangle = |0\rangle, |1\rangle$ and $|+\rangle$ the fidelities are $0.77 \pm_{0.07}^{0.06}$, $0.75 \pm_{0.09}^{0.07}$ and $0.76 \pm_{0.07}^{0.06}$, respectively, comparable to the best fidelities of three-qubit entangled states realized in superconducting qubits so far [[DiCarlo10](#), [Neeley10](#)]. Also, the measured correlations (colored bars) present in $\hat{\rho}_m$ expressed in terms of Pauli sets are shown in [Figure 6.20c](#). It displays the expectation values of all tensor products \hat{P} of identity \hat{I} and Pauli

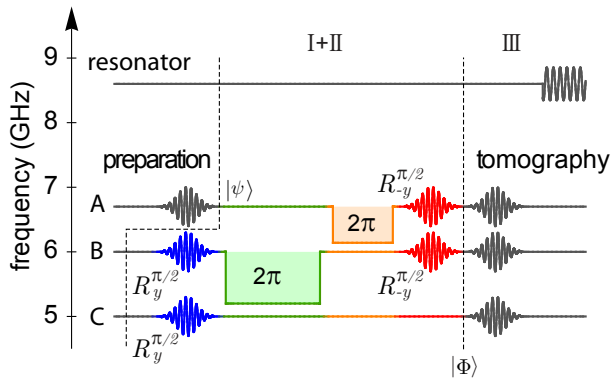


Figure 6.19: Illustration of the pulse sequence for the implementation of the circuit diagram shown in [Figure 6.18b](#). Single and two-qubit operations for the generation of the three qubit entangled state $|\Phi\rangle$ (I+II) are carried out with resonant microwave and magnetic flux pulses respectively (color code as in [Figure 6.18b](#)). The tomography (III) consists of microwave pulses that turn the qubit states to the desired measurement axis and a subsequent microwave pulse applied to the resonator for the joint dispersive qubit read-out.

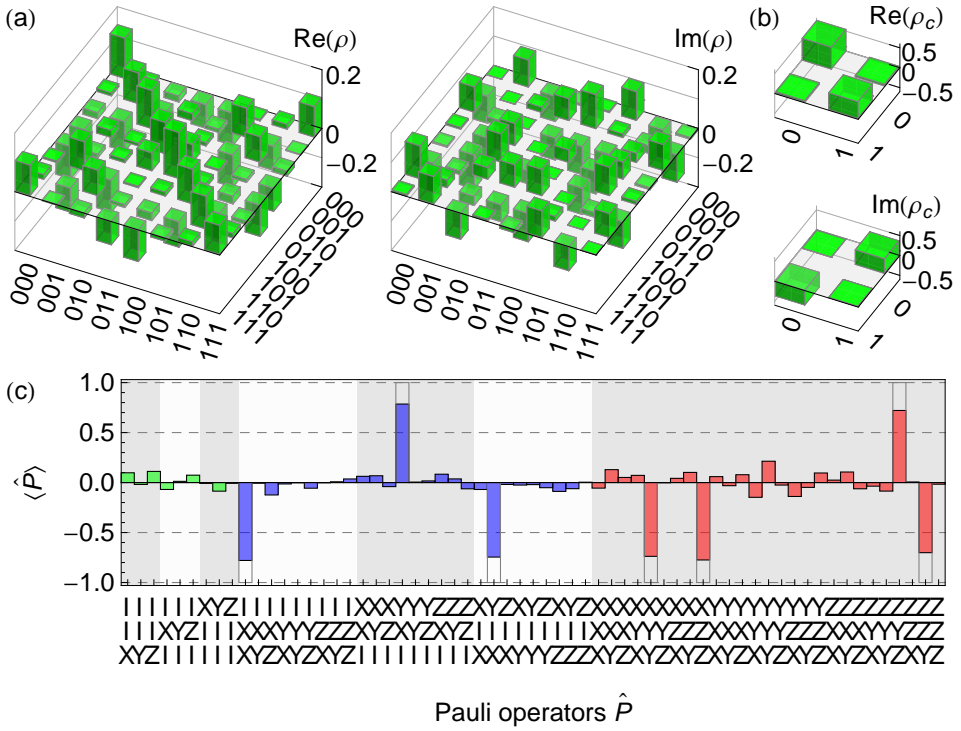


Figure 6.20: a) Real and imaginary part of the measured three-qubit density matrix $\hat{\rho}_m$ when applying the circuit shown in Figure 6.18b to the input state $|\psi\rangle = (|0\rangle - i|1\rangle)/\sqrt{2}$. b) Teleported single qubit state at qubit C found by projecting $\hat{\rho}_m$ from a) onto $|00\rangle$ and tracing out qubits A and B. c) Pauli sets for the state shown in a).

operators $\hat{X}, \hat{Y}, \hat{Z}$ for three-qubits, excluding the identity operator $\hat{I} \otimes \hat{I} \otimes \hat{I}$, which are in good agreement with the expected ones (wireframe).

Generally, the ideal three-qubit state $|\Phi\rangle$ generated by the circuit is genuine tripartite entangled as can be verified by calculating the three tangle (residual tangle) defined for pure states [Coffman00]. Only for $|\psi\rangle = |0\rangle$ and $|1\rangle$ the output state $|\Phi\rangle$ remains biseparable. To quantify the amount of entanglement in the measured state $\hat{\rho}_m$, we estimate the three tangle $\tau_3(\hat{\rho})$ for mixed states via the convex-roof extension [Uhlmann98]. A more detailed discussion about multipartite entanglement and entanglement measures can be found in Appendix A.3 and Appendix A.4, respectively. The values $\tau_3(\hat{\rho}) = \{0.45 \pm_{0.09}^{0.10}, 0.48 \pm_{0.12}^{0.13}\} > 0$ demonstrate that GHZ-type tripartite entanglement was prepared for $|\psi\rangle = \{|-\rangle, |+\rangle\}$. If we only want to verify that $\hat{\rho}_m$ contains genuine tripartite entanglement without distinguishing between the GHZ and W class, we can use a witness operator $\hat{W} = \alpha \hat{I} - |\Phi\rangle\langle\Phi|$ [Bourennane04], see also Appendix A.5. Here, α is the maximal squared overlap of any biseparable state with $|\Phi\rangle$, which yields 0.5 for $|\psi\rangle = |\pm\rangle$. For all biseparable states we find $\text{Tr}(\hat{W}\hat{\rho}) \geq 0$, whereas for the ideal tripartite entangled state $\hat{\rho} = |\Phi\rangle\langle\Phi|$ we find $\text{Tr}(\hat{W}\hat{\rho}) = \alpha - 1$. According to this criterion $\text{Tr}(\hat{W}\hat{\rho}_m) = -0.24 \pm_{0.06}^{0.06} < 0$ the measured state shown in Figure 6.20a clearly has tripartite entanglement. As derived in [Eisert07], the expectation value of the witness operator also directly leads to a lower bound to the generalized robustness of entanglement. It measures the minimal amount of mixing of $\hat{\rho}_m$ with an arbitrary density matrix $\hat{\sigma}$ such that $\hat{\rho}_m + s\hat{\sigma}$ is separable, for which we find $s \geq 0.47 \pm_{0.11}^{0.13}$.

To determine the fidelity of the teleportation process up to the measurement, we calculate the projection of $\hat{\rho}_m$ onto the four basis states of qubit A and B $|00\rangle, |01\rangle, |10\rangle, |11\rangle$. The state of qubit C is then reconstructed by tracing out qubits A and B and renormalizing the density matrix to $\hat{\rho}_C^{ij} = \text{Tr}_{AB}(\hat{P}_{ij}\hat{\rho}_m\hat{P}_{ij}^\dagger)/\text{Tr}(\hat{P}_{ij}\hat{\rho}_m)$, where \hat{P}_{ij} are the projectors $|ij\rangle\langle ij| \otimes \hat{I}$. For the projector \hat{P}_{00} , this state is expected to be identical to the input state $|\psi\rangle$. Figure 6.20b shows $\hat{\rho}_C^{00}$ reconstructed from the measured data for the input state $|-\rangle$ with a fidelity of $0.87 \pm_{0.10}^{0.08}$. For the other three projections, we find the resulting states of qubit C $-\hat{\sigma}_x|-\rangle, -\hat{\sigma}_z|-\rangle$ and $-i\hat{\sigma}_y|-\rangle$ with respective fidelities of $0.80 \pm_{0.10}^{0.09}, 0.82 \pm_{0.09}^{0.09}$ and $0.87 \pm_{0.11}^{0.08}$.

To fully characterize the teleportation circuit, we have performed quantum process tomography of the state transfer by repeating the procedure described above for $|\psi\rangle = |0\rangle, |1\rangle, |-\rangle, |+\rangle$. With the known input states and the reconstructed state of qubit C after teleportation, we calculate the completely positive map of the teleportation process $\mathcal{E}^{ij}(|\psi\rangle\langle\psi|) = \hat{\rho}_C^{ij} = \sum_{m,n} \chi_{mn}^{ij} \hat{E}_m |\psi\rangle\langle\psi| \hat{E}_n^\dagger$ characterized by the matrix

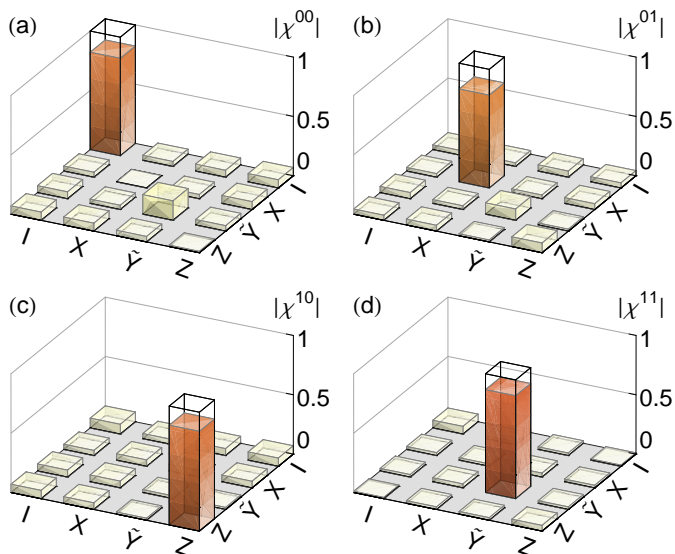


Figure 6.21: Absolute value of the χ matrix representation for the teleportation process which transfers the state of qubit A to qubit C for qubit A and B being projected to a) $|00\rangle$, b) $|01\rangle$, c) $|10\rangle$ and d) $|11\rangle$.

χ^{ij} expressed in the modified Pauli operator basis $\{\hat{E}_m\} = \{\hat{I}, \hat{\sigma}_x, \hat{\sigma}_y = -i\hat{\sigma}_y, \hat{\sigma}_z\}$. The extracted matrices χ^{ij} clearly demonstrate that the effective processes acting on the target qubit during teleportation are the unitary operations expected from Equation (6.26), see Figure 6.21. Since the χ^{ij} have only small imaginary elements < 0.07 , we display the absolute value of χ^{ij} for the different projections \hat{P}_{ij} on qubits A and B to emphasize the deviations from the ideal matrices χ_t^{ij} indicated by wireframes. The corresponding process fidelities $F_p^{ij} = \text{Tr}(\chi^{ij} \cdot \chi_t^{ij})$ are $0.80 \pm_{0.08}^{0.07}$, $0.76 \pm_{0.09}^{0.09}$, $0.80 \pm_{0.09}^{0.08}$, $0.83 \pm_{0.10}^{0.09}$, yielding $0.80 \pm_{0.05}^{0.05}$ averaged over all measurement outcomes. The average output state fidelity $\bar{F}^{ij} = (2F_p^{ij} + 1)/3$ is $0.86 \pm_{0.06}^{0.05}$, $0.84 \pm_{0.07}^{0.05}$, $0.87 \pm_{0.06}^{0.06}$, $0.88 \pm_{0.06}^{0.06}$ for each individual process, and $0.86 \pm_{0.04}^{0.03}$ on average. These are all well above the classical limit of $\bar{F} = 2/3$, suggesting that full teleportation is likely to become possible in the near future with superconducting qubits.

6.3.1 Outlook

To demonstrate full quantum teleportation including feedback, we need to be able to perform a measurement of qubits A and B, without affecting qubit C, such that the final state $\hat{\rho}_m$ gets projected onto the four different basis states of qubit A and B. In addition, this readout must be efficient enough to determine their individual states in one single experimental realization, rather than performing three-qubit tomography using measurement data averaged over many realizations. This is clearly not possible with our current three-qubit circuit, as the transmission measurement of the resonator inevitably yields information about all three qubits.

One possibility to fulfill these requirements would be to combine our setup with the architecture described in References [Mallet09, Dewes12]. There, each qubit is coupled to an individual Josephson bifurcation amplifier, which allows for single-shot and quantum non-demolition readout with fidelities of 92%. Together with our average output state fidelities of $> 85\%$, full quantum teleportation above the classical limit could be realized.

Another possibility could be to use two resonators, where the first only couples to qubit A and B, and the second only couples to B and C. While the two resonators are used as the coupling bus for the two controlled-PHASE gate operations required to generate the final three-qubit entangled state, the first resonator also serves as a measurement device to readout qubit A and B, without affecting qubit C. The state teleported from A to C can then be detected by measuring transmission through the second resonator. In order to reach high readout fidelities, we could add one of our ultra low noise parametric amplifiers [Sandberg08, Vijay11, Eichler11a] to each resonator output, and quantum feedback could be realized using the FPGA [Bozyigit11] developed in our lab for real-time analysis of the acquired measurement signal.

Realization of the Toffoli gate

As we have seen throughout this thesis, it is demanding to accurately control the state of multiple qubits. Already tiny errors in the control parameters due to inaccurate calibrations or random fluctuations induce significant errors in the quantum operation. Additionally, imperfect isolation of the qubits from their environment inevitably leads to decoherence of the quantum state. Complete elimination of the latter error source is probably impossible, as it is in contradiction with the need for accurate control and measurement of the qubit state. Therefore, the quantum states and operations are to be protected against errors using quantum error correction. In this chapter I first describe the basic principles of quantum error correction ([Section 7.1](#)), and then discuss our realization of the three-qubit quantum Toffoli gate [[Fedorov12](#)] ([Section 7.2](#)). This gate is particularly interesting, as it is useful for the implementation of the most simple quantum error correction scheme using three qubits. In parallel and independent work, this scheme has been fully demonstrated [[Reed12](#)] using a three-qubit gate, which only approximates the Toffoli gate (it differs by a spurious two-qubit phase), and a Toffoli gate between two qubits and a resonator has been realized [[Mariantoni11b](#)], but not fully characterized.

7.1 Error correction

Before going to the quantum version, I shortly review the basic principles of classical error correction. Suppose we have one bit of information and we want

to send it via a classical communication channel to another location. During this process, the bit would randomly flip its state with a probability of $p > 0$ due to the noise in the channel, and be transmitted without an error with probability $1 - p$. In order to protect the qubit from this error, we can encode the bit of information in a state consisting of three identical copies of the bit: $1 \rightarrow 111$ and $0 \rightarrow 000$, called the repetition code. Instead of transmitting a single bit, we send the bit strings 000 or 111, and the receiver then decodes the original bit using a majority vote. That is, if 0 appears more often in the bit string, the original bit was 0 and 1 otherwise. As an example, when 000 was sent and the first bit flipped its state, then the receiver still recovers the correct original state 0 from the measured value of 100. If more than one bit flip their state, then the error correction code would fail. The probability of this happening can be calculated as follows. The probability that a particular pair of bits flipped and the third did not is given by $p^2(1 - p)$. Since there are three different pairs and the probability that all three bits flipped their state is p^3 , the probability of an error occurring in the encoded bit is $p_e = 3p^2 - 2p^3$. The transmission of information is thus more reliable with encoding, as long as $p < 0.5$, and can be made arbitrarily accurate by increasing the number of bits used for the repetition code.

As we will shortly see, a similar concept can be used for quantum error correction, even though there are some important differences in comparison with the classical case. First, cloning a quantum state is forbidden by the basic laws of quantum mechanics (no-cloning theorem) [Wootters82]. It is thus impossible to encode the information by copying the state a number of times. Furthermore, the measurement of a quantum state destroys the quantum information. This makes it impossible to implement the decoding procedure described above, since it relies on the measurement of the encoded message.

Instead of copying the information many times, quantum error correction codes employ entanglement to protect the information from errors. As an example, assume that we want to send a qubit in the state $|\psi\rangle$ via a noisy quantum channel to another location. The noise acts on the qubit by applying the flip operation $\hat{\sigma}_x|\psi\rangle$ to its state with probability p , and leaves it unchanged with probability $1 - p$. We can protect the qubit from these errors using the encoding given by

$$\alpha|0\rangle + \beta|1\rangle \rightarrow \alpha|000\rangle + \beta|111\rangle. \quad (7.1)$$

Instead of copying the whole state, we replace the computational basis states with the three qubit repetition code as in the classical case: $|0\rangle \rightarrow |000\rangle$ and

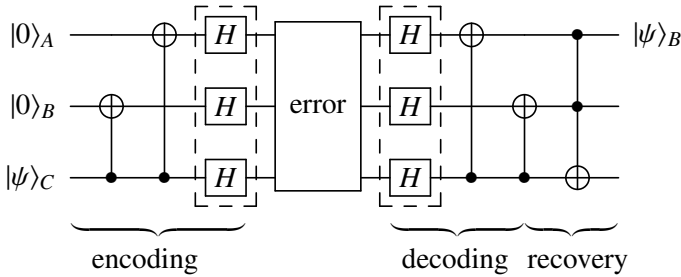


Figure 7.1: Quantum error correction protocol that corrects for bit flip or phase flip (including the dashed boxes) errors. The data qubit to be encoded is qubit C.

$|1\rangle \rightarrow |111\rangle$. A quantum circuit which implements this encoding using two CNOT operations is shown in [Figure 7.1](#), where qubit C is the data qubit to be encoded. For $\alpha = \beta = 1/\sqrt{2}$, this state is a genuine tripartite entangled state, commonly known as the Greenberger-Horne-Zeilinger (GHZ) state. We have experimentally generated this state using the encoding procedure explained above as an example, and reconstructed its density matrix with state tomography. In addition to showing the density matrix, we also display the expectation values of all combinations of the Pauli matrices and the identity (Pauli sets), calculated from the measured density matrix, see [Figure 7.2](#). As discussed below, the Pauli sets provide more information relevant to the error detection.

The error detection is done similarly to the classical case using a majority vote. In this step it is crucial that the measurement involved only gives information about which qubit experienced an error, but gives no information about the amplitudes α and β of the encoded quantum state. Otherwise the quantum coherence would be destroyed. To do so, we can use the fact that the encoded state $\alpha|000\rangle + \beta|111\rangle$ is an eigenstate of both observables $\hat{\sigma}_z^A \hat{\sigma}_z^B$ and $\hat{\sigma}_z^B \hat{\sigma}_z^C$ with eigenvalue $+1$ for all α, β , see as an example [Figure 7.2c](#). If for instance qubit C undergoes a bit flip, the measurement of $\hat{\sigma}_z^B \hat{\sigma}_z^C$ would result in -1 whereas the measurement of the observable $\hat{\sigma}_z^A \hat{\sigma}_z^B$ would remain $+1$. This uniquely identifies that qubit C has changed its state. However, no information is gained about the state $|\psi\rangle$. More generally, with the four possible measurement outcomes of $\hat{\sigma}_z^A \hat{\sigma}_z^B$ and $\hat{\sigma}_z^B \hat{\sigma}_z^C$ (the error syndrome) we can determine on which qubit the bit flip occurred. For the results $(+1, +1)$, $(+1, -1)$, $(-1, +1)$ or $(-1, -1)$, no qubit, qubit C, qubit A or qubit B are flipped, respectively. To perform a fault-tolerant measurement of

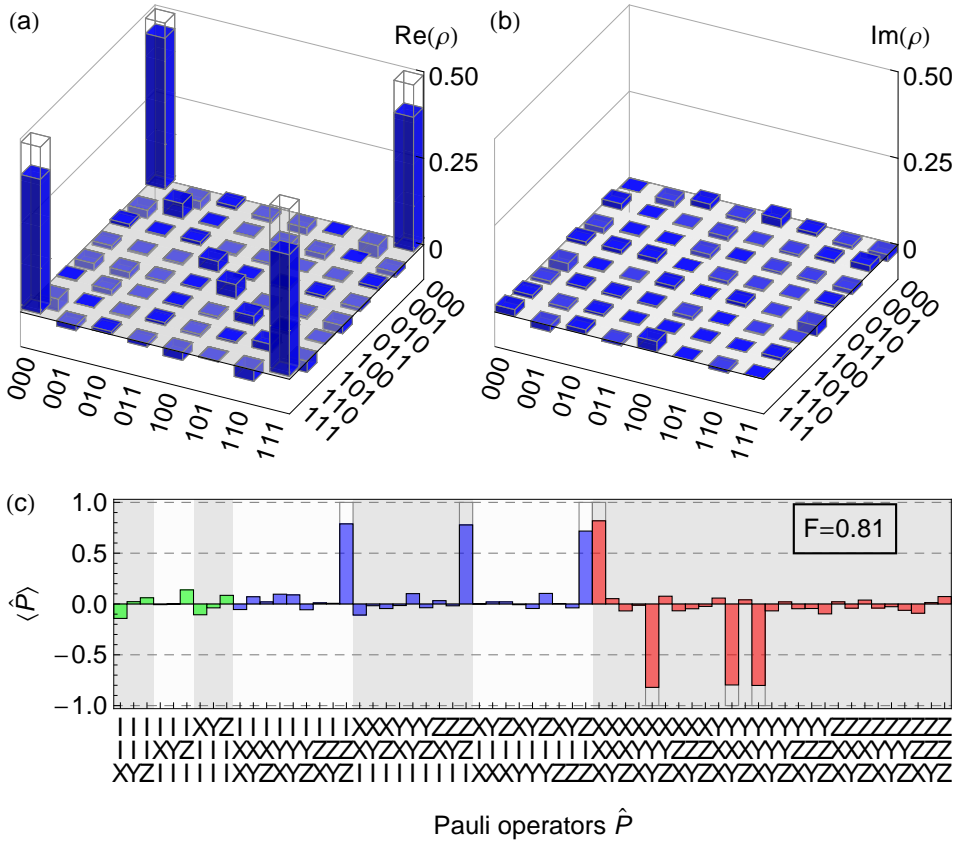


Figure 7.2: [a) and b)] Real and imaginary part of the measured density matrix of the three-qubit GHZ state. c) Measured expectation values of the Pauli operators \hat{P} for the three-qubit GHZ state. Wireframes indicate the theoretically expected values. The fidelity is $F = 0.82$.

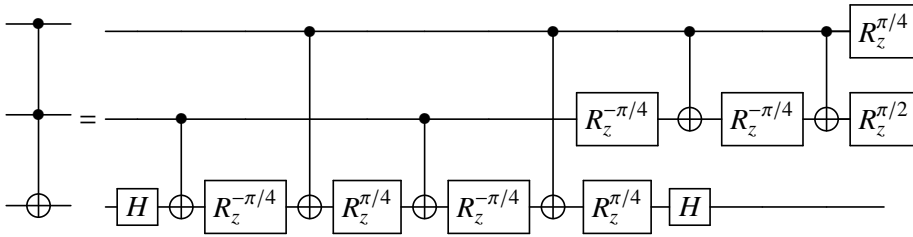


Figure 7.3: Quantum circuit implementation of the Toffoli gate using only two-qubit CNOT gates and single-qubit operations

the error syndrome, additional ancilla qubits would be required. However as a proof of principle we can perform the decoding circuit shown in [Figure 7.1](#) which maps the error syndrome onto the populations of the ancilla qubits A and B: $(+1, +1) \rightarrow |00\rangle_{AB}$, $(+1, -1) \rightarrow |11\rangle_{AB}$, $(-1, +1) \rightarrow |10\rangle_{AB}$ and $(-1, -1) \rightarrow |01\rangle_{AB}$. In other words, if a bit flip occurred on qubit C, the ancilla qubits would be in state $|11\rangle$. Applying a Toffoli gate, which performs a NOT operation on qubit C conditioned on the state of qubits A and B, then allows to correct for the error on qubit C.

Similar to the bit-flip error correction code, the quantum state can also be protected against phase-flip errors, where the operation $\hat{\sigma}_z|\psi\rangle$ is applied to the qubit with a probability p . The protocol only differs by the Hadamard gates shown in [Figure 7.1](#), and the syndrome measurements are performed by measuring the observables $\hat{\sigma}_x^A \hat{\sigma}_x^B$ and $\hat{\sigma}_x^B \hat{\sigma}_x^C$. If we want to protect the qubit from both errors at the same time, the nine qubit Shor code can be used, which is a straightforward combination of the bit and phase-flip codes described above. More details about quantum error correction can be found in [[Nielsen00](#), [Gottesman09](#)].

7.2 Toffoli gate

Implementing the Toffoli gate needed for the recovery step involved in the error correcting scheme shown in [Figure 7.1](#) is demanding. The best known decomposition into single-qubit and CNOT operations as depicted in [Figure 7.3](#) [[Nielsen00](#), [Barenco95](#)], consists of six CNOT and ten single-qubit gates. With the accuracy of our gates however, the process fidelity of the Toffoli operation according to

this scheme would be lower than $F_p < 0.5$. Here we demonstrate a method to significantly reduce the number of elementary gates needed, by exploiting the third energy level of the transmon qubit [Fedorov12]. This scheme requires in total two qubit-qutrit, one qubit-qubit and two single-qubit operations, which allows us to realize the Toffoli gate with a process fidelity of $F_p = 69\%$, extracted from full process tomography. A similar approach [Mariantoni11b] to realizing characteristic features of a Toffoli-class gate has been demonstrated with two qubits and a resonator and achieved a limited characterization considering only the phase fidelity. A slightly different approach, using the third and also the fourth level of the transmon qubit, was used by Reed *et al.* [Reed12] for the realization of the quantum error correction discussed above. However, their gate only approximates the Toffoli gate, and differs by a spurious two-qubit phase which is not relevant in this specific error correction scheme.

In the conventional realization of the Toffoli gate, a NOT operation is applied to the target qubit (C) if the control qubits (A and B) are in the state $|11\rangle$. In our setup, it is more natural to construct a variation of the Toffoli gate shown in Figure 7.4a, in which the state of the target qubit is inverted if the control qubits are in $|01\rangle$. This gate can easily be transformed to the conventional Toffoli gate by a redefinition of the computational basis states of qubit A or by applying two π -pulses on qubit A.

The Toffoli gate can be constructed from a controlled-controlled-PHASE (CCPHASE) gate sandwiched between two Hadamard gates, realized using $\pm\pi/2$ rotations about the y axis, acting on the target qubit. The CCPHASE gate leads to a phase shift of π for the state $|1\rangle$ of the target qubit if and only if the control qubits are in state $|01\rangle$. In other words, this corresponds to a sign change of only one of the eight computational three-qubit basis states: $|011\rangle \leftrightarrow -|011\rangle$.

The basic idea of “hiding” states by transforming them into non-computational states to simplify the implementation of the Toffoli gate was theoretically proposed in References [Ralph07, Borrelli11] and has been experimentally implemented for linear optics and ion trap systems [Lanyon09, Monz09]. The implementation of the scheme of Reference [Ralph07] in our setup would require three CPHASE gates, six single-qubit and two single-qutrit operations. Instead, we construct the CCPHASE gate from a single two-qubit CPHASE gate and two qubit-qutrit gates. The latter gates are called π -SWAP and 3π -SWAP, respectively (Figure 7.4b, red frames). The application of a single CPHASE gate to qubits B and C (Figure 7.4b, blue frame) inverts the sign of both $|111\rangle$ and $|011\rangle$. To create the CCPHASE operation, the computational basis state $|111\rangle$ is transferred to the non-computational state $i|201\rangle$ by the π -SWAP gate, effectively hiding it from the CPHASE operation acting on qubits B and C. After the

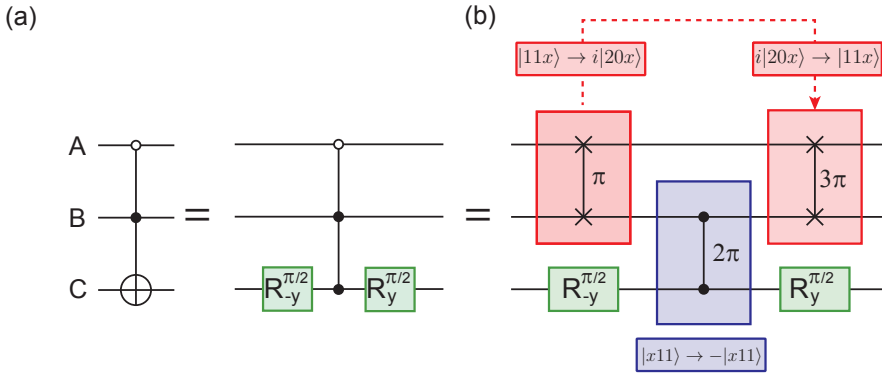


Figure 7.4: a) The Toffoli gate can be decomposed into a CPHASE gate and $\pm\pi/2$ rotations about the y axis. b) The CPHASE gate is implemented with two two-qubit/qutrit gates between qubit A and B (red) which hide (recover) the state $|11x\rangle$ into (from) $|20x\rangle$, such that only the state $|011\rangle$ adds a phase when applying the controlled-PHASE gate between qubit B and C (blue).

path	initial state	after π -SWAP	after CPHASE gate	after 3π -SWAP
1	$ 011\rangle$	$ 011\rangle$	$- 011\rangle$	$- 011\rangle$
2	$ 11x\rangle$	$i 20x\rangle$	$i 20x\rangle$	$ 11x\rangle$
3	$ x0y\rangle$	$ x0y\rangle$	$ x0y\rangle$	$ x0y\rangle$
3	$ 010\rangle$	$ 010\rangle$	$ 010\rangle$	$ 010\rangle$

Table 7.1: List of states after each step of the CPHASE gate

CPHASE operation, $|111\rangle$ is recovered from the non-computational level $i|201\rangle$ by the 3π -SWAP gate.

All three-qubit basis states show three distinct evolution paths through our CPHASE gate, see Table 7.1. Only the input state $|011\rangle$ is affected by the CPHASE gate acting on qubits B and C, which transfers $|011\rangle$ to the desired state, $-|011\rangle$. The states $|11x\rangle$ with $x \in \{0, 1\}$ are transferred by the π -SWAP gate to the states $i|20x\rangle$. The subsequent CPHASE gate therefore has no influence on those states. The last gate (3π -SWAP) transfers $i|20x\rangle$ back to $|11x\rangle$. Together the two SWAP gates realize a rotation by 4π , such that the state $|11x\rangle$ does not acquire any extra phase relative to the other states. The states of the last group ($|010\rangle$ and $|x0y\rangle$ with $y \in \{0, 1\}$) do not change during the CPHASE gate sequence.

7.2.1 Gate calibration

I have already discussed the realization of the `CPHASE` gate using the interaction between $|11\rangle$ and $|20\rangle$ in [Section 6.2.3](#). I am thus going to focus here on the actual experimental implementation and accurate calibration of the `SWAP` gates and on specific points that need to be considered when hiding the computational $|11\rangle$ state into the non-computational $|20\rangle$ state.

SWAP calibration

The `SWAP` gate is based on the same interaction as the `CPHASE` gate. There the state $|11\rangle$ is non-adiabatically tuned into resonance with $|20\rangle$ using a short magnetic flux pulse. The system then oscillates between this pair of states with a frequency $2J_{10}$. Waiting for an interaction time $2\pi/2J_{10}$ that corresponds to one full period of the oscillation, the `CPHASE` gate is realized. Choosing an interaction time $\pi/2J_{10}^{AB} = 7$ ns or $3\pi/2J_{10}^{AB} = 21$ ns instead, realizes a π -`SWAP` (sometimes also referred to as the `iswap-gate`) and a 3π -`SWAP` between qubits A and B, respectively. For the accurate operation of the Toffoli gate, it is important that these `SWAP` operations fully swap the state $|11\rangle$ to $|20\rangle$ without leaving any residual population in $|11\rangle$. A coarse calibration of the length L and amplitude ΔA of the flux pulse is carried out by measuring the $|11\rangle \leftrightarrow |20\rangle$ oscillations as shown in [Figure 6.13](#). The optimal value ΔA_0 , where $|11\rangle$ is on resonance with $|20\rangle$, is found by determining the ΔA for which the oscillation frequency is minimal. From a single trace with amplitude ΔA_0 we then extract the L_0 required for the π - and 3π -`SWAP`. However, further fine tuning is required for two reasons. First, the determination of ΔA_0 and L_0 from these oscillations is inaccurate. This is because the oscillation frequency and the population around ΔA_0 and L_0 , respectively, are to first order insensitive to variations in ΔA and L . Second, the individual calibration of subsequent flux pulses is affected by long term drifts on the millisecond timescale. These drifts are believed to be caused by heating or persistent on-chip currents.

In order to include the influence of subsequent flux pulses in the calibration, we fine tune the coarse calibration of each flux pulse within the full flux pulse sequence of the Toffoli gate, instead of calibrating each flux pulse on its own. The pulse scheme to calibrate the π -`SWAP` is shown in [Figure 7.5a](#) as an example. In order to understand how this works let us take a look at the evolution of the two-qubit states of qubit A and B when going through each step in this pulse scheme, starting with

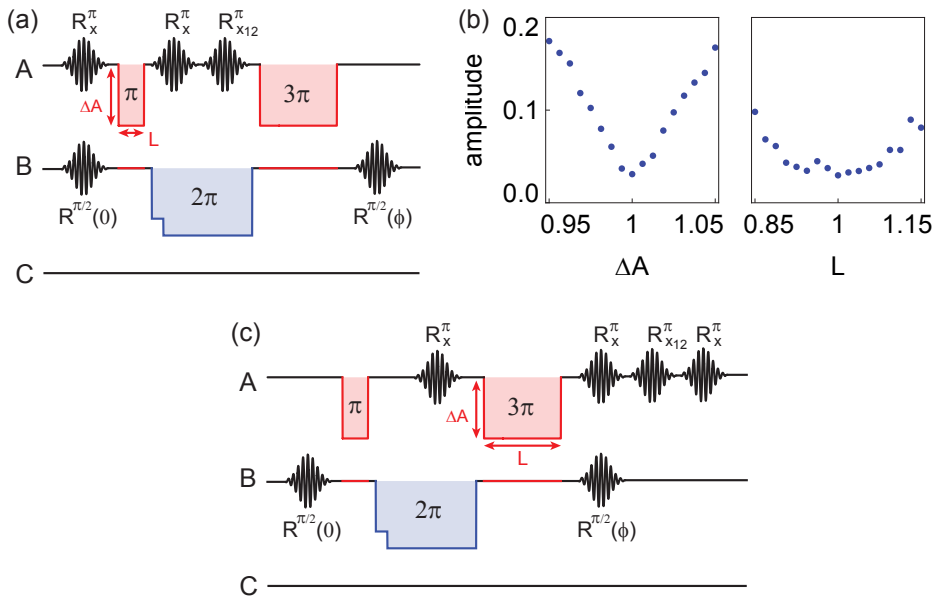


Figure 7.5: a) Pulse scheme to accurately calibrate the length L and amplitude ΔA of the flux pulse used for the π -SWAP gate. b) For each setting of ΔA or L , a Ramsey type experiment is carried out on qubit B where the phase of the second $\pi/2$ pulse is varied. The extracted amplitude of the Ramsey oscillation is then plotted as a function of ΔA or L , respectively. Optimal values for ΔA and L are determined by finding the minimal Ramsey oscillation amplitude. c) A similar scheme can be used to calibrate the 3π -SWAP by placing the first π -pulse on qubit A in between the two SWAP operations and applying $R_x^\pi R_{x_{12}}^\pi R_x^\pi$ after the 3π -SWAP on qubit A.

$|00\rangle_{AB}$

$$|00\rangle_{AB} \xrightarrow{\hat{R}_x^\pi \otimes \hat{R}_x^{\pi/2}} |10\rangle_{AB} + |11\rangle_{AB}, \quad (7.2)$$

$$\xrightarrow{\pi\text{-SWAP}} |10\rangle_{AB} + \sqrt{1 - \varepsilon^2} |20\rangle_{AB} + \varepsilon |11\rangle_{AB}, \quad (7.3)$$

$$\xrightarrow{\hat{R}_x^\pi \otimes \hat{I}} |00\rangle_{AB} + \sqrt{1 - \varepsilon^2} |20\rangle_{AB} + \varepsilon |01\rangle_{AB}, \quad (7.4)$$

$$\xrightarrow{\hat{R}_{x_{12}}^\pi \otimes \hat{I}} |00\rangle_{AB} + \sqrt{1 - \varepsilon^2} |10\rangle_{AB} + \varepsilon |01\rangle_{AB}, \quad (7.5)$$

$$\xrightarrow{3\pi\text{-SWAP}} \sqrt{1 - \varepsilon^2} (|0\rangle_A + |1\rangle_A) \otimes |0\rangle_B + \varepsilon |0\rangle_A \otimes (|0\rangle_B + |1\rangle_B). \quad (7.6)$$

Here we have omitted the normalization and all dynamic phases acquired during the frequency tuning of qubits A and B for simplicity, as the phases are not relevant to understand the principle. Additionally, we assume that all gates are perfect with the exception of the π -SWAP, which leaves a small but finite population ε in the $|11\rangle$ state. As we can see, the π -pulses on the 01 (R_x^π) and 12-transition ($R_{x_{12}}^\pi$) on qubit A in between the two SWAP operations are used to eliminate the influence of the 3π -SWAP operation on the final state. This allows us to independently calibrate the π -SWAP even in the presence of the 3π -SWAP gate in the end.

The imperfect π -SWAP operation leaves qubit B with small probability ε^2 in a superposition state, while for perfect operation ($\varepsilon = 0$) it completely returns to the ground state, see Equation (7.6). The value of ε can be probed by measuring qubit population as a function of the phase ϕ of the final $\pi/2$ -pulse on qubit B. For $\varepsilon = 0$, the final state is independent of ϕ and no oscillations are observed. On the other hand, if $\varepsilon > 0$, the oscillation amplitude A_R is equal to ε . Figure 7.5b shows the dependence of A_R as a function of the flux pulse amplitude ΔA and length L , respectively, and optimal flux pulse calibration is found by finding the minimum of $A_R(\Delta A, L)$.

A similar scheme is used to calibrate the 3π -SWAP, see Figure 7.5c, by applying the first π -pulse to qubit A in between the two SWAP operations and applying $R_x^\pi R_{x_{12}}^\pi R_x^\pi$ after the 3π -SWAP on qubit A.

Phase calibration

While most of the dynamic single-qubit phases acquired throughout the pulse sequence can be adjusted at the very end by rotating the phase of subsequent microwave pulses or single-qubit PHASE gates, the dynamic phase acquired by the

state $|20\rangle$ during the hiding process must be compensated in between the SWAP operations. This can be understood by analyzing the temporal evolution of the two initial states $|\psi_1\rangle = (|0\rangle_A + |1\rangle_A) \otimes |0\rangle_B$ and $|\psi_2\rangle = (|0\rangle_A + |1\rangle_A) \otimes |1\rangle_B$ when hiding $|11\rangle$ into $|20\rangle$ for a waiting time t

$$|\psi_1\rangle = (|0\rangle_A + |1\rangle_A) \otimes |0\rangle_B \longrightarrow (|0\rangle_A + |1\rangle_A) \otimes |0\rangle_B, \quad (7.7)$$

$$|\psi_2\rangle = (|0\rangle_A + |1\rangle_A) \otimes |1\rangle_B \xrightarrow{\pi\text{-SWAP}} |01\rangle_{AB} + i|20\rangle_{AB} \quad (7.8)$$

$$\xrightarrow{\text{waiting time } t} |01\rangle_{AB} + ie^{i\phi_2}|20\rangle_{AB} \quad (7.9)$$

$$\xrightarrow{3\pi\text{-SWAP}} (|0\rangle_A + e^{i\phi_2}|1\rangle_A) \otimes |1\rangle_B \quad (7.10)$$

Again, we assume that the frequency tuning of the qubits does not acquire any dynamic phase without loss of generality, as these are easily corrected after the full pulse sequence. While $|\psi_1\rangle$ remains unchanged, $|\psi_2\rangle$ acquires a dynamic phase $\phi_2 = \alpha \cdot t$ determined by the anharmonicity α^A of qubit A and the time t . This is because the phase of $|11\rangle$ rotates at a frequency $\omega = \omega_{01}^A + \omega_{01}^B$, whereas the phase of $|20\rangle$ rotates with frequency $\omega - \alpha^A$. For the correct realization of the Toffoli gate however, these two states are required to have the same phase after the pulse sequence, which is impossible to realize with single-qubit PHASE gates at the end of the sequence.

Instead, we adjust the phase of $|11\rangle$ to be in phase with $|20\rangle$ before the 3π -SWAP by tuning the amplitude ΔB of a short magnetic flux pulse applied on qubit B before the CPHASE gate, see [Figure 7.6a](#). The accurate value of ΔB is found by measuring the dynamic phase of qubit A for $|\psi_1\rangle$ and $|\psi_2\rangle$ after the pulse sequence with a Ramsey type experiment, where we apply a final $\pi/2$ -pulse with phase ϕ on qubit A and measure its population as a function of ϕ . We repeat this experiment for different values of ΔB , until the two Ramsey oscillations are in phase, see [Figure 7.6b](#) (red solid dots for $|\psi_1\rangle$ and green open squares for $|\psi_2\rangle$). Additionally, we also make a control measurement for the case that qubit B and C are initially prepared in $|01\rangle_{BC}$ (blue open triangles) and $|11\rangle_{BC}$ (orange stars). As expected, the curve corresponding to $|11\rangle_{BC}$ is phase shifted by π , since the CPHASE gate changes the sign of $|011\rangle$. Fitting the data to a sine allows us to determine the dynamic phase acquired by the qubit A. The same experiment is repeated for qubits B and C, and the dynamic phases are compensated by rotating the phase of the subsequent microwave pulses (tomography pulses).

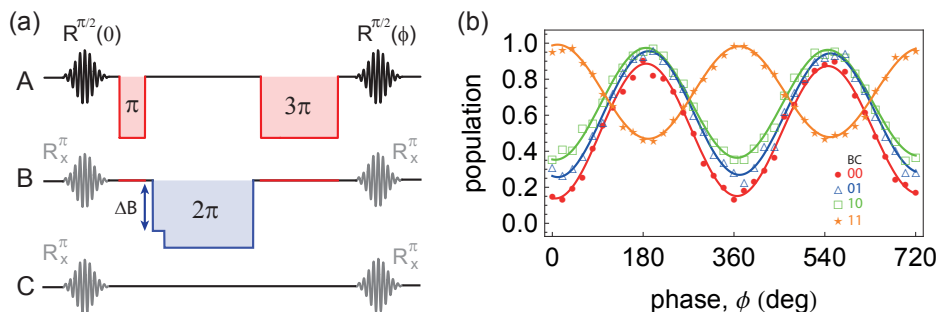


Figure 7.6: a) Pulse scheme to compensate for the dynamic phase acquired by $|20\rangle$ when hiding the state $|11\rangle$, by adjusting the amplitude of the flux pulse buffer ΔB on qubit B. b) Ramsey oscillation experiment on qubit A where the phase of the second $\pi/2$ -pulse is varied, for qubits B and C in initially in the state $|00\rangle$ (red solid dots), $|01\rangle$ (blue open triangles), $|10\rangle$ (green open squares) and $|11\rangle$ (orange stars), respectively. Solid lines are fits to a sine to determine the overall dynamic phase acquired by qubit A.

7.2.2 Gate characterization

We have characterized the performance of this realization of a Toffoli gate by measuring the truth table and by full process tomography. The truth table depicted in [Figure 7.7](#) shows the population of all computational basis states after applying the Toffoli gate to each of the computational basis states. It reveals the characteristic properties of the Toffoli gate, namely that a NOT operation is applied to the target qubit (C) only if the control qubits (A and B) are in the state $|01\rangle$. The fidelities of the output states show a significant dependence on qubit lifetime. In particular, input states with qubit A (with the shortest lifetime) in the excited state generally have the lowest fidelity, indicating that the fidelity of the protocol is mainly limited by the qubit lifetime. The fidelity of the measured truth table, U_m , with respect to the ideal one, U_t , namely $F_T = (1/8)\text{Tr}(U_m U_t) = 76.0\%$, shows the average performance of our gate when acting on the eight basis states.

As an essential addition to the classical characterization of the gate by the truth table, we have performed full three-qubit quantum process tomography and reconstructed the process matrix, χ_m , to completely characterize the quantum operation of the experimentally realized Toffoli gate. For this purpose, we prepared a complete set of 64 distinct input states by applying all combinations of single-qubit

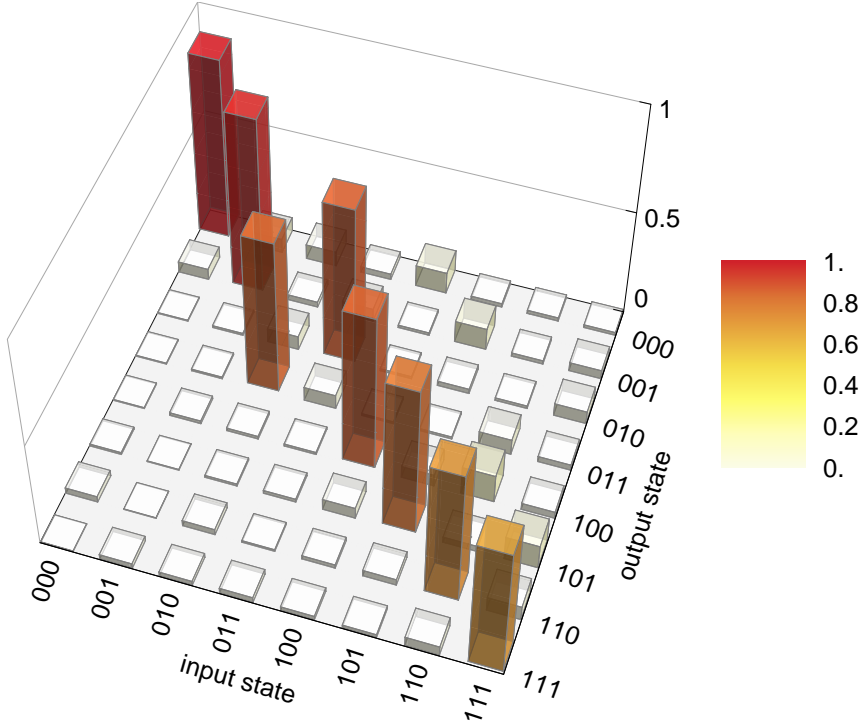


Figure 7.7: Measured truth table of the Toffoli gate with truth table fidelity of 76%.

operations chosen from the set $\{\hat{I}, \hat{R}_x^{\pi/2}, \hat{R}_y^{\pi/2}, \hat{R}_x^{\pi}\}$ for each qubit, and performed state tomography on the respective output states. The process matrix reconstructed directly from the data (see [Section 5.5.2](#) and [Section A.2.2](#)) has a fidelity of $F_P = \text{Tr}(\chi_m \cdot \chi_t) = 70 \pm 3\%$ (the error represents a 90% confidence interval), where χ_t is the ideal process matrix. Using a maximum-likelihood procedure [[Ježek03](#)] to correct for unphysical properties of χ_m , we find that the obtained process matrix, χ_m^{ML} , has a fidelity of $F = \text{Tr}(\chi_m^{\text{ML}} \cdot \chi_t) = 69\%$ with expected errors at the level of 3%. In [Figure 7.8a](#), χ_m shows the same key features as χ_t ([Figure 7.8b](#)).

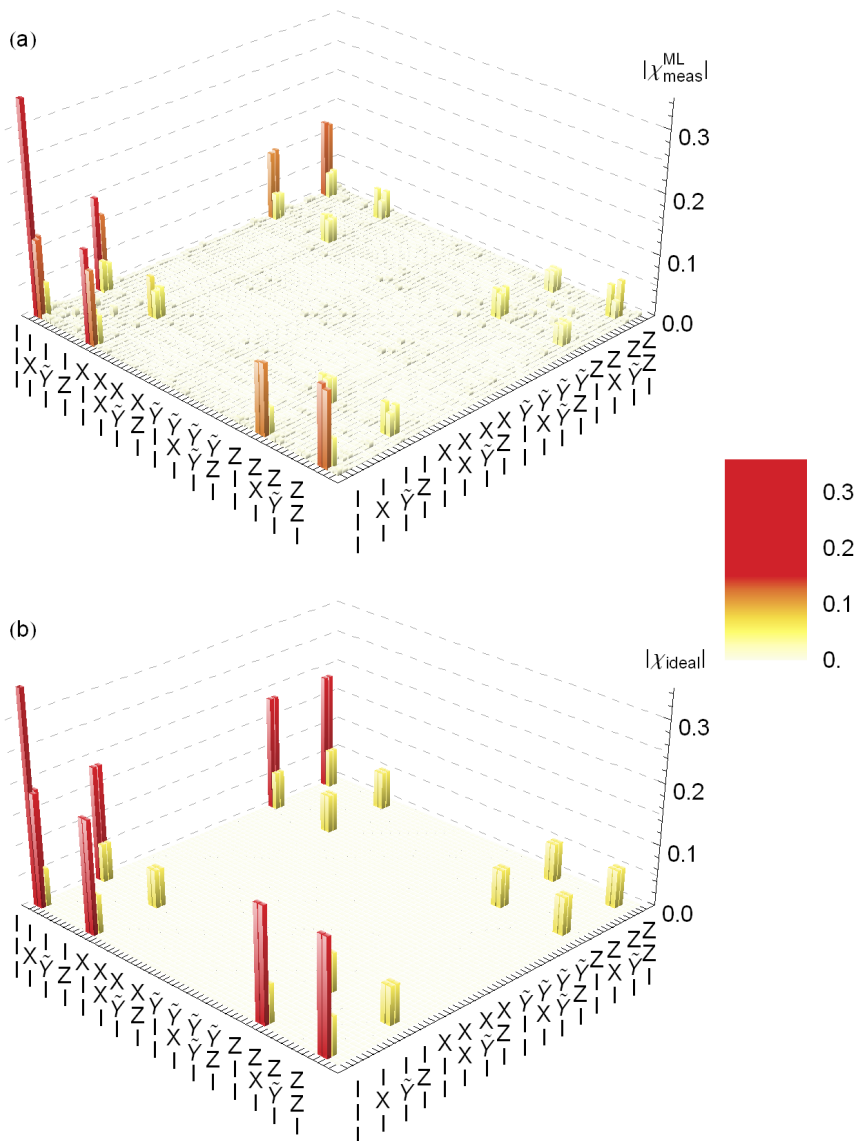


Figure 7.8: Bar chart of the absolute value of the measured process matrix χ_m^{ML} (a) and ideal process matrix χ_t (b). The elements are displayed in the operator basis $\{III, IIX, II\bar{Y}, IIZ, IXI, IXX, \dots, ZZZ\}$ and the process fidelity is 69%.

7.3 Conclusion

In this chapter, we have experimentally demonstrated the two building blocks needed for the most simple quantum error correction scheme. This is the preparation of three-qubits in the bit-flip error correction code, and the realization of the three-qubit Toffoli gate. To achieve the latter, a novel and efficient pulse scheme has been found to decompose the Toffoli gate into only one two-qubit and two qubit-qutrit operations, compared to the best known decomposition into two-qubit $CNOT$ and single-qubit operations, which requires six $CNOT$ and ten single-qubit gates. Using quantum process tomography, we have fully characterized the three-qubit operation, and find a gate fidelity of $\sim 69\%$.

At the current state of the art, quantum algorithms [DiCarlo09, Yamamoto10, Dewes11, Lucero12] and quantum operations [DiCarlo10, Mariantoni11b, Baur12, Fedorov12] with up to three superconducting quantum bits have been achieved. In these experiments, single-qubit operations could be realized with fidelities $> 99\%$ [Chow10], and the fidelities of two-qubit operations of $< 90\%$ have mainly been limited by the coherence time of the qubits. While these fidelities are good enough for the demonstration of simple quantum operations with up to three qubits, they are too low to perform experiments with more than four qubits.

An important step towards the realization of a scalable quantum computer with superconducting transmon qubits was the recent increase of qubit coherence by a factor of 100 to almost 1 ms by coupling a transmon qubit to the electromagnetic field inside a three dimensional microwave cavity [Paik11, Rigetti12]. Eventhough this architecture does not seem to be as well suited for scalable quantum computation as the on-chip circuit QED architecture, it allowed to identify the main source of decoherence in transmon qubits. As already suspected several years ago [Martinis05], the most significant contributor is likely the dielectric loss due to two-level states at metal to air and metal to substrate interfaces. Due to the 10 – 100 times larger size of the transmon qubit in these 3D cavities, the electric field between the two electrodes of the transmon qubit is significantly smaller, which in turn makes the qubit less sensitive to surface dielectric loss, in agreement with the experimental results.

An immediate goal for the future should be to try to implement high fidelity gate

operations between two qubits coupled to the same 3D cavity, by using techniques already developed for the planar circuit QED architecture. One example could be to use sideband transitions [Blais07, Leek09, Leek10] as described in Section 6.1. Because not many more than two qubits can be coupled within such a 3D cavity, one then needs to start thinking about how to couple two qubits within two distinct 3D cavities.

Another approach could be to try to increase the coherence times of the transmon qubits coupled to the coplanar waveguide resonators with the help of the insights gained from the 3D cavity experiments. First results in this direction have already been made [Chow12], by increasing the gap between the transmon electrodes from $\sim 2\ \mu\text{m}$ to $10\ \mu\text{m}$. Using such a design, the authors demonstrate coherence times of $\sim 10\ \mu\text{s}$ and single and two-qubit gate operations exceeding 95%. These are no longer limited by qubit coherence, but rather by systematic errors in the pulse calibration. More sophisticated methods to calibrate gate operations should therefore be developed. Furthermore, the increased coherence could open the door to implement quantum teleportation of a single-qubit [Bennett93] and two-qubit [Rigolin05] states including full quantum feedback, entanglement swapping [Żukowski93, Pan98] or even quantum simulation of Hamiltonians [Gerritsma10, Kim10, Ma11, Lanyon11], by scaling the system to more than three qubits.

Eventhough the current fidelities of quantum operations are rather large, they are still too low for large scale quantum computation. As an example, the full quantum algorithm to factor a number 15 requires 4608 gates operating on 21 qubits. It is thus clear, that a quantum computer can probably never be realized without quantum error correction. First experiments in this direction have been made by demonstrating the most basic quantum error correction scheme [Reed12], which is however not fault tolerant and only corrects for either bit or phase flip errors. Next hallmark experiments would therefore be to realize codes that correct for arbitrary errors, such as the 7 qubit Steane code [Steane96a], and to realize simple fault tolerant error correcting codes [Nielsen00] with the big goal in mind to demonstrate a logical qubit, consisting of many physical ones, that never decays. Probably the most promising fault tolerant error correction schemes for superconducting qubits are based on two-dimensional surface codes [Dennis02, Kitaev03, DiVincenzo09]. The error per gate operation threshold for these codes is estimated to be on the order of several percent, close to the values reached in current superconducting qubit experiments. A first layout, consisting of a grid of resonators and four qubits coupled to each of them, is proposed as a possible implementation of the surface

code [DiVincenzo09]. A major step forward would be to demonstrate simple realizations of such qubit-resonator grid structures and then try to scale it up to demonstrate the working principle of surface codes.

A.1 Derivation of the phase ramping for DRAG

The reduced anharmonicity of the transmon qubit requires the use of optimal control techniques to realize fast single qubit operations with high fidelity. As described in [Section 5.4.2](#), we use derivative removal by adiabatic gate (DRAG) pulses [[Motzoi09](#), [Gambetta11](#)] for this purpose. In the derivation for the required pulse shape, the authors assume accurate real time control of the qubit frequency. In experiments however, this is difficult as the relation between the current applied to the flux line and the qubit frequency must be carefully calibrated. Instead, we can replace $\delta_1(t) = \omega_{01}(t) - \omega_d$, where ω_d is the drive frequency, with phase ramping since we can accurately control the phase of the drive applied to the qubit. The Hamiltonian of a three-level system including a drive with amplitude $\varepsilon(t)$, frequency ω_d and a constant and time varying phase ϕ_0 and $\phi(t)$, has the following form

$$\hat{H} = \sum_{k=1}^2 \omega_k |k\rangle\langle k| + \frac{\varepsilon(t)}{2} \lambda_k \left(e^{i(\omega_d t + \phi(t) + \phi_0)} + e^{-i(\omega_d t + \phi(t) + \phi_0)} \right) (|k-1\rangle\langle k| + |k\rangle\langle k-1|). \quad (\text{A.1})$$

Here, $\omega_2 = \omega_1 + \alpha$ with α being the anharmonicity of the qubit and $\lambda_1 = 1$, $\lambda_2 = \sqrt{2}$ weights the relative coupling strength of the 01- and 12-transition, which is a good approximation to the actual matrix elements [\(3.90\)](#) of a transmon qubit. Only the drive terms between nearest neighbor energy levels are taken into account

since other transitions are strongly suppressed due to the near harmonicity of the transmon. After performing the rotating wave approximation, the Hamiltonian reads

$$\hat{H}^{\text{RWA}} = \sum_{k=1}^2 \omega_k |k\rangle\langle k| + \frac{\varepsilon(t)}{2} \lambda_k \left(e^{i(\omega_d t + \phi(t) + \phi_0)} |k-1\rangle\langle k| + h.c. \right). \quad (\text{A.2})$$

We use a rotating frame by applying the unitary transformation

$$\hat{U} = \exp\left(i \sum_{k=1}^2 k(\omega_d t + \phi(t)) |k\rangle\langle k|\right). \quad (\text{A.3})$$

In this frame, the Hamiltonian $\hat{H}_{\text{RF}}^{\text{RWA}} = \hat{U} \hat{H}^{\text{RWA}} \hat{U}^\dagger - i \hat{U} \dot{\hat{U}}^\dagger$ reads

$$\begin{aligned} \hat{H}_{\text{RF}}^{\text{RWA}} &= \begin{pmatrix} 0 & \frac{\varepsilon}{2} e^{i\phi_0} & 0 \\ \frac{\varepsilon}{2} e^{-i\phi_0} & \omega_1 - \omega_d - \dot{\phi}(t) & \lambda_2 \frac{\varepsilon}{2} e^{i\phi_0} \\ 0 & \lambda_2 \frac{\varepsilon}{2} e^{-i\phi_0} & \alpha + 2\omega_1 - 2\omega_d - 2\dot{\phi}(t) \end{pmatrix} \\ &= \begin{pmatrix} 0 & \frac{\varepsilon_x(t) + i\varepsilon_y(t)}{2} & 0 \\ \frac{\varepsilon_x(t) - i\varepsilon_y(t)}{2} & \omega_1 - \omega_d - \dot{\phi}(t) & \lambda_2 \frac{\varepsilon_x(t) + i\varepsilon_y(t)}{2} \\ 0 & \lambda_2 \frac{\varepsilon_x(t) - i\varepsilon_y(t)}{2} & \alpha + 2\omega_1 - 2\omega_d - 2\dot{\phi}(t) \end{pmatrix}, \end{aligned} \quad (\text{A.4})$$

where $\varepsilon_x(t) = \varepsilon(t) \cos(\phi_0)$ and $\varepsilon_y(t) = \varepsilon(t) \sin(\phi_0)$. Note here that the definition of ε_y in the DRAG paper [Motzoi09, Gambetta11] differs by a factor of -1 from the one used above! This relates to the fact that in the DRAG paper, the phase of the drive is $\phi_0 = -\frac{\pi}{2}$ for a y-pulse, whereas in the above definition it is $\phi_0 = +\frac{\pi}{2}$. Let us now consider the two cases, where first the drive frequency matches the qubit frequency ($\omega_d = \omega_1$), and second the drive is slightly off-resonant from the qubit.

Resonant case

Comparing the two Hamiltonians (5.11) and (A.4) for the condition where $\omega_1 - \omega_d = 0$, we find that the negative derivative of the time dependent phase of the drive must be equal to the qubit frequency shift $-\dot{\phi}(t) = \delta_1(t)$. Thus, an equivalent effect can

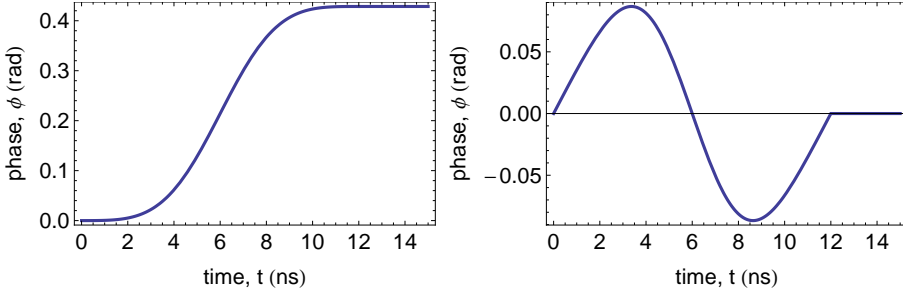


Figure A.1: The time dependent phases during a DRAG pulse with phase ramping, with a standard deviation of $\sigma = 3$ ns, truncation 2 and a maximal Rabi frequency of 100 MHz. The total duration of the pulse is 12 ns. Left panel: Phase ramping in the resonant case. Right panel: Phase ramping in the off-resonant case.

be made use of by phase ramping

$$\phi(t) = - \int_0^t \delta_1(s) ds. \quad (\text{A.5})$$

An example of this phase ramping for a typical DRAG pulse is shown in the left panel of [Figure A.1](#). The phase starts from zero, increases monotonically and ends at a value bigger than zero. If a second pulse is applied, the next phase ramp needs to start with the phase at the end of the previous pulse. This means that for this implementation, the phases of all previous pulses has to be tracked.

Off-resonant case

Let us assume, that the drive is slightly detuned from the qubit frequency by the average value of the time dependent qubit frequency pull discussed in the DRAG paper [[Motzoi09](#), [Gambetta11](#)] ($\omega_1 - \omega_d = \delta_{\text{average}}$), with

$$\delta_{\text{average}} = \frac{1}{t_g} \int_0^{t_g} \delta_1(t) dt. \quad (\text{A.6})$$

Here, t_g is total length of the pulse. If we now compare the two Hamiltonians [\(5.11\)](#) and [\(A.4\)](#), we find $\delta_{\text{average}} - \dot{\phi}(t) = \delta_1(t)$. Solving this differential equation results

in

$$\phi(t) = - \int_0^t (\delta_1(s) - \delta_{\text{average}}) ds, \quad (\text{A.7})$$

which is identical to the phase ramping described in the DRAG paper. An example for a typical DRAG pulse is shown in the right panel of [Figure A.1](#). The difference to [\(A.5\)](#) is that here, the phase at the beginning and end of the pulse is zero. We thus don't have to track the phases of all previous pulses in a pulse train. However, since the drive is off-resonant, phase is accumulated during the waiting time between pulses. This phase has to be tracked and added accordingly to the pulses. This version of phase ramping has therefore no advantage over [\(A.5\)](#) and only adds complexity due to the off-resonant driving.

A.2 Quantum state and quantum process tomography

A.2.1 State maximum-likelihood estimation

In order to experimentally determine an expectation value of a Hermitian operator $\langle \hat{M}_k \rangle$, a single measurement of the operator \hat{M}_k is not enough. The experiment must be repeated N times, and the statistical mean of all measurement outcomes gives an estimate m_k of $\langle \hat{M}_k \rangle$. Even for a perfect measurement apparatus however, this estimate always has a statistical uncertainty (a standard deviation of $1/\sqrt{N}$), which only goes to zero for infinitely many repetitions of the experiment. Furthermore, in real experiments, additional noise is added due to an imperfect measurement apparatus. The perfect reconstruction of a quantum state from the measured estimates m_k with quantum state tomography is thus not possible. Instead, we can find the state, which is most likely to yield m_k . In this maximum-likelihood estimation, one assumes that the m_k obey the Gaussian probability distribution

$$p(m_k | \hat{\rho}) = \frac{1}{\sqrt{2\pi}\sigma_k} e^{-(m_k - \text{Tr}(\hat{M}_k \hat{\rho}))^2 / (2\sigma_k^2)}, \quad (\text{A.8})$$

with the standard deviation σ_k . The most likely state $\hat{\rho}$ is then found by maximizing the likelihood function

$$\mathcal{L} = \prod_k \frac{1}{\sqrt{2\pi}\sigma_k} e^{-(m_k - \text{Tr}(\hat{M}_k \hat{\rho}))^2 / (2\sigma_k^2)}, \quad (\text{A.9})$$

or by minimizing the log likelihood function [James01]

$$\mathcal{L}_{\log} = \sum_k \frac{1}{2\sigma_k^2} (m_k - \text{Tr}(\hat{M}_k \hat{\rho}))^2. \quad (\text{A.10})$$

We can further assume that $\sigma_k = \sigma_{k'}$ for all $k = k'$, since the main contribution to the noise is amplifier noise, whose magnitude is independent of the measurement observable. Minimizing the log likelihood function (A.10) is then equivalent to minimizing [Smolin12]

$$\|\hat{\mu} - \hat{\rho}\|_2^2 = \text{Tr}[(\hat{\mu} - \hat{\rho})^2] = \sum_{ij} |\mu_{ij} - \rho_{ij}|^2, \quad (\text{A.11})$$

where $\hat{\mu}$ is the non-physical noisy “density” matrix reconstructed with state tomography from the noisy measurement results m_k . By construction, this matrix is Hermitian and has trace 1, but may have negative eigenvalues. In practice, Equation (A.11) is minimized with standard minimization functions, such as *FindMinimum* in *Mathematica 8.0*. Finding the solution however can be computationally expensive. As shown by Smolin *et al.* [Smolin12], one can do much better by realizing that the 2-norm is basis independent, such that we can use an eigenbasis of $\hat{\mu}$. Due to the square in Equation (A.11), it is clear that $\hat{\rho}$ is also diagonal in this basis because all off-diagonal terms could only increase the 2-norm. To find the most likely physical density matrix (positive-semidefinite, Hermitian with trace 1) we just need to minimize

$$\sum_i (\mu_i - \lambda_i)^2 \text{ such that } \sum_i \mu_i = \sum_i \lambda_i \text{ and } \lambda_i \geq 0. \quad (\text{A.12})$$

This can be accomplished very efficiently using this algorithm¹ [Smolin12]

1. Calculate the eigenvalues and eigenvectors of $\hat{\mu}$. Arrange the eigenvalues in order from largest to smallest. Call these μ_i , $|\mu_i\rangle$, $1 \leq i \leq d$, where d is the dimension of the density matrix.
2. Let $i = d$ and set an accumulator $a = 0$.
3. If $\mu_i + a/i$ is non-negative, go on to step 4. Otherwise, set $\lambda_i = 0$ and add μ_i to a . Reduce i by 1 and repeat step 3.

¹We have implemented this algorithm in *Mathematica* which can be found in the *StateTomography.m* library under the name *MLState*.

4. Set $\lambda_j = \mu_j + a/i$ for all $j \leq i$.
5. Construct $\hat{\rho} = \sum_i \lambda_i |\lambda_i\rangle\langle\lambda_i|$.

A.2.2 Quantum process tomography

Assume that we are given a black box which performs an arbitrary quantum operation on a quantum system $\hat{\rho}$ and returns $\hat{\rho}'$

$$\hat{\rho}' = \mathcal{E}(\hat{\rho}). \quad (\text{A.13})$$

This process is fully described by a linear, completely positive map \mathcal{E} from the set of density operators onto itself, and includes the dynamics of any unitary operation, measurement or decoherence. It can be shown, that (A.13) can be written in the operator-sum representation

$$\mathcal{E}(\hat{\rho}) = \sum_k \hat{E}_k \hat{\rho} \hat{E}_k^\dagger, \quad (\text{A.14})$$

where the operation element (also called Kraus operators) \hat{E}_k satisfy $\sum_k \hat{E}_k^\dagger \hat{E}_k \leq \hat{I}$. Equality is given if the quantum process is trace preserving, which means that the trace of $\hat{\rho}'$ is equal to the trace of $\hat{\rho}$. The goal of quantum process tomography is to determine all the \hat{E}_k 's, which fully describe the quantum process \mathcal{E} .

There are four different common approaches to process tomography. (1) Standard quantum process tomography [Chuang97, Poyatos97, Childs01, O'Brien04] which involves preparing a complete set of input states, applying the quantum process to be characterized to each of them, and then performing quantum state tomography on every output. (2) Ancilla-assisted process tomography which introduces an extra ancilla qubit and involves the preparation and tomography of only one input state of the combined system, rather than a set of input states [D'Ariano01, Altepeter03, D'Ariano03]. (3) As a special case of ancilla-assisted process tomography, entanglement-assisted process tomography describes the situation where the ancilla is initially maximally entangled with the system being characterized. (4) Single-measurement ancilla-assisted process tomography has also been proposed [Mohseni06], where a single joint measurement of the system under consideration combined with an ancilla system is performed on a set of input states. No state tomography is required in this case.

Depending on the experimental system that is used, one or the other implementa-

tion might be easier to realize. In this thesis, I only present the standard quantum process tomography in more detail. I will closely follow the derivation given in the book by Nielsen & Chuang [Nielsen00].

In order to determine the Kraus operators \hat{E}_k from experimentally extracted expectation values, it is convenient to first transform Equation (A.14) into the so called χ matrix representation. To do so, choose a fixed basis $\{\hat{E}_k\}$ for the operators \hat{E}_k on the state space and express the operation elements as a linear combination of the basis states $\hat{E}_k = \sum_m e_{km} \hat{E}_m$, where the coefficients e_{km} are complex numbers. Substituting \hat{E}_k in Equation (A.14) we may rewrite the equation in the χ matrix representation

$$\mathcal{E}(\hat{\rho}) = \sum_{mn} \hat{E}_m \hat{\rho} \hat{E}_n^\dagger \chi_{mn}, \quad (\text{A.15})$$

where $\chi_{mn} = \sum_i e_{im} e_{in}^*$ is a positive semidefinite Hermitian matrix and has trace one if the quantum process is trace preserving. Since $\hat{E}_{m/n}$ and $\hat{\rho}$ are known, this χ matrix completely describes the quantum process in the chosen operator basis. The choice of basis is in principle arbitrary, but it is common to express the basis in terms of the Pauli matrices σ_i and the identity matrix \hat{I} . We have chosen the basis $\{\hat{I}, \hat{\sigma}_x, -i\hat{\sigma}_y, \hat{\sigma}_z\}$, where $\hat{\sigma}_y$ is multiplied with $-i$ to make all basis operators real. This ensures that complex entries in operation elements appear as complex entries in the χ matrix. The goal now is to determine χ experimentally from measurable quantities.

To do so, we choose a fixed linearly independent basis $\{\hat{\rho}_j\}$ for the space of $d \times d$ matrices, where d is the dimension of the state space. Since the output of a quantum process is always a density matrix, we may write the output state of a quantum process applied to a basis element as a linear combination of the basis matrices

$$\mathcal{E}(\hat{\rho}_j) = \sum_k \lambda_{jk} \hat{\rho}_k. \quad (\text{A.16})$$

In order to determine the complex coefficients λ_{jk} experimentally, we measure the output state $\mathcal{E}(\hat{\rho}_j)$ for all basis states with quantum state tomography. λ_{jk} is then extracted by solving the set of linear equations (A.16). The choice of the basis states $\{\hat{\rho}_j\}$ is again arbitrary, up to the fact that they have to be experimentally realizable. We have chosen $\hat{\rho}_j \rightarrow \{|0\rangle\langle 0|, |1\rangle\langle 1|, |-\rangle\langle -|, |+\rangle\langle +|\}$ for single qubit quantum process tomography, and all the tensor products of these for n-qubit QPT. Here $|-\rangle = (|0\rangle - i|1\rangle)/\sqrt{2}$ and $|+\rangle = (|0\rangle + |1\rangle)/\sqrt{2}$.

The goal now is to extract the process matrix χ from the experimentally deter-

mined λ . For this, we may write

$$\hat{E}_m \hat{\rho}_j \hat{E}_n^\dagger = \sum_k \beta_{jk}^{mn} \hat{\rho}_k, \quad (\text{A.17})$$

where β is a complex matrix which can be determined without any measurements from the given \hat{E}_m and $\hat{\rho}_j$. From Equations (A.15, A.16, A.17) and the linear independence of the basis operators $\hat{\rho}_j$, it follows

$$\sum_{mn} \beta_{jk}^{mn} \chi_{mn} = \lambda_{jk} \quad (\text{A.18})$$

With the knowledge of β and λ , this system of linear equations can be solved for χ .² Having determined χ , the operator-sum representation (A.14) for \mathcal{E} is obtained in the following manner. Let the unitary matrix \hat{U}^\dagger diagonalize χ such that the matrix equation $D = \hat{U}^\dagger \chi \hat{U}$ is satisfied, where D is the diagonal matrix. The operation elements are then constructed with the equation

$$\hat{E}_k = \sqrt{D_{kk}} \sum_j \hat{U}_{jk} \hat{E}_j. \quad (\text{A.19})$$

As a summary, process tomography involves the following steps:

1. Chose a fixed linearly independent basis $\{\hat{\rho}_j\}$ for the space of $d \times d$ matrices and perform state tomography on the output of the quantum process applied to all basis states. Extract from this measurement the matrix λ .
2. Chose a fixed basis $\{\hat{E}_k\}$ for the space of operators acting on the state space and calculate the matrix β for the given basis $\hat{\rho}_j$.
3. Calculate the χ matrix from the knowledge of λ and β .

A.2.3 Process maximum-likelihood estimation

As for quantum state tomography (see Section A.2.1), the χ matrix obtained with the procedure explained above is not necessarily physical due to the presence of noise on the measurement signal. Therefore, the goal is to find the physical matrix χ^{ML} (which describes a completely positive map and is Hermitian) that is

²For example in *Mathematica 8.0* with the *LeastSquares* function.

most likely to give the measured data and fulfills the additional trace preservation constraint $\sum_{mn} \chi_{mn} \hat{E}_n^\dagger \hat{E}_m = \hat{I}$. To accomplish this task we first write a Hermitian parametrization of χ^{ML} using the Cholesky decomposition

$$\chi^{\text{ML}}(\vec{t}) = T^\dagger T, \quad (\text{A.20})$$

where T is a lower triangular matrix parametrized by the vector \vec{t} . If we assume that the measured data m_{jk} are normally distributed (A.8), then we can find the closest χ^{ML} by minimizing the function [O'Brien04]

$$\mathcal{L}(\vec{t}) = \sum_{jk} \left[m_{jk} - \sum_{mn} \chi_{mn}^{\text{ML}}(\vec{t}) \text{Tr}(\hat{M}_k \hat{E}_m \hat{\rho}_j \hat{E}_n^\dagger) \right]^2 \quad (\text{A.21})$$

$$+ \lambda \sum_i \left[\sum_{m,n} \chi_{mn}^{\text{ML}}(\vec{t}) \text{Tr}(\hat{E}_m \hat{E}_i \hat{E}_n^\dagger) - \text{Tr}(\hat{E}_i) \right]. \quad (\text{A.22})$$

Here, m_{jk} is the measurement outcome for the case that the state $\hat{\rho}_j$ was prepared and the observable \hat{M}_k was measured, and λ is the Lagrange multiplier. To solve this minimization problem we use the iterative algorithm described in [Jeřek03].

A.3 Entanglement classes

While most physicists are familiar with entanglement between two quantum systems, the properties of entanglement between multiple quantum systems are typically less well known. Besides the fully separable and fully entangled states, there also exist many types of partial separability. Additionally, the different types of entanglement can then be further divided into different entanglement classes. I thus shortly review the basic principles for tripartite systems.

Let us first consider a pure three-qubit state. It is called *fully separable*, if states $|\alpha\rangle_A$, $|\beta\rangle_B$ and $|\gamma\rangle_C$ of the three subsystems can be found such that the three-qubit state can be written as

$$|\psi^{\text{fs}}\rangle_{ABC} = |\alpha\rangle_A \otimes |\beta\rangle_B \otimes |\gamma\rangle_C. \quad (\text{A.23})$$

A state is called *biseparable*, if it is not fully separable, but can be written as a product between a one-qubit and a non-separable two-qubit state $|\delta\rangle$. The three

possibilities of grouping the quantum systems are

$$|\psi^{\text{bs}}\rangle_{A(BC)} = |\alpha\rangle_A \otimes |\delta\rangle_{BC}, \quad (\text{A.24})$$

$$|\psi^{\text{bs}}\rangle_{B(AC)} = |\beta\rangle_B \otimes |\delta\rangle_{AC}, \quad (\text{A.25})$$

$$|\psi^{\text{bs}}\rangle_{C(AB)} = |\gamma\rangle_C \otimes |\delta\rangle_{AB}. \quad (\text{A.26})$$

A three-qubit state is *genuine tripartite entangled*, if it is neither fully separable nor biseparable. This type of states can further be classified into the GHZ and the W class. Even though the states in both classes are genuinely tripartite entangled, they cannot be transformed into each other using stochastic local operations and classical communication [Dür00]. An example for a state in the GHZ and W class, respectively, is the Greenberger-Horne-Zeilinger (GHZ) state [Greenberger90]

$$|\text{GHZ}_3\rangle = \frac{1}{\sqrt{2}} (|000\rangle + |111\rangle), \quad (\text{A.27})$$

and the W state [Dür00]

$$|W_3\rangle = \frac{1}{\sqrt{3}} (|001\rangle + |010\rangle + |100\rangle). \quad (\text{A.28})$$

These states have a significantly different entanglement robustness against particle loss. While $|\text{GHZ}_3\rangle$ turns into a separable state $\hat{\rho}_{AB} = \text{Tr}_C (|\text{GHZ}_3\rangle\langle\text{GHZ}_3|) = \sum_i \langle i|_C |\text{GHZ}_3\rangle\langle\text{GHZ}_3| |i\rangle_C$, the reduced density matrix of the W state $\hat{\rho}_{AB} = \text{Tr}_C (|W_3\rangle\langle W_3|)$ remains entangled.

The definition of separability can readily be extended to mixed states. A mixed state $\hat{\rho}^{\text{fs}}$ is called *fully separable*, if it can be written as a convex combination of fully separable pure states

$$\hat{\rho}^{\text{fs}} = \sum_i p_i |\psi_i^{\text{fs}}\rangle\langle\psi_i^{\text{fs}}|, \quad (\text{A.29})$$

with probabilities $p_i \geq 0$. A state $\hat{\rho}^{\text{bs}}$ is *biseparable*, if it is not fully separable, but can be written as a convex combination of pure biseparable states

$$\hat{\rho}_{A(BC)}^{\text{bs}} = \sum_i p_i |\psi_i^{\text{bs}}\rangle\langle\psi_i^{\text{bs}}|, \quad (\text{A.30})$$

where each $|\psi_i^{\text{bs}}\rangle$ is biseparable with respect to at least one of the three possible

partitions $(A(BC), B(AC), C(AB))$. Finally, a state $\hat{\rho}$ is genuinely tripartite entangled if it is neither fully separable nor biseparable. Again there are the two different entanglement classes, and they can be written as convex combinations of the pure GHZ or W class states, respectively. A graphical representation of the convex sets of the different entanglement classes is shown in [Figure A.2](#).

A.4 Entanglement measures

In any experiment that creates entangled states, we would like to be able to ensure that entanglement really was produced, to determine the type of entanglement and further to quantify the degree of entanglement in the system. There are many ways to accomplish this task, including entanglement monotones to quantify entanglement (shortly introduced in this section) and entanglement witnesses to detect entanglement ([Section A.5](#)). More information can be found in the review articles [[Horodecki09](#), [Gühne09](#), [Plenio07](#)].

The two properties that any entanglement measure $E(\hat{\rho})$ should possess are the following [[Bennett96](#), [Horodecki09](#)]

1. $E(\hat{\rho}) = 0$ if $\hat{\rho}$ is separable,
2. *Monotonicity under LOCC*: Entanglement cannot increase under local operations and classical communication (LOCC). For any LOCC operation Λ the following must be fulfilled

$$E(\Lambda(\hat{\rho})) \leq E(\hat{\rho}). \quad (\text{A.31})$$

Any function E satisfying these conditions is called an entanglement monotone, and is used to quantify the degree of entanglement present in a state $\hat{\rho}$. More specifically, for a bipartite system, it gives $E(\hat{\rho}) = 0$ for a separable state, and monotonically increases as the amount of entanglement is increased. A state $\hat{\rho}$ is called maximally entangled, such as a Bell state, if $E(\hat{\rho})$ is maximal. For a multipartite entangled state, this mapping is not that simple anymore. The term maximal entanglement is no longer well defined, since it depends on the chosen entanglement measure. Additionally, one needs to distinguish between many different classes of entanglement. Some examples of entanglement monotones for bipartite and tripartite systems are the concurrence, entanglement of formation and three tangle, as described in [Section A.4.2](#), [Section A.4.3](#) and [Section A.4.4](#).

A.4.1 Convex roof extension

When searching for new entanglement monotones, it is often easiest to first define one for pure states $E(|\psi\rangle)$. It can then be extended to mixed states by the convex roof construction [Uhlmann98]

$$E(\hat{\rho}) = \inf \sum_i p_i E(|\phi_i\rangle). \quad (\text{A.32})$$

Here, the infimum is taken over all possible decompositions of $\hat{\rho}$ into pure states, i.e. over all p_i and $|\phi_i\rangle$ for which $\hat{\rho} = \sum_i p_i |\phi_i\rangle\langle\phi_i|$. The optimization of Equation (A.32) is in general not straightforward to compute. There are only a few examples where analytic results are known. One such example is the concurrence, see Section A.4.2. For the other cases, the optimization can be performed numerically [Cao10].

A.4.2 Concurrence

An example of an entanglement monotone defined for bipartite entanglement is the concurrence, which was first introduced by [Hill97] for pure states. Any pure two-qubit state defined in the Hilbert space $\mathcal{H} = \mathcal{H}_A \otimes \mathcal{H}_B$ can be written as a linear combination of the computational basis states

$$|\psi\rangle = a_{00}|00\rangle + a_{01}|01\rangle + a_{10}|10\rangle + a_{11}|11\rangle. \quad (\text{A.33})$$

The concurrence is then defined as

$$C(|\psi\rangle) = 2|a_{00}a_{11} - a_{01}a_{10}|. \quad (\text{A.34})$$

Sometimes one can also find the definition [Horodecki09]

$$C(|\psi\rangle) = \sqrt{2(1 - \text{Tr}[\hat{\rho}_A^2])}, \quad (\text{A.35})$$

where $\hat{\rho}_A = \text{Tr}_B |\psi\rangle\langle\psi|$ is the reduced state of $|\psi\rangle$ on subsystem A. This monotone is bounded between 0 for separable states and 1 for maximally entangled two-qubit states.

There are two reasons why this measure is important. First, the concurrence is directly related to the entanglement of formation of two qubits, see Section A.4.3. Second, it can easily be extended to mixed states as the convex roof can be analytically computed [Wootters98]. Given the mixed state $\hat{\rho}$, it is calculated according to

the formula

$$C(\hat{\rho}) = \max \{0, \sqrt{\lambda_1} - \sqrt{\lambda_2} - \sqrt{\lambda_3} - \sqrt{\lambda_4}\}, \quad (\text{A.36})$$

in which $\lambda_1, \dots, \lambda_4$ are the eigenvalues in decreasing order of the expression

$$\hat{\rho}(\hat{\sigma}_y \otimes \hat{\sigma}_y)\hat{\rho}^*(\hat{\sigma}_y \otimes \hat{\sigma}_y). \quad (\text{A.37})$$

A.4.3 Entanglement of formation

The entanglement of formation of a mixed two-qubit state $\hat{\rho}$ [Bennett96] is the minimum average entanglement of an ensemble of pure states that represents $\hat{\rho}$. It is closely connected to the von Neumann entropy [Gühne09]. For an arbitrary state of two qubits, this quantity can directly be calculated from the concurrence C by [Wootters98]

$$E_F(\hat{\rho}) = h\left(\frac{1 + \sqrt{1 - C^2(\hat{\rho})}}{2}\right), \quad (\text{A.38})$$

$$h(x) = -x \log_2 x - (1 - x) \log_2(1 - x). \quad (\text{A.39})$$

$E_F(\hat{\rho})$ is a monotonically increasing function of the concurrence C and ranges from 0 to 1 as C goes from 0 to 1.

A.4.4 Three-tangle

The three-tangle τ_3 (residual entanglement), as introduced in [Coffman00], is an entanglement measure for pure three-qubit states $|\psi\rangle = \sum_{i,j,k=0}^1 a_{ijk}|ijk\rangle$. It is defined as

$$\tau_3 = C_{A(BC)}^2 - C_{AB}^2 - C_{AC}^2. \quad (\text{A.40})$$

Here, C_{AB} is the concurrence between qubit A and B, and $C_{A(BC)}$ is the concurrence between qubit A and the other two qubits. Even though the state space of BC is four dimensional, it makes sense to speak of the concurrence $C_{A(BC)}$, because only two of those dimensions are necessary to express the state $|\psi\rangle$ (the two dimensions that are spanned by the eigenstates of $\hat{\rho}_{BC}$ corresponding to the nonzero eigenvalues) [Coffman00]. We can thus regard A and BC as two qubits. This is true because A is a qubit and the three-qubit state is pure. In words, Equation (A.40) states that the full entanglement of A with BC consists of three forms: entanglement with B, entanglement with C, and a three-way entanglement of the triplet. The

three tangle has the following properties:

- $\tau_3 = 0$ for any (bi-)separable state.
- $\tau_3 = 1$ for the GHZ class states, because each qubit pair is only classically correlated ($C_{AB} = C_{AC} = 0$).
- τ_3 may also vanish for some pure tripartite entangled states, which still contain bipartite entanglement when tracing out one subsystem ($C_{AB}, C_{AC} \neq 0$). An example is the W state, where $\tau_3 = 0$.

We can calculate the three-tangle for pure states using the equation [Coffman00]

$$\tau_3 = 4|d_1 - 2d_2 + 4d_3|, \quad (\text{A.41})$$

where

$$d_1 = a_{000}^2 a_{111}^2 + a_{001}^2 a_{110}^2 + a_{010}^2 a_{101}^2 + a_{100}^2 a_{011}^2, \quad (\text{A.42})$$

$$d_2 = a_{000} a_{111} a_{011} a_{100} + a_{000} a_{111} a_{101} a_{010} + a_{000} a_{111} a_{110} a_{001} \\ + a_{011} a_{100} a_{101} a_{010} + a_{011} a_{100} a_{110} a_{001} + a_{101} a_{010} a_{110} a_{001}, \quad (\text{A.43})$$

$$d_3 = a_{000} a_{110} a_{101} a_{011} + a_{111} a_{001} a_{010} a_{100}. \quad (\text{A.44})$$

For mixed states, the three-tangle can numerically be computed via the convex roof extension [Cao10].

A.5 Entanglement witnesses

One drawback of the entanglement monotones is the fact that one needs to reconstruct the full density matrix in order to quantify the amount of entanglement a state has. Furthermore, there may exist no entanglement measure for a certain state, and if it exists, it may be computationally expensive to compute the convex roof extension for mixed states. One therefore often makes use of so called entanglement witnesses to determine whether an experimentally prepared mixed state contains entanglement. An entanglement witness is formally defined as a Hermitian operator \hat{W} , which fulfills the following properties [Horodecki96]

$$\begin{aligned} \text{Tr}(\hat{W}\hat{\rho}_s) &\geq 0 && \text{for all separable states } \hat{\rho}_s, \\ \text{Tr}(\hat{W}\hat{\rho}_e) &< 0 && \text{for at least one entangled state } \hat{\rho}_e. \end{aligned} \quad (\text{A.45})$$

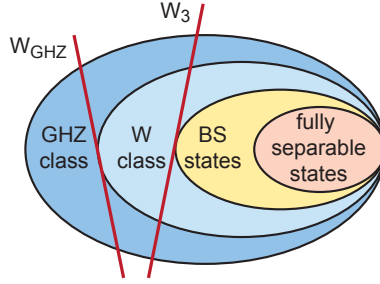


Figure A.2: Schematic picture of the structure of mixed three qubit states that is formed by a convex set of fully separable states surrounded by the convex sets of biseparable (BS) and genuine tripartite entangled states (consisting of the W and GHZ class). The different entanglement classes can be detected using a witness $\hat{\mathcal{W}}$ represented by a hyperplane (one of the red solid lines) that cuts the space into two halves. All states $\hat{\rho}$ along the hyperplane give an expectation value $\text{Tr}(\hat{\mathcal{W}}\hat{\rho}) = 0$. The entanglement of the states on the left side is detected by \mathcal{W} , as these states give a negative expectation value.

Since $\hat{\mathcal{W}}$ is a Hermitian operator, it is a measurable quantity and thus very useful in experiments where the quantum state $\hat{\rho}$ cannot fully be reconstructed. If one measures a negative expectation value of the observable $\hat{\mathcal{W}}$, one knows for sure that $\hat{\rho}$ is entangled, otherwise, no information can be gained. One says that entanglement of $\hat{\rho}$ is detected by $\hat{\mathcal{W}}$ if and only if $\text{Tr}(\hat{\mathcal{W}}\hat{\rho}) < 0$.

In the same way, one can also define witness operators which can be used to distinguish between different classes of multipartite entanglement. How this works is best illustrated with [Figure A.2](#). It visualizes the structure of mixed three qubit states that is formed by a convex set of fully separable states surrounded by the convex sets of biseparable (BS) and genuine tripartite entangled states (W and GHZ class). These sets of states are cut into two halves by a hyperplane (one of the red lines depicted in [Figure A.2](#), depending on the witness considered) corresponding to an entanglement witness $\hat{\mathcal{W}}$, defined by the set of states for which $\text{Tr}(\hat{\mathcal{W}}\hat{\rho}) = 0$. All the states on the left side of the hyperplane are entangled and detected by $\hat{\mathcal{W}}$ since $\text{Tr}(\hat{\mathcal{W}}\hat{\rho}) < 0$. All states on the right side give $\text{Tr}(\hat{\mathcal{W}}\hat{\rho}) \geq 0$, for which no statement about the separability can be made.

An entanglement witness can be constructed by using the fact that states close to an entangled pure state $|\psi\rangle$ must also be entangled. For a given entangled pure

state $|\psi\rangle$ one can thus define down the witness operator [Gühne09]

$$\hat{\mathcal{W}} = \alpha \hat{I} - |\psi\rangle\langle\psi|. \quad (\text{A.46})$$

Here,

$$\alpha = \max|\langle\phi|\psi\rangle|^2 \quad (\text{A.47})$$

is the maximal overlap between $|\psi\rangle$ and all fully separable, biseparable or W class pure states $|\phi\rangle$, respectively, depending on which type of states one wants to exclude. If we want to distinguish between the GHZ and the W class for example, we can use the witness operator

$$\hat{\mathcal{W}}_{\text{GHZ}} = \frac{3}{4} \hat{I} - |\text{GHZ}_3\rangle\langle\text{GHZ}_3|. \quad (\text{A.48})$$

The constant 3/4 is the maximal overlap between the state $|\text{GHZ}_3\rangle$ and all the pure W class states [Acín01]. This means that if an experimentally prepared state ρ has a fidelity larger than 0.75 with respect to $|\text{GHZ}_3\rangle$, then we can be sure that we prepared a GHZ class state.

A witness operator for detecting genuine tripartite entanglement around the GHZ state $|\text{GHZ}_3\rangle$ without distinguishing between the GHZ and W class is given by

$$\hat{\mathcal{W}}_3 = \frac{1}{2} \hat{I} - |\text{GHZ}_3\rangle\langle\text{GHZ}_3|, \quad (\text{A.49})$$

and around the W state $|W_3\rangle$ it is

$$\hat{\mathcal{W}}_W = \frac{2}{3} \hat{I} - |W_3\rangle\langle W_3|. \quad (\text{A.50})$$

In general, the computation of α is not straightforward. If we are just interested in the maximal overlap between a state $|\psi\rangle$ and all biseparable states however, a step by step procedure is provided in [Bourennane04].

Bibliography

- [Abdumalikov10] A. A. Abdumalikov, O. Astafiev, A. M. Zagoskin, Y. A. Pashkin, Y. Nakamura, and J. S. Tsai. “Electromagnetically induced transparency on a single artificial atom.” *Phys. Rev. Lett.*, **104**, 193601 (2010). Cited on page 4.
- [Acín01] A. Acín, D. Bruß, M. Lewenstein, and A. Sanpera. “Classification of mixed three-qubit states.” *Phys. Rev. Lett.*, **87**, 040401 (2001). Cited on page 200.
- [Aliferis04] P. Aliferis and D. W. Leung. “Computation by measurements: A unifying picture.” *Phys. Rev. A*, **70**, 062314 (2004). Cited on page 156.
- [Allen87] L. Allen and J. Eberly. *Optical resonance and two-level atoms*. Dover (1987). Cited on page 92.
- [Altepeter03] J. B. Altepeter, D. Branning, E. Jeffrey, T. C. Wei, P. G. Kwiat, R. T. Thew, J. L. O’Brien, M. A. Nielsen, and A. G. White. “Ancilla-assisted quantum process tomography.” *Phys. Rev. Lett.*, **90**, 193601–(2003). Cited on page 190.
- [Altomare10] F. Altomare, J. I. Park, K. Cicak, M. A. Sillanpää, M. S. Allman, D. Li, A. Sirois, J. A. Strong, W. J. D., and R. W. Simmonds.

- “Tripartite interactions between two phase qubits and a resonant cavity.” *Nat. Phys.*, **6**, 777 – 781 (2010). Cited on pages 4 and 40.
- [Ambegaokar63] V. Ambegaokar and A. Baratoff. “Tunneling between superconductors.” *Phys. Rev. Lett.*, **10**, 486 (1963). Cited on page 24.
- [Anderson63] P. Anderson and J. Rowell. “Probable observation of the josephson superconducting tunneling effect.” *Phys. Rev. Lett.*, **10**, 230 (1963). Cited on page 21.
- [Ansmann09] M. Ansmann, H. Wang, R. C. Bialczak, M. Hofheinz, E. Lucero, M. Neeley, A. D. O’Connell, D. Sank, M. Weides, J. Wenner, A. N. Cleland, and J. M. Martinis. “Violation of Bell’s inequality in Josephson phase qubits.” *Nature*, **461**, 504–506 (2009). Cited on page 4.
- [Astafiev07] O. Astafiev, K. Inomata, A. O. Niskanen, T. Yamamoto, Y. A. Pashkin, Y. Nakamura, and J. S. Tsai. “Single artificial-atom lasing.” *Nature*, **449**, 588–590 (2007). Cited on page 4.
- [Astafiev10] O. Astafiev, A. M. Zagoskin, A. A. Abdumalikov Jr., Y. A. Pashkin, T. Yamamoto, K. Inomata, Y. Nakamura, and J. S. Tsai. “Resonance fluorescence of a single artificial atom.” *Science*, **327**, 840–843 (2010). Cited on pages 4 and 95.
- [Autler55] S. H. Autler and C. H. Townes. “Stark effect in rapidly varying fields.” *Phys. Rev.*, **100**, 703–722 (1955). Cited on pages 90 and 94.
- [Barenco95] A. Barenco, C. H. Bennett, R. Cleve, D. P. DiVincenzo, N. Margolus, P. Shor, T. Sleator, J. A. Smolin, and H. Weinfurter. “Elementary gates for quantum computation.” *Phys. Rev. A*, **52**, 3457–3467 (1995). Cited on page 169.
- [Barends11] R. Barends, J. Wenner, M. Lenander, Y. Chen, R. C. Bialczak, J. Kelly, E. Lucero, P. O’Malley, M. Mariantoni, D. Sank, H. Wang, T. C. White, Y. Yin, J. Zhao, A. N. Cleland, J. M. Martinis, and J. J. A. Baselmans. “Minimizing quasiparticle generation from stray infrared light in superconducting quantum circuits.” *Appl. Phys. Lett.*, **99**, 113507 (2011). Cited on page 101.

- [Barrett04] M. Barrett, J. Chiaverini, T. Schaetz, J. Britton, W. Itano, J. Jost, E. Knill, C. Langer, D. Leibfried, R. Ozeri, and D. Wineland. “Deterministic quantum teleportation of atomic qubits.” *Nature*, **429**, 737–739 (2004). Cited on page 156.
- [Baur09] M. Baur, S. Filipp, R. Bianchetti, J. M. Fink, M. Göppl, L. Steffen, P. J. Leek, A. Blais, and A. Wallraff. “Measurement of autler-townes and mollow transitions in a strongly driven superconducting qubit.” *Physical Review Letters*, **102**, 243602–4 (2009). Cited on pages 4, 90 and 95.
- [Baur12] M. Baur, A. Fedorov, L. Steffen, S. Filipp, M. P. da Silva, and A. Wallraff. “Benchmarking a quantum teleportation protocol in superconducting circuits using tomography and an entanglement witness.” *Phys. Rev. Lett.*, **108**, 040502 (2012). Cited on pages 4, 17, 47, 156 and 181.
- [Beckman96] D. Beckman, A. N. Chari, S. Devabhaktuni, and J. Preskill. “Efficient networks for quantum factoring.” *Phys. Rev. A*, **54**, 1034–1063 (1996). Cited on page 3.
- [Bennett93] C. H. Bennett, G. Brassard, C. Crépeau, R. Jozsa, A. Peres, and W. K. Wootters. “Teleporting an unknown quantum state via dual classical and Einstein-Podolsky-Rosen channels.” *Phys. Rev. Lett.*, **70**, 1895–1899 (1993). Cited on pages 156 and 182.
- [Bennett96] C. H. Bennett, D. P. DiVincenzo, J. A. Smolin, and W. K. Wootters. “Mixed-state entanglement and quantum error correction.” *Phys. Rev. A*, **54**, 3824–3851 (1996). Cited on pages 138, 195 and 197.
- [Bialczak10] R. C. Bialczak, M. Ansmann, M. Hofheinz, E. Lucero, M. Neeley, A. D. O’Connell, D. Sank, H. Wang, J. Wenner, M. Steffen, A. N. Cleland, and J. M. Martinis. “Quantum process tomography of a universal entangling gate implemented with josephson phase qubits.” *Nat Phys*, **6**, 409–413 (2010). Cited on pages 138 and 145.
- [Bianchetti09] R. Bianchetti, S. Filipp, M. Baur, J. M. Fink, M. Göppl, P. J. Leek, L. Steffen, A. Blais, and A. Wallraff. “Dynamics of dispersive single-qubit readout in circuit quantum electrodynamics.” *Physical Review A*, **80**, 043840 (2009). Cited on pages 4, 45, 46 and 92.

- [Bianchetti10a] R. Bianchetti. *Control and readout of a superconducting artificial atom*. Ph.D. thesis, ETH Zurich (2010). Cited on pages 60, 63 and 65.
- [Bianchetti10b] R. Bianchetti, S. Filipp, M. Baur, J. M. Fink, C. Lang, L. Steffen, M. Boissonneault, A. Blais, and A. Wallraff. “Control and tomography of a three level superconducting artificial atom.” *Physical Review Letters*, **105**, 223601 (2010). Cited on pages 4 and 47.
- [Birnbaum05] K. M. Birnbaum, A. Boca, R. Miller, A. D. Boozer, T. E. Northup, and H. J. Kimble. “Photon blockade in an optical cavity with one trapped atom.” *Nature*, **436**, 87–90 (2005). Cited on page 38.
- [Bishop09] L. S. Bishop, J. M. Chow, J. Koch, A. A. Houck, M. H. Devoret, E. Thuneberg, S. M. Girvin, and R. J. Schoelkopf. “Nonlinear response of the vacuum Rabi resonance.” *Nat. Phys.*, **5**, 105 (2009). Cited on pages 4 and 40.
- [Blais04] A. Blais, R.-S. Huang, A. Wallraff, S. M. Girvin, and R. J. Schoelkopf. “Cavity quantum electrodynamics for superconducting electrical circuits: An architecture for quantum computation.” *Physical Review A*, **69**, 062320 (2004). Cited on pages 4, 38, 46 and 47.
- [Blais07] A. Blais, J. Gambetta, A. Wallraff, D. I. Schuster, S. M. Girvin, M. H. Devoret, and R. J. Schoelkopf. “Quantum-information processing with circuit quantum electrodynamics.” *Physical Review A*, **75**, 032329 (2007). Cited on pages 48, 96, 121, 122 and 182.
- [Bluhm09] H. Bluhm, J. A. Bert, N. C. Koshnick, M. E. Huber, and K. A. Moler. “Spinlike susceptibility of metallic and insulating thin films at low temperature.” *Phys. Rev. Lett.*, **103**, 026805 (2009). Cited on page 78.
- [Borrelli11] M. Borrelli, L. Mazzola, M. Paternostro, and S. Maniscalco. “Simple trapped-ion architecture for high-fidelity toffoli gates.” *Phys. Rev. A*, **84**, 012314 (2011). Cited on page 170.
- [Boschi98] D. Boschi, S. Branca, F. De Martini, L. Hardy, and S. Popescu. “Experimental realization of teleporting an unknown pure quantum

- state via dual classical and einstein-podolsky-rosen channels.” *Phys. Rev. Lett.*, **80**, 1121–1125 (1998). Cited on page 156.
- [Bouchiat98] V. Bouchiat, D. Vion, P. Joyez, D. Esteve, and M. H. Devoret. “Quantum coherence with a single Cooper pair.” *Phys. Scr.*, **T76**, 165–170 (1998). Cited on pages 20, 26, 27 and 29.
- [Bourennane04] M. Bourennane, M. Eibl, C. Kurtsiefer, S. Gaertner, H. Weinfurter, O. Gühne, P. Hyllus, D. Bruß, M. Lewenstein, and A. Sanpera. “Experimental detection of multipartite entanglement using witness operators.” *Phys. Rev. Lett.*, **92**, 087902– (2004). Cited on pages 161 and 200.
- [Bouwmeester97] D. Bouwmeester, J. W. Pan, K. Mattle, M. Eibl, H. Weinfurter, and A. Zeilinger. “Experimental quantum teleportation.” *Nature*, **390**, 575–579 (1997). Cited on page 156.
- [Bozyigit10] D. Bozyigit. *Correlation Function Measurements of a Microwave Frequency Single Photon Source*. Master’s thesis, Communication Technology Laboratory and Laboratory of solid state physics, ETH Zurich (2010). Cited on page 79.
- [Bozyigit11] D. Bozyigit, C. Lang, L. Steffen, J. M. Fink, C. Eichler, M. Baur, R. Bianchetti, P. J. Leek, S. Filipp, M. P. da Silva, A. Blais, and A. Wallraff. “Antibunching of microwave-frequency photons observed in correlation measurements using linear detectors.” *Nature Physics*, **7**, 154–158 (2011). Cited on pages 4 and 163.
- [Briegel98] H.-J. Briegel, W. Dür, J. I. Cirac, and P. Zoller. “Quantum repeaters: The role of imperfect local operations in quantum communication.” *Phys. Rev. Lett.*, **81**, 5932– (1998). Cited on page 156.
- [Brune96] M. Brune, F. Schmidt-Kaler, A. Maali, J. Dreyer, E. Hagley, J. M. Raimond, and S. Haroche. “Quantum Rabi oscillation: A direct test of field quantization in a cavity.” *Phys. Rev. Lett.*, **76**, 1800–1803 (1996). Cited on pages 38 and 40.
- [Büttiker87] M. Büttiker. “Zero-current persistent potential drop across small-capacitance josephson junctions.” *Phys. Rev. B*, **36**, 3548–3555 (1987). Cited on page 26.

- [Cao10] K. Cao, Z.-W. Zhou, G.-C. Guo, and L. He. “Efficient numerical method to calculate the three-tangle of mixed states.” *Phys. Rev. A*, **81**, 034302– (2010). Cited on pages 196 and 198.
- [Chiaverini04] J. Chiaverini, D. Leibfried, T. Schaetz, M. Barrett, R. Blakestad, J. Britton, W. Itano, J. Jost, E. Knill, C. Langer, R. Ozeri, and D. Wineland. “Realization of quantum error correction.” *Nature*, **432**, 602–605 (2004). Cited on page 3.
- [Childs00] A. M. Childs and I. L. Chuang. “Universal quantum computation with two-level trapped ions.” *Phys. Rev. A*, **63**, 012306– (2000). Cited on pages 120 and 138.
- [Childs01] A. M. Childs, I. L. Chuang, and D. W. Leung. “Realization of quantum process tomography in nmr.” *Phys. Rev. A*, **64**, 012314– (2001). Cited on page 190.
- [Childs05] A. M. Childs, D. W. Leung, and M. A. Nielsen. “Unified derivations of measurement-based schemes for quantum computation.” *Phys. Rev. A*, **71**, 032318 (2005). Cited on page 156.
- [Chiorescu04] I. Chiorescu, P. Bertet, K. Semba, Y. Nakamura, C. J. P. M. Harman, and J. E. Mooij. “Coherent dynamics of a flux qubit coupled to a harmonic oscillator.” *Nature*, **431**, 159–162 (2004). Cited on page 120.
- [Choi09] S. Choi, D.-H. Lee, S. G. Louie, and J. Clarke. “Localization of metal-induced gap states at the metal-insulator interface: Origin of flux noise in squids and superconducting qubits.” *Phys. Rev. Lett.*, **103**, 197001 (2009). Cited on page 78.
- [Chow09] J. M. Chow, J. M. Gambetta, L. Tornberg, J. Koch, L. S. Bishop, A. A. Houck, B. R. Johnson, L. Frunzio, S. M. Girvin, and R. J. Schoelkopf. “Randomized benchmarking and process tomography for gate errors in a solid-state qubit.” *Phys. Rev. Lett.*, **102**, 090502 (2009). Cited on page 108.
- [Chow10] J. M. Chow, L. DiCarlo, J. M. Gambetta, F. Motzoi, L. Frunzio, S. M. Girvin, and R. J. Schoelkopf. “Optimized driving of superconducting

- artificial atoms for improved single-qubit gates.” *Phys. Rev. A*, **82**, 040305 (2010). Cited on pages 105, 109 and 181.
- [Chow11] J. M. Chow, A. D. Córcoles, J. M. Gambetta, C. Rigetti, B. R. Johnson, J. A. Smolin, J. R. Rozen, G. A. Keefe, M. B. Rothwell, M. B. Ketchen, and M. Steffen. “Simple all-microwave entangling gate for fixed-frequency superconducting qubits.” *Phys. Rev. Lett.*, **107**, 080502 (2011). Cited on page 119.
- [Chow12] J. M. Chow, J. M. Gambetta, A. D. Corcoles, S. T. Merkel, J. A. Smolin, C. Rigetti, S. Poletto, G. A. Keefe, M. B. Rothwell, J. R. Rozen, M. B. Ketchen, and M. Steffen. “Complete universal quantum gate set approaching fault-tolerant thresholds with superconducting qubits.” *arXiv:1202.5344* (2012). Cited on page 182.
- [Chuang97] I. L. Chuang and M. A. Nielsen. “Prescription for experimental determination of the dynamics of a quantum black box.” *J. Mod. Opt.*, **44**, 2455–2467 (1997). Cited on page 190.
- [Chuang98] I. L. Chuang, L. M. K. Vandersypen, X. Zhou, D. W. Leung, and S. Lloyd. “Experimental realization of a quantum algorithm.” *Nature*, **393**, 143–146 (1998). Cited on page 3.
- [Cirac95] J. I. Cirac and P. Zoller. “Quantum computations with cold trapped ions.” *Phys. Rev. Lett.*, **74**, 4091–4094 (1995). Cited on pages 120 and 138.
- [Clarke08] J. Clarke and F. K. Wilhelm. “Superconducting quantum bits.” *Nature*, **453**, 1031–1042 (2008). Cited on pages 3, 20 and 103.
- [Coffman00] V. Coffman, J. Kundu, and W. K. Wootters. “Distributed entanglement.” *Phys. Rev. A*, **61**, 052306– (2000). Cited on pages 161, 197 and 198.
- [Cohen-Tannoudji98] C. Cohen-Tannoudji, J. Dupont-Roc, and G. Grynberg. *Atom-Photon Interactions: Basic Processes and Applications*. Wiley Science Paperback Series (1998). Cited on pages 92 and 93.
- [Córcoles11] A. D. Córcoles, J. M. Chow, J. M. Gambetta, C. Rigetti, J. R. Rozen, G. A. Keefe, M. B. Rothwell, M. B. Ketchen, and M. Steffen. “Pro-

- protecting superconducting qubits from radiation.” *Appl. Phys. Lett.*, **99**, 181906 (2011). Cited on page 101.
- [Cory98] D. G. Cory, M. D. Price, W. Maas, E. Knill, R. Laflamme, W. H. Zurek, T. F. Havel, and S. S. Somaroo. “Experimental quantum error correction.” *Phys. Rev. Lett.*, **81**, 2152–2155 (1998). Cited on page 3.
- [Cottet02] A. Cottet. *Implementation of a quantum bit in a superconducting circuit*. Ph.D. thesis, Université Paris 6 (2002). Cited on page 28.
- [D’Ariano01] G. M. D’Ariano and P. Lo Presti. “Quantum tomography for measuring experimentally the matrix elements of an arbitrary quantum operation.” *Phys. Rev. Lett.*, **86**, 4195– (2001). Cited on page 190.
- [D’Ariano03] G. M. D’Ariano and P. Lo Presti. “Imprinting complete information about a quantum channel on its output state.” *Phys. Rev. Lett.*, **91**, 047902– (2003). Cited on page 190.
- [deGroot10] P. C. de Groot, J. Lisenfeld, R. N. Schouten, S. Ashhab, A. Lupaşcu, C. J. P. M. Harmans, and J. E. Mooij. “Selective darkening of degenerate transitions demonstrated with two superconducting quantum bits.” *Nat. Phys.*, **6**, 763– 766 (2010). Cited on page 119.
- [Deleglise08] S. Deleglise, I. Dotsenko, C. Sayrin, J. Bernu, M. Brune, J.-M. Raimond, and S. Haroche. “Reconstruction of non-classical cavity field states with snapshots of their decoherence.” *Nature*, **455**, 510–514 (2008). Cited on page 38.
- [Dennis02] E. Dennis, A. Kitaev, A. Landahl, and J. Preskill. “Topological quantum memory.” *Journal of Mathematical Physics*, **43**, 4452–4505 (2002). Cited on page 182.
- [Deutsch85] D. Deutsch. “Quantum theory, the Church-Turing principle and the universal quantum computer.” *Proceedings of the Royal Society of London. Series A, Mathematical and Physical Sciences*, **400**, 97–117 (1985). Cited on page 2.
- [Deutsch92] D. Deutsch and R. Jozsa. “Rapid solution of problems by quantum computation.” *Proceedings: Mathematical and Physical Sciences*, **439**, 553–558 (1992). Cited on pages 2, 15 and 139.

- [Devoret85] M. H. Devoret, J. M. Martinis, and J. Clarke. “Measurements of macroscopic quantum tunneling out of the zero-voltage state of a current-biased josephson junction.” *Phys. Rev. Lett.*, **55**, 1908–1911 (1985). Cited on page 18.
- [Devoret97] M. H. Devoret. “Quantum fluctuations in electrical circuits.” In S. Reynaud, E. Giacobino, and J. Zinn-Justin, editors, “Quantum Fluctuations: Les Houches Session LXIII,” 351–386. Elsevier (1997). Cited on page 19.
- [Dewes11] A. Dewes, R. Lauro, F. R. Ong, V. Schmitt, P. Milman, P. Bertet, D. Vion, and D. Esteve. “Demonstrating quantum speed-up in a superconducting two-qubit processor.” arXiv:1110.5170v1 [quant-ph] (2011). Cited on pages 4, 156 and 181.
- [Dewes12] A. Dewes, F. R. Ong, V. Schmitt, R. Lauro, N. Boulant, P. Bertet, D. Vion, and D. Esteve. “Characterization of a two-transmon processor with individual single-shot qubit readout.” *Phys. Rev. Lett.*, **108**, 057002 (2012). Cited on pages 145 and 163.
- [DiCarlo09] L. DiCarlo, J. M. Chow, J. M. Gambetta, L. S. Bishop, B. R. Johnson, D. I. Schuster, J. Majer, A. Blais, L. Frunzio, S. M. Girvin, and R. J. Schoelkopf. “Demonstration of two-qubit algorithms with a superconducting quantum processor.” *Nature*, **460**, 240–244 (2009). Cited on pages 3, 4, 15, 17, 47, 119, 138, 139, 146, 151, 156 and 181.
- [DiCarlo10] L. DiCarlo, M. D. Reed, L. Sun, B. R. Johnson, J. M. Chow, J. M. Gambetta, L. Frunzio, S. M. Girvin, M. H. Devoret, and R. J. Schoelkopf. “Preparation and measurement of three-qubit entanglement in a superconducting circuit.” *Nature*, **467**, 574–578 (2010). Cited on pages 4, 47, 146, 158 and 181.
- [DiVincenzo09] D. P. DiVincenzo. “Fault-tolerant architectures for superconducting qubits.” *Phys. Scr.*, **2009**, 014020 (2009). Cited on pages 3, 105, 182 and 183.
- [Doherty99] A. C. Doherty and K. Jacobs. “Feedback control of quantum systems using continuous state estimation.” *Phys. Rev. A*, **60**, 2700–2711 (1999). Cited on page 156.

- [Duan10] L.-M. Duan and C. Monroe. “Colloquium: Quantum networks with trapped ions.” *Rev. Mod. Phys.*, **82**, 1209–1224 (2010). Cited on page 3.
- [Dür00] W. Dür, G. Vidal, and J. I. Cirac. “Three qubits can be entangled in two inequivalent ways.” *Phys. Rev. A*, **62**, 062314 (2000). Cited on page 194.
- [Eichler11a] C. Eichler, D. Bozyigit, C. Lang, M. Baur, L. Steffen, J. M. Fink, S. Filipp, and A. Wallraff. “Observation of two-mode squeezing in the microwave frequency domain.” *Phys. Rev. Lett.*, **107**, 113601 (2011). Cited on pages 4 and 163.
- [Eichler11b] C. Eichler, D. Bozyigit, C. Lang, L. Steffen, J. Fink, and A. Wallraff. “Experimental state tomography of itinerant single microwave photons.” *Phys. Rev. Lett.*, **106**, 220503 (2011). Cited on page 4.
- [Einstein35] A. Einstein, B. Podolsky, and N. Rosen. “Can quantum-mechanical description of physical reality be considered complete?” *Phys. Rev.*, **47**, 777–780 (1935). Cited on page 10.
- [Eisert07] J. Eisert, F. G. S. L. Brandão, and K. M. R. Audenaert. “Quantitative entanglement witnesses.” *New J. Phys.*, **9**, 46 (2007). Cited on page 161.
- [Esteve86] D. Esteve, M. H. Devoret, and J. M. Martinis. “Effect of an arbitrary dissipative circuit on the quantum energy levels and tunneling of a josephson junction.” *Phys. Rev. B*, **34**, 158–163 (1986). Cited on pages 21 and 76.
- [Faoro08] L. Faoro and L. B. Ioffe. “Microscopic origin of low-frequency flux noise in josephson circuits.” *Phys. Rev. Lett.*, **100**, 227005 (2008). Cited on page 78.
- [Fedorov12] A. Fedorov, L. Steffen, M. Baur, M. P. da Silva, and A. Wallraff. “Implementation of a toffoli gate with superconducting circuits.” *Nature*, **481**, 170–172 (2012). Cited on pages 4, 17, 47, 165, 170 and 181.
- [Feynman82] R. P. Feynman. “Simulating physics with computers.” *Int. J. Theor. Phys.*, **21**, 467–488 (1982). Cited on page 2.

- [Filipp09] S. Filipp, P. Maurer, P. J. Leek, M. Baur, R. Bianchetti, J. M. Fink, M. Göppl, L. Steffen, J. M. Gambetta, A. Blais, and A. Wallraff. “Two-qubit state tomography using a joint dispersive readout.” *Phys. Rev. Lett.*, **102**, 200402 (2009). Cited on pages 4, 47 and 139.
- [Filipp11a] S. Filipp, M. Göppl, J. M. Fink, M. Baur, R. Bianchetti, L. Steffen, and A. Wallraff. “Multimode mediated qubit-qubit coupling and dark-state symmetries in circuit quantum electrodynamics.” *Phys. Rev. A*, **83**, 063827 (2011). Cited on pages 138 and 143.
- [Filipp11b] S. Filipp, A. F. van Loo, M. Baur, L. Steffen, and A. Wallraff. “Preparation of subradiant states using local qubit control in circuit qed.” *Phys. Rev. A*, **84**, 061805 (2011). Cited on page 145.
- [Fink08] J. M. Fink, M. Göppl, M. Baur, R. Bianchetti, P. J. Leek, A. Blais, and A. Wallraff. “Climbing the Jaynes-Cummings ladder and observing its nonlinearity in a cavity QED system.” *Nature*, **454**, 315–318 (2008). Cited on pages 4, 40, 56 and 134.
- [Fink10] J. Fink. *Quantum nonlinearities in strong coupling circuit QED*. Ph.D. thesis, ETH Zurich (2010). Cited on page 58.
- [Forn-Díaz10] P. Forn-Díaz, J. Lisenfeld, D. Marcos, J. J. García-Ripoll, E. Solano, C. J. P. M. Harmans, and J. E. Mooij. “Observation of the Bloch-Siegert shift in a qubit-oscillator system in the ultrastrong coupling regime.” *Phys. Rev. Lett.*, **105**, 237001 (2010). Cited on pages 4 and 39.
- [Fragner08] A. Fragner, M. Göppl, J. M. Fink, M. Baur, R. Bianchetti, P. J. Leek, A. Blais, and A. Wallraff. “Resolving vacuum fluctuations in an electrical circuit by measuring the Lamb shift.” *Science*, **322**, 1357–1360 (2008). Cited on pages 4 and 43.
- [Friedman00] J. R. Friedman, V. Patel, W. Chen, S. K. Tolpygo, and J. E. Lukens. “Quantum superposition of distinct macroscopic states.” *Nature*, **406**, 43–46 (2000). Cited on pages 19 and 20.
- [Furusawa98] A. Furusawa, J. L. Sørensen, S. L. Braunstein, C. A. Fuchs, H. J. Kimble, and E. S. Polzik. “Unconditional quantum teleportation.” *Science*, **282**, 706–709 (1998). Cited on page 156.

- [Gambetta06] J. Gambetta, A. Blais, D. I. Schuster, A. Wallraff, L. Frunzio, J. Majer, M. H. Devoret, S. M. Girvin, and R. J. Schoelkopf. “Qubit-photon interactions in a cavity: Measurement-induced dephasing and number splitting.” *Physical Review A*, **74**, 042318 (2006). Cited on page 44.
- [Gambetta08] J. Gambetta, A. Blais, M. Boissonneault, A. A. Houck, D. I. Schuster, and S. M. Girvin. “Quantum trajectory approach to circuit qed: Quantum jumps and the zeno effect.” *Phys. Rev. A*, **77**, 012112 (2008). Cited on page 99.
- [Gambetta11] J. M. Gambetta, F. Motzoi, S. T. Merkel, and F. K. Wilhelm. “Analytic control methods for high-fidelity unitary operations in a weakly nonlinear oscillator.” *Phys. Rev. A*, **83**, 012308– (2011). Cited on pages 33, 105, 106, 185, 186 and 187.
- [Gerritsma10] R. Gerritsma, G. Kirchmair, F. Zahring, E. Solano, R. Blatt, and C. F. Roos. “Quantum simulation of the Dirac equation.” *Nature*, **463**, 68–71 (2010). Cited on page 182.
- [Gisin02] N. Gisin, G. Ribordy, W. Tittel, and H. Zbinden. “Quantum cryptography.” *Rev. Mod. Phys.*, **74**, 145–195 (2002). Cited on page 156.
- [Göppl08] M. Göppl, A. Fragner, M. Baur, R. Bianchetti, S. Filipp, J. M. Fink, P. J. Leek, G. Puebla, L. Steffen, and A. Wallraff. “Coplanar waveguide resonators for circuit quantum electrodynamics.” *Journal of Applied Physics*, **104**, 113904 (2008). Cited on pages 17, 52 and 54.
- [Göppl09] M. Göppl. *Engineering Quantum Electronic Chips - Realization and Characterization of Circuit Quantum Electrodynamics Systems*. Ph.D. thesis, ETH Zurich (2009). Cited on pages 58 and 89.
- [Gottesman99] D. Gottesman and I. L. Chuang. “Demonstrating the viability of universal quantum computation using teleportation and single-qubit operations.” *Nature*, **402**, 390–393 (1999). Cited on page 156.
- [Gottesman09] D. Gottesman. “An introduction to quantum error correction and fault-tolerant quantum computation.” arXiv:0904.2557v1 [quant-ph] (2009). Cited on page 169.

- [Grajcar08] M. Grajcar, S. H. W. van der Ploeg, A. Izmailkov, E. Il'ichev, H.-G. Meyer, A. Fedorov, A. Shnirman, and G. Schön. “Sisyphus cooling and amplification by a superconducting qubit.” *Nat. Phys.*, **4**, 612–616 (2008). Cited on page 4.
- [Greenberger90] D. M. Greenberger, M. A. Horne, A. Shimony, and A. Zeilinger. “Bell’s theorem without inequalities.” *American Journal of Physics*, **58**, 1131–1143 (1990). Cited on page 194.
- [Gühne09] O. Gühne and G. Tóth. “Entanglement detection.” *Physics Reports*, **474**, 1 – 75 (2009). Cited on pages 195, 197 and 200.
- [Gulde03] S. Gulde, M. Riebe, G. P. T. Lancaster, C. Becher, J. Eschner, H. Häffner, F. Schmidt-Kaler, I. L. Chuang, and R. Blatt. “Implementation of the deutsch-jozsa algorithm on an ion-trap quantum computer.” *Nature*, **421**, 48–50 (2003). Cited on page 3.
- [Häffner08] H. Häffner, C. F. Roos, and R. Blatt. “Quantum computing with trapped ions.” *Physics Reports-review Section of Physics Letters*, **469**, 155–203 (2008). Cited on page 3.
- [Hahn50] E. L. Hahn. “Spin echoes.” *Phys. Rev.*, **80**, 580–594 (1950). Cited on page 104.
- [Haroche89] S. Haroche and D. Kleppner. “Cavity quantum electrodynamics.” *Phys. Today*, **42**, 24–30 (1989). Cited on pages 4 and 36.
- [Haroche92] S. Haroche. *Fundamental Systems in Quantum Optics*, chapter Cavity quantum electrodynamics, 767. Elsevier (1992). Cited on page 39.
- [Hill97] S. Hill and W. K. Wootters. “Entanglement of a pair of quantum bits.” *Phys. Rev. Lett.*, **78**, 5022– (1997). Cited on page 196.
- [Hoffman11] A. J. Hoffman, S. J. Srinivasan, S. Schmidt, L. Spietz, J. Aumentado, H. E. Türeci, and A. A. Houck. “Dispersive photon blockade in a superconducting circuit.” *Phys. Rev. Lett.*, **107**, 053602 (2011). Cited on page 44.

- [Hofheinz08] M. Hofheinz, E. M. Weig, M. Ansmann, R. C. Bialczak, E. Lucero, M. Neeley, A. D. O’Connell, H. Wang, J. M. Martinis, and A. N. Cleland. “Generation of Fock states in a superconducting quantum circuit.” *Nature*, **454**, 310–314 (2008). Cited on pages 4 and 40.
- [Hofheinz09] M. Hofheinz, H. Wang, M. Ansmann, R. C. Bialczak, E. Lucero, M. Neeley, A. D. O’Connell, D. Sank, J. Wenner, J. M. Martinis, and A. N. Cleland. “Synthesizing arbitrary quantum states in a superconducting resonator.” *Nature*, **459**, 546–549 (2009). Cited on page 4.
- [Horodecki96] M. Horodecki, P. Horodecki, and R. Horodecki. “Separability of mixed states: necessary and sufficient conditions.” *Physics Letters A*, **223**, 1–8 (1996). Cited on page 198.
- [Horodecki09] R. Horodecki, P. Horodecki, M. Horodecki, and K. Horodecki. “Quantum entanglement.” *Rev. Mod. Phys.*, **81**, 865 (2009). Cited on pages 195 and 196.
- [Houck07] A. Houck, D. Schuster, J. Gambetta, J. Schreier, B. Johnson, J. Chow, L. Frunzio, J. Majer, M. Devoret, S. Girvin, and R. Schoelkopf. “Generating single microwave photons in a circuit.” *Nature*, **449**, 328–331 (2007). Cited on pages 4 and 44.
- [Houck08] A. A. Houck, J. A. Schreier, B. R. Johnson, J. M. Chow, J. Koch, J. M. Gambetta, D. I. Schuster, L. Frunzio, M. H. Devoret, S. M. Girvin, and R. J. Schoelkopf. “Controlling the spontaneous emission of a superconducting transmon qubit.” *Phys. Rev. Lett.*, **101**, 080502–4 (2008). Cited on pages 44, 76, 77 and 101.
- [Hulet85] R. G. Hulet, E. S. Hilfer, and D. Kleppner. “Inhibited spontaneous emission by a rydberg atom.” *Phys. Rev. Lett.*, **55**, 2137–2140 (1985). Cited on page 37.
- [Ithier05] G. Ithier, E. Collin, P. Joyez, P. J. Meeson, D. Vion, D. Esteve, F. Chiarello, A. Shnirman, Y. Makhlin, J. Schrieffer, and G. Schön. “Decoherence in a superconducting quantum bit circuit.” *Phys. Rev. B*, **72**, 134519 (2005). Cited on pages 33, 101 and 104.

- [James01] D. F. V. James, P. G. Kwiat, W. J. Munro, and A. G. White. “Measurement of qubits.” *Phys. Rev. A*, **64**, 052312 (2001). Cited on page 189.
- [Jaynes63] E. Jaynes and F. Cummings. “Comparison of quantum and semi-classical radiation theories with application to the beam maser.” *Proceedings of the IEEE*, **51**, 89–109 (1963). Cited on page 36.
- [Ježek03] M. Ježek, J. Fiurášek, and Z. Hradil. “Quantum inference of states and processes.” *Phys. Rev. A*, **68**, 012305 (2003). Cited on pages 116, 150, 177 and 193.
- [Jhe87] W. Jhe, A. Anderson, E. A. Hinds, D. Meschede, L. Moi, and S. Haroche. “Suppression of spontaneous decay at optical frequencies: Test of vacuum-field anisotropy in confined space.” *Phys. Rev. Lett.*, **58**, 666–669 (1987). Cited on page 37.
- [Jin10] X.-M. Jin, J.-G. Ren, B. Yang, Z.-H. Yi, F. Zhou, X.-F. Xu, S.-K. Wang, D. Yang, Y.-F. Hu, S. Jiang, T. Yang, H. Yin, K. Chen, C.-Z. Peng, and J.-W. Pan. “Experimental free-space quantum teleportation.” *Nat. Photon.*, **4**, 376–381 (2010). Cited on page 156.
- [Johansson06] J. Johansson, S. Saito, T. Meno, H. Nakano, M. Ueda, K. Semba, and H. Takayanagi. “Vacuum Rabi oscillations in a macroscopic superconducting qubit LC oscillator system.” *Phys. Rev. Lett.*, **96**, 127006 (2006). Cited on page 4.
- [Johnson10] B. R. Johnson, M. D. Reed, A. A. Houck, D. I. Schuster, L. S. Bishop, E. Ginossar, J. M. Gambetta, L. DiCarlo, L. Frunzio, S. M. Girvin, and R. J. Schoelkopf. “Quantum non-demolition detection of single microwave photons in a circuit.” *Nat. Phys.*, 663 – 667 (2010). Cited on page 123.
- [Jorrand05] P. Jorrand and S. Perdrix. “Unifying quantum computation with projective measurements only and one-way quantum computation.” *Proc. SPIE*, **5833**, 44–51 (2005). Cited on page 156.
- [Josephson62] B. D. Josephson. “Possible new effects in superconductive tunnelling.” *Physics Letters*, **1**, 251–253 (1962). Cited on page 21.

- [Kim10] K. Kim, M.-S. Chang, S. Korenblit, R. Islam, E. E. Edwards, J. K. Freericks, G.-D. Lin, L.-M. Duan, and C. Monroe. “Quantum simulation of frustrated Ising spins with trapped ions.” *Nature*, **465**, 590–593 (2010). Cited on page 182.
- [Kim11] Z. Kim, B. Suri, V. Zaretsky, S. Novikov, K. D. Osborn, A. Mizel, F. C. Wellstood, and B. S. Palmer. “Decoupling a cooper-pair box to enhance the lifetime to 0.2 ms.” *Phys. Rev. Lett.*, **106**, 120501 (2011). Cited on page 33.
- [Kitaev03] A. Y. Kitaev. “Fault-tolerant quantum computation by anyons.” *Annals of Physics*, **303**, 2 – 30 (2003). Cited on page 182.
- [Knill05] E. Knill. “Quantum computing with realistically noisy devices.” *Nature*, **434**, 39–44 (2005). Cited on pages 2, 3 and 105.
- [Koch07a] J. Koch, T. M. Yu, J. Gambetta, A. A. Houck, D. I. Schuster, J. Majer, A. Blais, M. H. Devoret, S. M. Girvin, and R. J. Schoelkopf. “Charge-insensitive qubit design derived from the Cooper pair box.” *Phys. Rev. A*, **76**, 042319 (2007). Cited on pages 17, 20, 33, 34, 35, 39, 42, 44, 54, 55, 56, 75, 77 and 99.
- [Koch07b] R. H. Koch, D. P. DiVincenzo, and J. Clarke. “Model for $1/f$ flux noise in squids and qubits.” *Phys. Rev. Lett.*, **98**, 267003 (2007). Cited on page 78.
- [Kofman09] A. G. Kofman and A. N. Korotkov. “Two-qubit decoherence mechanisms revealed via quantum process tomography.” *Phys. Rev. A*, **80**, 042103– (2009). Cited on page 115.
- [Kok07] P. Kok, W. J. Munro, K. Nemoto, T. C. Ralph, J. P. Dowling, and G. J. Milburn. “Linear optical quantum computing with photonic qubits.” *Rev. Mod. Phys.*, **79**, 135–174 (2007). Cited on page 3.
- [Lamb47] W. E. Lamb and R. Retherford. “Fine structure of the hydrogen atom by a microwave method.” *Phys. Rev.*, **72**, 241 (1947). Cited on page 37.
- [Lang11] C. Lang, D. Bozyigit, C. Eichler, L. Steffen, J. M. Fink, A. A. Abdumalikov Jr., M. Baur, S. Filipp, M. P. da Silva, A. Blais, and

- A. Wallraff. “Observation of resonant photon blockade at microwave frequencies using correlation function measurements.” *Physical Review Letters*, **106**, 243601 (2011). Cited on pages 4 and 95.
- [Lanyon07] B. P. Lanyon, T. J. Weinhold, N. K. Langford, M. Barbieri, D. F. V. James, A. Gilchrist, and A. G. White. “Experimental demonstration of a compiled version of Shor’s algorithm with quantum entanglement.” *Phys. Rev. Lett.*, **99**, 250505 (2007). Cited on page 3.
- [Lanyon09] B. P. Lanyon, M. Barbieri, M. P. Almeida, T. Jennewein, T. C. Ralph, K. J. Resch, G. J. Pryde, J. L. O’Brien, A. Gilchrist, and A. G. White. “Simplifying quantum logic using higher-dimensional hilbert spaces.” *Nat. Phys.*, **5**, 134–140 (2009). Cited on page 170.
- [Lanyon11] B. P. Lanyon, C. Hempel, D. Nigg, M. Müller, R. Gerritsma, F. Zähringer, P. Schindler, J. T. Barreiro, M. Rambach, G. Kirchmair, M. Hennrich, P. Zoller, R. Blatt, and C. F. Roos. “Universal digital quantum simulation with trapped ions.” *Science*, **334**, 57–61 (2011). Cited on pages 120 and 182.
- [Lee11] N. Lee, H. Benichi, Y. Takeno, S. Takeda, J. Webb, E. Huntington, and A. Furusawa. “Teleportation of nonclassical wave packets of light.” *Science*, **332**, 330–333 (2011). Cited on page 156.
- [Leek07] P. J. Leek, J. M. Fink, A. Blais, R. Bianchetti, M. Göppl, J. M. Gambetta, D. I. Schuster, L. Frunzio, R. J. Schoelkopf, and A. Wallraff. “Observation of Berry’s phase in a solid-state qubit.” *Science*, **318**, 1889 (2007). Cited on pages 4 and 33.
- [Leek09] P. J. Leek, S. Filipp, P. Maurer, M. Baur, R. Bianchetti, J. M. Fink, M. Göppl, L. Steffen, and A. Wallraff. “Using sideband transitions for two-qubit operations in superconducting circuits.” *Physical Review B*, **79**, 180511 (2009). Cited on pages 47, 119, 120 and 182.
- [Leek10] P. J. Leek, M. Baur, J. M. Fink, R. Bianchetti, L. Steffen, S. Filipp, and A. Wallraff. “Cavity quantum electrodynamics with separate photon storage and qubit readout modes.” *Physical Review Letters*, **104**, 100504 (2010). Cited on pages 4, 119, 120 and 182.

- [Lindblad76] G. Lindblad. “On the generators of quantum dynamical semigroups.” *Communications in Mathematical Physics*, **48**, 119–130 (1976). Cited on page 130.
- [Lu07] C.-Y. Lu, D. E. Browne, T. Yang, and J.-W. Pan. “Demonstration of a compiled version of Shor’s quantum factoring algorithm using photonic qubits.” *Phys. Rev. Lett.*, **99**, 250504 (2007). Cited on page 3.
- [Lucero10] E. Lucero, J. Kelly, R. C. Bialczak, M. Lenander, M. Mariantoni, M. Neeley, A. D. O’Connell, D. Sank, H. Wang, M. Weides, J. Wenner, T. Yamamoto, A. N. Cleland, and J. M. Martinis. “Reduced phase error through optimized control of a superconducting qubit.” *Phys. Rev. A*, **82**, 042339 (2010). Cited on pages 105 and 109.
- [Lucero12] E. Lucero, R. Barends, Y. Chen, J. Kelly, M. Mariantoni, A. Megrant, P. O’Malley, D. Sank, A. Vainsencher, J. Wenner, T. White, Y. Yin, A. N. Cleland, and J. M. Martinis. “Computing prime factors with a Josephson phase qubit quantum processor.” *Nat. Phys.*, **adv. online publ.**, – (2012). Cited on page 181.
- [Ma11] X.-S. Ma, B. Dakic, W. Naylor, A. Zeilinger, and P. Walther. “Quantum simulation of the wavefunction to probe frustrated Heisenberg spin systems.” *Nat Phys*, **7**, 399–405 (2011). Cited on page 182.
- [Majer07] J. Majer, J. M. Chow, J. M. Gambetta, J. Koch, B. R. Johnson, J. A. Schreier, L. Frunzio, D. I. Schuster, A. A. Houck, A. Wallraff, A. Blais, M. H. Devoret, S. M. Girvin, and R. J. Schoelkopf. “Coupling superconducting qubits via a cavity bus.” *Nature*, **449**, 443–447 (2007). Cited on pages 4, 17, 119, 138, 139 and 143.
- [Mallet09] F. Mallet, F. R. Ong, A. Palacios-Laloy, F. Nguyen, P. Bertet, D. Vion, and D. Esteve. “Single-shot qubit readout in circuit quantum electrodynamics.” *Nat. Phys.*, **5**, 791–795 (2009). Cited on pages 156 and 163.
- [Mallet11] F. Mallet, M. A. Castellanos-Beltran, H. S. Ku, S. Glancy, E. Knill, K. D. Irwin, G. C. Hilton, L. R. Vale, and K. W. Lehnert. “Quantum state tomography of an itinerant squeezed microwave field.” *Phys. Rev. Lett.*, **106**, 220502 (2011). Cited on page 4.

- [Marcikic03] I. Marcikic, H. de Riedmatten, W. Tittel, H. Zbinden, and N. Gisin. “Long-distance teleportation of qubits at telecommunication wavelengths.” *Nature*, **421**, 509–513 (2003). Cited on page 156.
- [Mariantoni11a] M. Mariantoni, H. Wang, R. C. Bialczak, M. Lenander, E. Lucero, M. Neeley, A. D. O’Connell, D. Sank, M. Weides, J. Wenner, T. Yamamoto, Y. Yin, J. Zhao, J. M. Martinis, and A. N. Cleland. “Photon shell game in three-resonator circuit quantum electrodynamics.” *Nat Phys*, **7**, 287–293 (2011). Cited on pages 4 and 123.
- [Mariantoni11b] M. Mariantoni, H. Wang, T. Yamamoto, M. Neeley, R. C. Bialczak, Y. Chen, M. Lenander, E. Lucero, A. D. O’Connell, D. Sank, M. Weides, J. Wenner, Y. Yin, J. Zhao, A. N. Korotkov, A. N. Cleland, and J. M. Martinis. “Implementing the quantum von neumann architecture with superconducting circuits.” *Science*, **334**, 61–65 (2011). Cited on pages 123, 165, 170 and 181.
- [Martinis02] J. M. Martinis, S. Nam, J. Aumentado, and C. Urbina. “Rabi oscillations in a large Josephson-junction qubit.” *Phys. Rev. Lett.*, **89**, 117901 (2002). Cited on pages 20 and 25.
- [Martinis05] J. M. Martinis, K. B. Cooper, R. McDermott, M. Steffen, M. Ansmann, K. D. Osborn, K. Cicak, S. Oh, D. P. Pappas, R. W. Simmonds, and C. C. Yu. “Decoherence in Josephson qubits from dielectric loss.” *Phys. Rev. Lett.*, **95**, 210503 (2005). Cited on pages 101 and 181.
- [McCumber68] D. E. McCumber. “Effect of ac impedance on dc voltage-current characteristics of superconductor weak-link junctions.” *J. Appl. Phys.*, **39**, 3113–3118 (1968). Cited on page 21.
- [Megrant12] A. Megrant, C. Neill, R. Barends, B. Chiaro, Y. Chen, L. Feigl, J. Kelly, E. Lucero, M. Mariantoni, P. J. J. O’Malley, D. Sank, A. Vainsencher, J. Wenner, T. C. White, Y. Yin, J. Zhao, C. J. Palmstrøm, J. M. Martinis, and A. N. Cleland. “Planar superconducting resonators with internal quality factors above one million.” *arXiv:1201.3384* (2012). Cited on page 54.
- [Mohseni06] M. Mohseni and D. A. Lidar. “Direct characterization of quantum dynamics.” *Phys. Rev. Lett.*, **97**, 170501– (2006). Cited on page 190.

- [Mollow69] B. R. Mollow. “Power spectrum of light scattered by two-level systems.” *Phys. Rev.*, **188**, 1969–1975 (1969). Cited on page 90.
- [Monroe95] C. Monroe, D. M. Meekhof, B. E. King, W. M. Itano, and D. J. Wineland. “Demonstration of a fundamental quantum logic gate.” *Phys. Rev. Lett.*, **75**, 4714–4717 (1995). Cited on pages 120 and 138.
- [Monz09] T. Monz, K. Kim, W. Hänsel, M. Riebe, A. S. Villar, P. Schindler, M. Chwalla, M. Hennrich, and R. Blatt. “Realization of the quantum Toffoli gate with trapped ions.” *Phys. Rev. Lett.*, **102**, 040501 (2009). Cited on page 170.
- [Monz11] T. Monz, P. Schindler, J. T. Barreiro, M. Chwalla, D. Nigg, W. A. Coish, M. Harlander, W. Hänsel, M. Hennrich, and R. Blatt. “14-qubit entanglement: Creation and coherence.” *Phys. Rev. Lett.*, **106**, 130506 (2011). Cited on page 3.
- [Motzoi09] F. Motzoi, J. M. Gambetta, P. Rebentrost, and F. K. Wilhelm. “Simple pulses for elimination of leakage in weakly nonlinear qubits.” *Phys. Rev. Lett.*, **103**, 110501 (2009). Cited on pages 105, 106, 185, 186 and 187.
- [Muller07] A. Muller, E. B. Flagg, P. Bianucci, X. Y. Wang, D. G. Deppe, W. Ma, J. Zhang, G. J. Salamo, M. Xiao, and C. K. Shih. “Resonance fluorescence from a coherently driven semiconductor quantum dot in a cavity.” *Phys. Rev. Lett.*, **99**, 187402 (2007). Cited on page 95.
- [Nakamura97] Y. Nakamura, C. D. Chen, and J. S. Tsai. “Spectroscopy of energy-level splitting between two macroscopic quantum states of charge coherently superposed by josephson coupling.” *Phys. Rev. Lett.*, **79**, 2328–2331 (1997). Cited on page 19.
- [Nakamura99] Y. Nakamura, Y. A. Pashkin, and J. S. Tsai. “Coherent control of macroscopic quantum states in a single-cooper-pair box.” *Nature*, **398**, 786–788 (1999). Cited on pages 20, 26 and 101.
- [Neeley10] M. Neeley, R. C. Bialczak, M. Lenander, E. Lucero, M. Mariantoni, A. D. O’Connell, D. Sank, H. Wang, M. Weides, J. Wenner, Y. Yin, T. Yamamoto, A. N. Cleland, and J. M. Martinis. “Generation of

- three-qubit entangled states using superconducting phase qubits.” *Nature*, **467**, 570–573 (2010). Cited on pages 4 and 158.
- [Nick Vamivakas09] A. Nick Vamivakas, Y. Zhao, C.-Y. Lu, and M. Atature. “Spin-resolved quantum-dot resonance fluorescence.” *Nat. Phys.*, **5**, 198–202 (2009). Cited on page 95.
- [Nielsen98] M. A. Nielsen, E. Knill, and R. Laflamme. “Complete quantum teleportation using nuclear magnetic resonance.” *Nature*, **396**, 52–55 (1998). Cited on page 156.
- [Nielsen00] M. A. Nielsen and I. L. Chuang. *Quantum Computation and Quantum Information*. Cambridge University Press (2000). Cited on pages 7, 14, 169, 182 and 191.
- [Niemczyk10] T. Niemczyk, F. Deppe, H. Huebl, E. P. Menzel, F. Hocke, M. J. Schwarz, J. J. Garcia-Ripoll, D. Zueco, T. Hümmer, E. Solano, A. Marx, and R. Gross. “Circuit quantum electrodynamics in the ultrastrong-coupling regime.” *Nat. Phys.*, **6**, 772–776 (2010). Cited on pages 4 and 39.
- [Nogues99] G. Nogues, A. Rauschenbeutel, S. Osnaghi, M. Brune, J. M. Raimond, and S. Haroche. “Seeing a single photon without destroying it.” *Nature*, **400**, 239–242 (1999). Cited on page 38.
- [O’Brien04] J. L. O’Brien, G. J. Pryde, A. Gilchrist, D. F. V. James, N. K. Langford, T. C. Ralph, and A. G. White. “Quantum process tomography of a controlled-not gate.” *Phys. Rev. Lett.*, **93**, 080502– (2004). Cited on pages 190 and 193.
- [Oliver05] W. D. Oliver, Y. Yu, J. C. Lee, K. K. Berggren, L. S. Levitov, and T. P. Orlando. “Mach-zehnder interferometry in a strongly driven superconducting qubit.” *Science*, **310**, 1653–1657 (2005). Cited on page 95.
- [Olmschenk09] S. Olmschenk, D. N. Matsukevich, P. Maunz, D. Hayes, L.-M. Duan, and C. Monroe. “Quantum teleportation between distant matter qubits.” *Science*, **323**, 486–489 (2009). Cited on page 156.

- [Paik11] H. Paik, D. I. Schuster, L. S. Bishop, G. Kirchmair, G. Catelani, A. P. Sears, B. R. Johnson, M. J. Reagor, L. Frunzio, L. I. Glazman, S. M. Girvin, M. H. Devoret, and R. J. Schoelkopf. “Observation of high coherence in josephson junction qubits measured in a three-dimensional circuit qed architecture.” *Phys. Rev. Lett.*, **107**, 240501 (2011). Cited on pages 101 and 181.
- [Palacios-Laloy10] A. Palacios-Laloy, F. Mallet, F. Nguyen, P. Bertet, D. Vion, D. Esteve, and A. N. Korotkov. “Experimental violation of a bell’s inequality in time with weak measurement.” *Nat. Phys.*, **advance online publication**, – (2010). Cited on page 4.
- [Pan98] J.-W. Pan, D. Bouwmeester, H. Weinfurter, and A. Zeilinger. “Experimental entanglement swapping: Entangling photons that never interacted.” *Phys. Rev. Lett.*, **80**, 3891– (1998). Cited on page 182.
- [Pappas11] D. Pappas, M. Vissers, D. Wisbey, J. Kline, and J. Gao. “Two level system loss in superconducting microwave resonators.” *Applied Superconductivity, IEEE Transactions on*, **21**, 871 –874 (2011). Cited on page 54.
- [Pittman05] T. B. Pittman, B. C. Jacobs, and J. D. Franson. “Demonstration of quantum error correction using linear optics.” *Phys. Rev. A*, **71**, 052332 (2005). Cited on page 3.
- [Plenio07] M. B. Plenio and S. Virmani. “An introduction to entanglement measures.” *Quantum Information & Computation*, **7**, 1–51 (2007). Cited on page 195.
- [Politi09] A. Politi, J. C. F. Matthews, and J. L. O’Brien. “Shor’s quantum factoring algorithm on a photonic chip.” *Science*, **325**, 1221 (2009). Cited on page 3.
- [Poyatos97] J. F. Poyatos, J. I. Cirac, and P. Zoller. “Complete characterization of a quantum process: The two-bit quantum gate.” *Phys. Rev. Lett.*, **78**, 390– (1997). Cited on page 190.
- [Pojar93] D. M. Pojar. *Microwave Engineering*. Addison-Wesley Publishing Company (1993). Cited on pages 48, 84 and 125.

- [Purcell46] E. M. Purcell. “Spontaneous emission probabilities at radio frequencies.” *Phys. Rev.*, **69**, 681 (1946). Cited on pages 37 and 44.
- [Raimond01] J. M. Raimond, M. Brune, and S. Haroche. “Manipulating quantum entanglement with atoms and photons in a cavity.” *Rev. Mod. Phys.*, **73**, 565–582 (2001). Cited on page 36.
- [Ralph07] T. C. Ralph, K. J. Resch, and A. Gilchrist. “Efficient toffoli gates using qudits.” *Phys. Rev. A*, **75**, 022313 (2007). Cited on page 170.
- [Ramsey50] N. F. Ramsey. “A molecular beam resonance method with separated oscillating fields.” *Phys. Rev.*, **78**, 695–699 (1950). Cited on page 102.
- [Raussendorf01] R. Raussendorf and H. J. Briegel. “A one-way quantum computer.” *Phys. Rev. Lett.*, **86**, 5188–5191 (2001). Cited on page 158.
- [Reed10] M. D. Reed, L. DiCarlo, B. R. Johnson, L. Sun, D. I. Schuster, L. Frunzio, and R. J. Schoelkopf. “High-fidelity readout in circuit quantum electrodynamics using the jaynes-cummings nonlinearity.” *Phys. Rev. Lett.*, **105**, 173601 (2010). Cited on page 4.
- [Reed12] M. D. Reed, L. DiCarlo, S. E. Nigg, L. Sun, L. Frunzio, S. M. Girvin, and R. J. Schoelkopf. “Realization of three-qubit quantum error correction with superconducting circuits.” *Nature*, **482**, 382–385 (2012). Cited on pages 3, 4, 47, 165, 170 and 182.
- [Riebe04] M. Riebe, H. Häffner, C. F. Roos, W. Hänsel, J. Benhelm, G. P. T. Lancaster, T. W. Körber, C. Becher, F. Schmidt-Kaler, D. F. V. James, and R. Blatt. “Deterministic quantum teleportation with atoms.” *Nature*, **429**, 734–737 (2004). Cited on page 156.
- [Riebe07] M. Riebe, M. Chwalla, J. Benhelm, H. Häffner, W. Hänsel, C. F. Roos, and R. Blatt. “Quantum teleportation with atoms: quantum process tomography.” *New J. Phys.*, **9**, 211 (2007). Cited on page 156.
- [Rigetti12] C. Rigetti, J. M. Gambetta, S. Poletto, B. L. T. Plourde, J. M. Chow, A. D. Córcoles, J. A. Smolin, S. T. Merkel, J. R. Rozen, G. A. Keefe, M. B. Rothwell, M. B. Ketchen, and M. Steffen. “Superconducting

- qubit in a waveguide cavity with a coherence time approaching 0.1 ms.” *Phys. Rev. B*, **86**, 100506– (2012). Cited on page 181.
- [Rigolin05] G. Rigolin. “Quantum teleportation of an arbitrary two-qubit state and its relation to multipartite entanglement.” *Phys. Rev. A*, **71**, 032303 (2005). Cited on page 182.
- [Roos04] C. F. Roos, G. P. T. Lancaster, M. Riebe, H. Häffner, W. Hänsel, S. Gulde, C. Becher, J. Eschner, F. Schmidt-Kaler, and R. Blatt. “Bell states of atoms with ultralong lifetimes and their tomographic state analysis.” *Phys. Rev. Lett.*, **92**, 220402 (2004). Cited on page 136.
- [Saffman10] M. Saffman, T. G. Walker, and K. Mølmer. “Quantum information with Rydberg atoms.” *Rev. Mod. Phys.*, **82**, 2313–2363 (2010). Cited on page 3.
- [Sandberg08] M. Sandberg, C. Wilson, F. Persson, G. Johansson, V. Shumeiko, T. Duty, and P. Delsing. “In-situ frequency tuning of photons stored in a high q microwave cavity.” (2008). Cited on page 163.
- [Santavicca08] D. F. Santavicca and D. E. Prober. “Impedance-matched low-pass stripline filters.” *Meas. Sci. Technol.*, **19**, 087001 (2008). Cited on pages 65 and 76.
- [Sayrin11] C. Sayrin, I. Dotsenko, X. Zhou, B. Peaudecerf, T. Rybarczyk, S. Gleyzes, P. Rouchon, M. Mirrahimi, H. Amini, M. Brune, J.-M. Raimond, and S. Haroche. “Real-time quantum feedback prepares and stabilizes photon number states.” *Nature*, **477**, 73–77 (2011). Cited on page 38.
- [Schindler11] P. Schindler, J. T. Barreiro, T. Monz, V. Nebendahl, D. Nigg, M. Chwalla, M. Hennrich, and R. Blatt. “Experimental repetitive quantum error correction.” *Science*, **332**, 1059–1061 (2011). Cited on page 3.
- [Schmidt-Kaler03] F. Schmidt-Kaler, H. Häffner, M. Riebe, S. Gulde, G. Lancaster, T. Deuschle, C. Becher, C. Roos, J. Eschner, and R. Blatt. “Realization of the Cirac-Zoller controlled-not quantum gate.” *Nature*, **422**, 408–411 (2003). Cited on pages 120 and 138.

- [Schuda74] F. Schuda, C. R. Stroud, Jr, and M. Hercher. “Observation of the resonant stark effect at optical frequencies.” *Journal of Physics B: Atomic and Molecular Physics*, **7**, L198 (1974). Cited on page 94.
- [Schuster05] D. I. Schuster, A. Wallraff, A. Blais, L. Frunzio, R.-S. Huang, J. Majer, S. M. Girvin, and R. J. Schoelkopf. “AC Stark shift and dephasing of a superconducting qubit strongly coupled to a cavity field.” *Physical Review Letters*, **94**, 123602 (2005). Cited on pages 43, 89 and 129.
- [Schuster07a] D. I. Schuster. *Circuit Quantum Electrodynamics*. Ph.D. thesis, Yale University (2007). Cited on pages 38 and 71.
- [Schuster07b] D. I. Schuster, A. A. Houck, J. A. Schreier, A. Wallraff, J. M. Gambetta, A. Blais, L. Frunzio, J. Majer, B. Johnson, M. H. Devoret, S. M. Girvin, and R. J. Schoelkopf. “Resolving photon number states in a superconducting circuit.” *Nature*, **445**, 515–518 (2007). Cited on pages 44 and 89.
- [Schuster08] I. Schuster, A. Kubanek, A. Fuhrmanek, T. Puppe, P. W. H. Pinkse, K. Murr, and G. Rempe. “Nonlinear spectroscopy of photons bound to one atom.” *Nat. Phys.*, **4**, 382–385 (2008). Cited on page 40.
- [Sendelbach09] S. Sendelbach, D. Hover, M. Mück, and R. McDermott. “Complex inductance, excess noise, and surface magnetism in dc squids.” *Phys. Rev. Lett.*, **103**, 117001 (2009). Cited on page 78.
- [Shor94] P. W. Shor. “Algorithms for quantum computation: Discrete logarithms and factoring.” In “Proceedings, 35th Annual Symposium on Foundations of Computer Science, Santa Fe,” 124. IEEE Computer Society Press (1994). Cited on page 2.
- [Shor95] P. W. Shor. “Scheme for reducing decoherence in quantum computer memory.” *Phys. Rev. A*, **52**, R2493–R2496 (1995). Cited on page 2.
- [Sillanpää07] M. A. Sillanpää, J. I. Park, and R. W. Simmonds. “Coherent quantum state storage and transfer between two phase qubits via a resonant cavity.” *Nature*, **449**, 438–442 (2007). Cited on page 4.

- [Sillanpää09] M. A. Sillanpää, J. Li, K. Cicak, F. Altomare, J. I. Park, R. W. Simmonds, G. S. Paraoanu, and P. J. Hakonen. “Autler-Townes effect in a superconducting three-level system.” *Phys. Rev. Lett.*, **103**, 193601 (2009). Cited on pages 4 and 95.
- [Simons01] R. N. Simons. *Coplanar waveguide circuits, components and systems*. Wiley Series in Microwave and Optical Engineering. Wiley Inter-Science (2001). Cited on page 53.
- [Smolin12] J. A. Smolin, J. M. Gambetta, and G. Smith. “Efficient method for computing the maximum-likelihood quantum state from measurements with additive gaussian noise.” *Phys. Rev. Lett.*, **108**, 070502 (2012). Cited on pages 114, 158 and 189.
- [Sørensen99] A. Sørensen and K. Mølmer. “Quantum computation with ions in thermal motion.” *Phys. Rev. Lett.*, **82**, 1971–1974 (1999). Cited on page 120.
- [Steane96a] A. Steane. “Multiple-particle interference and quantum error correction.” *Proceedings of the Royal Society of London. Series A: Mathematical, Physical and Engineering Sciences*, **452**, 2551–2577 (1996). Cited on page 182.
- [Steane96b] A. M. Steane. “Simple quantum error-correcting codes.” *Phys. Rev. A*, **54**, 4741–4751 (1996). Cited on page 2.
- [Steffen11] M. Steffen. “Superconducting qubits are getting serious.” *Physics*, **4**, 103 (2011). Cited on page 101.
- [Strauch03] F. W. Strauch, P. R. Johnson, A. J. Dragt, C. J. Lobb, J. R. Anderson, and F. C. Wellstood. “Quantum logic gates for coupled superconducting phase qubits.” *Phys. Rev. Lett.*, **91**, 167005– (2003). Cited on pages 119, 138 and 146.
- [Takeuchi00] S. Takeuchi. “Experimental demonstration of a three-qubit quantum computation algorithm using a single photon and linear optics.” *Phys. Rev. A*, **62**, 032301– (2000). Cited on page 3.
- [Tamarat95] P. Tamarat, B. Lounis, J. Bernard, M. Orrit, S. Kummer, R. Kettner, S. Mais, and T. Basche. “Pump-probe experiments with a single-

- molecule-ac-stark effect and nonlinear-optical response.” *Phys. Rev. Lett.*, **75**, 15141517 (1995). Cited on page 95.
- [Taylor67] B. N. Taylor, W. H. Parker, D. N. Langenberg, and A. Denenstein. “On the use of the ac josephson effect to maintain standards of electromotive force.” *Metrologia*, **3**, 89 (1967). Cited on page 23.
- [Thompson92] R. J. Thompson, G. Rempe, and H. J. Kimble. “Observation of normal-mode splitting for an atom in an optical cavity.” *Phys. Rev. Lett.*, **68**, 1132–1135 (1992). Cited on page 38.
- [Tinkham96] M. Tinkham. *Introduction to Superconductivity*. McGraw-Hill International Editions (1996). Cited on pages 21, 22, 27 and 30.
- [Tuorila10] J. Tuorila, M. Silveri, M. Sillanpää, E. Thuneberg, Y. Makhlin, and P. Hakonen. “Stark effect and generalized bloch-siegert shift in a strongly driven two-level system.” *Phys. Rev. Lett.*, **105**, 257003 (2010). Cited on page 95.
- [Turing37] A. M. Turing. “On computable numbers, with an application to the entscheidungsproblem.” *Proceedings of the London Mathematical Society*, **s2-42**, 230–265 (1937). Cited on page 1.
- [Uhlmann98] A. Uhlmann. “Entropy and optimal decompositions of states relative to a maximal commutative subalgebra.” *Open Systems & Information Dynamics*, **5**, 209–228 (1998). Cited on pages 161 and 196.
- [Vandersypen01] L. M. K. Vandersypen, M. Steffen, G. Breyta, C. S. Yannoni, M. H. Sherwood, and I. L. Chuang. “Experimental realization of Shor’s quantum factoring algorithm using nuclear magnetic resonance.” *Nature*, **414**, 883 (2001). Cited on page 3.
- [Vandersypen04] L. M. K. Vandersypen and I. L. Chuang. “Nmr techniques for quantum control and computation.” *Rev. Mod. Phys.*, **76**, 1037 (2004). Cited on page 3.
- [vanderWal00] C. H. van der Wal, A. C. J. ter Haar, F. K. Wilhelm, R. N. Schouten, C. J. P. M. Harmans, T. P. Orlando, S. Lloyd, and J. E. Mooij. “Quantum superposition of macroscopic persistent-current states.” *Science*, **290**, 773–777 (2000). Cited on pages 19 and 20.

- [Vaughan72] R. W. Vaughan, D. D. Elleman, L. M. Stacey, W.-K. Rhim, and J. W. Lee. “A simple, low power, multiple pulse nmr spectrometer.” *Review of Scientific Instruments*, **43**, 1356–1364 (1972). Cited on page 108.
- [Vijay11] R. Vijay, D. H. Slichter, and I. Siddiqi. “Observation of quantum jumps in a superconducting artificial atom.” *Phys. Rev. Lett.*, **106**, 110502 (2011). Cited on pages 4 and 163.
- [Vion02] D. Vion, A. Aassime, A. Cottet, P. Joyez, H. Pothier, C. Urbina, D. Esteve, and M. H. Devoret. “Manipulating the quantum state of an electrical circuit.” *Science*, **296**, 886–889 (2002). Cited on pages 20, 33 and 140.
- [Vion03] D. Vion, A. Aassime, A. Cottet, P. Joyez, H. Pothier, C. Urbina, D. Esteve, and M. H. Devoret. “Rabi oscillations, ramsey fringes and spin echoes in an electrical circuit.” *Fortschritte der Physik*, **51**, 462–468 (2003). Cited on pages 33 and 140.
- [Voss81] R. F. Voss and R. A. Webb. “Macroscopic quantum tunneling in 1- μm Nb Josephson junctions.” *Phys. Rev. Lett.*, **47**, 265 (1981). Cited on page 18.
- [Walker95] B. Walker, M. Kaluza, B. Sheehy, P. Agostini, and L. F. Dimauero. “Observation of continuum-continuum autler-townes splitting.” *Phys. Rev. Lett.*, **75**, 633636 (1995). Cited on page 95.
- [Wallraff04] A. Wallraff, D. I. Schuster, A. Blais, L. Frunzio, R.-S. Huang, J. Majer, S. Kumar, S. M. Girvin, and R. J. Schoelkopf. “Strong coupling of a single photon to a superconducting qubit using circuit quantum electrodynamics.” *Nature*, **431**, 162–167 (2004). Cited on pages 4, 38, 88 and 96.
- [Wallraff05] A. Wallraff, D. I. Schuster, A. Blais, L. Frunzio, J. Majer, S. M. Girvin, and R. J. Schoelkopf. “Approaching unit visibility for control of a superconducting qubit with dispersive readout.” *Phys. Rev. Lett.*, **95**, 060501 (2005). Cited on pages 17, 46 and 139.
- [Wallraff07] A. Wallraff, D. I. Schuster, A. Blais, J. M. Gambetta, J. Schreier, L. Frunzio, M. H. Devoret, S. M. Girvin, and R. J. Schoelkopf.

- “Sideband transitions and two-tone spectroscopy of a superconducting qubit strongly coupled to an on-chip cavity.” *Physical Review Letters*, **99**, 050501 (2007). Cited on pages 119 and 120.
- [Wang11] H. Wang, M. Mariani, R. C. Bialczak, M. Lenander, E. Lucero, M. Neeley, A. D. O’Connell, D. Sank, M. Weides, J. Wenner, T. Yamamoto, Y. Yin, J. Zhao, J. M. Martinis, and A. N. Cleland. “Deterministic entanglement of photons in two superconducting microwave resonators.” *Phys. Rev. Lett.*, **106**, 060401 (2011). Cited on pages 4 and 123.
- [Wellstood87] F. Wellstood, C. Urbina, and J. Clarke. “Low frequency noise in dc superconducting quantum interference devices below 1k.” *Appl. Phys. Lett.*, **50**, 772 (1987). Cited on pages 75 and 78.
- [Wendin05] G. Wendin and V. Shumeiko. “Superconducting quantum circuits, qubits and computing.” *arXiv:cond-mat/0508729* (2005). Cited on page 27.
- [Wieman99] C. E. Wieman, D. E. Pritchard, and D. J. Wineland. “Atom cooling, trapping, and quantum manipulation.” *Rev. Mod. Phys.*, **71**, S253–S262 (1999). Cited on page 120.
- [Wilson07] C. M. Wilson, T. Duty, F. Persson, M. Sandberg, G. Johansson, and P. Delsing. “Coherence times of dressed states of a superconducting qubit under extreme driving.” *Phys. Rev. Lett.*, **98**, 257003 (2007). Cited on page 95.
- [Wisbey10] D. S. Wisbey, J. Gao, M. R. Vissers, F. C. S. da Silva, J. S. Kline, L. Vale, and D. P. Pappas. “Effect of metal/substrate interfaces on radio-frequency loss in superconducting coplanar waveguides.” *J. Appl. Phys.*, **108**, 093918 (2010). Cited on page 54.
- [Wootters82] W. K. Wootters and W. H. Zurek. “A single quantum cannot be cloned.” *Nature*, **299**, 802–803 (1982). Cited on page 166.
- [Wootters98] W. K. Wootters. “Entanglement of formation of an arbitrary state of two qubits.” *Phys. Rev. Lett.*, **80**, 2245–2248 (1998). Cited on pages 136, 138, 196 and 197.

- [Wrigge08] G. Wrigge, I. Gerhardt, J. Hwang, G. Zumofen, and V. Sandoghdar. “Efficient coupling of photons to a single molecule and the observation of its resonance fluorescence.” *Nat. Phys.*, **4**, 60–66 (2008). Cited on page 95.
- [Xu07] X. D. Xu, B. Sun, P. R. Berman, D. G. Steel, A. S. Bracker, D. Gammon, and L. J. Sham. “Coherent optical spectroscopy of a strongly driven quantum dot.” *Science*, **317**, 929–932 (2007). Cited on page 95.
- [Yamamoto10] T. Yamamoto, M. Neeley, E. Lucero, R. C. Bialczak, J. Kelly, M. Lenander, M. Mariantoni, A. D. O’Connell, D. Sank, H. Wang, M. Weides, J. Wenner, Y. Yin, A. N. Cleland, and J. M. Martinis. “Quantum process tomography of two-qubit controlled-z and controlled-not gates using superconducting phase qubits.” *Phys. Rev. B*, **82**, 184515 (2010). Cited on pages 4, 15, 119, 138, 139, 146, 151, 156 and 181.
- [Yoshihara06] F. Yoshihara, K. Harrabi, A. O. Niskanen, Y. Nakamura, and J. S. Tsai. “Decoherence of flux qubits due to $1/f$ flux noise.” *Phys. Rev. Lett.*, **97**, 167001 (2006). Cited on page 78.
- [Yoshihara10] F. Yoshihara, Y. Nakamura, and J. S. Tsai. “Correlated flux noise and decoherence in two inductively coupled flux qubits.” *Phys. Rev. B*, **81**, 132502– (2010). Cited on page 78.
- [Yurke84] B. Yurke and J. S. Denker. “Quantum network theory.” *Phys. Rev. A*, **29**, 1419–1437 (1984). Cited on page 19.
- [Zhou00] X. Zhou, D. W. Leung, and I. L. Chuang. “Methodology for quantum logic gate construction.” *Phys. Rev. A*, **62**, 052316 (2000). Cited on page 156.
- [Żukowski93] M. Żukowski, A. Zeilinger, M. A. Horne, and A. K. Ekert. ““event-ready-detectors” bell experiment via entanglement swapping.” *Phys. Rev. Lett.*, **71**, 4287–4290 (1993). Cited on page 182.

List of Publications

Most Relevant Publications for this Thesis

1. M. Baur, A. Fedorov, L. Steffen, S. Filipp, M. P. da Silva, and A. Wallraff. “Benchmarking a Quantum Teleportation Protocol in Superconducting Circuits Using Tomography and an Entanglement Witness.” *Phys. Rev. Lett.*, **108**, 040502 (2012)
2. M. Baur, S. Filipp, R. Bianchetti, J. M. Fink, M. Göppl, L. Steffen, P. J. Leek, A. Blais, and A. Wallraff. “Measurement of Autler-Townes and Mollow transitions in a strongly driven superconducting qubit.” *Phys. Rev. Lett.*, **102**, 243602-4 (2009)
3. A. Fedorov, L. Steffen, M. Baur, M. P. da Silva, and A. Wallraff. “Implementation of a Toffoli gate with superconducting circuits.” *Nature*, **481**, 170-172 (2012)
4. P. J. Leek, M. Baur, J. M. Fink, R. Bianchetti, L. Steffen, S. Filipp, and A. Wallraff. “Cavity QED with separate photon storage and qubit readout modes.” *Phys. Rev. Lett.*, **104**, 100504 (2010)
5. P. J. Leek, S. Filipp, P. Maurer, M. Baur, R. Bianchetti, J. M. Fink, M. Goepl, L. Steffen, and A. Wallraff. “Using Sideband Transitions for Two-Qubit Operations in Superconducting Circuits.” *Phys. Rev. B*, **79**, 180511(R) (2009)
6. S. Filipp, P. Maurer, P. J. Leek, M. Baur, R. Bianchetti, J. M. Fink, M. Goepl, L. Steffen, J. M. Gambetta, A. Blais and A. Wallraff. “Two-Qubit State

Tomography using a Joint Dispersive Read-Out.” *Phys. Rev. Lett.*, **102**, 200402 (2009)

Other Publications

1. S. Filipp, A. F. van Loo, M. Baur, L. Steffen, and A. Wallraff. “Preparation of Subradiant States using Local Qubit Control in Circuit QED.” *Phys. Rev. A*, **84**, 061805(R) (2011)
2. C. Eichler, D. Bozyigit, C. Lang, M. Baur, L. Steffen, J. M. Fink, S. Filipp, and A. Wallraff. “Photon State Tomography for Two-Mode Correlated Itinerant Microwave Fields.” *Phys. Rev. Lett.*, **107**, 113601 (2011)
3. S. Filipp, M. Göppl, J. M. Fink, M. Baur, R. Bianchetti, L. Steffen, and A. Wallraff. “Multi-Mode Mediated Qubit-Qubit Coupling and Dark-State Symmetries in Circuit Quantum Electrodynamics.” *Phys. Rev. A*, **83**, 063827 (2011)
4. C. Lang, D. Bozyigit, C. Eichler, L. Steffen, J. M. Fink, A. A. Abdumalikov, M. Baur, S. Filipp, M. P. da Silva, A. Blais and A. Wallraff. “Observation of Resonant Photon Blockade at Microwave Frequencies using Correlation Function Measurements.” *Phys. Rev. Lett.*, **106**, 243601 (2011)
5. D. Bozyigit, C. Lang, L. Steffen, J. M. Fink, C. Eichler, M. Baur, R. Bianchetti, P. J. Leek, S. Filipp, M. P. da Silva, A. Blais, and A. Wallraff. “Antibunching of Microwave Frequency Photons observed in Correlation Measurements using Linear Detectors.” *Nat. Phys.*, **7**, 154-158 (2011)
6. D. Bozyigit, C. Lang, L. Steffen, J. M. Fink, C. Eichler, M. Baur, R. Bianchetti, P. J. Leek, S. Filipp, M. P. da Silva, A. Blais, and A. Wallraff. “Correlation Measurements of Individual Microwave Photons Emitted from a Symmetric Cavity.” *J. Phys.: Conf. Ser.*, **264**, 012024 (2011)
7. R. Bianchetti, S. Filipp, M. Baur, J. M. Fink, C. Lang, L. Steffen, M. Boissonneault, A. Blais, and A. Wallraff. “Control and Tomography of a Three Level Superconducting Artificial Atom.” *Phys. Rev. Lett.*, **105**, 223601 (2010)
8. J. M. Fink, L. Steffen, P. Studer, Lev S. Bishop, M. Baur, R. Bianchetti, D. Bozyigit, C. Lang, S. Filipp, P. J. Leek, and A. Wallraff. “Quantum-To-

Classical Transition in Cavity Quantum Electrodynamics.” *Phys. Rev. Lett.*, **105**, 163601 (2010)

9. J. M. Fink, M. Baur, R. Bianchetti, S. Filipp, M. Göppl, P. J. Leek, L. Steffen, A. Blais, and A. Wallraff. “Thermal Excitation of Multi-Photon Dressed States in Circuit Quantum Electrodynamics” *Phys. Scr.*, **T137**, 014013 (2009)
10. R. Bianchetti, S. Filipp, M. Baur, J. M. Fink, M. Goepl, P. J. Leek, L. Steffen, A. Blais, and A. Wallraff. “Dynamics of dispersive single qubit read-out in circuit quantum electrodynamics.” *Phys. Rev. A*, **80**, 043840 (2009)
11. J. M. Fink, R. Bianchetti, M. Baur, M. Goepl, L. Steffen, S. Filipp, P. J. Leek, A. Blais, and A. Wallraff. “Dressed Collective Qubit States and the Tavis-Cummings Model in Circuit QED.” *Phys. Rev. Lett.*, **103**, 083601 (2009)
12. A. Fragner, M. Goepl, J. M. Fink, M. Baur, R. Bianchetti, P. J. Leek, A. Blais, and A. Wallraff. “Resolving Vacuum Fluctuations in an Electrical Circuit by Measuring the Lamb Shift.” *Science*, **322**, 1357-1360 (2008)
13. M. Göppl, A. Fragner, M. Baur, R. Bianchetti, S. Filipp, J. M. Fink, P. J. Leek, G. Puebla, L. Steffen, and A. Wallraff. “Coplanar Waveguide Resonators for Circuit Quantum Electrodynamics.” *J. Appl. Phys.*, **104**, 113904 (2008)
14. J. M. Fink, M. Göppl, M. Baur, R. Bianchetti, P. J. Leek, A. Blais, and A. Wallraff. “Climbing the Jaynes-Cummings ladder and observing its square root of n nonlinearity in a cavity QED system.” *Nature*, **454**, 315-318 (2008)

Acknowledgements

The work presented in this thesis would never have been possible without the help and support of numerous people. I would therefore like to take this opportunity to express my personal thank to all of them for their collaboration.

First and foremost, I want to thank my supervisor ANDREAS WALLRAFF for giving me the opportunity to work in his Quantum Device Lab on the exciting field of quantum information processing with superconducting quantum bits. I have not only profited from his scientific skills and exceptionally good experimental intuition, but also from his steady encouragement and time to teach me how to write scientific reports. I also like to thank PETER LEEK, with whom I worked together on the sideband project. I was always amazed about how fast he understands the problems and finds the right ideas when discussing the experiments with him. A great help during the final year was ARKADY FEDOROV, working together with me and LARS STEFFEN on the teleportation experiment and the realization of the Toffoli gate. He was not only extremely helpful whenever I had troubles with theory, but he also kept providing new ideas for experiments. I also thank him, JOOANS GOVENIUS and JONAS MLYNEK to remind me about the beauty of rock climbing and for the enjoyable climbing trips we have spent together in the Swiss Alps or nearby Zurich. I should also thank STEFAN FILIPP for his patience whenever I came to him with my theory questions, WILL ZENG who was an undergraduate at Yale University and joined our lab for a summer project, working together with me on quantum process tomography. Thanks to LARS STEFFEN for working on the realization of the Toffoli gate, the mask designs and the photolithography part of the sample fabrication. Thanks to JOHANNES FINK and MARTIN GÖPPL for teaching me how to make transmon qubits with nanolithography techniques and fabricating the first samples, and to ROMEO BIANCHETTI who worked together with JOHANNES on the installation and setup of the dilution refrigerator. I am also very grateful for ABDUFARRUKH ABDUMALIKOV's help on solving cryostat problems in the middle of the night and for CHRISTIAN LANG's Labview programming skills. Finally I want to express my gratitude to ALEXANDRE BLAIS from the Université de Sherbrooke and MARCUS DA SILVA for fruitful collaborations, and DENIS VION from CEA-Saclay for taking his time to co-supervise my thesis.

Last but not least, I also want to thank my parents, who always supported me in studying physics and showed great interest in my scientific research done for this thesis.

Curriculum Vitae

Personal Data

Name: Matthias Tobias Baur
Date of birth: 21st of September 1983
Nationality: Swiss

Education

2008 - 2012 Ph.D. studies at *ETH Zurich*
Thesis: "Realizing Quantum Gates and Algorithms with Three Superconducting Qubits"
Examiner: Prof. Dr. Andreas Wallraff
Co-examiner: Dr. Denis Vion

2002 - 2007 Master of Science ETH (Physics)
Master Thesis: "Quantum Electrodynamics with Superconducting Circuits: Measurement of the Cavity Photon Number using Ramsey Interference"

1998 - 2002 Matura, mathematisch-naturwissenschaftliches Profil, Kantonsschule Im Lee, Winterthur

Work Experience

2008-2011 Research Assistant and Teaching Assistant
Department of Physics, ETH Zurich, Solid State Physics

Fall 2006 Teaching Assistant
ETH Zurich, Mathematics 1 for chemists and biologists.